GEMS & GEMOLOGY

FALL 2023
VOLUME LIX

THE QUARTERLY JOURNAL OF THE GEMOLOGICAL INSTITUTE OF AMERICA

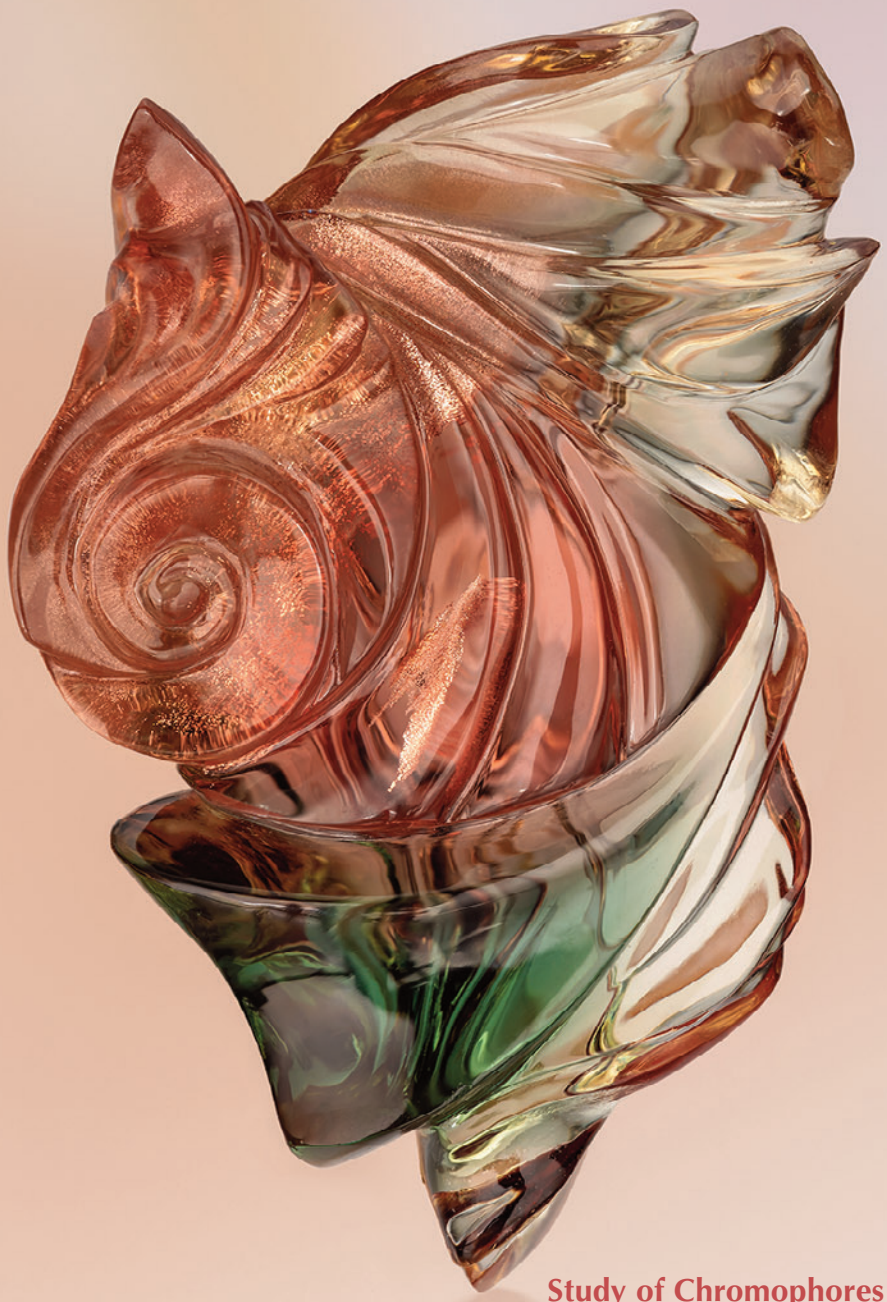

Study of Chromophores in Yellow Sapphire
Colors and Optical Effects of Oregon Sunstone
Analysis of Etch Pits in Ukrainian Beryl
Iolite from British Columbia

GEMS & GEMOLOGY®
Fall 2023
VOLUME 59, No. 3


p. 284

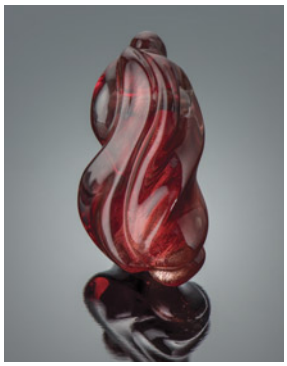
p. 320


p. 348


p. 364


p. 378


p. 380

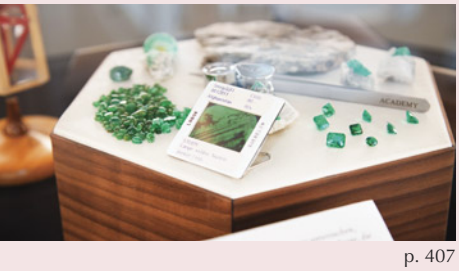
p. 407

Editorial

Feature Articles

Regular Features

GEMS & GEMOLOGY®

gia.edu/gems-gemology

Customer Service
(760) 603-4200
gandg@gia.edu

Subscriptions
Copies of the current issue may be purchased for $29.95 plus shipping. Subscriptions are $79.99 for one year (4 issues) in the U.S. and $99.99 elsewhere. Canadian subscribers should add GST. Discounts are available for renewals, group subscriptions, GIA alumni, and current GIA students. To purchase print subscriptions, visit store.gia.edu or contact Customer Service. For institutional rates, contact Customer Service.

Database Coverage
Gems & Gemology's impact factor is 2.6, according to the 2022 Journal Citation Reports by Clarivate Analytics (issued June 2023). *G&G* is abstracted in Thomson Reuters products (Current Contents: Physical, Chemical & Earth Sciences and Science Citation Index—Expanded, including the Web of Knowledge) and other databases. For a complete list of sources abstracting *G&G*, go to gia.edu/gems-gemology, and click on "Publication Information."

Manuscript Submissions
Gems & Gemology, a peer-reviewed journal, welcomes the submission of articles on all aspects of the field. Please see the Author Guidelines at gia.edu/gems-gemology or contact the Managing Editor. Letters on articles published in *G&G* are also welcome. Please note that Field Reports, Lab Notes, Gem News International, Micro-World, Colored Stones Unearthed, Diamond Reflections, Charts, and In the Spotlight are not peer-reviewed sections but do undergo technical and editorial review.

Gems & Gemology is published quarterly by the Gemological Institute of America, a nonprofit educational organization for the gem and jewelry industry.

Postmaster: Return undeliverable copies of *Gems & Gemology* to GIA, The Robert Mouawad Campus, 5345 Armada Drive, Carlsbad, CA 92008.

Our Canadian goods and service registration number is 126142892RT.

About the Cover

"The Rose," Darryl Alexander's 52 ct sunstone carving, displays three distinct areas of color: reddish orange, yellow, and green. Carved from rough uncovered in the Sunstone Butte mine in Harney County, Oregon, the piece exhibits the schiller effect, also known as aventurescence, caused by reflective copper platelets. Schiller and other optical effects of Oregon sunstone are explored in a study featured in this issue. Photo by Robert Weldon; courtesy of Darryl Alexander.

Printing is by L+L Printers, Carlsbad, CA.

GIA World Headquarters The Robert Mouawad Campus 5345 Armada Drive Carlsbad, CA 92008 USA

ISSN 0016-626X

FSC www.fsc.org MIX Paper from responsible sources FSC® C006300

Cause of Color in Yellow Sapphire, Plus Characterization of Oregon Sunstone, Ukrainian Beryl, and British Columbian Iolite

Welcome to the Fall 2023 issue of *Gems & Gemology*! This issue delivers four feature articles covering a range of colored stone topics, from a color study of yellow sapphire to a new source of violet-blue iolite in Canada.

In our lead article, Dr. John Emmett and coauthors investigate the various chromophores responsible for color in four types of yellow sapphire—natural, heat-treated, beryllium-diffused, and synthetic. These chromophores include Fe^{3+}, a trapped hole associated with iron ($h^{\bullet}$-Fe^{3+}), and a combination of the two, all of which are involved in the coloration of natural and treated yellow sapphire. Synthetic yellow sapphire, on the other hand, is usually colored by the Ni^{3+} chromophore or by a combination of Ni^{3+} and Cr^{3+}.

"...investigate the various chromophores responsible for color in four types of yellow sapphire—natural, heat-treated, beryllium-diffused, and synthetic."

Next, Dr. Shiyun Jin and colleagues share their research on the special colors and optical effects caused by metallic copper inclusions in Oregon sunstone. Using samples from different mines in Oregon, they explore absorption and scattering, pleochroism, and color zoning in this gem-quality feldspar known for its wide range of beautiful colors.

A team led by Dr. Gerhard Franz reports on the morphological characteristics of green beryl and the yellow beryl variety heliodor from the Volyn pegmatite field in Ukraine. The authors observe an abundance of characteristic etch pits throughout the samples and offer details on distinguishing Volyn green beryl and heliodor from those found in other localities.

Dr. Philippe Belley contributes our final feature article, an examination of violet-blue iolite from new deposits in the Thor-Odin dome in British Columbia, Canada. Various samples are analyzed to reveal the nature of their chemical composition, mineral and fluid inclusions, and chatoyancy. The abundance of cordierite-rich rocks in the Thor-Odin dome indicates potential for future iolite discoveries in the area.

G&G's regular columns contain exciting gemological findings from all over the world. *Lab Notes* details recent noteworthy submissions to GIA's laboratories, including a 4.04 ct ring fashioned from a single-crystal CVD-grown diamond, a nacreous atypical bead cultured pearl featuring a flame-like surface structure, and a heart-shaped ruby filled with zinc glass. Observations of fascinating internal features are captured in the *Micro-World* section, including a rare iridescent ferropericlase in brown diamond, bladed columbite crystals in topaz, and zigzag-patterned fingerprints in blue sapphire. *Diamond Reflections* returns in this issue, focusing on diamonds formed within eclogitic mantle host rocks. Finally, *Gem News International* offers brief studies of Burmese chameleon amber, Guatemalan omphacite jade, and other gem materials, as well as coverage of the recent Turquoise United conference and the Chicago Responsible Jewelry Conference.

Congratulations to this year's *G&G* Challenge participants who received a perfect score! See a list of the top scorers on page 322. Thank you to those who put their knowledge to the test.

We hope you enjoy the latest edition of *Gems & Gemology*!

Duncan Pay | Editor-in-Chief | dpay@gia.edu

YELLOW SAPPHIRE: NATURAL, HEAT-TREATED, BERYLLIUM-DIFFUSED, AND SYNTHETIC

John L. Emmett, Ungkhana Atikarnsakul, Jennifer Stone-Sundberg, and Supharart Sangsawong

Natural yellow sapphires are colored by one of two entirely different chromophores or by a combination of the two. These two chromophores are iron (Fe^{3+}) and a trapped hole paired with iron ($h^{\bullet}$-Fe^{3+}). The color saturation of the Fe^{3+} chromophore, as previously documented, does not linearly depend on its areal density, unlike the other five chromophores in natural corundum. It exhibits a complex dependence on areal density, a relationship that is explored here. Low-iron-content natural yellow sapphires are colored solely by the $h^{\bullet}$-Fe^{3+} chromophore. The yellow sapphires from Sri Lanka are colored in this way. Some of the basalt-hosted high-iron sapphires from Australia and Thailand are colored by $h^{\bullet}$-Fe^{3+} in addition to Fe^{3+}. Natural sapphires that are colorless or weakly yellow often develop strong yellow coloration via heat treatment. They depend on formation of the $h^{\bullet}$-Fe^{3+} chromophore for that change. In these natural stones that respond to heat treatment, one of two different internal chemistries is present, which must be altered to bring about the color enhancement. These two chemistries, which require two different heat treatment processes, are presented. The diffusion of beryllium into various types of sapphire can shift their chemistry from donor- to acceptor-dominated, forming the trapped hole, $h^{\bullet}$, which pairs with iron to produce the intense yellow coloration. Although crystals with the $h^{\bullet}$-Fe^{3+} chromophore were grown as a part of our study, synthetic yellow sapphires are not often colored by the same chromophores of natural sapphires. They are usually colored by the Ni^{3+} chromophore or by Ni^{3+} and Cr^{3+}. Somewhat surprisingly, the color saturation of Czochralski-grown nickel-doped sapphire can sometimes be enhanced by heat treatment.

The complexities of yellow sapphire have been discussed in some detail for many years (e.g., Schmetzer et al., 1983; Nassau and Valente, 1987). A clear understanding of the nature of the multiple types of yellow sapphire was inhibited by the lack of understanding of the individual chromophores and their individual absorption spectra. The chromophores that cause yellow color in natural corundum have been recently elucidated (Emmett et al., 2017a; Dubinsky et al., 2020), allowing the more detailed study of yellow sapphire and its heat treatment, presented here. This work intends to provide a clear basis for future study of yellow sapphire and its individual color stabilities.

Yellow sapphires are found in a wide range of deposits worldwide. They are colored by two entirely different chromophores: the iron (Fe^{3+}) chromophore and the trapped hole paired with iron ($h^{\bullet}$-Fe^{3+})[1] (figure 1). These two chromophores represent the two extremes of natural chromophore strength in corundum. In faceted stones up to several carats, a few thousand ppma of Fe^{3+} are required for good coloration, while only a few ppma of $h^{\bullet}$-Fe^{3+} produce similar levels of color saturation (Dubinsky et al., 2020). It is not unusual for high-iron yellow sapphires from basalt-hosted deposits to be colored by both chromophores. In the past, the combination of these two chromophores in the same stone at dramatically different concentrations has impeded a complete understanding of the cause of color.

The $h^{\bullet}$-Fe^{3+} chromophore arises in natural stones that are acceptor dominated, meaning the divalent cation concentration exceeds the sum of the tetravalent cation concentration and the excess divalent cation concentration is not charge compensated by

See end of article for About the Authors and Acknowledgments.
GEMS & GEMOLOGY, Vol. 59, No. 3, pp. 268–297,
http://dx.doi.org/10.5741/GEMS.59.3.268

[1]The symbol $h^{\bullet}$ is the symbol for an electron hole in Kröger-Vink notation, and $h^{\bullet}$-Fe^{3+} means that the hole has paired with an Fe^{3+} ion. See box B.

Figure 1. These exceptional natural yellow sapphires from Madagascar (2.1–2.6 ct) represent both the Fe^{3+} chromophore and the trapped hole paired with Fe^{3+}. Photo by Ronnakorn Manorotkul/Lotus Gemology; courtesy of GemFever.

H^+ or oxygen vacancies. Because heating in an oxygen atmosphere can diffuse hydrogen out of the stone or oxidize the oxygen vacancies, colorless or weakly yellow stones can often be heat treated to create rich yellow gems.

The total amount of iron in natural corundum ranges from a few ppma to nearly 5000 ppma. Iron in natural corundum can exist in two valence states: Fe^{2+} and Fe^{3+}. The cation site in corundum is trivalent (Al^{3+}). When iron alone occupies this site, it will be primarily trivalent. For Fe^{2+} to exist in natural corundum, it must be charge compensated by a donor such as Si^{4+}, Ti^{4+}, H^+, or one-half of an oxygen vacancy, as the crystal must remain electrically neutral. Oxygen vacancies and H^+ only exist in natural corundum at low concentrations (a few ppma). Thus, any significant amount of Fe^{2+} can only exist if it is paired with Ti^{4+} or Si^{4+}. Concentrations of Ti^{4+} and Si^{4+} rarely exceed a few hundred ppma in natural corundum, and it is unclear how much of that is actually in solution in the lattice. Some portion of the Si^{4+} and Ti^{4+} will also have to preferentially charge compensate Mg^{2+} if present, as its level lies below that of Fe^{2+} in the band gap. Only Fe^{2+} charge compensated by H^+ ions or by oxygen vacancies would be expected to exhibit an Fe^{2+} spectrum. Such spectra are expected to be in the near-infrared region and be very weak. If charge compensated by Ti^{4+} or Si^{4+}, extremely strong pair spectra will result (e.g., the Fe^{2+}-Ti^{4+} pair resulting in the blue color of sapphire).

In Brief

- Natural yellow sapphires are colored by the iron (Fe^{3+}) chromophore or the trapped hole paired with iron ($h^{\bullet}$-Fe^{3+}) chromophore, or a combination of the two.
- Yellow coloration in colorless or weakly yellow sapphire can be developed via heat treatment in an oxygen atmosphere to form the $h^{\bullet}$-Fe^{3+} chromophore under two different conditions, depending on if the stone contains hydrogen or not.
- The addition of beryllium by diffusion in an oxidizing atmosphere can shift internal chemistry from donor- to acceptor-dominated, resulting in the formation of additional trapped holes ($h^{\bullet}$) to pair with available Fe^{3+} and thus a stronger yellow coloration.
- Unlike natural stones, synthetic yellow sapphires are usually colored by the Ni^{3+} chromophore or by Ni^{3+} and Cr^{3+}.

MATERIALS AND METHODS

The corundum samples in this study represent many different deposits around the world and were chosen from the Crystal Chemistry collection and GIA's colored stone reference collection in Bangkok. Samples with three- and four-digit designations are from the Crystal Chemistry collection, while those with nine- to twelve-digit designations are from GIA's colored stone reference collection. Samples used to characterize the Fe^{3+} and $h^{\bullet}$-Fe^{3+} chromophores originated from Myanmar, Thailand, Cambodia, Sri Lanka, Australia, Nigeria, Cameroon, Rwanda, Nigeria, Kenya, and the United States (Montana). Additionally, several synthetic crystals were grown using the Czochralski method by Saint-Gobain Crystals and Detectors and by Teledyne FLIR Scientific Materials. A yellow syn-

thetic nickel-doped sapphire grown using the Verneuil method was purchased from RusGems in Bangkok. All wafer samples were crystallographically oriented using a crystal alignment instrument with the *c*-axis either perpendicular or parallel to the plane of the wafer (Thomas et al., 2014). Trace element concentrations were determined either by laser ablation–inductively coupled plasma–mass spectrometry (LA-ICP-MS) using the current standards at GIA in Bangkok (Stone-Sundberg et al., 2017), by secondary ion mass spectrometry (SIMS) against ion implant standards at Caltech (Stone-Sundberg et al., 2020), or by both. In addition, ultraviolet/visible/near-infrared (UV-Vis-NIR) spectra of 102 of these wafer samples were measured, from which 24 were chosen for this study of the 450 nm Fe^{3+} band, as they represent equal concentration intervals of iron from most to least concentrated. Because the trace element concentrations in natural sapphires are often not uniform, the 24 samples used for the study of the Fe^{3+} chromophore were measured at four points on each side of the sample within the optical aperture of the sample plate. We required that the standard deviation of these eight data points be less than 6%. These sample selection criteria greatly minimized spatial concentration variations. The iron concentration in these samples covered the 56.5–4730 ppma region. The 450 nm Fe^{3+} absorption cross section[2] was too weak to accurately fit the curve below this lower value.

In addition, large samples (25–50 g each) of rough stones in the 3.5–7.0 mm range were used for many individual heat treatment experiments to test for acceptor domination before spectroscopic samples were chosen for these types of material. These stones were from the Rock Creek, Dry Cottonwood Creek, and Eldorado Bar deposits in Montana; Sri Lanka; the Chimwadzulu Hill deposit in Malawi; several Madagascar deposits; the Kings Plain deposit in New South Wales, Australia; and the Songea deposit in Tanzania.

Optical absorption measurements were obtained with Hitachi 2900 and 2910 spectrophotometers at Crystal Chemistry and with a Hitachi 2910 at GIA in Bangkok. The Hitachi 2910 units were reengineered by Tim Thomas (Applied Materials, Portland, Oregon) to have a rotatable polarized optical beam so that both E⊥c and E||c spectra could be measured on wafers with the *c*-axis in the plane of the wafer. These instruments measure the spectra to a resolution of 1.5 nm. The optical absorption data was corrected for the multiple reflections between the two optical surfaces of the sample wafers (see box A).

Fourier-transform infrared (FTIR) spectra were measured using Thermo Nicolet 6700 and iS50 FTIR spectrometers operating with a Pike 4× beam condenser accessory at a resolution of 2 cm^{-1}. The FTIR spectrometer was also connected to an air compressor with a purge gas generator (Parker Balston model 75-52) to minimize water and carbon dioxide contamination of the sample and the air in the sample chamber, as these compounds absorb light and obscure spectral peaks of interest. This helps to minimize moisture and carbon dioxide features, improve signal-to-noise ratio, and achieve a flat baseline. Spectra were collected from each sample through a hole of size chosen to accommodate a particular sample in the aluminum sample plate from the same location where the optical absorption spectra were collected.

The low-temperature heat treatment experiments of wafer samples in air were conducted at GIA in Bangkok using a Thermolyne FB1400 benchtop 1100°C muffle furnace manufactured by Thermo Scientific. The high-temperature (>1100°C) experiments in controlled atmospheres were conducted by Crystal Chemistry and by Columbia Gem House (Vancouver, Washington) with modified Thermal Technology 1000A graphite furnaces, using Coors Tek 998 alumina muffle tubes to allow the use of carefully controlled atmospheres.

The beryllium diffusion experiments were conducted at Crystal Chemistry in the Thermal Technology furnace described above. Diffusion experiments were run at 1780° or 1800°C in pure oxygen for 33 hours. This procedure is discussed at length in Emmett et al. (2003).

Color coordinates (Berns, 2000) were calculated from the sample's transmission spectrum and the characteristics of the light source. Calculations of the color coordinates for a given color temperature were performed via Thermo Scientific's GRAMS/AI spectroscopy software, a general-purpose spectra manipulation code that includes color coordinate calculations. Among the many color coordinate systems, the CIE 1976 L*a*b* system was chosen for its approximately uniform color space, and we selected a color temperature of 5000K.

RESULTS

The Fe^{3+} Chromophore. Fe^{3+} exists in essentially all natural sapphire. The resulting stones can be color-

[2]The terms *absorbance*, *absorption coefficient*, *absorption cross section*, *ion density*, and *areal defect density* are defined in box A.

BOX A: PRESENTING DATA

It is perhaps unfortunate, but like many other measurements that have been devised, there are multiple sets of units used to quantify the optical absorption features of gemstones, minerals, and other materials.

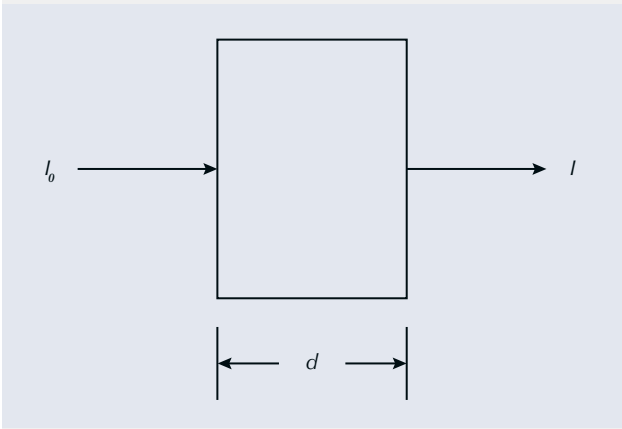

Figure A-1. Illustration of incident light being transmitted through a sample of a given thickness.

Assuming zero reflection losses from the two sample surfaces in figure A-1, the Beer-Lambert law can be expressed using several different units:

$$\frac{I}{I_0} = \frac{T}{100} = 10^{-A} = 10^{-ad} = 10^{-\varepsilon cd} = e^{-\alpha d} = e^{-\sigma Cd} \quad \text{(A-1)}$$

Where:

- I_0 = incident light intensity
- I = transmitted light intensity
- T = transmission in percent
- A = decadic true absorbance as measured by the spectrophotometer (a unitless ratio)
- a = decadic absorption coefficient in cm^{-1}
- d = sample thickness in cm
- ε = molar absorptivity in liter $mole^{-1}$ cm^{-1}, also called the extinction coefficient
- c = chromophore concentration in moles per liter
- α = naperian true absorption coefficient in cm^{-1}
- C = chromophore concentration in absorbers per cm^3
- σ = true absorption cross section in cm^2
- e = base of the natural logarithm = 2.71828…

Absorbance

Current commercial spectroscopic instruments measure the absorbance, A, in decadic units defined as:

$$I/I_0 = 10^{-A} \quad \text{(A-2)}$$

Thus, data presented in the literature in units of A are unambiguous.

Absorption Coefficient

Two different absorption coefficients are currently present in the literature. As a very general statement, physicists and materials scientists studying the absorption strength of ions in crystals and glasses tend to use:

$$I/I_0 = 10^{-A} = e^{-\alpha d} \quad \text{(A-3)}$$

This is the set of units we have used in this article and in Emmett et al. (2017a) and Dubinsky et al. (2020). It is also the system of units used in GIA's colored stone reference collection database. Chemists and mineralogists (e.g., Rossman, 1988) have generally expressed absorption coefficient as:

$$I/I_0 = 10^{-A} = 10^{-ad} \quad \text{(A-4)}$$

These two representations are very simply related by:

$$\alpha = 2.303a \quad \text{(A-5)}$$

While we have used a and α to clearly show the difference, α is often used in the literature for either absorption coefficient.

With the rise of multidisciplinary sciences and the rapid spread of materials science, the usage has become very mixed. In fact, one can often find both conventions in papers presented at the same technical meeting. It is important to note that just because the term *absorption coefficient* is used with the symbol α, it is not clear which system is in use unless the simple equation is stated. Therefore, it is very important for scientists to present the simple equation that defines their units in both published papers and presentations.

Absorption Cross Section and Extinction Coefficient

Now suppose we were to compare different chromophores in corundum, or the same chromophore in different hosts, in terms of their absorption strength and the depth of color they produce. If we divide the absorption coefficient by the concentration, C, of the chromophore, we can define an absorption cross section spectrum, σ, which is independent of concentration or sample thickness, as shown in equation A-1. The absorption cross section is calculated from α or A as:

$$\sigma = \alpha/C = 2.303A/dC \quad \text{(A-6)}$$

The absorption cross section spectrum depends only on the characteristics of an individual chromophore ion (e.g., Cr^{3+}) and the particular host (i.e., corundum), and it is measured in square centimeters (cm^2). The unit of square centimeters denotes an area, and one can think

of the cross section as the "area" of an individual ion as seen by the photons in a light beam. However, it does not represent the physical size of the ion. This absorption cross section is used for comparisons in this article and in Dubinsky et al. (2020).

In chemistry and mineralogy, epsilon (ε) is often used for the extinction coefficient, which is the same concept but in a different set of units. From equation A-1, we have:

$$A = \varepsilon cd \quad \text{(A-7)}$$

As shown above, the units of ε are liter mole^{-1} cm^{-1}. The extinction coefficient for corundum is easily calculated from σ by the following from equation A-1:

$$10^{-\varepsilon cd} = e^{-\sigma Cd} \quad \text{(A-8)}$$

Thus:

$$\varepsilon = (2.615 \times 10^{20})\sigma \quad \text{(A-9)}$$

Figure A-2 compares the numerical values of the extinction coefficient and the absorption cross section for the Cr^{3+} ion in corundum. The term *extinction coefficient* is also called the molar absorptivity in some publications, but the units are the same.

Units Used on Plots

A variety of descriptions are used on spectra plots when the axis values are far larger or smaller than can be easily represented without exponents. In figure A-2, the values plotted on the vertical axis range from 0 to 4×10^{-19} cm^2. There are several ways in which these units have been represented in the literature:

1. Absorption Cross Section $\times 10^{19}$ cm^2
2. Absorption Cross Section in units of 10^{-19} cm^2
3 Absorption Cross Section $\times 10^{-19}$ cm^2

In previous publications we have used unit 1, which is quantitatively correct but confusing to readers unfamiliar with exponential notation (Emmett et al., 2017a; Dubinsky et al., 2020). Unit 2 is probably the clearest and simplest but takes up more space on the graph. Unit 3 is very common in the scientific literature, but it is formally incorrect since the numbers shown on the plot are 0 to 4. As unit 2 is the clearest, we have chosen to use it instead of unit 1 in this article with the hope of eliminating ambiguity.

Concentration Units

Generally, there are two major ion concentration units in the literature: ions/cm^3 and moles/liter. The literature often uses ppma, which is ions/cm^3 divided by 10^6 (1 ppma in corundum is 1.178×10^{17} ions/cm^3). Moles/liter is easily converted to ions/cm^3. One mole/liter equals Avogadro's number divided by 1000 cm^3, or 6.0221×10^{20} ions/cm^3. For corundum, 1 mole/liter equals 5111 ppma.

Areal Density

The areal density (ρ_A) is simply the product of the ion concentration, in ions/cm^3 times the sample thickness, d, in cm. Thus, the units are ions/cm^2. Under the color circles in this paper, we present the areal density in ppma-cm. This factor is:

$$ppma\text{-}cm = Cd/(1.178 \times 10^{17}\ ions/cm^3) \quad \text{(A-10)}$$

where 1.178×10^{17} is the number of ions in 1 cubic centimeter of Al_2O_3 determined by:

$$1\ ppma = 5A\rho/M = 1.178 \times 10^{17}\ ions/cm^3 \quad \text{(A-11)}$$

where A is Avogadro's number (6.022×10^{23} molecules/mole), ρ is the density of corundum (taken as 3.99 grams/cm^3), and M is the molecular weight of corundum (101.961 grams/mole).

Correction for Surface Reflection Losses

To determine the true absorbance A as defined in equation A-1 above, the instrument-measured absorbance, must first be corrected for the loss from multiple reflections between the two polished surfaces of the sample. This is done by summing all the reflections between the two surfaces (T.S. Hemphill, pers. comm., 2011) and

less, yellow, green, or blue, depending on the relative concentrations of the various trace elements present. This study examined 102 samples, from which 24 of the 102 data sets were chosen to represent the entire set based upon their evenly spaced representation of the iron concentrations for the 102 samples. Yellow sapphires colored primarily by iron are often found in basalt-hosted blue sapphire deposits. A single crystal will often contain both deep blue and deep yellow regions in varying proportions. Although bicolor stones are occasionally faceted, these will usually be cut as either blue or yellow gems, depending on the predominant color. Several of the high-iron samples from this study were bicolor stones containing well-defined blue and yellow regions. These samples were fabricated with their planes either perpendicular or parallel to the *c*-axis, depending on which orientation most clearly separated the blue and yellow regions.

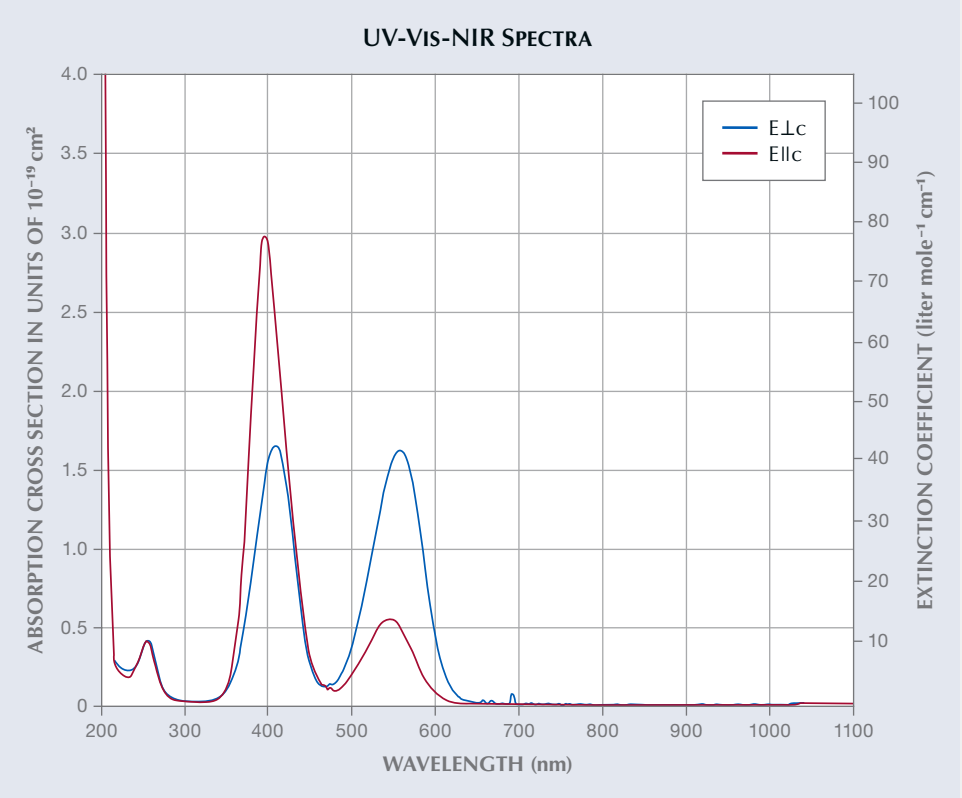

Figure A-2. UV-Vis-NIR plot of both the absorption cross section and the extinction coefficient for oriented spectra of Cr^{3+}:Al_2O_3.

using a three-term Sellmeier equation for corundum to determine the sample's refractive index as a function of wavelength (Tatian, 1984). The index input data to the Sellmeier equation is a combination of all relatively recent data from the suppliers of high-purity synthetic corundum material used to fabricate high-purity optical elements. The Sellmeier equation fit to these data was performed for us by John Trenholme (formerly with Lawrence Livermore National Laboratory) using TableCurve 2D software. Correcting for this loss, we have the true absorbance, *A*. This correction is important because it is greatest where the absorption is least, and it is just this region of the absorption spectrum that transmits the most intense light and thus contributes most to the color. This reflection correction has been made for all spectra presented in this article and for all spectra used in deriving these results. It is also important to remember that very strong absorption peaks, if very narrow, will have little impact on color.

Since commercial instrumentation is now available to measure the refractive index of flat samples at multiple wavelengths, it is suggested that these technologies be acquired by major gemological laboratories to add to their databases and to provide for correction of optical spectra of other gem minerals.

Figure 2 shows a selection of yellow wafers for spectroscopy. Figure 3 shows a selection of the bicolor wafers.

Often in the study of corundum chromophores, an effective procedure has been to grow a crystal containing only one chromophore. However, that procedure was not successful for Fe^{3+} because of decomposition and vaporization of the iron oxides at the Czochralski growth temperature. Thus, 23 of the 24 natural samples chosen for this study were selected from a wide range of deposits worldwide.

Figure 4 shows both the E⊥c and E||c absorption spectra of sample 1245, from the Garba Tula deposit in Kenya. This sample contains 3126 ppma iron. There are three absorption bands from Fe^{3+} and Fe^{3+} pairs in the visible region of the spectrum (Ferguson and Fielding, 1971, 1972; Krebs and Maisch, 1971) at 450, 530, and 700 nm. Of these, the 450 nm band is

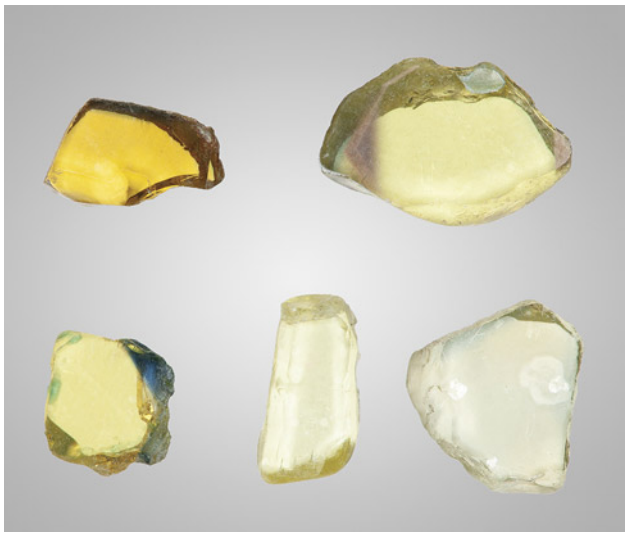

Figure 2. A selection of the 102 wafers studied for this report. The three pale yellow wafers are colored by Fe^{3+} only at a level around 2000 ppma, while the more color-saturated wafer with a blue edge is colored by a much higher concentration of Fe^{3+} (around 3500 ppma). The deep yellow wafer is colored by Fe^{3+} and by $h^{\bullet}$-Fe^{3+}. Photo by John L. Emmett.

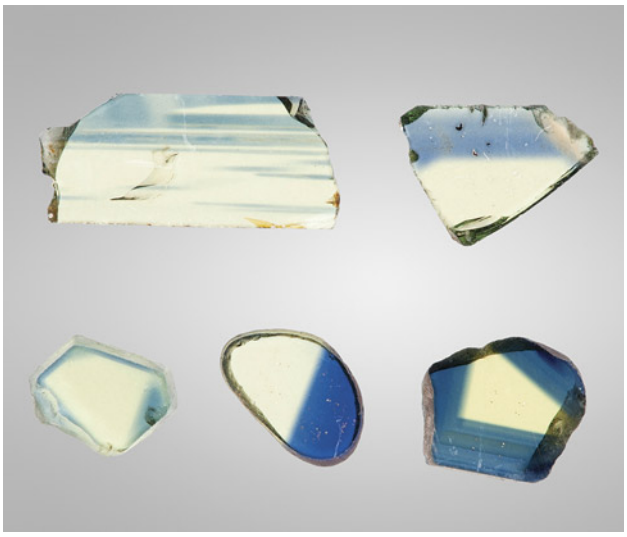

Figure 3. A selection of bicolor wafers. The weak color saturation in the yellow areas of some samples results from fabricating them thin enough that both yellow and blue areas were well within the dynamic range of the UV-Vis-NIR spectrophotometers. Photo by John L. Emmett.

by far the dominant cause of color. Because it absorbs in the blue region of the spectrum, the transmitted color is yellow. The 530 and 700 nm bands are broad and very weak. Taken together, this combination has little impact on color. The 450 nm E||c band is nearly identical to the E⊥c band, but the peak amplitude is

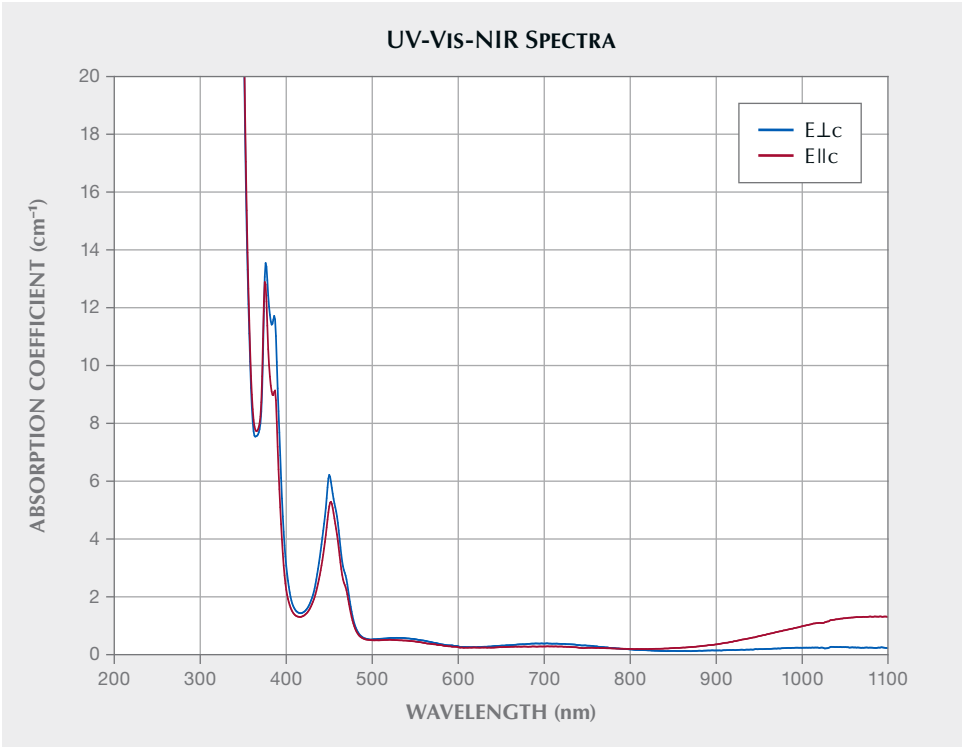

Figure 4. UV-Vis-NIR absorption coefficient spectrum of sample 1245, a bicolor sapphire from Kenya's Garba Tula deposit. The spectrum is taken in the yellow region. The iron concentration in the yellow region is 3126 ± 65 ppma, and the sample thickness is 0.99 mm.

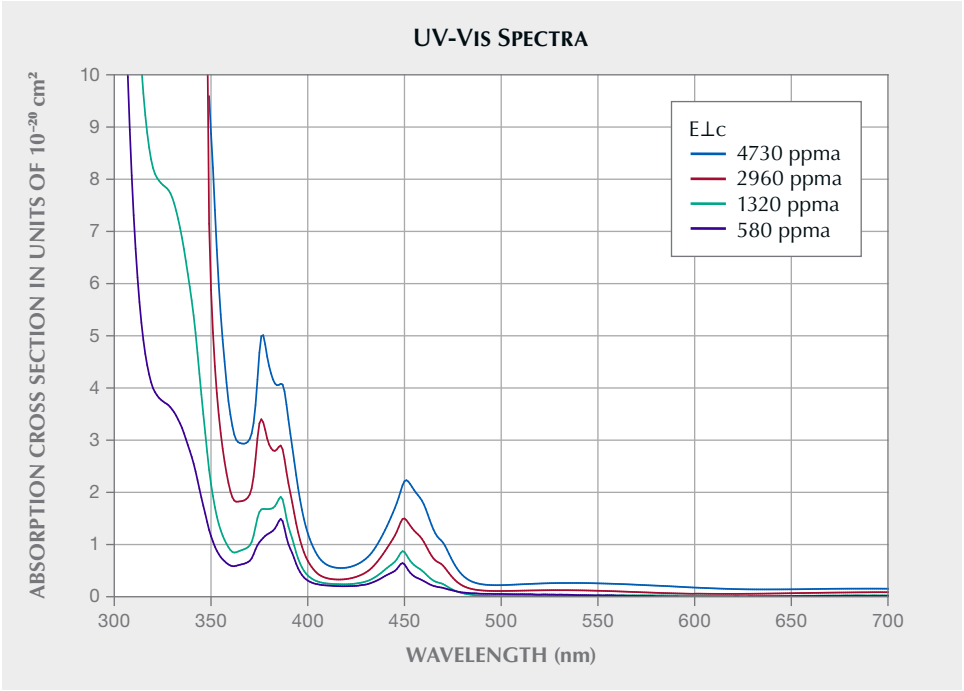

Figure 5. UV-Visible absorption cross section spectra. The E⊥c absorption cross section of the 450 nm absorption band of Fe^{3+} in corundum increases in amplitude and in width (FWHM) with increasing concentration (Dubinsky et al., 2020).

about 16% less. Thus, we have focused our study of the iron chromophore on the 450 nm E⊥c band.

In the course of previous work on the Fe^{3+} chromophore (Dubinsky et al., 2020), two unique features were observed with the 450 nm absorption band, which is the primary determinant of color. First, the peak absorption cross section increases with iron concentration; second, the full width at half maximum (FWHM) of the band increases by about a factor of two from the lowest to the highest iron concentrations (figure 5; see also figure 7 of Dubinsky et al., 2020). Such increases in both peak absorption cross section and width of the 450 nm absorption band more than linearly increase the strength of the chromophore with concentration. Other chromophores in natural corundum do not show these changes and thus exhibit a constant strength with concentration.

The concentration of Fe^{3+} in natural corundum ranges from <5 ppma to at least 4730 ppma. Since the 450 nm Fe^{3+} absorption cross section is low (~10^{-20} cm^2), optical measurements were limited to samples whose concentration was above 50 ppma. For example, the peak absorption coefficient at 450 nm of sample 1272 with 79.2 ppma and a thickness of 3.415 mm is 0.042 cm^{-1}. The peak absorbance as measured by the spectrophotometer is therefore 0.0062. At 10–20% of this peak value we see instrumental noise problems. Thus, spectrophotometer noise and sample thickness determined the minimum concentration used. Therefore, for this study we were limited to using samples with Fe^{3+} concentrations that ranged from 56.5 to 4730 ppma.

Of the samples used for this study, 24 were chosen, covering the range from 56.5 to 4730 ppma iron for the iron chromophore data presented here. The E⊥c spectra of these samples were accurately curve fit to make the best determination of the 450 nm band magnitude and shape. Curve fitting was performed with GRAMS/AI (Thermo Scientific) using a linear baseline plus four Lorentzian bands (as suggested by Dr. Ren Lu of the Gemmological Institute, China University of Geosciences in Wuhan). The usual variety of other band shapes were evaluated for the quality of the fit, and the Lorentzian bands produced the best match for four bands or fewer.

Determining the baseline for the 450 nm E⊥c band presented some difficulty, as it was overlapped to some degree by the 388 nm Fe^{3+} band and by the 580 nm E⊥c Fe^{2+}-Ti^{4+} band in the blue sapphires. Because these interferences vary widely in magnitude throughout the large number of samples used, it was necessary to modify the spectra of some of the deep blue sapphire samples so that the 450 nm band did not fall on a steeply rising portion of the Fe^{2+}-Ti^{4+} band. The modification was achieved by subtracting successively larger portions of an Fe^{2+}-Ti^{4+} spectrum from the sample spectrum until the minima on either side of the 450 nm peak were of the same amplitude. The spectrum used for this subtraction is the absorption cross section determined for the Fe^{2+}-Ti^{4+} pair

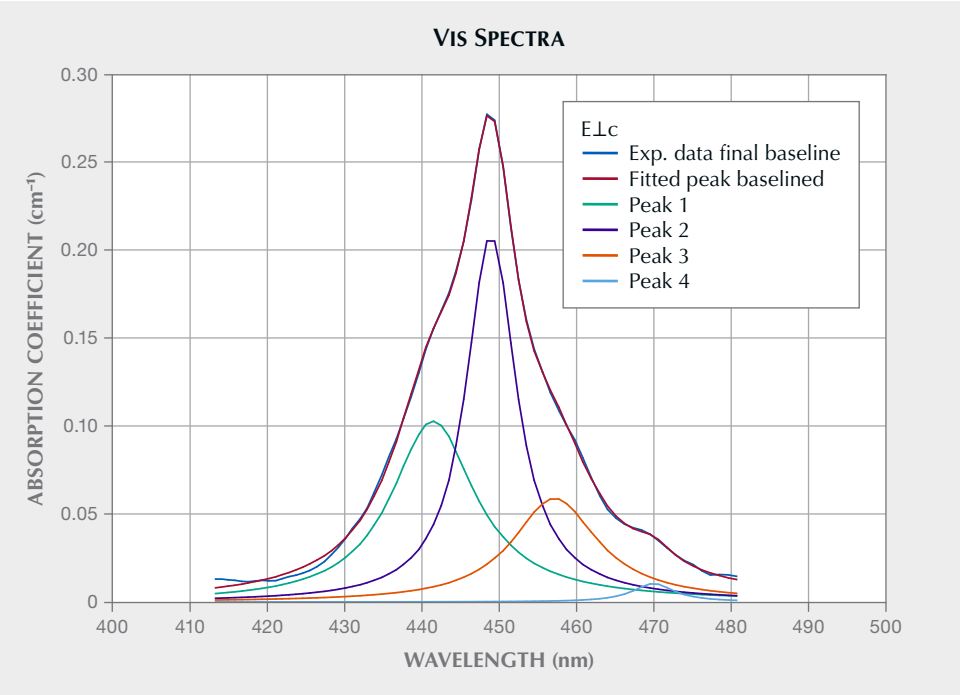

Figure 6. Visible absorption spectra of sample 1017 from Myanmar, containing 447 ppma iron. The experimental data of the 450 nm E⊥c peak is accurately fitted by four Lorentzian curves. This provides an accurate measure of the absorption band in terms of peak absorption coefficient, FWHM, and band shape.

(Dubinsky et al., 2020), multiplied by appropriate concentrations.

Even though the 450 nm band is quite narrow, the use of a linear baseline creates some error because the background decreases toward the 450 nm peak from longer wavelengths and shorter wavelengths. This error is estimated as ≤10% of the peak amplitude. A typical curve fit is shown in figure 6 for a sample containing 447 ppma iron. Note the typical quality of the fit by comparing the experimental data final baseline with the fitted peak baselined in figure 6.

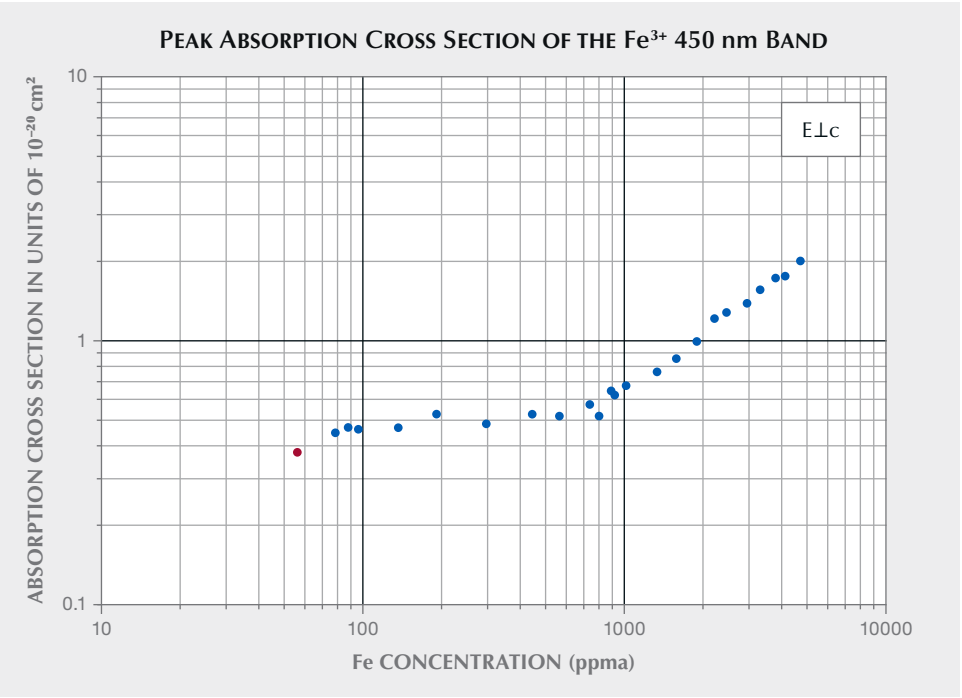

Figure 7A. Peak absorption cross section of the Fe^{3+} 450 nm band, with iron concentration in ppma. The plot shows the increase in absorbance cross section when Fe^{3+} concentration increases beyond approximately 700 ppma. The red data point identifies the only synthetic sample in this plot.

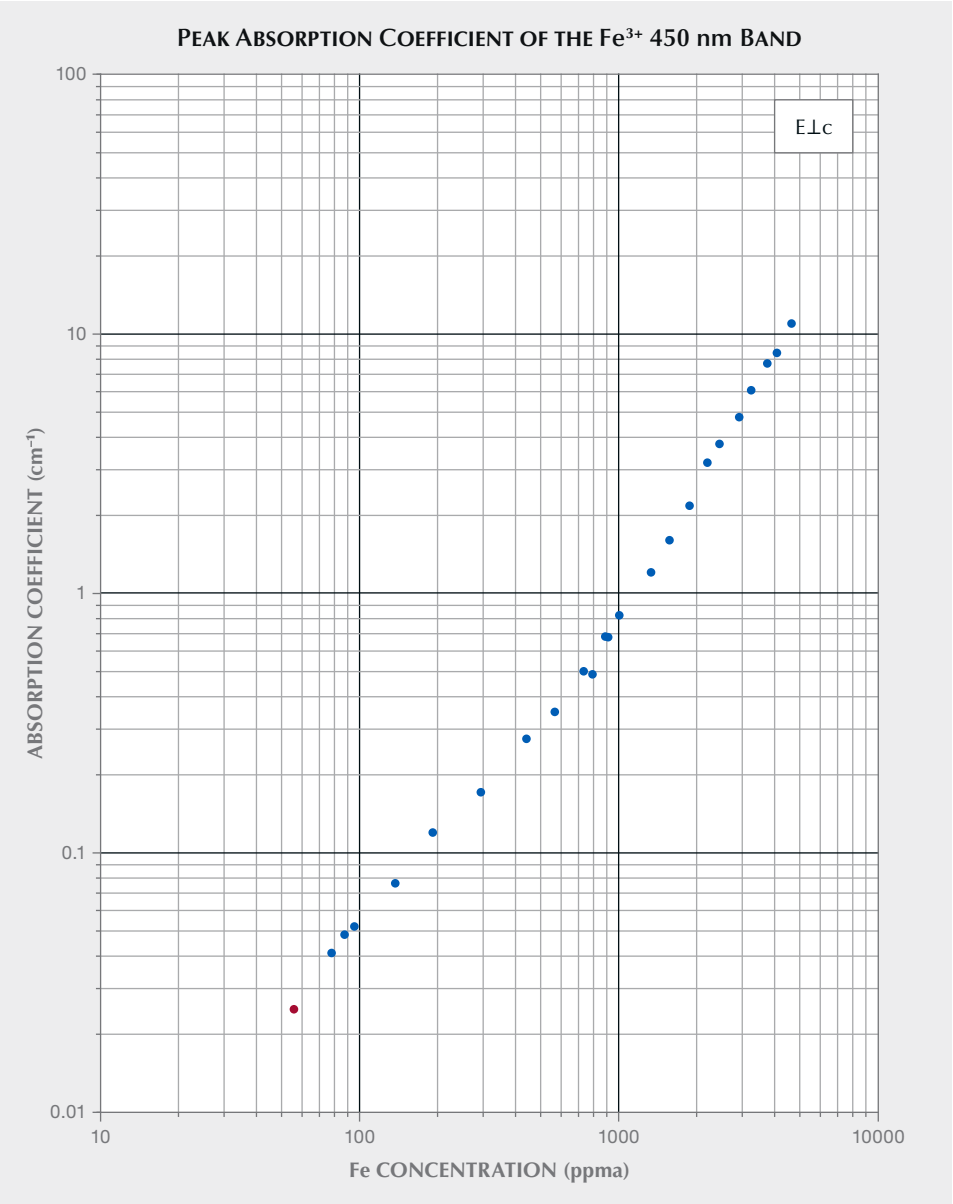

Figure 7B. The absorption coefficient is plotted as a function of the iron concentration. The red data point identifies the only synthetic sample in this plot.

Figure 7A shows the 450 nm Fe^{3+} band peak absorption cross section data as a function of iron concentration of the 24 curve-fit samples.

From this plot, we can see that the absorption cross section is essentially constant as the iron concentration increases from low values up to ~700 ppma. Above 700 ppma, it increases to a value at 4730 ppma iron, which is about 4.5 times the low concentration value. The slope of the curve over the region from 900 to 4730 ppma iron is approximated by the proportionality given in equation 1, where σ is the absorption cross section:

$$\sigma \propto [Fe]^{0.75 \pm 0.08} \quad (1)$$

In figure 7A, the lowest concentration measured was of a synthetic iron-doped crystal grown by Saint-Gobain Crystals and Detectors. The cross section of this sample (shown in red) is noticeably smaller than that of the three natural samples containing less than 100 ppma iron. This may imply that the clustering of iron in corundum is dependent on the thermal history of the sample.

The data of figure 7A could also be presented as the 450 nm peak absorption coefficient versus the Fe^{3+} concentration. This allows an estimate of the Fe^{3+} concentration if the peak absorption coefficient has been measured, or vice versa. The plotting of data in this fashion is shown in figure 7B.

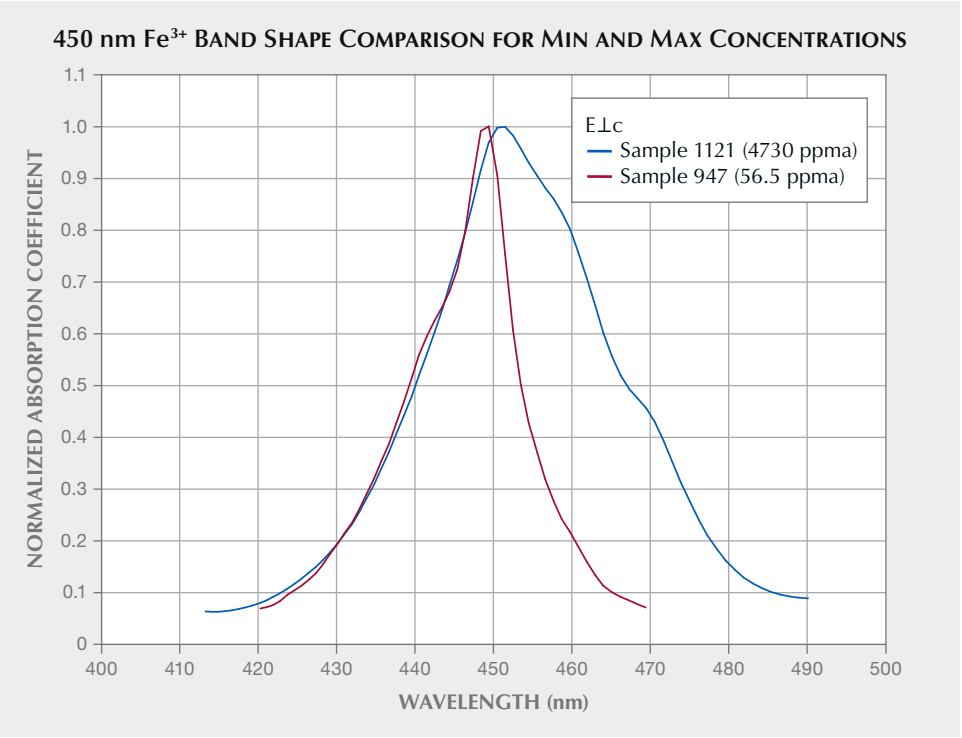

Figure 8. The E⊥c 450 nm Fe^{3+} absorption coefficient plots show the band shapes for the sample with the lowest Fe^{3+} concentration and the sample with the highest Fe^{3+} concentration studied. Peak values are normalized to 1.0.

As indicated earlier, in addition to the absorption cross section increase with concentration, the FWHM of the 450 nm peak also increases substantially with concentration. The strength of the Fe^{3+} chromophore is determined by both the peak absorption cross section and the FWHM of the 450 nm band. Figure 8 compares the curve shape of the lowest- and highest-concentration samples. The peak value of each spectrum is normalized to 1.0.

As shown in figure 8, the peak of the low-Fe^{3+} sample is at 449.5 nm while that of the high-Fe^{3+} sample is at 451.5 nm, a shift of about 2 nm. The shape of the band on the left side (short-wavelength side) at the half maximum wavelength doesn't change with iron concentration. However, the right side (long-wavelength side) of the peak changes significantly. The position of the half maximum increases significantly with concentration from about 453 to about 466 nm, resulting in a doubling of the FWHM from about 13 nm to 26 nm going from 56.5 ppma to 4730 ppma iron.

The shifting of the long-wavelength half maximum to longer wavelengths (lower energies) with concentration is an indication of the energy per ion reduction as a result of pairing or more complex cluster formation.

Figure 9 shows the normalized spectra as in figure 8, but with eight of the 24 curve-fit samples presented. Note that the half maximum on the short-wavelength side of the peak is nearly constant at 440 ± 0.7 nm. Expanding the region of the graph around the short-wavelength half maximum shows that the spread is not systematic with concentration, but apparently nearly random. Thus, much of the spread is probably a result of slightly different calibrations of the three Hitachi spectrophotometers over several years. The two traces in figure 8 (which represent the Fe^{3+} concentration extremes) were measured on the same instrument by the same operator. The short-wavelength half maximum points are at 439.3 and 440.0 nm, a difference of only 0.7 nm.

The long-wavelength half maximum increases from 453.5 nm at the lowest concentration to 467.2 nm at the highest. With this data on all 24 curve-fit samples, we can plot a curve, shown in figure 10, of the long-wavelength half maximum (left vertical axis) as a function of Fe^{3+} concentration. By taking the short-wavelength half maximum (right vertical axis) as 440 nm, figure 10 also presents the FWHM.

With the quantitative data presented for the amplitude and width of the 450 nm band of Fe^{3+}, we can now examine the dependence of the color on the concentration produced by this chromophore. The color produced by most corundum chromophores depends solely on the areal density (ρ_A, in ions per cm^2) of the chromophore. The areal density is simply

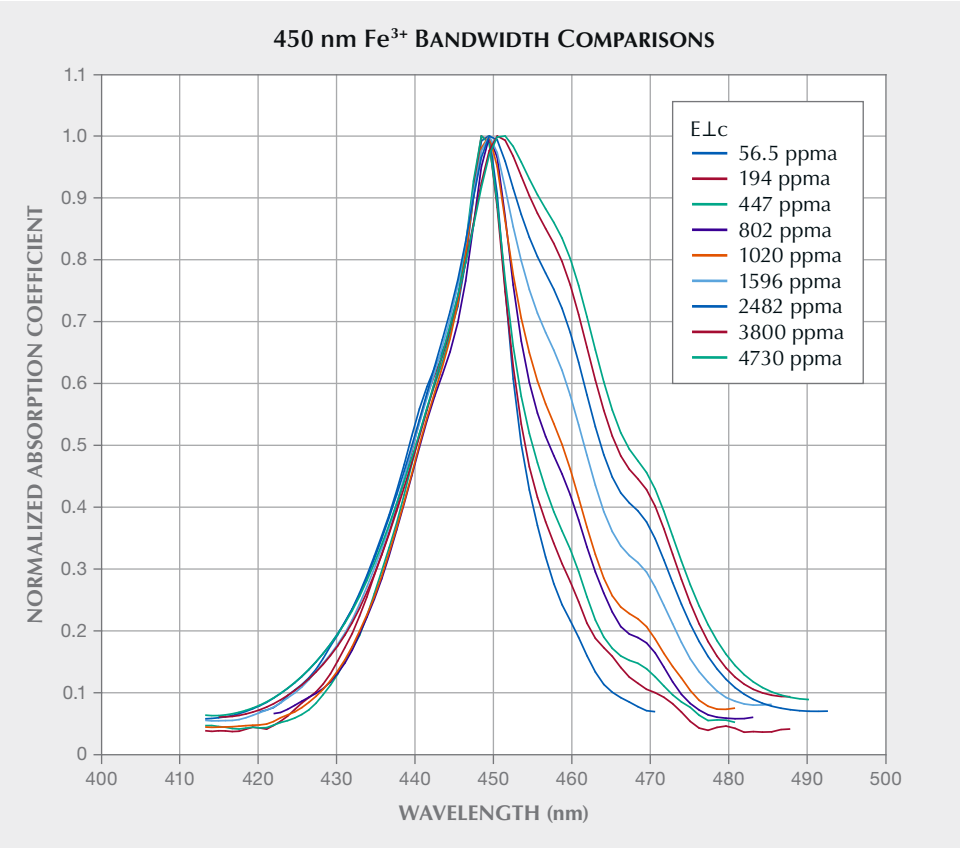

Figure 9. This visible absorption coefficient plot shows eight of the 24 curve-fit E⊥c band shapes covering the range from 56.5 to 4730 ppma Fe^{3+}. Peak values are normalized to 1.0.

the product of the chromophore concentration (*C*, in ions per cm^3) and the sample's path length (*d*, in cm). The areal density is the number of chromophore ions in the sample per cm^2 as measured by

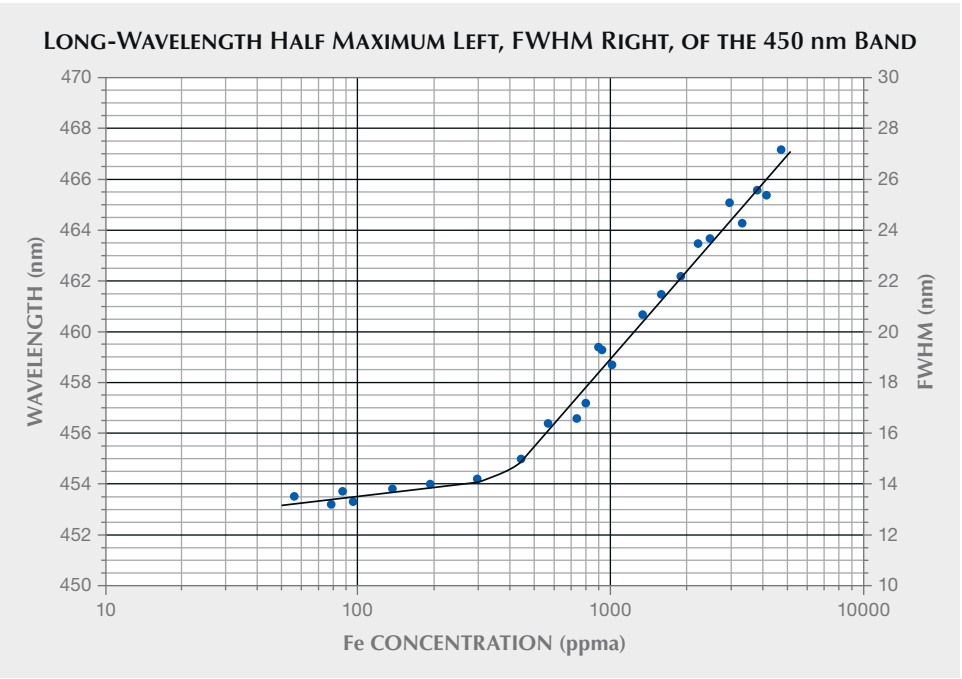

Figure 10. This plot presents the long-wavelength half maximum on the left axis and the FWHM on the right axis as a function of Fe^{3+} concentration for the 450 nm E⊥c band.

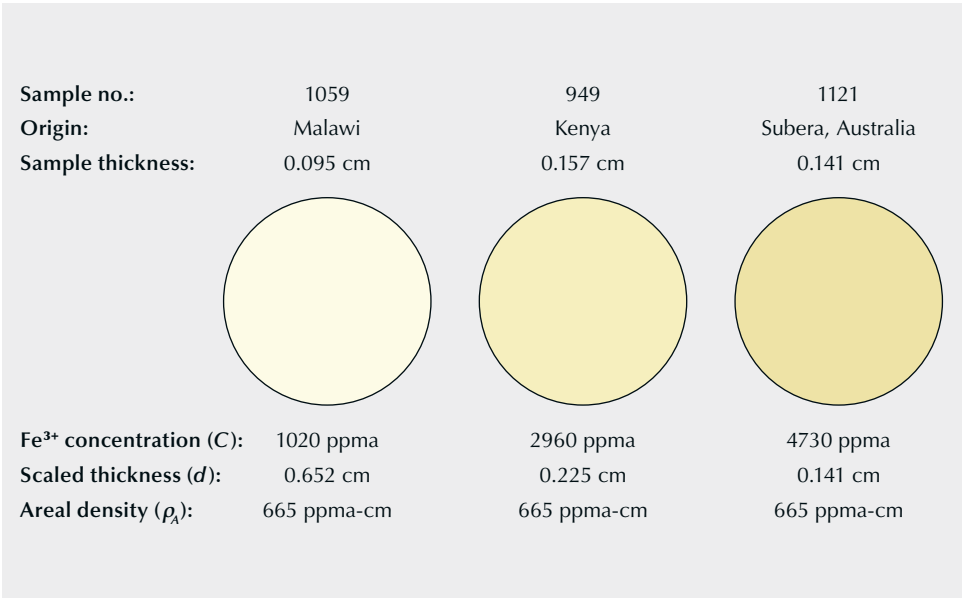

Figure 11. These three color circles show the increase in chromophore strength with Fe^{3+} concentration at constant areal density.

a light beam traversing the sample, as shown in equation 2:

$$\rho_A = Cd \quad (2)$$

For the chromium chromophore, a sample with 500 ppma Cr^{3+} and a thickness of 1 cm has the same absorbance and color as a sample with 1000 ppma and a thickness of 0.5 cm, because it has the same areal density. The Fe^{3+} chromophore does not share this simple relationship because, as shown in figure 7A, the absorption cross section is not independent of concentration.

In addition to the peak cross section of the 450 nm Fe^{3+} band being dependent on concentration, the band's FWHM increases with concentration (see figure 10). Thus, the magnitude and shape of the band change with concentration. Since the strength of the Fe^{3+} chromophore depends on both factors, it exhibits a complex dependence on Fe^{3+} concentration. For these reasons, a color calculation for this chromophore requires both the concentration and the sample thickness. The concentration determines the peak cross section and the band shape. A series of band shapes for a range of concentrations is presented in figure 9 and in appendix 1 (https://www.gia.edu/doc/fall-2023-yellow-sapphire-chromophores-appendix1.pdf).

To illustrate these relationships, we present three color circles in figure 11. These three color circles, calculated for a 5000K illumination and a 2° angle of observation, have the same areal density of 665 ppma-cm. For a chromophore such as Cr^{3+}, all three color circles would be identical. As we have shown, however, the strength of the Fe^{3+} chromophore increases with the density of Fe^{3+} ions in the sample, even at constant areal density.

Sample 1121 in figure 11 has the highest Fe^{3+} density (4730 ppma) and a strong yellow coloration, even though it is only 0.141 cm thick. The areal density of the sample is 665 ppma-cm. Sample 949 has a lower density at 2960 ppma; to calculate the color, the thickness has been increased to 0.225 cm, producing a matching areal density of 665 ppma-cm. Note that the color saturation is significantly reduced. Finally, sample 1059 has a relatively low iron concentration of 1020 ppma. For the color circle, its thickness has been increased to 0.652 cm to provide a matching areal density of 665 ppma-cm. Again, there is a significant decrease in color saturation. For these reasons, strongly yellow sapphires colored only by iron usually have iron concentrations above 3000 ppma.

As demonstrated above, there is no single curve shape that characterizes the 450 nm Fe^{3+} absorption band. Thus, the effect of iron concentration on the color of ruby or blue sapphire must be calculated separately for each concentration of either Cr^{3+} or Fe^{2+}-Ti^{4+}, and Fe^{3+}. The most straightforward calculation would be to simply add in one of the curves presented in appendix 1 to either of the other two chromophores' spectra for each iron concentration.

The weakest chromophore in natural corundum is Fe^{3+}. Yet some very deeply colored yellow sapphires are found in basalt-hosted corundum deposits. These deeply yellow sapphires are colored by the combination of the Fe^{3+} chromophore and the $h^{\bullet}$-Fe^{3+} chromophore, and these will be discussed later.

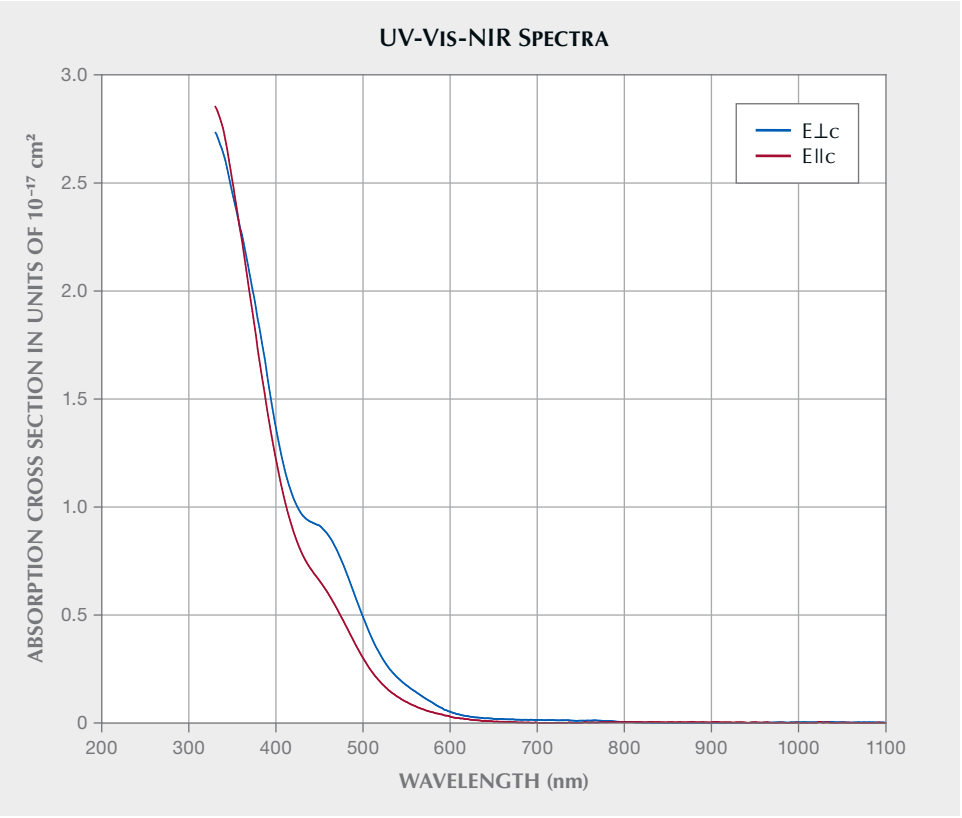

Figure 12. Oriented UV-Vis-NIR absorption cross section plots of the $h^{\bullet}$-Fe^{3+} chromophore in sapphire (Dubinsky et al., 2020).

The $h^{\bullet}$-Fe^{3+} Chromophore and Heat Treatment.[3] Trace elements in the corundum lattice that have a valence less than the 3+ of aluminum are termed *acceptors*, while those with a valence of greater than 3+ are termed *donors* (Smyth, 2000). If the sapphire is acceptor dominated, we have the following relationship:[4]

$$[acceptors] - [donors] = [Mg^{2+} + Ni^{2+}] - [Si^{4+} + Ti^{4+}] > 0 \quad (3)$$

where square brackets indicate concentrations in ppma or ions/cm^3. Since solids must be electrically neutral, acceptor excess will be charge compensated by either hydrogen ions, oxygen vacancies (V_o^{2+}), or trapped holes ($h^{\bullet}$) with a 1+ charge, as shown here:

$$[Mg^{2+} + Ni^{2+}] - [Si^{4+} + Ti^{4+}] - [H^{+} + 2V_o^{2+} + h^{+}] = 0 \quad (4)$$

Whether in nature or in the laboratory, the elimination of the hydrogen ion and/or oxygen vacancies that are a part of the charge compensation of the acceptor excess results in an increase of the trapped hole concentration to maintain charge neutrality. The trapped hole in corundum is an oxygen ion with a charge of –1 rather than the normal –2. The O^{1-} ion paired with Fe^{3+} is the absorbing specie that creates the yellow coloration, not the divalent ions (figure 12; see also Dubinsky et al., 2020).

While equations 3 and 4 look simple, determining acceptor domination is not. Based on calibrated SIMS measurements at the California Institute of Technology, Division of Geological and Planetary Sciences (Stone-Sundberg et al., 2017, 2020), we have learned that silicon (Si^{4+}), a donor, is about as common in natural corundum as magnesium (Emmett et al., 2017b). Unfortunately, only a very small portion of the research samples at Crystal Chemistry and in GIA's colored stone reference collection in Bangkok have been analyzed for silicon by SIMS. The majority of our samples have only been analyzed by quadrupole LA-

[3]As discussed in Dubinsky et al. (2020), $h^{\bullet}$ will pair with either Cr^{3+} or Fe^{3+}. If both are present, it will preferentially pair with Cr^{3+}, which lies above Fe^{3+} in the band gap. The absorption spectra of $h^{\bullet}$-Cr^{3+} is very different from the $h^{\bullet}$-Fe^{3+} spectra, even with the excess Cr^{3+} spectra subtracted out. In this study, we discuss only stones with yellow coloration that contain Fe^{3+} but not Cr^{3+}.

[4]Nickel is included in these equations because it was discovered in significant concentrations in various types of natural sapphire by author JS-S. For example, concentrations ranging from 1 to 15 ppma were found in the blue sapphires from Yogo Gulch, Montana. The valence of nickel in natural corundum depends on whether the sum of concentrations of all aliovalent elements results in acceptor or donor domination. Acceptor domination would make nickel 3+, while donor domination would make it 2+. Nickel as a chromophore in corundum will be addressed later in this article.

Figure 13. Sapphires from Rock Creek, Montana. The wafers in the top row are cut perpendicular to the c*-axis and the wafers in the bottom row are cut parallel to the* c*-axis. These stones have been heat treated at 1200°C in oxygen. Photo by John L. Emmett.*

ICP-MS, which cannot accurately measure silicon in corundum due to close-in-mass interferences, and thus we cannot demonstrate acceptor domination.

Even with measurements for all four trace elements by SIMS, we often cannot determine whether or not a sample is acceptor dominated. This is because the standard deviation (SD) of the acceptor excess is the square root of the sum of the squares of the SDs for the concentrations of each of the four trace elements: magnesium, nickel, titanium, and silicon. Thus, the standard deviation of the acceptor excess can be large and can exceed the value of [$h^{\bullet}$] itself, making the determination of acceptor domination impossible. It is also important to note that our chemical analyses are only of several spots on the surface of fabricated wafer samples. We have learned from examination of many heat-treated yellow sapphires that the acceptor domination in a given sample is often spatially nonuniform, and thus our analyses may not have covered the acceptor-dominated region. Spatial nonuniformity in natural corundum is more typical of aliovalent ions than isovalent ions.

This spatial nonuniformity is typical of sapphires from Madagascar, Malawi, and most of the Montana deposits, as well as many of the stones from Sri Lanka. Examples of the nonuniformity of Rock Creek stones are given in Schmetzer and Schwarz (2007) and also shown in figure 13. The yellow region in these stones appears as a smooth spot when viewed down the *c*-axis. Observed along an *a*-axis in this figure, it can be seen that the acceptor-dominated region is far more spatially complex.

Figure 14 shows natural yellow sapphires from Sri Lanka colored by this chromophore. The iron concentration in these stones typically ranges from 30 to 250 ppma and is therefore far too small to contribute meaningfully to the coloration as an Fe^{3+} chromophore.

To understand how trapped holes are formed, it is helpful to express the chemical reaction equations in Kröger-Vink notation (see box B). For simplicity, we

Box B: Kröger-Vink Notation

Defect chemistry is the study of point defects in imperfect crystals. These include vacancies, interstitial atoms or ions, trace elements, electrons, or holes or any other deviation from the structure of a perfect crystal. Even absolutely pure crystals contain point defects at any temperature above absolute zero.

The presence of defects is described as "disorder" in a crystal. Modern technological uses of crystalline materials in lasers, semiconductors, lithium batteries, fuel cells, and the like depend on controlled disorder. Allochromatic gems are gems that are colored by impurities. If they were completely pure, they would be colorless. The color of all allochromatic gems is produced by defects. Thus, all color in corundum is caused by defects.

Writing the equations for chemical reactions among defects in a crystal is also called defect chemistry. In addition to the normal rules for writing chemical reactions in a liquid or gas, the reactions in a crystal have additional constraints. The set of rules for such reactions is as follows:

1. Mass is conserved: The mass on both sides of a chemical reaction must be equal.
2. Charge is conserved: The bulk of an ideal crystal is electrically neutral. Thus, charged defects must be created or destroyed in combinations that are electrically neutral. Atoms or molecules added to or removed from a crystal must be in electrically neutral combinations.
3. Site balance is conserved: Cation or anion sites can only be created or destroyed in ratios corresponding to the stoichiometry of a perfect crystal. These are also electrically neutral combinations. This is the single most important difference between chemical reactions in a crystal and those in a liquid or gas.

The most commonly used formalism for writing chemical reactions with the rules above is the Kröger-Vink notation. The notations are as follows:

1. The *main symbol* is the species, neutral or ionized, indicated by its usual chemical symbol. Va-

cancies are denoted by *V*. The symbol V for vanadium is usually shown in a different font.

2. A *subscript* indicates a lattice site labeled by its occupant in a perfect crystal. An interstitial site is marked by the subscript *i* next to a chemical symbol.
3. A *superscript* indicates the charge of the specie *relative to the charge of that site in a perfect crystal*. One or more dots ($^{\bullet}$) are used for extra positive charge(s). One or more slashes ($^{/}$) are used for extra negative charge(s). An *x* is used for zero charge difference.

Some examples of this notation for corundum are:

- Cation and anions on proper sites Al_{Al}^{x} O_{o}^{x}
- Ionized cation and anion vacancies $V_{Al}^{///}$ $V_{o}^{\bullet\bullet}$
- Ionized cation and anion interstitials $Al_{i}^{\bullet\bullet\bullet}$ $O_{i}^{//}$
- Tetravalent cation impurity on cation site $Ti_{Al}^{\bullet}$
- Trivalent cation impurity on cation site Cr_{Al}^{x}
- Divalent cation impurity on cation site $Mg_{Al}^{/}$
- Trivalent anion impurity on anion site $N_{o}^{/}$
- Divalent anion impurity on anion site S_{o}^{x}
- Monovalent anion impurity on anion site $F_{o}^{\bullet}$
- Electrons in the lattice $e^{/}$
- Electron holes in the lattice $h^{\bullet}$

Chemical reactions in corundum are written using these symbols. Isovalent ions, which are those ions with the same valence as aluminum or oxygen, can be incorporated as follows:

$$Cr_2O_3 \xrightarrow{Al_2O_3} 2Cr_{Al}^{x} + 3O_{o}^{x} \quad \text{(B-1)}$$

$$Fe_2O_3 \xrightarrow{Al_2O_3} 2Fe_{Al}^{x} + 3O_{o}^{x} \quad \text{(B-2)}$$

$$Ga_2O_3 \xrightarrow{Al_2O_3} 2Ga_{Al}^{x} + 3O_{o}^{x} \quad \text{(B-3)}$$

These equations show metal oxides being incorporated into an aluminum oxide (Al_2O_3) crystal. No point defects other than the metals themselves are being incorporated, because these trivalent metal ions can have the same valence as aluminum.

When corundum crystals are heated in an oxygen atmosphere, oxygen ions take oxygen sites on the surface of the crystal, resulting in the de facto formation of aluminum vacancies on the surface and trapped holes for charge compensation. Oxidation in the bulk of the crystal is by inward diffusion of the resulting aluminum vacancies and holes. The diffusion coefficient of these defects is several orders of magnitude greater than the diffusion of oxygen ions. Therefore, the following equation is a good description of the process:

$$\frac{1}{2}O_2(g) \xrightarrow{Al_2O_3} O_{o}^{x} + \frac{2}{3}V_{Al}^{///} + 2h^{\bullet} \quad \text{(B-4)}$$

Aliovalent ions, which have a valence different from that of aluminum or oxygen, can be incorporated into a corundum lattice by the creation of additional defects. For example, charge compensation of divalent ions can be achieved by incorporation of additional oxygen and by the formation of holes as shown here:

$$MgO + \frac{1}{4}O_2(g) \xrightarrow{Al_2O_3} Mg_{Al}^{/} + \frac{3}{2}O_{o}^{x} + h^{\bullet} \quad \text{(B-5)}$$

In nature, when aliovalent ions are incorporated they are often charge compensated by other aliovalent ions. Here the magnesium is charge compensated by co-incorporation of titanium:

$$MgO + TiO_2 \xrightarrow{Al_2O_3} Mg_{Al}^{/} + Ti_{Al}^{\bullet} + 3O_{o}^{x} \quad \text{(B-6)}$$

The use of Kröger-Vink notation eliminates several other conceptual reaction possibilities because of the necessity of both charge and site balance. This formalism was proposed in Kröger and Vink (1956) and discussed in even greater detail in Kröger (1974). An excellent reference from which to learn this approach is Smyth (2000).

will assume that the only acceptor is magnesium and that the acceptor excess ($Mg_{excess}^{/}$) is simply written as $Mg^{/}$.

Acceptor-dominated natural sapphire is often formed in a wet environment. Under these conditions, hydrogen provides the charge compensation, as shown here, and no trapped holes are formed:

$$MgO + \frac{1}{2}H_2O \xrightarrow{Al_2O_3} Mg_{Al}^{/} + \frac{1}{2}O_{o}^{x} + (OH)_{o}^{\bullet} \quad (5)$$

However, if the stones are later equilibrated in a warm, dry environment, part or all of the hydrogen may diffuse out of the stones, creating $h^{\bullet}$, as shown here:

$$Mg_{Al}^{/} + \frac{1}{2}O_{o}^{x} + (OH)_{o}^{\bullet} \xrightarrow{heat} Mg_{Al}^{/} + \frac{3}{2}O_{o}^{x} + h^{\bullet} + \frac{1}{2}H_2(g) \quad (6)$$

Since nearly all natural corundum contains significant Fe^{3+}, the trapped hole will associate with the Fe^{3+}, forming the $h^{\bullet}$-Fe^{3+} pair and creating the yellow

coloration (see footnote 3). These conditions are common in sapphire from Sri Lanka and the Rock Creek deposit in Montana, where a range of colorless to weakly yellow stones occurs naturally. When the process shown in equation 6 occurs in nature, yellow sapphires are formed, as shown in figure 14.

We usually do not think of hydrogen having a role in the visual color of gem corundum, as we assume the concentrations are very low (Beran and Rossman, 2006), a few ppma at most. Because their absorption cross sections are low ($1–2 \times 10^{-19}$ cm^2), a change of only a few ppma in the valence of the transition metal chromophores will make little or no difference in the apparent color. However, the $h^{\bullet}$-Fe^{3+} pair has cross sections of $1–2 \times 10^{-17}$ cm^2, which means that a few ppma change can induce or eliminate intense coloration.

The natural process shown in equation 6 can also be conducted in the laboratory. This is demonstrated in Atikarnsakul and Emmett (2021). If hydrogen-containing acceptor-dominated corundum is heated in an atmosphere that does not contain hydrogen or water vapor, the hydrogen will diffuse out of the stone. For time scales of one hour to several hours and temperatures in the 1000°–1400°C range, hydrogen will be removed from samples whose thickness ranges from a few millimeters to a centimeter.

Diffusion is described by the proportionality in the following equation:

$$x \propto \sqrt{(Dt)} \quad (7)$$

which states that the diffusion distance, x, in cm is directly proportional to the square root of the diffusion coefficient, D, in cm^2/sec, multiplied by the time, t, in seconds (Borg and Dienes, 1988).

The diffusion coefficient for hydrogen in aluminum oxide has been studied by many authors (Fowler et al., 1977; Kronenberg et al., 2000; Fukatsu et al., 2003; Belonoshko et al., 2004; Serra et al., 2005; Doremus, 2006; Van Orman and Crispin, 2010), with little agreement in the values they determined. Apparently, the diffusion coefficient is sensitive to impurities or structural issues in the crystal, but that remains to be quantified. For our rough estimates of the time at temperature required to remove the hydrogen from our samples, the hydrogen diffusion coefficient chosen is that given by Belonoshko et al. (2004), which at 1200°C is $D = 1.3 \times 10^{-6}$ cm^2/sec. From this value we can calculate the time required at 1200°C to remove ~90% of the hydrogen from a given size and shape of sample (Shewmon, 1989). For a 2 mm thick sample plate whose lateral dimension is large compared with 2 mm, the time is ~15 minutes. For sample plates that have a lateral dimension that is only a few to several times their thickness, the times would be somewhat less. For larger samples suitable for faceting, the times are significantly longer. For example, removing 90% of the hydrogen from a 1 cm diameter sphere at 1200°C would require heating for approximately 1.5 hours.

From our review of the literature, there is little consensus in the determination of the hydrogen diffusion coefficient in relatively pure sapphire crystals, and no information for natural crystals with the range and variety of trace elements found in gem sapphire. The uncertainty is more than one order of magnitude. According to equation 7, the uncertainty of the time required is then also an order of magnitude. Given the sensitivity of the yellow $h^{\bullet}$-Fe^{3+} coloration to hydrogen content, that chromophore might be used as a basis for experiments determining

Figure 14. Sri Lankan yellow sapphires ranging from 1.0 to 2.5 ct. The seven on the left are natural, and the four on the right are heat treated. Photo by Ronnakorn Manorotkul/Lotus Gemology; courtesy of Chaiyut Rungutaitawornsuk.

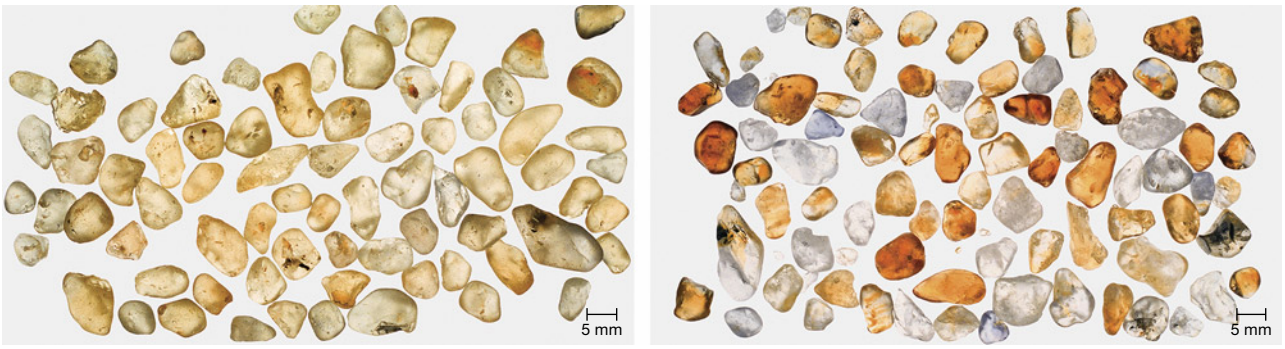

Figure 15. Left: Pale yellow natural sapphires from Sri Lanka. Right: The same sapphires after heat treatment at 1400°C, in oxygen, for five hours to remove hydrogen. Photos by John L. Emmett.

the hydrogen diffusion coefficient in natural or synthetic gem sapphire.

Acceptor domination of weakly colored sapphires from a single deposit ranges from 0 to 90% of the samples: 0% of the samples from Songea in Tanzania, ~20% from Chimwadzulu Hill in Malawi, ~50% from Sri Lanka, and ~90% from Rock Creek in Montana. Thus, it is important to initially test a large lot of small rough to determine the percentage that develop yellow coloration, in order to determine how many wafers must be fabricated to yield a few that turn yellow for the experiments and spectroscopy. This is the approach we have taken for this work, as presented below.

As seen in figure 15 (left), Sri Lankan yellow sapphires were initially a pale yellow color before heat treatment. Figure 15 (right) shows the same samples after heat treatment to quantitatively remove all hydrogen. More than half of the heated stones developed stronger yellow coloration, and many of them show the enhanced color following straight or angular growth structures. Compare the stones in figures 14 and 15. Thus far, it appears that nonuniform coloration is characteristic of this chromophore in natural corundum.

Figure 16 shows the detail of Sri Lankan sample 2802 undergoing this hydrogen removal process. Many natural Sri Lankan sapphires typically display a 3161 cm^{-1} OH peak or 3161 cm^{-1} OH series in FTIR spectra, which indicates they are acceptor dominated. The connection of the 3161 cm^{-1} series with

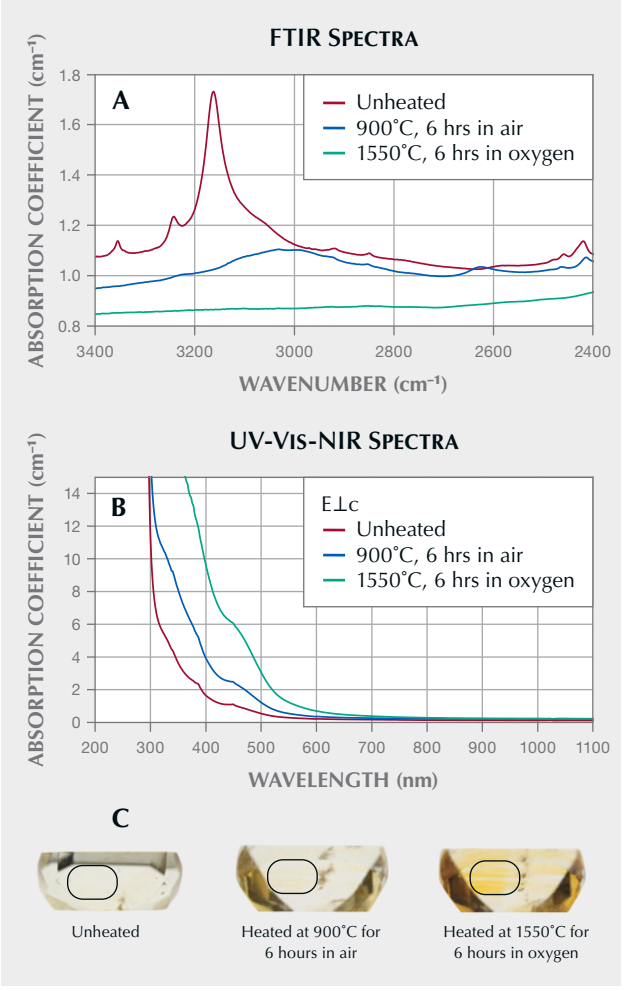

Figure 16. A: FTIR spectra of sample 2802 from Sri Lanka. B: UV-Vis-NIR spectra of the same sample. C: The color alteration of the sample before and after heat treatment. The outlined area indicates the analysis area where the FTIR and UV-Vis-NIR spectra were collected. Thickness 2.811 mm, 194 ± 26 ppma iron. Photos by Sasithorn Engniwat.

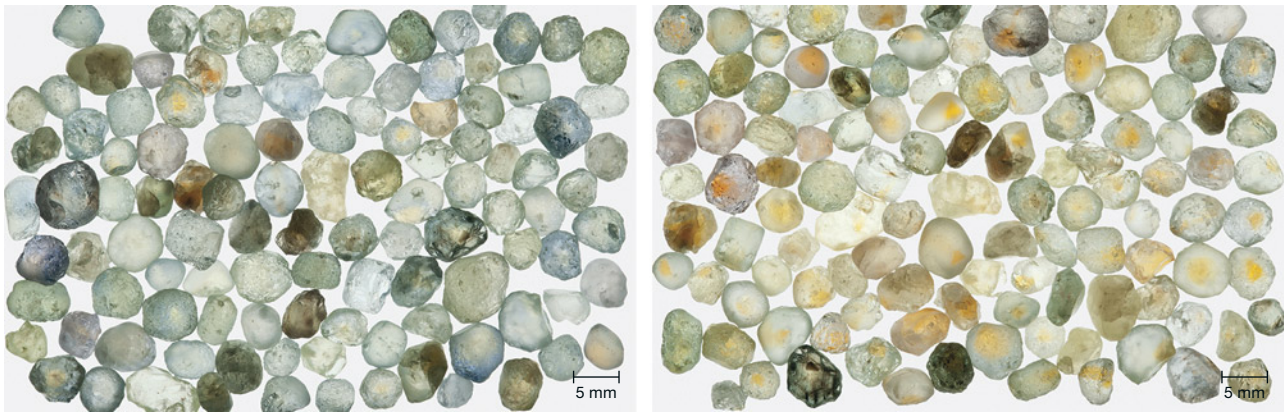

Figure 17. Left: Run-of-mine samples from Rock Creek, Montana, selected only for size (3.0–5.5 mm), before heat treatment. Right: The same samples are shown after heat treatment at 1200°C in oxygen for 10 hours. Photos by John L. Emmett.

high magnesium content (acceptor domination) was first described by Smith and van der Bogert (2006). Increased yellow coloration after heating (figure 16C) is directly related to the reduction of the amplitude of the OH-related peak at 3161 cm^{-1} (figure 16A) (Atikarnsakul and Emmett, 2021) and increased strength of the $h^{\bullet}$-Fe^{3+} absorption band in UV-Vis-NIR spectra (figure 16B). Interestingly, the natural characteristic 3161 cm^{-1} feature in certain samples could be occasionally transformed to the OH broadband series in the 3000 cm^{-1} region with a broadband at 2625 cm^{-1}, as shown in figure 16A when heated at 900°C in air. When heat treated at 1550°C in pure oxygen, the hydrogen was completely removed, as shown by the disappearance of the OH absorption features from the FTIR spectra. With the removal of the hydrogen, the $h^{\bullet}$-Fe^{3+} absorption spectrum and thus the yellow coloration increased.

As mined, sapphire from Rock Creek in Montana has little coloration, which indicates that the acceptor and donor concentrations are quite similar. In addition, about 8% of the stones show some yellow coloration, although only a few would cut a fine yellow gem. We also present hydrogen extraction results for this material, as it shows a different broadband OH absorption spectrum: the wide band 3000 cm^{-1} series. Interestingly, a few samples have both the 3000 cm^{-1} series and the 3161 cm^{-1} series, but thus far none have shown only the 3161 cm^{-1} series. When hydrogen is diffused into magnesium-doped synthetic sapphire, the OH spectrum is a broadband at 3000 cm^{-1} (Fukatsu et al., 2003). Similarly, when hydrogen is diffused into synthetic sapphire containing Ni^{3+} or Co^{3+}, the reduction of these dopants to the divalent state is accompanied by the formation of the broad OH band at 3000 cm^{-1} (Müller and Günthard, 1966). These facts, combined with the conversion of the 3161 cm^{-1} band to the 3000 cm^{-1} band in figure 16A, emphasize how little we understand OH in corundum. It would be worthwhile to study these OH features in a wide variety of acceptor-dominated corundum to determine the correlation of the various OH bands with the trace element chemistry and, perhaps, the formation temperature.

Figure 17 (left) shows run-of-mine samples of Rock Creek sapphire selected only for size (3.0–5.5 mm). Figure 17 (right) shows the same samples after heating for 10 hours at 1200°C in oxygen. Nearly 90% of the stones now show yellow coloration in some portion.

The development of yellow color zones in Rock Creek sapphires is similar to that seen in Sri Lankan sapphire, but the yellow region is often limited to a smaller portion of the stone, as shown in figure 13. Figure 18A shows the FTIR spectra of Rock Creek sample 1021 before and after heat treatment at 1500°C for five hours in pure oxygen. The heat treatment process has fully removed all the hydrogen from the sample.

Figure 18C shows the before and after photos of sample 1021. Heat treatment creates the strongly colored yellow spot that appears in the sample. Note that the optical measurement area is only centered on half of the yellow region (figure 18C, middle). A second sample plate was made so that optical measurements could also be centered on the yellow region, as shown in figure 18C, right.

Figure 18B shows the UV-Vis-NIR spectrum before and after heat treatment and in the second measurement area after heat treatment. The results revealed that the $h^{\bullet}$-Fe^{3+} spectrum increased significantly after heat treatment and was more obvious when the

analysis area was centered to be exclusively in the yellow area. By subtracting varying amounts of the $h^{\bullet}$-Fe^{3+} absorption spectrum from the spectrum in the second measurement area, we can determine that its concentration is approximately 6 ppma, the highest value measured thus far.

Figure 18. A: FTIR spectra of sample 1021 from Rock Creek. B: UV-Vis-NIR spectra of the same sample. C: The color alteration of the sample before and after heat treatment, and another measurement area after heat treatment. The outlined area indicates the analysis area where the FTIR and UV-Vis-NIR spectra were collected. Thickness 1.710 mm, 978 ± 111 ppma iron. Photos by Sasithorn Engniwat.

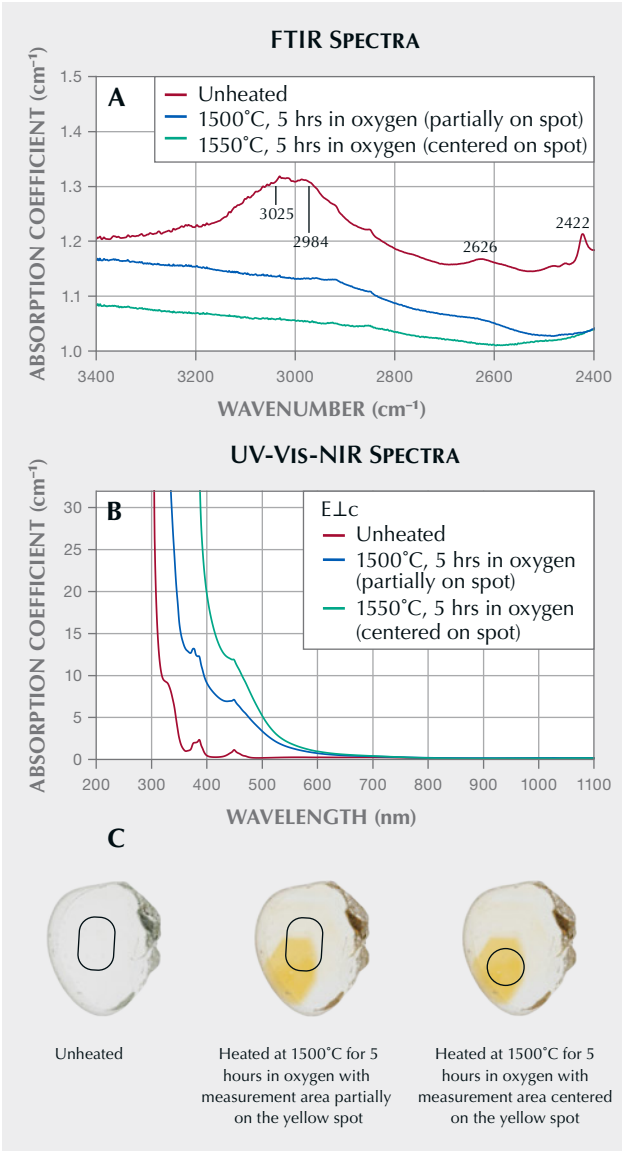

Yellow sapphires can also be created by heat treatment of an entirely different type of acceptor-dominated stone that does not contain hydrogen. If acceptor-dominated stones are formed at very low oxygen fugacity, the resulting reaction is:

$$MgO \xrightarrow{Al_2O_3} Mg'_{Al} + O_o^x + \frac{1}{2} V_o^{\bullet\bullet} \quad (8)$$

where the charge compensation is by oxygen vacancies. The result of this reaction is a colorless stone. If such stones are then heat treated at high temperature in an oxygen atmosphere, the oxidation reaction can be described as:

$$\frac{1}{2} O_2(g) \xrightarrow{Al_2O_3} O_o^x + \frac{2}{3} V_{Al}''' + 2h^{\bullet} \quad (9)$$

The oxidation is not caused by the inward diffusion of oxygen but by the inward diffusion of aluminum vacancies and holes formed on the surface. The combined reaction (equation 8 plus ½ equation 9) is:

$$Mg'_{Al} + O_o^x + \frac{1}{2} V_o^{\bullet\bullet} + \frac{1}{2} O_o^x + \frac{1}{3} V_{Al}''' + h^{\bullet} = Mg'_{Al} + \frac{3}{2} O_o^x + h^{\bullet} \quad (10)$$

This reaction shows how acceptor-dominated, hydrogen-free colorless stones can be heat treated in oxygen to create the $h^{\bullet}$-Fe^{3+} chromophore and thus the yellow coloration. The diffusion coefficient for the inward diffusion of aluminum vacancies and holes is much lower than the outward diffusion of hydrogen, so this reaction requires much higher temperatures and much longer times.

At present we know of three sources for sapphire formed in this way. Pale to colorless stones are found at the Eldorado Bar deposit on the Missouri River in Montana, at the Chimwadzulu Hill deposit in Malawi, and at deposits in Madagascar. In each case, only a fraction (5–30%) of the run-of-mine stones exhibit this chemistry. To study the formation of the $h^{\bullet}$-Fe^{3+} chromophore in this entirely different chemistry, the following experiments were conducted. A large 600 g parcel of Missouri River sapphire was processed through a precision splitter to make twelve 50 g test lots that were nearly identical. There were no identifiable yellow samples in the entire 600 g parcel. Twenty-five grams (one-half) of one of the test lots are shown in figure 19A. One each of the 50 g sublots were processed in pure oxygen in each of the following conditions: 1600°C for 10 hours (19B), 1700°C for 10 hours (19C), 1800°C for 10 hours (19D), and 1800°C for 31.6 hours (19E). The experiments at

lower temperatures (1200°C and 1400°C) did not produce any yellow stones. After heat treatment, all the yellow sapphires in the 50 g samples were sorted out and photographed separately, as shown in figure 19, B–E.

The stones in figure 19E represent about 23% by weight of the 50 g lot. Plotting the data from these experiments indicates that increasing both the temperature and time should further increase the yield of yellow sapphire and the degree of color saturation.

Comparing the heat treatment conditions of figure 17 (right) and figure 19E shows the dramatic difference between acceptor-dominated stones charge compensated with hydrogen and those charge compensated with oxygen vacancies. Sapphires from Chimwadzulu Hill in Malawi responded to high-temperature heat treatment in a similar way, with about 19% developing the yellow coloration.

If the corundum has excess acceptors and is grown or later equilibrated in a high-oxygen-fugacity natural environment, we have the following chemical reaction:

$$MgO + \frac{1}{4}O_2(g) \xrightarrow{Al_2O_3} Mg'_{Al} + \frac{3}{2}O_o^x + h^{\bullet} \quad (11)$$

which is the same as the after-heating result shown in equation 10. The interesting question is whether this condition occurs in nature to produce natural yellow sapphires. To answer this question, we need to find natural yellow sapphires whose coloration is due wholly or in part to the $h^{\bullet}$-Fe^{3+} pair yet show no OH absorption features in the FTIR spectrum. Such examples may be found in sapphires that are weakly or strongly yellow colored by Fe^{3+}.

Finding such samples is difficult for several reasons. The 3000 cm^{-1} broadband usually has a much lower peak absorption coefficient than the 3161 cm^{-1} band, as it is much broader. Thus, determining that there is zero OH absorption was difficult, as most of

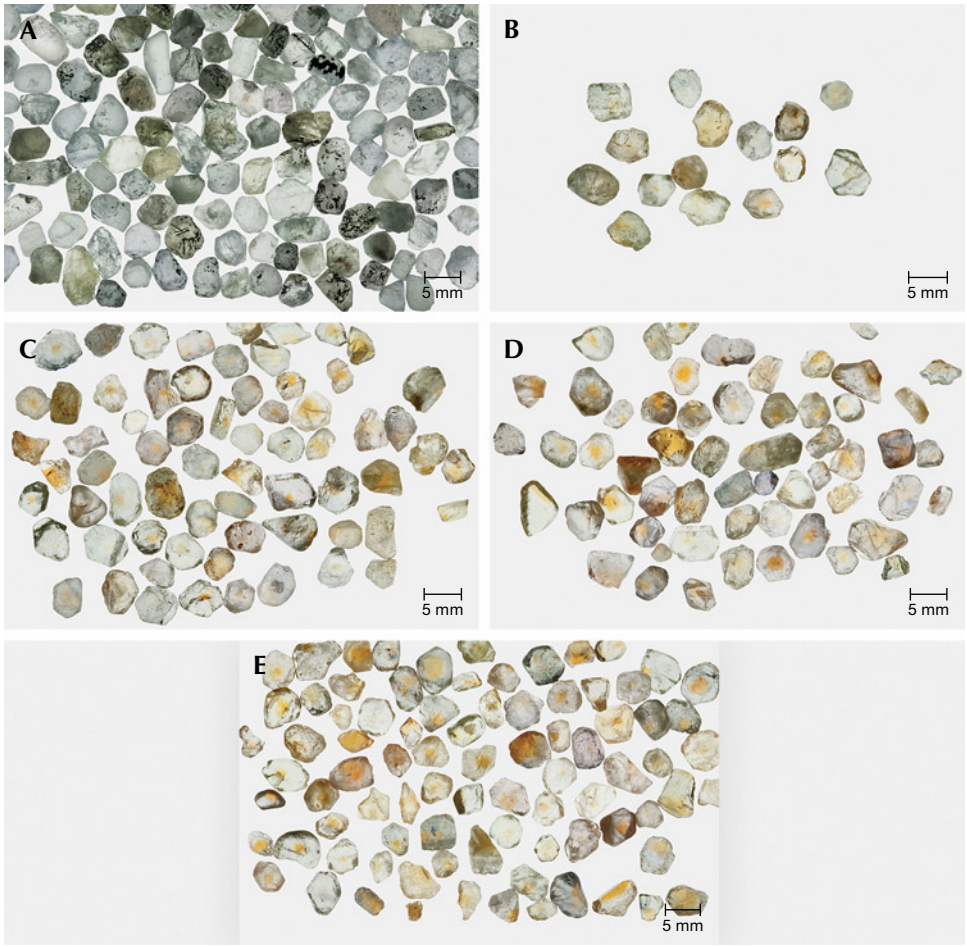

Figure 19. A: One-half of a 50 g lot from a 600 g parcel of Missouri River sapphire, selected only for size (3.5–5.5 mm), before heat treatment. B: Yellow stones produced from another 50 g lot after heat treatment at 1600°C in oxygen for 10 hours. C: Yellow stones produced from another 50 g lot after heat treatment at 1700°C in oxygen for 10 hours. D: Yellow stones produced from another 50 g lot after heat treatment at 1800°C in oxygen for 10 hours. E: Yellow stones produced from another 50 g lot after heat treatment at 1800°C in oxygen for 31.6 hours. Photos by John L. Emmett.

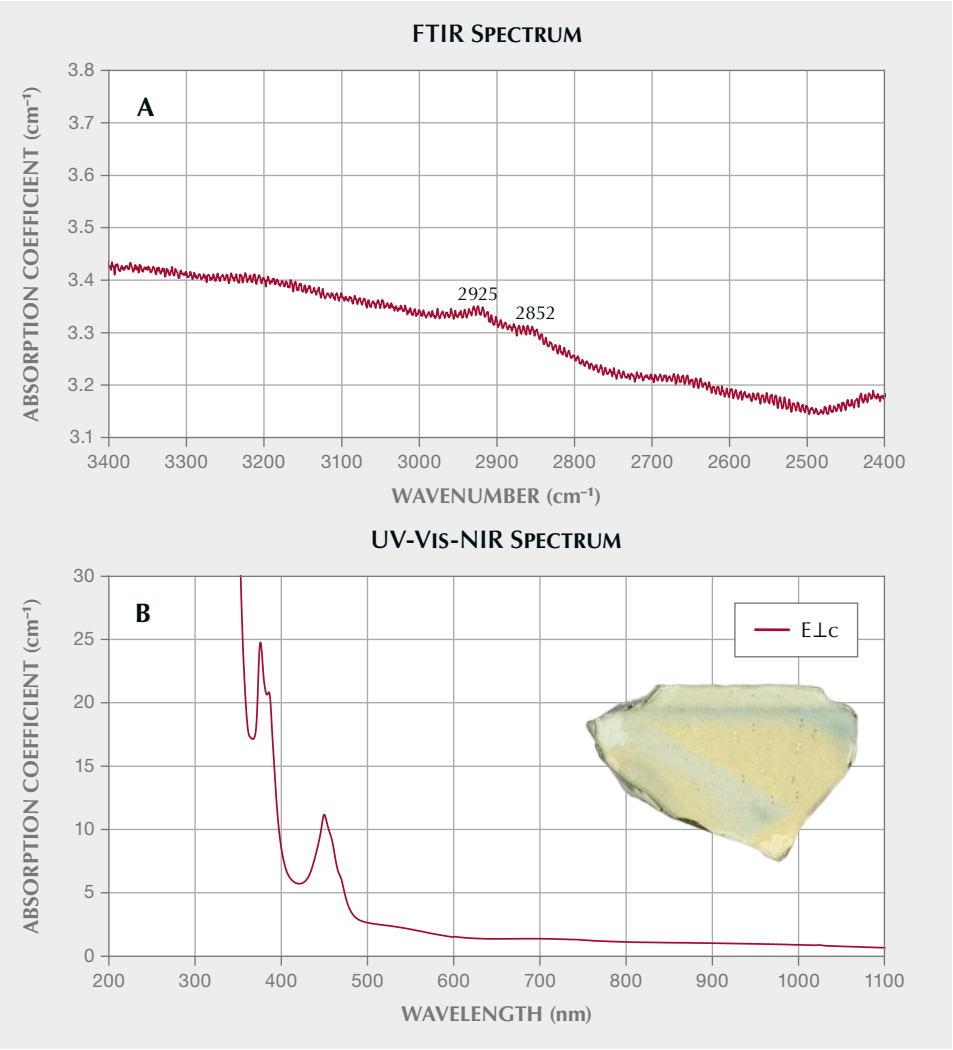

Figure 20. A: FTIR spectrum of sample 4713 from Chanthaburi, Thailand. B: UV-Vis-NIR spectrum of the same sample measured in the yellow region. E⊥c, thickness 0.465 mm, 3889 ± 229 ppma iron. Photo by John L. Emmett.

our research samples were rather thin. Additionally, weakly colored yellow sapphires that may also show these two characteristics are not often the focus of sample collection for research, as opposed to more strongly colored stones.

At present, our best example of such a sample is yellow sapphire 4713 from Chanthaburi, Thailand, which shows these two characteristics. As shown in figure 20, there is no indication of the 3161 cm^{-1} series or the 3000 cm^{-1} broadband series in this FTIR spectrum, but the $h^{\bullet}$-Fe^{3+} pair absorption in the UV-Vis-NIR spectrum is clear from the increasing absorption coefficient from 600 to 500 nm. This sample is weakly colored, as it is only 0.465 mm thick. Two small peaks centered at around 2925 and 2852 cm^{-1} are observed in the FTIR spectrum, but they are not a part of the 3000 cm^{-1} broadband series. They are typically seen overlying various other mid-infrared spectral features as a result of oil contamination on the surface of the stone or other materials present in open fractures. These peaks are related to the C-H stretching (2950–2850 cm^{-1}) of organic matter (Tanykova et al., 2021), and the peak positions were the same as those of oil-impregnated emerald (Johnson et al., 1999).

Presently, our only example of the equation 11 phenomenon is sample 4713. Definitive proof that natural stones are indeed formed in this way will require the collection of substantially more samples from a wider list of deposits. In addition, samples should be fabricated into significantly thicker wafers to facilitate the accurate measurement of their FTIR spectra.

Combination of the Fe^{3+} and $h^{\bullet}$-Fe^{3+} Chromophores. Untreated high-Fe^{3+} yellow sapphires from basalt-hosted deposits such as Australia and Thailand often have a quite uniform yellow color. The color is caused mainly by the Fe^{3+} chromophore, but some-

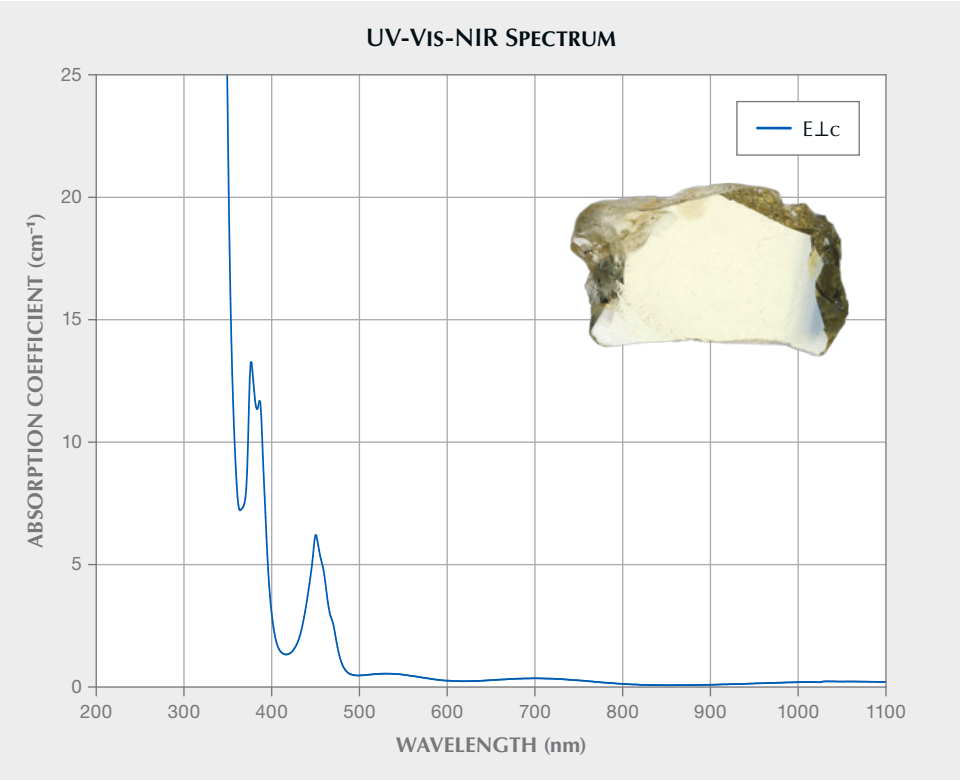

Figure 21. UV-Vis-NIR spectrum of sample 941 from Bang Kha Cha, Thailand. E⊥c, iron = 3093 ppma, areal density = 4979 ppma-mm, and t *= 1.61 mm. Photo by John L. Emmett.*

times it is substantially modified by the presence of the $h^{\bullet}$-Fe^{3+} chromophore as well.

Natural yellow sapphires of high iron concentration (>2800 ppma Fe^{3+}) usually exhibit a rather uni-

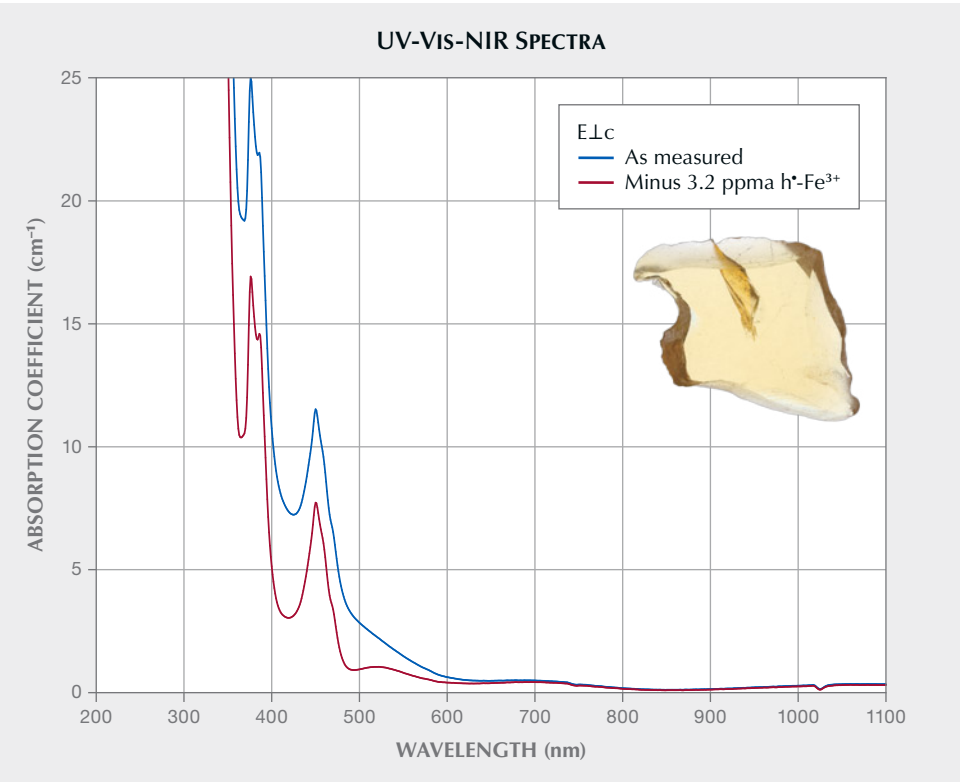

Figure 22. UV-Vis-NIR spectra of sample 940 from Bang Ka Cha, Thailand. E⊥c, iron = 3251 ppma, areal density = 4649 ppma-mm, and t *= 1.430 mm. Photo by John L. Emmett.*

form yellow coloration. This is because Fe^{3+} is soluble in corundum, easily replacing Al^{3+} because it has the same valence and a similar ionic radius. Unlike the chromophores containing aliovalent ions, Fe^{3+} solubility is not dependent on the presence of another ion. Perhaps more interesting is that these high-Fe^{3+} natural sapphires often incorporate the $h^{\bullet}$-Fe^{3+} chromophore as well. It is not unusual to find yellow sapphires colored by Fe^{3+} only and colored by both high Fe^{3+} concentration and the $h^{\bullet}$-Fe^{3+} chromophore in the same deposit. The Subera deposit in New South Wales, Australia, and the Khao Ploi Waen/Bang Kha Cha deposit in Thailand are two examples of this phenomenon.

Figures 21 and 22 compare two similar samples from Bang Kha Cha. Sample 941 (figure 21) is colored by Fe^{3+} only, while sample 940 (figure 22) is colored by both chromophores. Both samples exhibit a weak but broad OH band at 3000 cm^{-1}. Sample 940 has a peak absorption of about 0.04 cm^{-1}, while sample 941 has a peak absorption of about 0.07 cm^{-1}.

As discussed earlier, when comparing color caused by the Fe^{3+} chromophore only, both the Fe^{3+} concentration and its areal density must be taken into account. Samples 940 and 941 differ in Fe^{3+} concentration by only 5.1% and in areal density by only 7.1%. Therefore, the 450 nm absorption bands of Fe^{3+} of the two samples are nearly equal. These samples offer a direct comparison of high-iron corundum with and without the $h^{\bullet}$-Fe^{3+} chromophore.

The dramatic difference in the depth and character of the color between sample 940 and sample 941 is the result of the additional ~3.2 ppma of the $h^{\bullet}$-Fe^{3+} chromophore. When examining the spectra of yellow sapphire samples with high concentrations of Fe^{3+}, it is very easy to discern which contain only Fe^{3+} and which contain some addition of the $h^{\bullet}$-Fe^{3+} chromophore. In figure 21 there is a distinct minimum between the Fe^{3+} 450 nm band and the weak, broad Fe^{3+} band at 530 nm (Borg and Dienes, 1988). Depending on the Fe^{3+} concentration, the minimum between these two usually occurs between 490 and 502 nm. For sample 941, just 0.25 ppma of the $h^{\bullet}$-Fe^{3+} pair eliminates the minimum. The 3.2 ppma of the $h^{\bullet}$-Fe^{3+} chromophore in sample 940 is determined by subtracting incremental amounts of it from the spectrum of sample 940 until the minimum at 500 nm is restored. Typical concentrations of 1 ppma or more of the $h^{\bullet}$-Fe^{3+} chromophore result in a linear increase in the absorption coefficient from 600 to 500 nm, which is very easy to visually recognize. That sample 940 shows a well-saturated color and yet is only 1.43 mm thick attests to the extraordinary strength of the $h^{\bullet}$-Fe^{3+} chromophore.

The question naturally arises as to whether these high-iron stones, which also exhibit the $h^{\bullet}$-Fe^{3+} chromophore, respond to heat treatment. Figure 23 shows the result of some experiments. Figure 23A gives the FTIR spectra from sample 5270. This natural stone from Australia exhibits the 3000 cm^{-1} OH broadband series, not the 3161 cm^{-1} series. This OH absorption has been eliminated by heating at 900°C for six hours

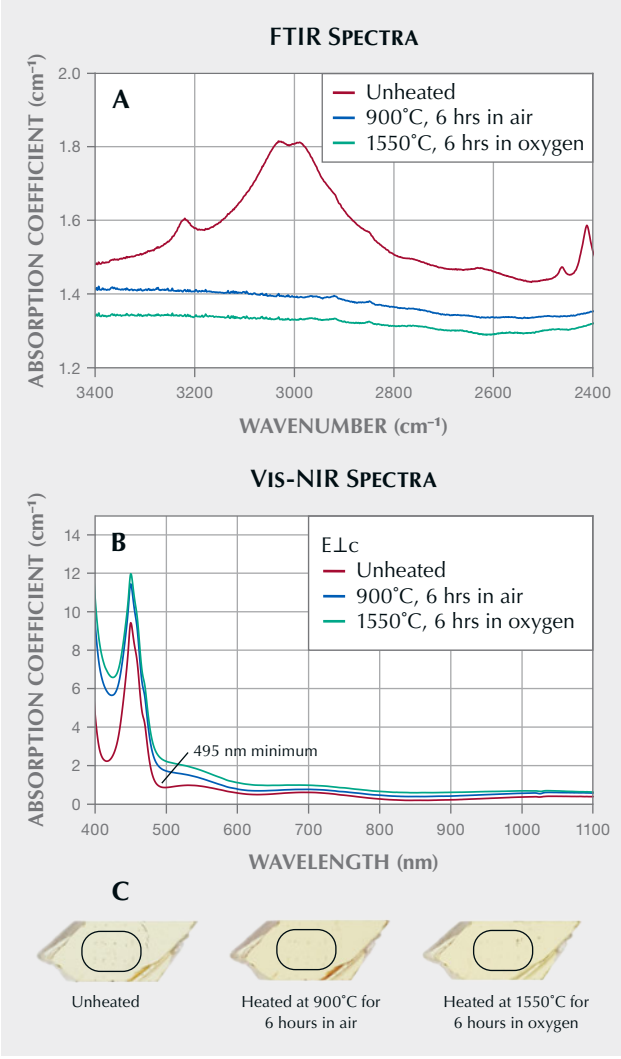

Figure 23. A: FTIR spectra of Australian sample 5270. B: UV-Vis-NIR spectra of the same sample. C: The color alteration of the sample after heat treatment. The outlined area indicates the analysis area where the FTIR and UV-Vis-NIR spectra were collected. Thickness 1.240 mm, 3557 ± 627 ppma iron. Photos by Sasithorn Engniwat.

Figure 24. This unusual gem from the Bang Kha Cha deposit is colored by a high concentration of both the Fe^{3+} and the $h^{\bullet}$-Fe^{3+} chromophores. The color is referred to as "Mekong Whisky." Photo by Ronnakorn Manorotkul/Lotus Gemology.

in air, and then by heating again at 1550°C for six hours in oxygen. Figure 23B illustrates that before heat treatment there is a minimum at ~495 nm, indicating the absence of the $h^{\bullet}$-Fe^{3+} chromophore. Heat treatment at 900°C substantially increases the depth of the yellow coloration, as shown in figure 23C.

The combination of high concentrations of both the Fe^{3+} and the $h^{\bullet}$-Fe^{3+} chromophores can create dramatic colors, as shown in figure 24.

Beryllium-Diffused Yellow Sapphires. The diffusion of divalent beryllium into natural corundum (Emmett et al., 2003) adds to the concentration of acceptor ions so that equations 3 and 4 become:

$$[acceptors] - [donors] = [Be^{2+} + Mg^{2+} + Ni^{2+}] - [Si^{4+} + Ti^{4+}] > 0 \quad (12)$$

$$[Be^{2+} + Mg^{2+} + Ni^{2+}] - [Si^{4+} + Ti^{4+}] - [H^{+} + 2V_o^{2+} + h^{+}] = 0 \quad (13)$$

The addition of beryllium by diffusion in an oxidizing atmosphere primarily results in the formation of additional trapped holes, which will form more $h^{\bullet}$-Fe^{3+} pairs with available Fe^{3+} and thus more yellow coloration. Because beryllium itself is not the chromophore, the coloration resulting from trapped holes formed by beryllium excess, by magnesium excess, or by both in excess is the same, as the chromophore is always $h^{\bullet}$-Fe^{3+}. We have demonstrated this fact by growing two crystals, the first doped with magnesium and iron and the second doped with beryllium and iron.

The E⊥c absorption cross sections of the two $h^{\bullet}$-Fe^{3+} chromophores presented in figure 25 are nearly

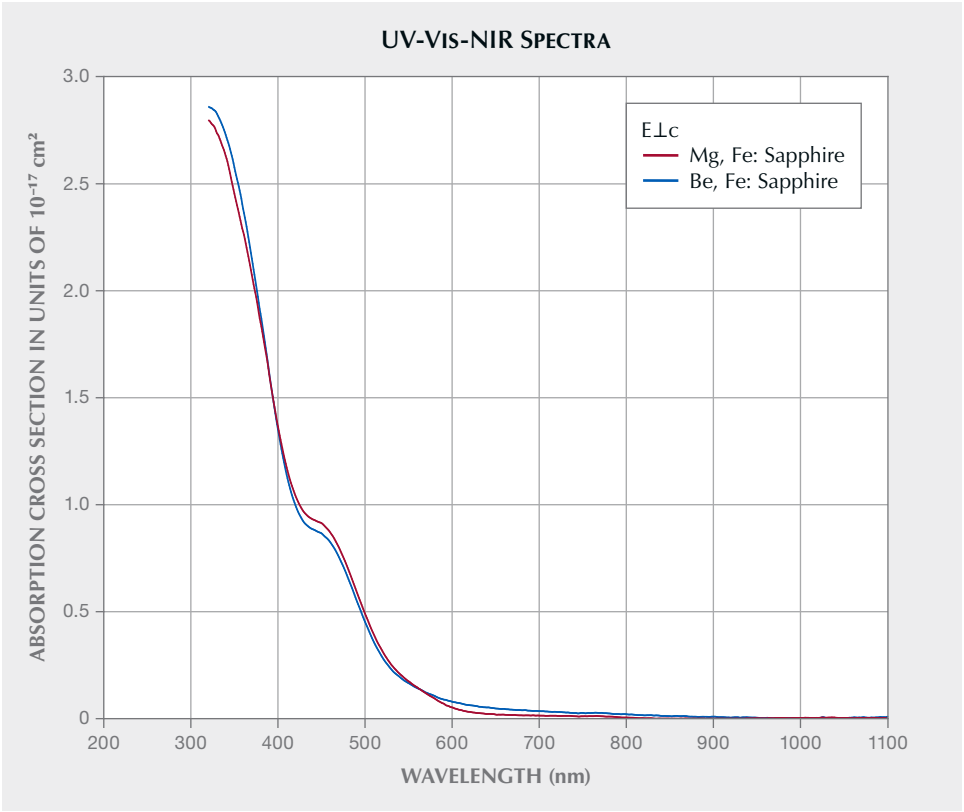

Figure 25. The UV-Vis-NIR E⊥c absorption cross section of the $h^{\bullet}$-Fe^{3+} pair in two different synthetic sapphire crystals. The first is doped with magnesium and iron and the second with beryllium and iron.

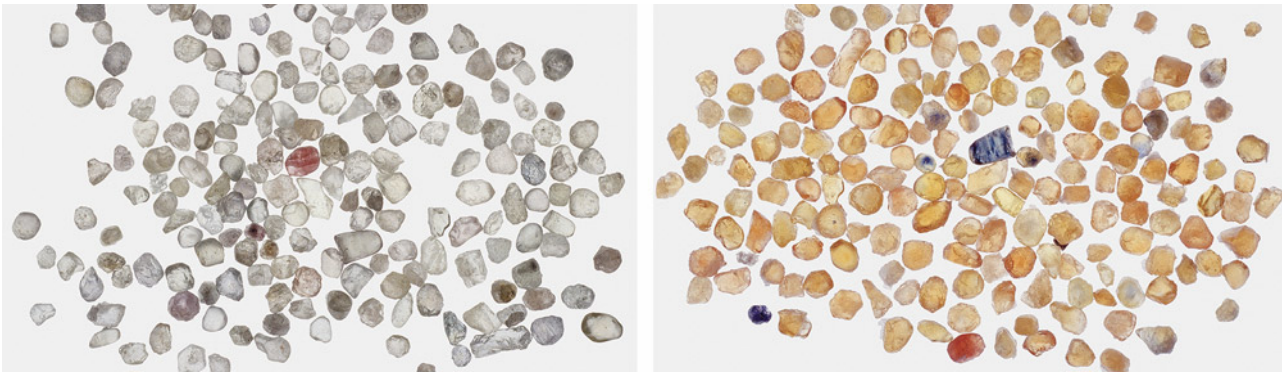

Figure 26. Left: Near-colorless sapphires from the Dry Cottonwood Creek deposit in Montana, with an average stone size of 4–5 mm. Right: The same group of sapphires after beryllium diffusion. Photos by John L. Emmett.

identical. A small vertical offset (0.127×10^{-17}) resulting from internal scatter in the crystal doped with beryllium and iron has been subtracted from its spectrum in figure 25.

Beryllium diffusion to alter the coloration of natural corundum is conducted in an air or pure oxygen atmosphere at temperatures of 1800°C or above for several tens of hours. The diffusion experiments described here were conducted in the Crystal Chemistry laboratory in a pure oxygen atmosphere, as were the experiments in Emmett et al. (2003). Heating in this way eliminates all of the H^+ and V_o^{2+} charge compensators, maximizing the degree of acceptor domination and the $h^{\bullet}$-Fe^{3+} concentration. This maximizes the yellow coloration of sapphire. Commercially this process is often conducted in air. If conducting the diffusion process in air, the water vapor in the air can contribute hydrogen to the process, contributing to some reduction of the $h^{\bullet}$-Fe^{3+} concentration. In addition, OH bands that would otherwise have been completely eliminated can appear in the FTIR spectra. This effect in synthetic sapphire is shown in Balmer and Krzemnicki (2015) and Sangsawong (2020).

As previously discussed, sapphires that are colorless or weakly colored are usually neutral or slightly acceptor dominated. If such stones are beryllium diffused, a strong yellow color results from a substantial increase in $h^{\bullet}$-Fe^{3+} concentration. Figure 26 (left) shows a group of near-colorless sapphires from the Dry Cottonwood Creek deposit in Montana. The great majority of sapphires from this deposit show little coloration. Figure 26 (right) shows the result of beryllium-diffusing this group at 1800°C in oxygen for 33 hours.

The amount of beryllium that can be added to natural corundum by diffusion often quite exceeds the acceptor excess that occurs in natural yellow sapphire. Thus, it is possible that even donor-dominated blue sapphires can be converted to acceptor-dominated yellow sapphires by beryllium diffusion. We conducted an experiment to demonstrate that possibility using deep blue sapphire mined at Kings Plain, New South Wales, Australia (figure 27, left).

Figure 27. Left: A group of run-of-mine deep blue sapphires from Kings Plain, New South Wales, Australia, with an average stone size of 4–5 mm. Right: The same group of sapphires after beryllium diffusion. Photos by John L. Emmett.

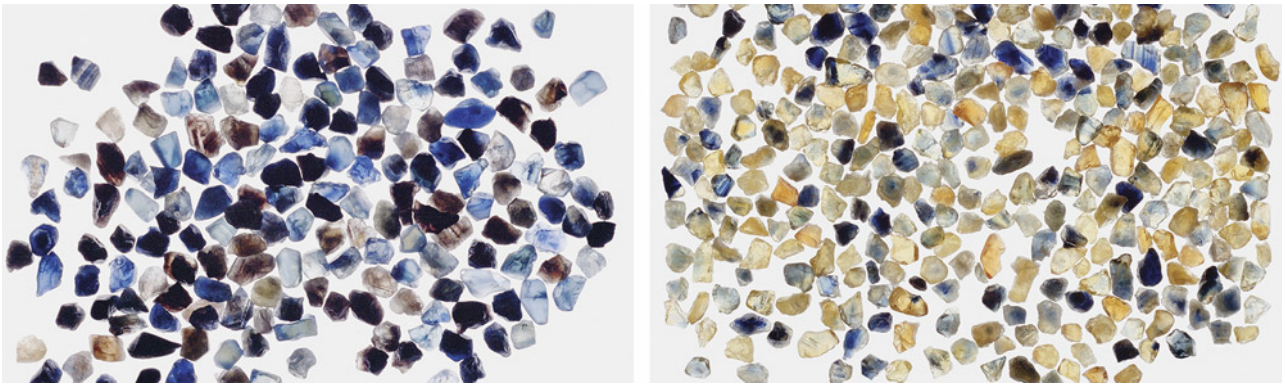

Figure 28. Synthetic sapphire colored only by the $h^{\bullet}$-Fe^{3+} chromophore. The three thickest sections are 12 mm thick. Photo by John L. Emmett.

Figure 27 (right) shows these stones after beryllium diffusion treatment. The majority of the blues have been converted to yellows, which are now acceptor dominated. Although the color has been reduced in degree, stones that were the deepest blue before diffusion have been lightened but remain donor dominated.

Synthetic Yellow Sapphires. Synthetic yellow sapphire, which is colored by the yellow $h^{\bullet}$-Fe^{3+} chromophore, was grown for the first time as a part of the study of the chromophores of natural corundum (Emmett et al., 2017a). The yellow crystal grown by author JS-S at Saint-Gobain Crystal and Detectors was doped with magnesium and iron to produce the $h^{\bullet}$-Fe^{3+} chromophore. Figure 28 shows sections of this Czochralski-grown boule, of which the three thickest are 12 mm thick. The other three samples are broken, providing some wedge sections. The $h^{\bullet}$-Fe^{3+} chromophore concentration is 2.1 ppma ± 9%. Note the uniformity of color compared to the natural samples colored with the same chromophore, which are often zoned.

Historically, synthetic sapphires have usually been doped with nickel or by nickel and chromium to produce the yellow coloration. The chromophores used have typically been the transition metals and the Fe^{2+}-Ti^{4+} pair. Thus, it is not surprising to see yellow synthetic sapphire colored primarily with Ni^{3+}. It is also interesting that the nickel concentration used is quite low compared with the other transition metals. The yellow coloration from Ni^{3+} does not result from transitions within the Ni^{3+} electronic structure, but from a charge transfer transition from the Al_2O_3 valence band to the Ni^{3+} ion (Tippins, 1970). What is most unusual is that this first charge transfer band of Ni^{3+} peaks is at 400 nm, providing significant absorption from 400 to 480 nm and thus strong yellow coloration. All other transition metals studied to date have their first charge transfer band well into the UV, and thus these bands do not contribute to color. For example, the first charge transfer bands for Fe^{3+} and Cr^{3+} are at 259 and 178 nm, respectively (Tippins, 1970). Charge transfer absorption cross sections are typically a few hundred times stronger than the internal electronic transitions in transition metals, which is why low concentrations of Ni^{3+} contribute significant color.

In the course of this study, we examined one crystal grown with the Verneuil process from RusGems in Bangkok and two crystals grown with the Czochralski technique by Milan Kokta at Saint-Gobain Crystals and Detectors. The Ni^{3+} concentration of the three crystals, analyzed by LA-ICP-MS at GIA and by SIMS at the California Institute of Technology, ranged from 1.6 to 8.0 ppma. To ensure that all the nickel was in the trivalent state, the spectroscopic samples cut from the boules were annealed in

Figure 29. Sample 1162, a Ni^{3+}-doped sapphire cut from boule SS9. The c-axis is in the plane of the wafer, which measures 10.0 × 10.0 × 2.14 mm. Photo by John L. Emmett.

oxygen at 1750°C for 10 hours. The oxygen anneal of one of the samples cut from the SS9 Czochralski-grown crystal increased the absorption coefficient of the first charge transfer band by a factor of about eight. This stems from the fact that the oxygen partial pressure of the growth atmosphere is approximately 10^{-3} atmospheres, and thus only a portion of the nickel was in the trivalent state following growth. The Verneuil-grown crystal from RusGems was fully oxidized as received. It is unknown whether this condition resulted from the very different growth conditions of the Verneuil process or from an oxygen anneal following growth.

Figure 29 shows sample 1162, cut from Czochralski boule SS9 after the oxygen anneal. Figure 30 shows UV-Vis-NIR absorption cross sections for both E⊥c and E||c before and after the oxygen anneal. The nickel concentration in this crystal is 3.58 ppma, as measured by SIMS at the California Institute of Technology, and the thickness is 2.14 mm.

As mentioned earlier, the reason for our interest in determining the Ni^{3+} absorption cross section is the fact that nickel in concentrations of up to 15 ppma has been found in natural sapphire. We determined its cross section, as we have done for the other natural chromophores in corundum. As shown here, only a few ppma of Ni^{3+} are necessary to produce sub-

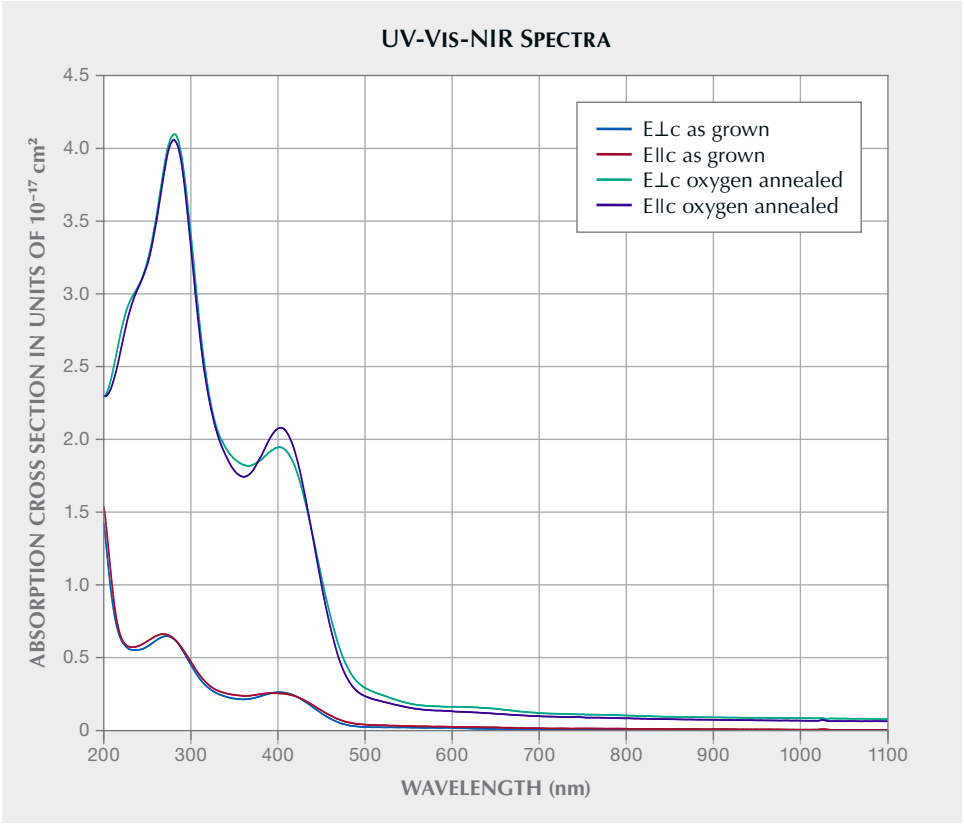

Figure 30. Sample 1162, a Ni^{3+}-doped Czochralski-grown sapphire.

stantial coloration. Since the absorption cross section in the visible region of Ni^{3+} exceeds even that of the $h^{\bullet}$-Fe^{3+} pair, only a few ppma in a neutral or acceptor-dominated stone would contribute strong absorption in the 400–480 nm region, adding additional yellow coloration. It is important to carefully study the absorption spectra of stones containing ≥1 ppma nickel to determine whether there is a seventh natural chromophore. The first six are discussed in Dubinsky et al. (2020).

CONCLUSIONS

This study of yellow sapphires was motivated by the lack of clarity in the literature as to the origin of the yellow coloration. In retrospect, this uncertainty was the result of three factors. First, the Fe^{3+} concentration in natural stones spans a range of approximately 4–4750 ppma, but only concentrations in the 2000–4750 ppma range contribute significantly to yellow coloration. Second, the $h^{\bullet}$-Fe^{3+} chromophore is about 1000 times as strong as the Fe^{3+} chromophore and is often distributed quite inhomogeneously in a given sample. Low concentrations, ≥0.5 ppma, produce substantial coloration, which could only be determined with the advent of LA-ICP-MS and SIMS in gemology. Third, both of these chromophores contribute to the yellow coloration in many natural yellow sapphires, making its cause of color difficult to determine.

We hope this paper will form a basis for further study of the yellow color stability of natural sapphire, a topic that has become increasingly important in recent years. From our work, it is clear that any study of color stability must first determine the trace element composition of the sample down to 1 ppma or better, the UV-Vis-NIR absorption spectra, and the FTIR absorption spectra of the OH ion. A study of color change by low-temperature heating, visible light illumination, or UV illumination will be needed to track the latter two factors.

ABOUT THE AUTHORS

Dr. John Emmett is director of Crystal Chemistry in Brush Prairie, Washington, and a consultant to GIA. Ungkhana Atikarnsakul is a staff gemologist at GIA's Bangkok laboratory. Dr. Jennifer Stone-Sundberg is a technical advisor on GIA education operations and a technical editor of Gems & Gemology *located in Portland, Oregon. Dr. Supharart Sangsawong is a former research scientist at GIA in Bangkok.*

ACKNOWLEDGMENTS

The authors would like to thank many people who have contributed to this work over very many years, especially Tom Moses, Ken Scarratt, Sudarat Saeseaw, Wasura Soonthorntantikul, Tim Thomas, Ziyin Sun, Milan Kokta, George Rossman, Yunbin Guan, Ren Lu, Zachary Cole and team, Dick Hughes, Wimon Manorotkul, Emily Dubinsky, and Augustus Pritchett. We would also like to extend our thanks to all the miners and contacts for their efforts in collecting and documenting some of the samples used for this study, as well as field gemologists Vincent Pardieu and Wim Vertriest. We want to extend our thanks to Sasithorn Engniwat, Charuwan Khowpong, and Suwasan Wongchacree from GIA's field gemology department for sample fabrication and the collection of photos and photomicrographs. Anonymous peer reviewers are also thanked for providing helpful comments and suggestions.

REFERENCES

Atikarnsakul U., Emmett J.L. (2021) Gem News International: Heat treatment effects on the behavior of the 3161 cm^{-1} feature in low-iron metamorphic yellow sapphire. *G&G*, Vol. 57, No. 3, pp. 286–288.

Balmer W.A., Krzemnicki M.S. (2015) Be-detection by FTIR on corundum: A preliminary report. *34th IGC Conference*. Vilnius, Lithuania, pp. 69–71.

Belonoshko A.B., Rosengren A., Dong Q., Hultquist G., Leygraf C. (2004) First-principles study of hydrogen diffusion in α-Al_2O_3 and liquid alumina. *Physical Review B*, Vol. 69, article no. 024302, http://dx.doi.org/10.1103/PhysRevB.69.024302

Beran A., Rossman G.R. (2006) OH in naturally occurring corundum. *European Journal of Mineralogy*, Vol. 18, No. 4, pp. 441–447, http://dx.doi.org/10.1127/0935-1221/2006/0018-0441

Berns R.S. (2000) *Billmeyer and Saltzman's Principles of Color Technology*. John Wiley & Sons, Inc., New York, 272 pp.

Borg R.J., Dienes G.J. (1988) *An Introduction to Solid State Diffusion*. Academic Press, Inc., San Diego, California.

Doremus R.H. (2006) Diffusion in alumina. *Journal of Applied Physics*, Vol. 100, No. 10, article no. 101301, http://dx.doi.org/10.1063/1.2393012

Dubinsky E.V., Stone-Sundberg J., Emmett J.L. (2020) A quantitative description of the causes of color in corundum. *G&G*, Vol. 56, No. 1, pp. 2–28, http://dx.doi.org/10.5741/GEMS.56.1.2

Emmett J.L., Scarratt K., McClure S.F., Moses T., Douthit T.R., Hughes R., Novak S., Shigley J.E., Wang W., Bordelon O., Kane R.E. (2003) Beryllium diffusion in ruby and sapphire. *G&G*, Vol. 39, No. 2, pp. 84–135, http://dx.doi.org/10.5741/GEMS.39.2.84

Emmett J.L., Dubinsky E.V., Hughes R.W., Scarratt K. (2017a) Color, spectra & luminescence. In R.W. Hughes et al., *Ruby & Sapphire: A Gemologist's Guide*. RWH Publishing, Bangkok, pp. 107–163.
Emmett J.L., Stone-Sundberg J., Guan Y., Sun Z. (2017b) The role of silicon in the color of gem corundum. *G&G*, Vol. 53, No. 1, pp. 42–47, http://dx.doi.org/10.5741/GEMS.53.1.42
Ferguson J., Fielding P.E. (1971) The origins of the colours of yellow, green and blue sapphires. *Chemical Physics Letters*, Vol. 10, No. 3, pp. 262–265, http://dx.doi.org/10.1016/0009-2614(71)80282-8
——— (1972) The origins of the colours of natural yellow, blue, and green sapphires. *Australian Journal of Chemistry*, Vol. 25, No. 7, pp. 1371–1385, http://dx.doi.org/10.1071/CH9721371
Fowler J.D., Chandra D., Elleman T.S., Payne A.W., Verghese K. (1977) Tritium diffusion in Al_2O_3 and BeO. *Journal of the American Ceramic Society*, Vol. 60, No. 3-4, pp. 155–161, http://dx.doi.org/10.1111/j.1151-2916.1977.tb15493.x
Fukatsu N., Kurita N., Oka Y., Yamamoto S. (2003) Incorporation of hydrogen into magnesium-doped α-alumina. *Solid State Ionics*, Vol. 162-163, pp. 147–159, http://dx.doi.org/10.1016/S0167-2738(03)00218-2
Johnson M.L., Elen S., Muhlmeister S. (1999) On the identification of various emerald filling substances. *G&G*, Vol. 35, No. 2, pp. 82–107, http://dx.doi.org/10.5741/GEMS.35.2.82
Krebs J.J., Maisch W.G. (1971) Exchange effects in the optical-absorption spectrum of Fe^{3+} in Al_2O_3. *Physical Review B*, Vol. 4, No. 3, pp. 757–769, http://dx.doi.org/10.1103/PhysRevB.4.757
Kröger F.A. (1974) *The Chemistry of Imperfect Crystals, Volume 2*. North-Holland Publishing Co., Amsterdam.
Kröger F.A., Vink H.J. (1956) Relations between the concentrations of imperfections in crystalline solids. In F. Seitz and D. Turnbull, Eds., *Solid State Physics*, Vol. 3., Academic Press, New York, pp. 307–435, http://dx.doi.org/10.1016/S0081-1947(08)60135-6
Kronenberg A.K., Castaing J., Mitchell T.E., Kirby S.H. (2000) Hydrogen defects in α-Al_2O_3 and water weakening of sapphire and alumina ceramics between 600 and 1000°C–I. Infrared characteristics of defects. *Acta Materialia*, Vol. 48, No. 7, pp. 1481–1494, http://dx.doi.org/10.1016/S1359-6454(99)00448-6
Müller R., Günthard H.H. (1966) Spectroscopic study of the reduction of nickel and cobalt ions in sapphire. *Journal of Chemical Physics*, Vol. 44, No. 1, pp. 365–373, http://dx.doi.org/10.1063/1.1726471
Nassau K., Valente G.K. (1987) The seven types of yellow sapphire and their stability to light. *G&G*, Vol. 23, No. 4, pp. 222–231, http://dx.doi.org/10.5741/GEMS.23.4.222
Rossman G.R. (1988) Optical spectroscopy. In F.C. Hawthorne, *Reviews in Mineralogy*, Vol. 18. Mineralogical Society of America, Washington DC, pp. 207–254.
Sangsawong S. (2020) Light orange beryllium diffused synthetic sapphire. *Gamma*, Vol. 1, No. 3, pp. 45–46.
Schmetzer K., Schwarz D. (2007) Color zoning in heat-treated yellow to yellowish-orange Montana sapphires. *Journal of Gemmology*, Vol. 30, No. 5-6, pp. 268–278.
Schmetzer K., Bosshart G., Hänni H.A. (1983) Naturally-coloured and treated yellow and orange-brown sapphires. *Journal of Gemmology*, Vol. 18, No. 7, pp. 607–622.
Serra E., Bini A.C., Cosoli G., Pilloni L. (2005) Hydrogen permeation measurements on alumina. *Journal of the American Ceramic Society*, Vol. 88, No. 1, pp. 15–18, http://dx.doi.org/10.1111/j.1551-2916.2004.00003.x
Shewmon P. (1989) *Diffusion in Solids*. The Minerals, Metals & Materials Series. Springer Cham, Warrendale, Pennsylvania.
Smith C.P., van der Bogert C. (2006) Infrared spectra of gem corundum. *G&G*, Vol. 42, No. 3, pp. 92–93.
Smyth D.M. (2000) *The Defect Chemistry of Metal Oxides*. Oxford University Press, New York.
Stone-Sundberg J., Thomas T., Sun Z., Guan Y., Cole Z., Equall R., Emmett J.L. (2017) Accurate reporting of key trace elements in ruby and sapphire using matrix-matched standards. *G&G*, Vol. 53, No. 4, pp. 438–451, http://dx.doi.org/10.5741/GEMS.53.4.438
Stone-Sundberg J., Guan Y., Sun Z., Ardon T. (2020) Accurate trace element reporting in corundum: Development of secondary ion mass spectrometry relative sensitivity factors. *Geostandards and Geoanalytical Research*, Vol. 45, No. 1, pp. 207–221, http://dx.doi.org/10.1111/ggr.12360
Tanykova N., Petrova Y., Kostina J., Kozlova E., Leushina E., Spasennykh M. (2021) Study of organic matter of unconventional reservoirs by IR spectroscopy and IR microscopy. *Geosciences*, Vol. 11, No. 7, article no. 277, http://dx.doi.org/10.3390/geosciences11070277
Tatian B. (1984) Fitting refractive-index data with the Sellmeier dispersion formula. *Applied Optics*, Vol. 23, No. 24, pp. 4477–4485, http://dx.doi.org/10.1364/AO.23.004477
Thomas T., Rossman G.R., Sandstrom M. (2014) Device and method of optically orienting biaxial crystals for sample preparation. *Review of Scientific Instruments*, Vol. 85, No. 9, 093105, http://dx.doi.org/10.1063/1.4894555
Thomas V.G., Mashkovtsev R.I., Smimov S.Z., Maltsev V.S. (1997) Tairus hydrothermal synthetic sapphire doped with nickel and chromium. *G&G*, Vol. 33, No. 3, pp. 188–202, http://dx.doi.org/10.5741/GEMS.33.3.188
Tippins H.H. (1970) Charge-transfer spectra of transition-metal ions in corundum. *Physical Review B*, Vol. 1, No. 1, pp. 126–135, http://dx.doi.org/10.1103/PhysRevB.1.126
Van Orman J.A., Crispin K.L. (2010) Diffusion in oxides. *Reviews in Mineralogy and Geochemistry*, Vol. 72, No. 1, pp. 757–825, http://dx.doi.org/10.2138/rmg.2010.72.17

Special Colors and Optical Effects Of Oregon Sunstone: Absorption, Scattering, Pleochroism, and Color Zoning

Shiyun Jin, Aaron C. Palke, Nathan D. Renfro, and Ziyin Sun

Oregon sunstone is a unique feldspar gemstone that displays a wide range of colors and optical effects due to the presence of metallic copper inclusions of various sizes and shapes. Most striking are the distinct green and red colors caused by copper particles, sometimes with strong red to green pleochroism. Recent computation work suggests that copper particles can strongly absorb and/or scatter light depending on the relative orientations of the feldspar crystal, the copper particles, and the polarization of the incident light, resulting in dramatically different appearances of the same crystal when viewed (or cut) along different directions. Common optical properties of Oregon sunstone are described and explained in detail in this paper, based on the optical theories of metallic nanoparticles in anisotropic media. Notably, it was found that the red to green colors observed can only be explained by considering both selective absorption and scattering from copper particles. The absorption and extinction spectra of the copper inclusions in Oregon sunstone are measured for different crystal orientations and polarizations. The scattering effect of the copper particles is quantified by subtracting absorption from extinction, the result of which agrees closely with the computed optical properties of spheroidal copper nanoparticles. The orientation of the anisotropic copper particles relative to the optical indicatrix of the feldspar is described. The correlation between the copper concentration profile and the "watermelon" color zoning in some Oregon sunstones is examined and discussed, along with a comparison to the color zones in treated, copper-diffused feldspar. Further studies on the diffusion and dissolution mechanisms of copper in feldspar crystals are required to fully understand the geologic processes that create these special gemstones in nature, which may provide additional methods to differentiate between treated and untreated stones.

Oregon sunstone is a significant feldspar gemstone with growing popularity, and certainly one of the most famous gemstones produced in the United States. Found in weathered lava flows, these basaltic phenocrysts have poorly developed cleavages and few inclusions or twins due to the disordered structure resulting from a fast cooling rate (Xu et al., 2017; Jin et al., 2018, 2019), making them more suitable for faceting than other feldspar gemstones. Their popularity comes mainly from the wide range of appealing colors (figure 1), from the more common yellow, pink, orange, and red to the extremely rare green-blue (www.oregonsunstoneguide.com/types-and-colors.html). Many of these colors have not been found in feldspar from anywhere else in the world. The term *sunstone* was originally defined (Andersen, 1915) as the gem variety of aventurine feldspar, showing intense play of light and colors caused by strong reflections from thin oriented metallic inclusions of visible sizes, a phenomenon known as aventurescence. The loosely defined word *schiller* is more commonly used to describe the aventurescence of sunstones in the gem community (the two terms are used interchangeably in this article). Most sunstones, such as those from India, Norway, and Tanzania, owe their aventurescence effect to hematite inclusions. Copper-containing aventurine feldspar was first documented by Andersen (1917), who studied specimens reportedly from Modoc County, California. This county borders southern Oregon, an area hosting

See end of article for About the Authors and Acknowledgments.
Gems & Gemology, Vol. 59, No. 3, pp. 298–322,
http://dx.doi.org/10.5741/GEMS.59.3.298

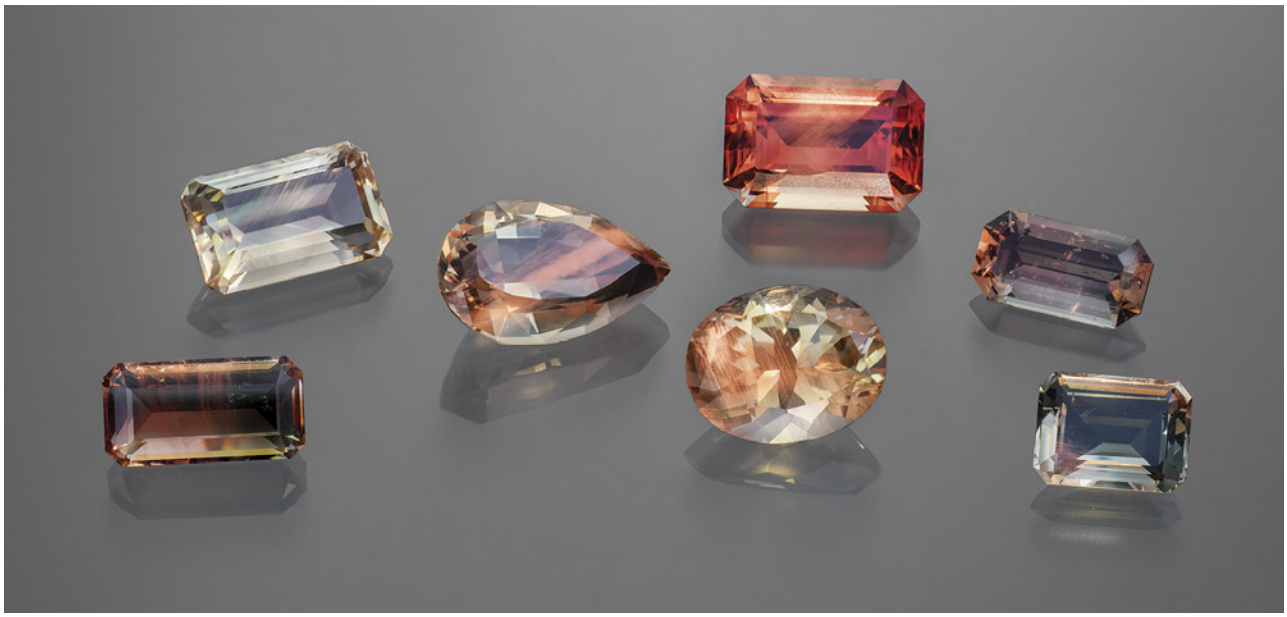

Figure 1. Faceted Oregon sunstone crystals (2.75–7.71 ct) representing the variety of colors observed. Photo by Adriana Robinson. Courtesy of the GIA Museum. Gifts of Western Ventures (pear shape), Dust Devil Mining Co. (oval), and John and Laura Ramsey (emerald cut on the far right).

many deposits known to produce gem-quality copper-included feldspars. Although many of the gem feldspars from Oregon that display red to bluish green colors do not technically fit the definition of "sunstone" due to their lack of reflective visible-sized inclusions, these copper-bearing gem feldspars from Oregon are all known as "Oregon sunstone" in the gem trade.

In Brief

- Oregon sunstones owe their colors to both absorption and scattering of light by copper particles.
- The absorbance of a scattering medium, such as a sunstone, can be measured using an integrating sphere.
- The pleochroism of Oregon sunstone results from the interplay between the elongated copper particles and the biaxial feldspar matrix.
- Color zoning in a copper-bearing feldspar is controlled by diffusion.

Copper inclusions in non-gem feldspar, though extremely rare, have been reported from localities such as Miyake-Jima in Japan and the Pinacate volcanic field in Mexico (Rossman, 2011). Oregon is the only verified occurrence of gem-quality copper-bearing sunstone. Similar gem materials have been reported from Ethiopia, though the deposit has not been independently verified (Kiefert et al., 2019; Sun et al., 2020). Moreover, copper has been shown to easily diffuse into feldspar, which can create rich red colors in originally colorless or light yellow crystals (Emmett and Douthit, 2009; Zhou et al., 2021, 2022). This discovery was made after a large quantity of red feldspar purportedly from Asia (Tibet) or Africa (Democratic Republic of the Congo) flooded the gem market, sparking controversy regarding the origin and authenticity of these gemstones (Rossman, 2011; Abduriyim et al., 2011). Major and trace element compositions can be used to separate copper-bearing feldspar from different geological origins (Sun et al., 2020), and argon isotope analysis has been used to test high-temperature treatment (Rossman, 2011). The diffused feldspars have much higher copper concentrations than natural Oregon sunstones of similar color intensities (Sun et al., 2020; Jin et al., 2022) and often show unnatural zoning patterns (McClure, 2009). While natural Oregon sunstone is straightforward to identify, there is not yet a simple and definitive way to confirm artificial copper diffusion in feldspar.

The aventurescence effect in Oregon sunstone is obviously created by the copper flakes oriented along the cleavage planes of the feldspar crystals, as they can be observed optically under the microscope (or even with the unaided eye). The origin of the body-color observed in some Oregon sunstone, on the

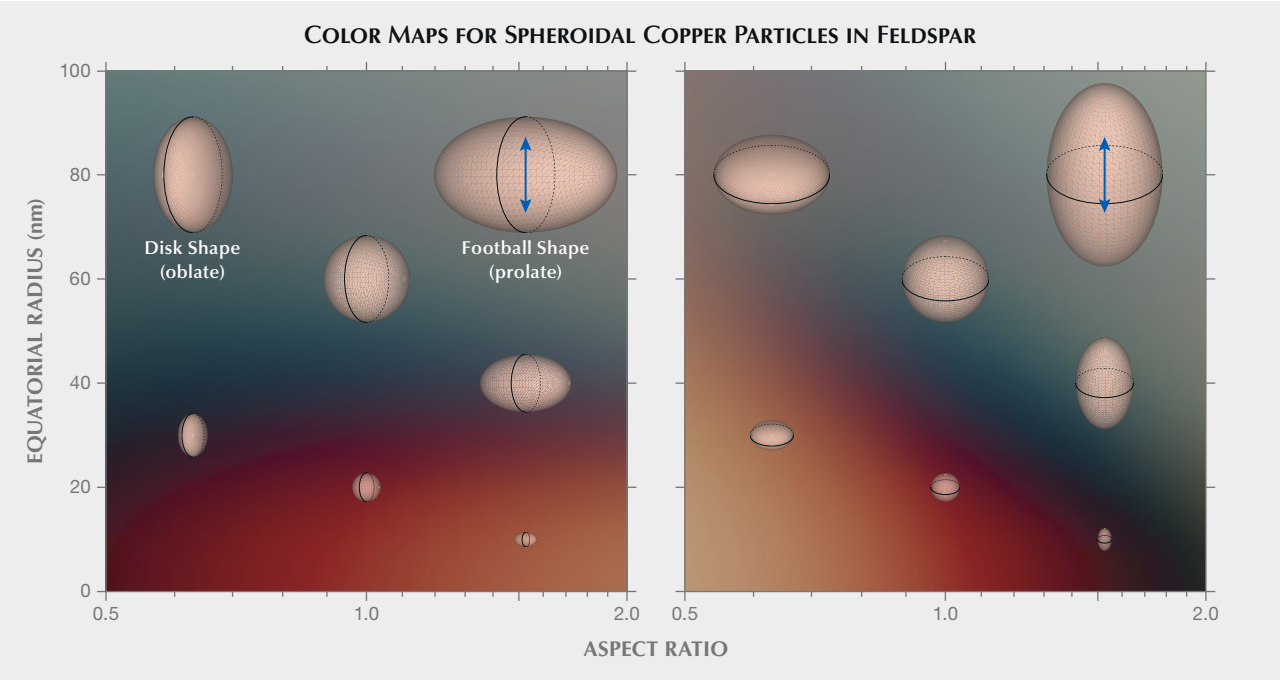

Figure 2. Calculated color maps from the computed UV-Vis spectra of spheroidal copper particles with different sizes (equatorial radius) and shapes (aspect ratio) under plane-polarized light. The particles of different sizes and shapes are schematically positioned on the maps, along with the polarization direction relative to the particles (marked with blue arrow).

other hand, is less obvious. Although the correlation between the special colors and the copper content is unmistakable, the exact mechanism by which copper can create these various colors had been elusive. Hofmeister and Rossman (1985) first studied the origin of color in relationship to the copper content and copper species in Oregon sunstone. They found that the red color in Oregon sunstone is the same as the color in red glass colored by copper/gold ("copper ruby glass"), both of which are caused by the optical properties of metallic copper colloids. In fact, copper and gold nanoparticles have been used to produce red glass for centuries, long before the physics and chemistry behind it was understood (Nakai et al., 1999; Freestone et al., 2007; Ruivo et al., 2008). The more desired green-blue colors of Oregon sunstone are much more puzzling, because no nanoparticle-colored glass counterpart with similar colors has been manufactured. Hofmeister and Rossman (1983) first hypothesized that anisotropic colloids could be causing the strong pleochroism often observed in green-blue Oregon sunstones, later supported by the observed correlation between the copper particle orientation and the color change (Farfan and Xu, 2008), as well as the direct transmission electron microscopy (TEM) observation of anisotropic copper nanoparticles (Wang et al., 2019).

A recent study computed the optical properties of spheroidal copper particles of various sizes and shapes embedded in feldspar, using methods based on simplified solutions of Maxwell's equations (Jin et al., 2022). The results explained the colors and pleochroism observed in both natural and treated copper-bearing sunstones. Smaller copper particles mainly absorb blue and green light, which can create a vivid red color. Slightly larger particles strongly scatter red and orange light to allow more green and blue light to pass directly through the crystal. Intense pleochroism can be created when elongated particles are aligned in the same direction, with the absorption and scattering much stronger when the polarization of the incident light is along the longer direction of the particles. A color map based on the computational results from Jin et al. (2022) is provided in figure 2, showing a rather dramatic change from red to green with increasing particle size and aspect ratio (the ratio between the long dimension and the short dimension of the particle). The copper nanoparticles absorb and scatter light so effectively that only a small amount (~20 ppmw) of exsolved metallic copper can produce saturated colors in mostly transparent crystals. Thicker crystals with denser numbers of copper particles would quickly turn opaque, allowing only the red backscattered light to be observed. Optical effects present in copper-bear-

TABLE 1. Sunstone samples used in this study.

Sample no.	Weight (ct)	Locality	Source	Composition[a]	Copper (ppmw)[a,b]	Color
SCH-001	11.78	Dust Devil mine, Oregon	Collected by Gabriela A. Farfan	$An_{67}Ab_{32}Or_1$	15–60	Strong schiller (figure 5)
SB-001	5.88	Sunstone Butte mine, Oregon	Collected by Shane F. McClure	$An_{68}Ab_{31}Or_1$	45–50	Strong red-green pleochroism (figures 6, 8, 9, 12)
A195	4.32	Ponderosa mine, Oregon	Collected by Shane F. McClure	$An_{72}Or_{28}Or_0$	20–130	"Watermelon" color with strong schiller (figure 15)
A278	12.23	Dust Devil mine, Oregon	Collected by Shane F. McClure	$An_{66}Ab_{33}Or_1$	2–100	"Watermelon" color with slight schiller (figure 13)
A314	10.96	Dust Devil mine, Oregon	Mariana Photiou	$An_{62}Ab_{37}Or_1$	5–120	"Watermelon" color with moderate schiller (figures 13, 15)
A319	11.80	Dust Devil mine, Oregon	Mariana Photiou	$An_{67}Ab_{32}Or_1$	5–100	"Watermelon" color with slight schiller (figures 13, 15)
A110	0.66	Reportedly from China	M.P. Gem Corp	$An_{48}Ab_{49}Or_3$	500–700	Red-green pleochroism with zoning (figures B-2, 6)

[a]*The compositions and copper concentrations of the samples were analyzed using LA-ICP-MS.*
[b]*Detection limit = 0.015 ppmw.*

ing feldspar can be further complicated by the crystal's low triclinic symmetry, resulting in complicated interactions between the light absorption/scattering by nanoparticles and the optical anisotropy of the matrix, the combination of which has not been studied in detail before. Given this newly published research about the optical properties of the copper particles, we revisit the colors and optical effects of Oregon sunstone in order to provide a comprehensive explanation of the special properties of this unique gemstone.

MATERIALS AND METHODS

The provenance, composition, copper concentration, and color of the seven samples studied in this paper are listed table 1. The chemical compositions and copper concentrations of the samples were analyzed with a laser ablation–inductively coupled plasma–mass spectrometer (LA-ICP-MS), consisting of a Thermo Scientific iCAP Qc ICP-MS connected to an Elemental Scientific Lasers NWR213 laser ablation system (frequency-quintupled Nd:YAG laser operated in Q-switched mode at a wavelength of 213 nm and pulse duration of 4 ns). Standard glasses GSD-1G, GSE-1G, and NIST SRM 610 were used for external calibration. All samples were analyzed on a traverse from edge to edge through the center of the crystal, with a 55 µm diameter laser beam size at a 20 Hz repetition rate and a fluence (energy density) of ~12 J/cm^2. No obvious zoning of the major elements was observed; therefore, only the average composition is reported. The copper concentration showed various zonation and is listed as a range in table 1.

All the samples were fabricated into wafers (not optically oriented) with at least two parallel polished surfaces for imaging and spectrometry analyses. The extinction spectra were collected on a PerkinElmer Lambda 950 ultraviolet/visible (UV-Vis) spectrometer, whereas the absorption spectra were collected with a GIA UV-Vis spectrometer, which is constructed from an AvaSphere-50 integrating sphere, an AvaLight-DS deuterium light source, and a QE Pro high-performance spectrometer. Custom-blended Laser Liquid from Cargille with a refractive index of 1.540 was used as an index-matching (immersion) liquid for orienting the feldspar crystals and measuring extinction spectra in different directions.

ABSORPTION AND SCATTERING BY COPPER PARTICLES

The feldspars containing copper inclusions are either colloids or suspensions, in which the copper particles are dispersed inside the feldspar host as a separate phase (see box A). The copper particles larger than a few micrometers in size (copper suspension) are al-

Box A: Dispersion Systems and Their Optical Properties

Due to the second law of thermodynamics, everything in nature is a mixture of multiple components, resulting from the tendency to maximize entropy. Even the purest material created by humans, single-crystal silicon for making computer chips, contains a few impure atoms for every trillion silicon atoms. It is simply impossible to make anything 100% pure. Most of the mixtures are systems known as dispersions, in which distributed particles of one material are dispersed in a continuous phase of another material. The two materials mixed in the dispersion system can be in identical or different states of matter (gas, liquid, or solid). The dispersions can be divided into three different categories (solution, colloid, and suspension) with very distinct optical properties, separated by the sizes of the dispersed particles.

In a solution, the dispersed particles are at the atomic scale, resulting in a thermodynamically stable homogenous system with one single phase. Common examples of solutions are air, an alcoholic beverage, seawater, and metal alloys. Most allochromatic gemstones (sapphire, ruby, emerald, and alexandrite) are solid solutions with trace amounts of color-absorbing ions (e.g., chromium, iron, or titanium) or point defects (vacancies) evenly dissolved in the crystal lattice of the gem mineral. Solutions almost exclusively absorb light through electron transitions (excitation) involving the dissolved ions and molecules, which can result in a color for the transmitted light (with back lighting or internal reflection in the case of faceted stones). When light is shining from the side (perpendicular to the viewing direction), the light beam is invisible inside the solution (figure A-1) because no light is deflected to the observer by the solution. Although Rayleigh and Raman scattering is theoretically possible in a solution, these effects are so weak that they cannot be observed unless on an extremely large scale (for example, Rayleigh scattering by the atmosphere causes the sky to appear blue).

In a suspension, the dispersed particles are at the micrometer scale or larger and optically visible (either under an optical microscope or without magnification). Suspensions are unstable heterogeneous mixtures, from which the suspended particles will settle out of the (fluid) mixture if left undisturbed for a prolonged period. Common examples of suspensions include muddy water, sandstorms, and lava flow. Minerals and gemstones with eye-visible inclusions are also suspensions, such as aventurine feldspar, rutilated quartz, "horsetail" demantoid, and star sapphire. The larger particles in suspension behave similarly to bulk macroscopic objects, which reflect and absorb light rays mostly on their surfaces. Depending on the particle density, a light beam shining from the side can be outlined by the illumined particles in the suspension, if not completely blocked by the dense particles (figure A-1).

A colloid is a dispersion with particle sizes in between those of solutions and suspensions. The particles in a colloid are smaller than a couple hundred nanometers, which is below the resolution of optical microscopy and cannot be directly observed using any optical device. However, the colloidal particles (also called nanoparticles) are much larger than atoms and small molecules, and they can strongly scatter light in all directions (Mie scattering). Therefore, the light path in a colloid is illuminated by the uniform scat-

Figure A-1. Diagram showing light interaction with dispersion systems of different particle sizes. Only the particles in a suspension are large enough to be visually observed. When a beam of light is shining from the side, no visible effect can be observed in a solution, but an illuminated path of light can be seen in a colloid and a suspension due to the scattering effect by the dispersed particles.

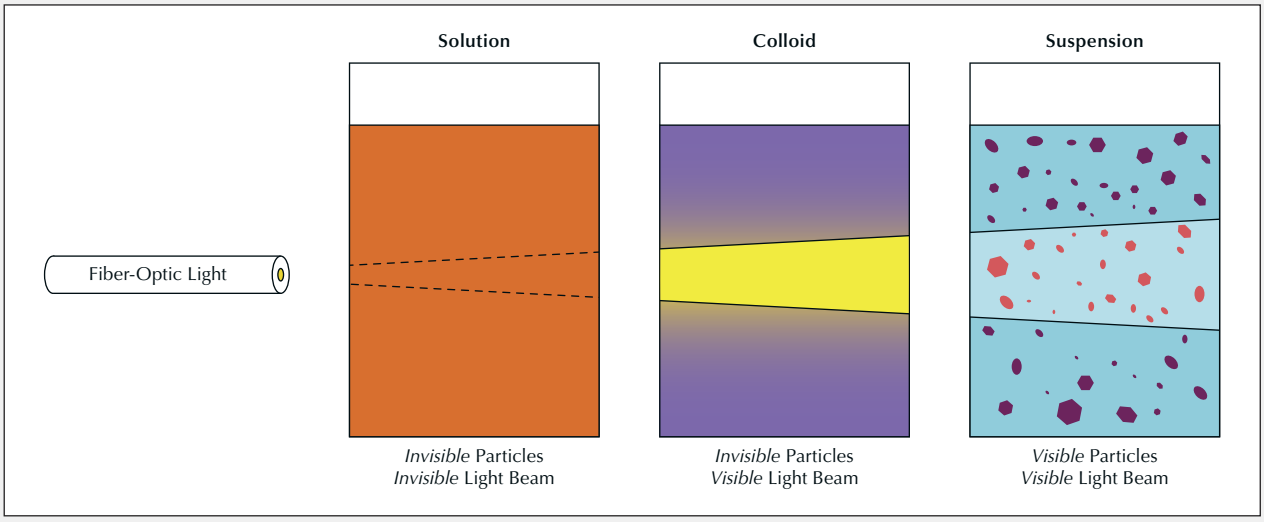

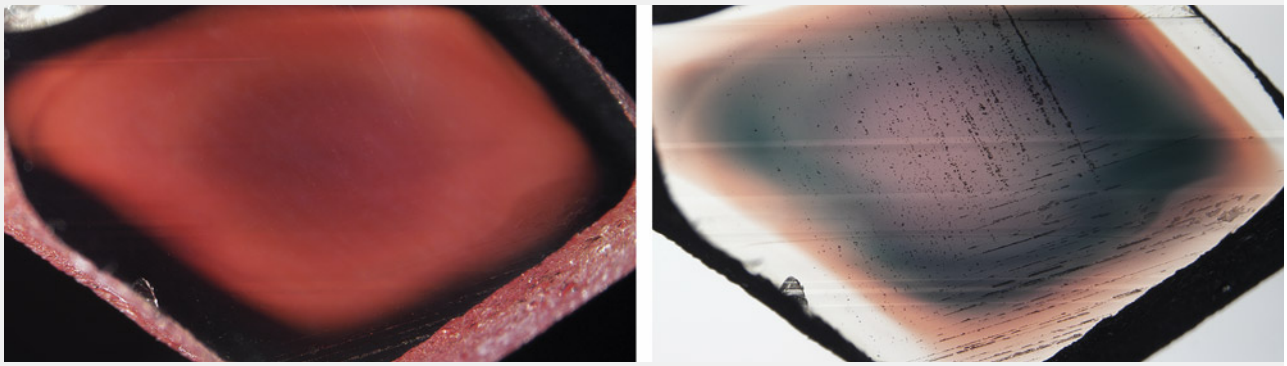

Figure A-2. Sample A110, a copper-diffused feldspar from China, under darkfield (left) and brightfield (right) illumination. The deep red color on the left is the color of the light scattered by the copper nanoparticles (Tyndall effect). The colors on the right are from the light transmitted through the crystal (neither absorbed nor scattered). The red zone on the left perfectly matches the green zone on the right, whereas the red rim on the right is almost invisible on the left. This means the green color is mainly produced by the scattering of red light, while the red color is mostly from the absorption of the copper particles. Photos by Shiyun Jin; field of view 7.1 mm.

tering from the invisible particles, known as the Tyndall effect (figures A-1 and A-2, left). A colloid is a metastable heterogeneous system, meaning the particles will not settle out when left undisturbed, but it can easily be destabilized if the particles' surface properties are altered (e.g., by adding an electrolyte in the host phase). Common examples of colloids are clouds, smoke, milk, ink, and cranberry glass (red glass colored by copper/gold). Colloid gemstones (those containing colloid particles, such as cloudy sapphire, fancy white diamond, and opal) often appear translucent due to the scattering particles. The metallic copper colloid in red copper-bearing feldspar has stronger absorption and weaker scattering than dielectric colloid particles, thus showing a solution-like appearance similar to other colored stones (note that the red rim in figure A-2, right, is almost invisible in figure A-2, left). The color of a colloid is also more complicated because the color from the scattered light and the transmitted light are often complementary to each other, making the observed color highly dependent on the type of illumination (back lighting, darkfield illumination, fiber-optic lighting) and the viewing direction.

When light travels through an absorbing solution, its intensity is absorbed following the Beer-Lambert law, with the absorbance (Abs) proportional to the path length in the medium (l), the molar absorption coefficient (ε), and the concentration (c) of the absorber:

$$Abs = \varepsilon lc \quad \text{(A-1)}$$

in which the absorbance is defined as the negative logarithm of transmittance (T), where T is the fraction of unabsorbed light intensity, I_0 is the incident light intensity, and I_A is the absorbed light intensity:

$$Abs = -\log T = -\log \frac{I_0 - I_A}{I_0} \quad \text{(A-2)}$$

In a scattering (non-absorbing) medium (colloid or suspension), the scatterance[1] (Sca) can be defined in the same way using scattered intensity (I_s):

$$Sca = -\log \frac{I_0 - I_S}{I_0} \quad \text{(A-3)}$$

For a medium that both absorbs and scatters light, the total effect of absorption and scattering is called extinction (Ext, or attenuation), for which the quantity of extinctance can be defined following the Beer-Lambert law:

$$Ext = -\log T = Abs + Sca \quad \text{(A-4)}$$

Note that transmittance (T) is the quantity that can be easily measured, which means extinctance is the most directly analyzed. In non-scattering solutions, which is the case for most colored gemstones, extinctance is the same as absorbance. The scattering effect, on the other hand, is much harder to measure directly, which requires specially designed instruments (e.g., Sullivan and Twardowski, 2009) and has only been successfully done on liquid suspensions (e.g., seawater) and jet streams of small particles. Fortunately, the absorbance of a scattering medium, though not as easy to measure as extinctance, can be measured using an integrating sphere (Elterman, 1970; Fry et al., 1992; Nelson and Prézelin, 1993; Mignani et al., 2009), which blends the scattered light together with the transmitted light. Therefore, scatterance is best quantified by subtracting absorbance from extinctance.

[1]This term (along with "extinctance" in the next paragraph) is uncommon because there are very few studies on the scattering properties of nanoparticles.

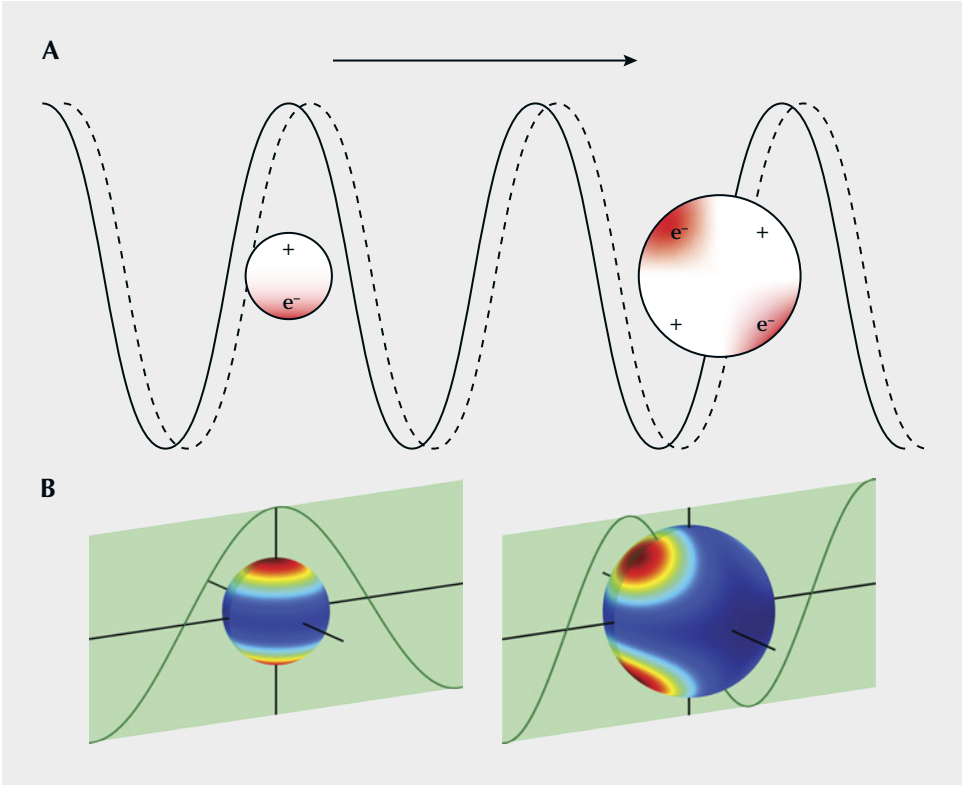

Figure 3. Schematic diagram of light (electromagnetic wave) interacting with copper (or other metal) nanoparticles. A: Free electrons in the nanoparticles oscillate under the force from an oscillating electric field, which absorb the energy of the incident light and transform it into heat. B: The bouncing electrons confined by the particle boundary create hot spots of electric field on the surface of the particles, which enhances their scattering power. Particles much smaller than the wavelength of the incident light behave as oscillating dipole moments (left), whereas larger particles that extend more than one spatial period of the incident light show more complicated multipole behavior (right).

most all aligned along the cleavage planes of the feldspar host, which means their shiny surfaces would reflect light simultaneously to create the schiller effect. However, if the copper particles are smaller than a couple hundred nanometers in size (copper colloid), they cannot be directly resolved optically. The copper nanoparticles, unlike the larger inclusions with flaky shapes, are mostly spherical or spheroidal, as directly observed by TEM (Wang et al., 2019). This is because the system always tries to minimize the excessive interfacial energy by reducing the surface area of the nanoparticles. The smaller the particle size, the larger the relative surface area (surface area per unit mass/volume) and the closer the particle shape is to a sphere. The anisotropy of the interfacial energy (with the anisotropic feldspar host) may distort the nanoparticles to spheroid or ellipsoid shapes.

The interaction between light and copper nanoparticles is quite complicated. The free electrons in metallic copper—what make copper a very good conductor of heat and electricity—are pushed back and forth from one end of the particle to the other by the incident light (oscillation of the electric and magnetic field) at extremely high frequencies (the frequency of visible light is ~400–800 terahertz, or 4–8 × 10^{14} cycles per second) (figure 3A). Therefore, the free electrons in the copper particles can absorb the energy from incident light and transform it into heat (kinetic energy of the electrons). This absorption is the strongest when the frequency of the light coincides with the intrinsic frequency of the free electrons—an effect known as localized surface plasmon resonance (LSPR) (Petryayeva and Krull, 2011)—creating a peak in the UV-Vis absorption spectrum that is strongly dependent on the size and shape of the copper particle. The oscillating free electrons constrained by the particle boundary create hot spots of electric field on the surface of the nanoparticle, which would enhance the scattering power of the copper particles. Particles much smaller than the wavelength of the incident light behave as oscillating electric dipoles, whereas larger particles that extend more than one spatial period of the incident light show more complicated multipole behavior (figure 3). The oscillating electrons also emit light (at the same frequency as the incident light) that contributes to the light scattered by the copper particle. The metal nanoparticles are sometimes referred to as "optical nano-antennas" due to their electromagnetic resonating properties (He et al., 2009), and the strongly concentrated electromagnetic field (at the particle surface) is often used to enhance signals from a small region in spectroscopic analyses such as Raman spectroscopy (Hossain et al., 2009) or laser-

induced breakdown spectroscopy (LIBS) (Palásti et al., 2020).

The extinctance of the copper particles in Oregon sunstone can be measured easily using a regular UV-Vis spectrometer by comparing the intensity of the attenuated light (transmitted through the medium) to the unattenuated intensity (directly from light source to detector) (figure 4A). However, the extinctance measured this way is not the same as absorbance, but the sum of absorbance and scatterance. The true absorbance needs to be measured inside an integrating sphere, with the detector positioned away from the direct path of the incident light (figure 4B). An integrating sphere is an optical device consisting of a hollow spherical cavity with its interior covered with a diffusely reflective coating. Light entering the integrating sphere is reflected and scattered multiple times before leaving through another port not in line with the incident light, which preserves the power of the light but destroys any directional or spatial information. When a scattering material is placed inside an integrating sphere, both the transmitted light and scattered light are blended together before entering the detector (figure 4B), which means the measured extinction (by comparing the detected intensity with and without the scattering crystal) is only due to the

Figure 4. Schematic configuration for measuring extinction (A) and absorption (B) spectra of a scattering crystal. The to-scale configuration used in this study is shown in C.

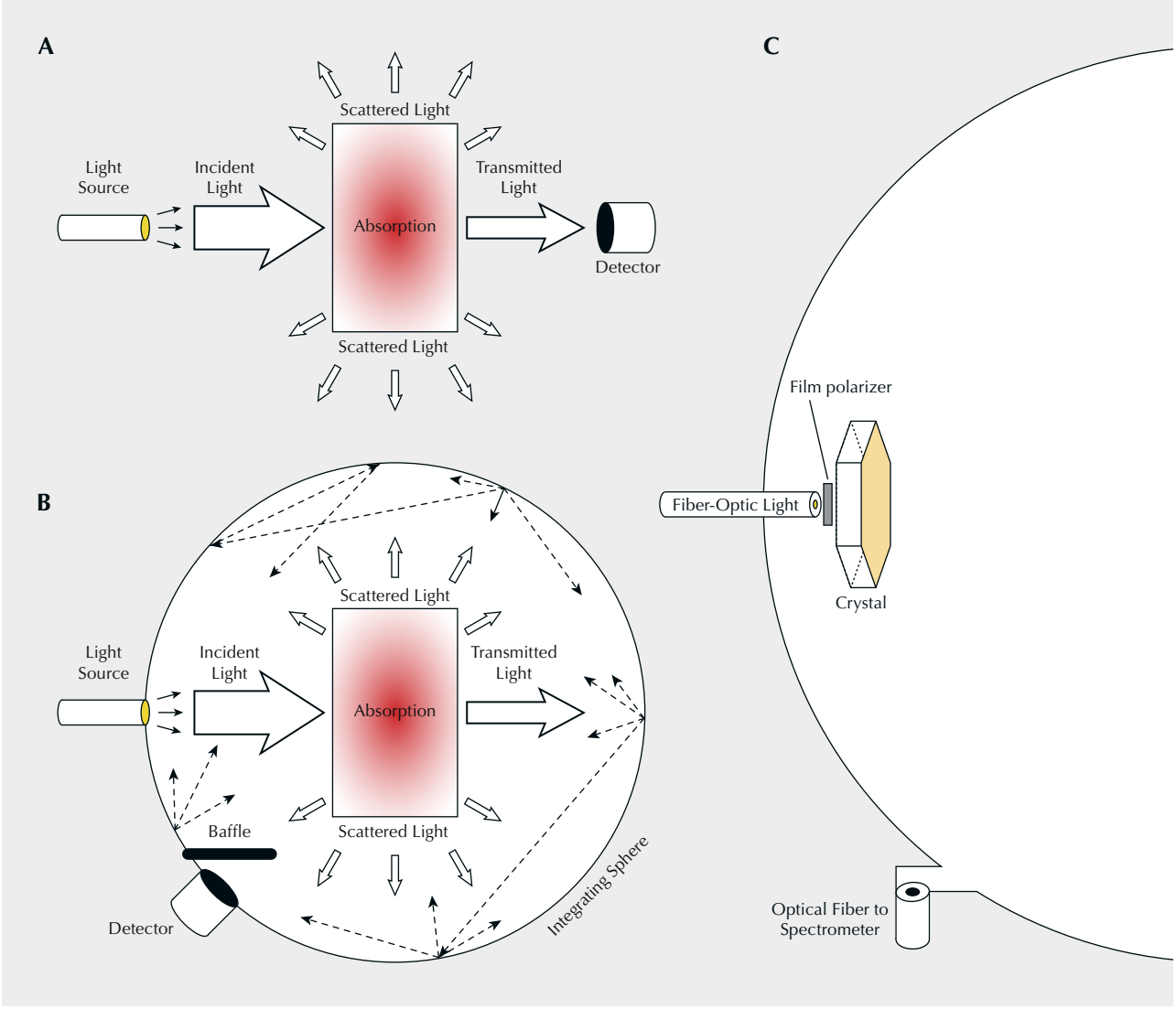

absorption of the crystal. It should be noted that, unlike the direct path configuration (figure 4A), light in the integrating sphere can be absorbed multiple times by the crystal itself, which may result in a higher absorbance depending on the relative size of the crystal to the integrating sphere. To minimize these errors, the integrating sphere used for optical measurement should be much larger than the measured sample. The to-scale illustration of the setup used in this study is shown in figure 4C. Once the total extinctance and absorbance are measured, scatterance of the copper particles in Oregon sunstone can be calculated by subtracting absorbance from extinctance.

The extinction spectrum (*Ext*, measured using the configuration in figure 4A) and absorption spectrum (*Abs*, see figures 4B and 4C) of sample SCH-001 are shown in figure 5. Because the micron-scaled copper inclusions in the schiller sunstone are large enough to block visible light of all wavelengths evenly, the extinction spectrum has a shape similar to a copper-free feldspar but elevated along the vertical axis. Because almost all the flaky copper inclusions are oriented in the same direction, the reflectance (backscattering) spectrum can also be directly measured. The measured reflectance spectrum (*Ref*) is the same as bulk copper metal (as expected), which accounts for most of the scattering by the copper inclusions. Therefore, the scattering spectrum (*Sca*) obtained from subtracting the absorbance from extinctance has a shape similar to the reflectance spectrum of copper, with red and orange light (>570 nm) preferably reflected (scattered) and blue/green light (<570 nm) absorbed. Note that reflectance is the intensity ratio (in percentage) between the reflected light and the incident light, whereas scatterance (by subtracting absorption from extinction) is the logarithm of the intensity ratio, which is why they cannot be plotted on the same scale and have slightly different shapes.

The absorption and scattering spectra of colloidal copper particles in feldspar can also be measured this way. As shown by the computational results from Jin et al. (2022), strong pleochroism can be created by elongated copper nanoparticles aligned in the same direction. To measure the scattering power with different polarization, a film polarizer is placed between the fiber-optic light and the feldspar crystal (again, see figure 4C). The experimentally measured spectra (figure 6) of two pleochroic copper-sunstone samples—sample A110 (treated) and sample SB-001 (natural)—match the computational result well. The red color is almost exclusively from absorption, with minimum scattering (extinction is almost the same

*Figure 5. Left: The extinction (*Ext*), absorption (*Abs*), scattering (*Sca*), and reflection (*Ref*) spectra of sample SCH-001. Right: The schiller effect of the sample from micron-scaled copper inclusions under reflective light. The scatterance is calculated by subtracting absorbance from extinctance. The reflectance (in percentage) is the fraction of light being reflected by the copper particles and thus cannot be plotted on the same scale as extinctance, absorbance, and scatterance, which are logarithms of intensity ratios. Photomicrograph by Shiyun Jin; field of view 13.5 mm.*

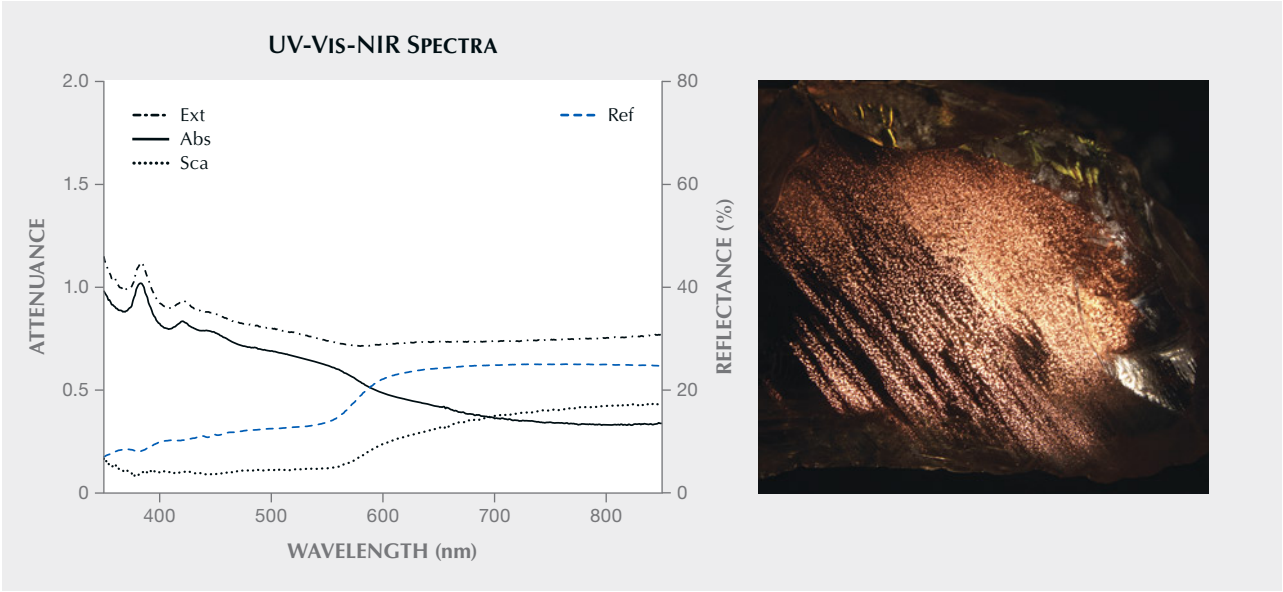

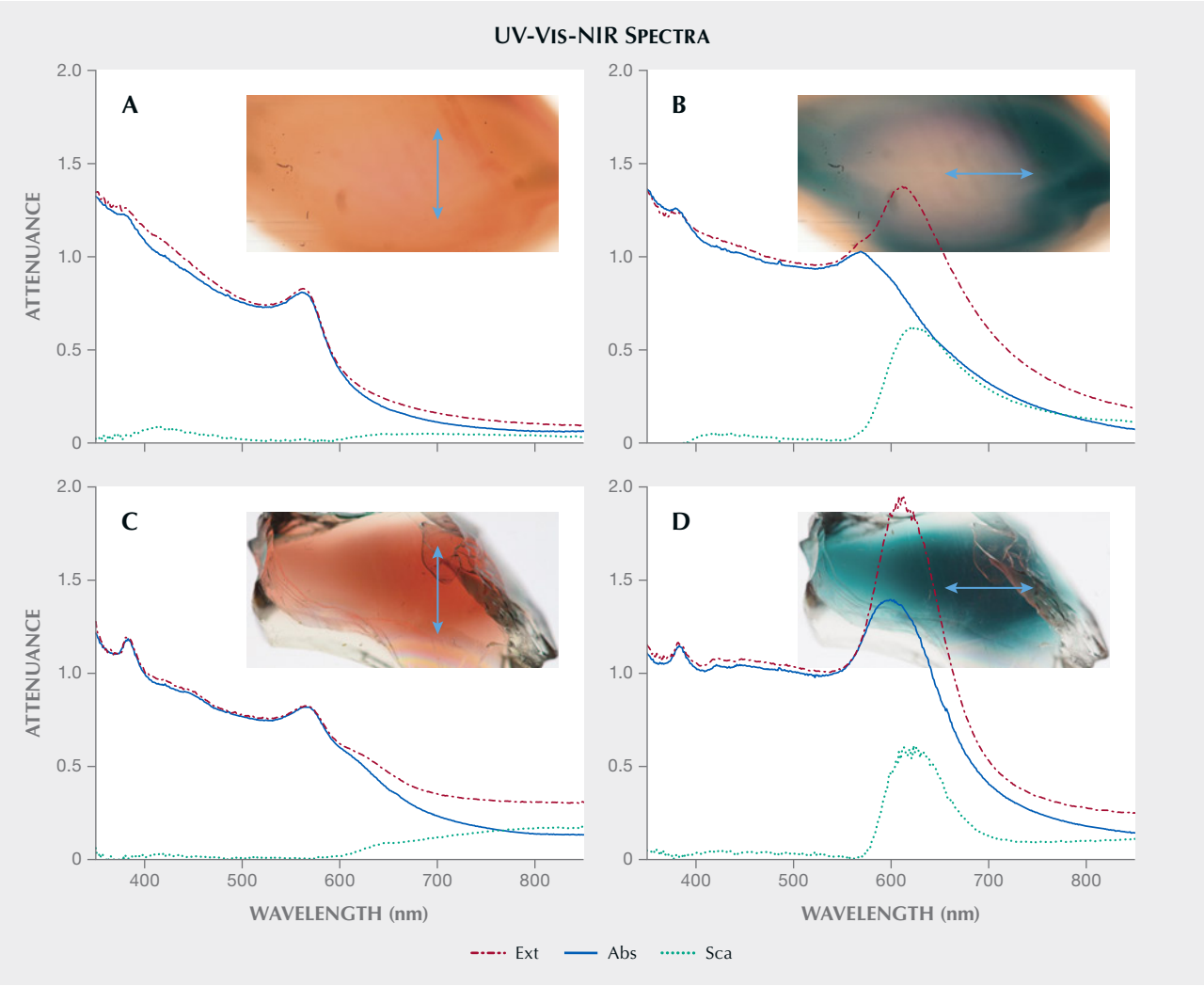

*Figure 6. Polarized extinction (*Ext*), absorption (*Abs*), and scattering (*Sca*) spectra of sample A110 (A and B) and sample SB-001 (C and D). The stone color (with polarization direction marked by arrows) corresponding to each spectrum is shown alongside the plotted spectra. A red color in sunstone is mostly created by absorption, and a green color gets significant contribution (if not all) from scattering, as predicted by the computational results from Jin et al. (2022). Photomicrographs by Shiyun Jin; fields of view 5 mm (A and B) and 20 mm (C and D).*

as absorption in figure 6, A and C), whereas the green color gets significant contribution from the scattering of red light (λ >600 nm) (figure 6, B and D). Note that the absorption spectrum for the polarization direction in which the sample appears green (figure 6B) is very similar to that corresponding to the polarization direction in which the sample appears red (figure 6A), with an LSPR peak at ~570 nm followed by a drop-off (less steep in figure 6B than in 6A), which is characteristic of particles with a radius of ~35 nm and an aspect ratio of ~1.3 (Jin et al., 2022). Sample SB-001, on the other hand, shows an absorption peak at 600 nm that is enhanced by the scattering peak at 625 nm, adding up to an exceptionally strong peak in the extinction spectra at 613 nm (figure 6D). This indicates a smaller particle radius (~20 nm) with a higher aspect ratio (~1.7) (Jin et al., 2022).

PLEOCHROISM OF OREGON SUNSTONE[2]

As shown by the computational results from Jin et al. (2022), a higher aspect ratio of the copper or other metal nanoparticles produces stronger pleochroism. In an optically isotropic medium such as glass, the

[2]The scattering effect is not considered in this section. Therefore, only terms related to absorption are used for simplicity, even though it is extinction being measured in the experiments.

transmittance (T) of light polarized at an angle of θ relative to the longer direction of the copper particles (assuming they are all oriented vertically) is an average of vertical (long direction of the particle, l) and horizontal (short direction of the particle, s) transmittance (figure 7A):

$$T(\theta) = T_s \sin^2\theta + T_l \cos^2\theta = 10^{-A_s}\sin^2\theta + 10^{-A_l}\cos^2\theta \quad (1)$$

This is because the vertical and horizontal components of the incident light are absorbed independently by the particle. Therefore, the absorbance (A) as a function of angle θ (figure 7, A and B) is:

$$A(\theta) = -\log(10^{-A_s}\sin^2\theta + 10^{-A_l}\cos^2\theta) \quad (2)$$

But in an optically anisotropic medium, the pleochroism (maximum and minimum absorption) for a certain orientation is determined by the optical orientation of the host crystal (feldspar in the case of Oregon sunstone) instead of the orientation of the light absorber (copper particles) (Libowitzky and Rossman, 1996). Light inside an anisotropic crystal is split into two perpendicularly polarized light rays following the directions of maximum/minimum refractive index (n_1/n_2) (the dashed arrows in figure 7C), which are absorbed (attenuated) independently. The absorbance is thus dependent on the angle α (between polarization direction and n_2) instead of θ (figure 7, C and D):

$$A(\alpha) = -\log(10^{-A_1}\sin^2\alpha + 10^{-A_2}\cos^2\alpha) \quad (3)$$

The absorbance A_1 and A_2 (along n_1 and n_2), on the other hand, are determined by the angle β between the long dimension of copper particles and n_2 (figure 7C):

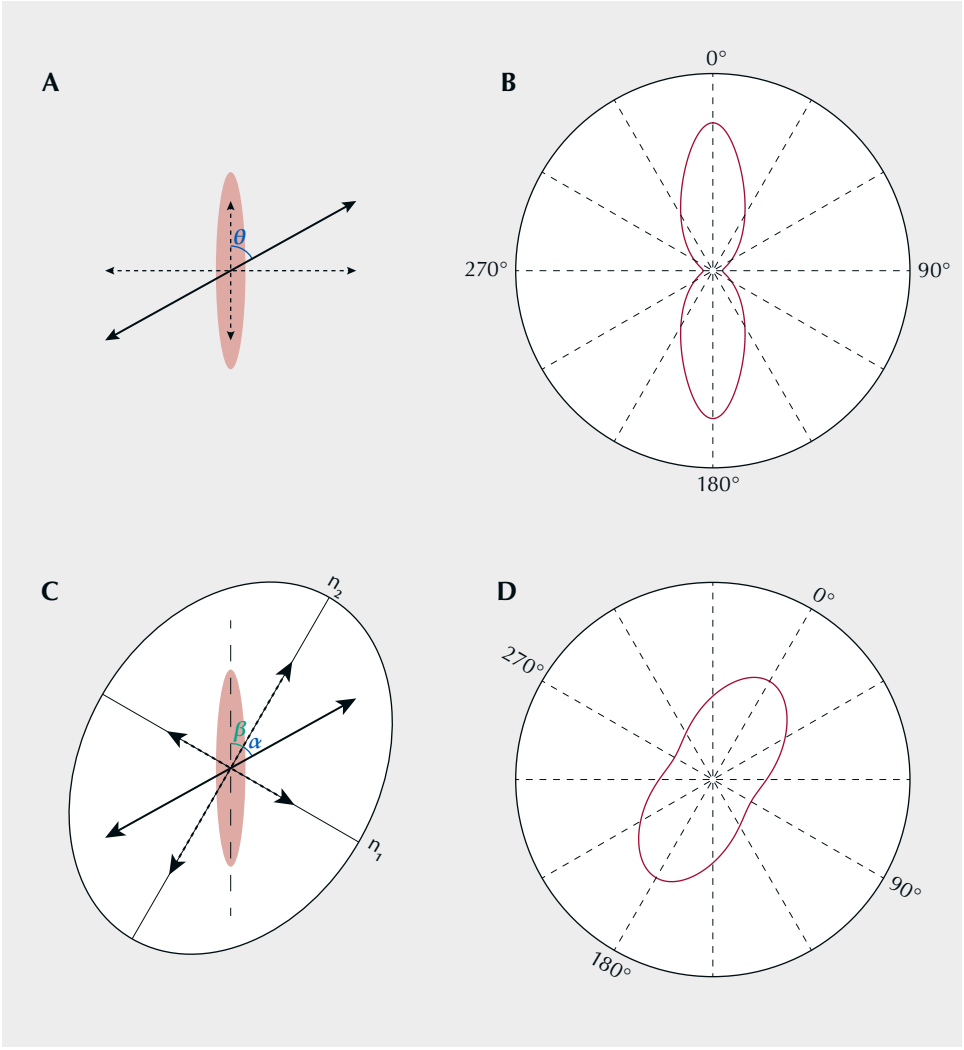

Figure 7. A: Plane-polarized incident light (at an angle of θ *with the long direction of the copper particle) in an isotropic medium can be decomposed into vertical and horizontal components (dashed arrows) that interact with the particle independently. B: The angular absorption figure (the polar plot of absorbance against* θ *at a certain wavelength) corresponding to the interaction shown in A. C: Plane-polarized incident light in an anisotropic medium is split into two polarized rays following the elliptical section of the optical indicatrix. The copper particles act on each ray independently. D: The orientation of the angular absorption figure of an anisotropic medium is determined by the optical orientation of the matrix instead of the orientation of the copper particles.*

$$A_1 = A_l \sin^2\beta + A_s \cos^2\beta \quad (4)$$

$$A_2 = A_l \cos^2\beta + A_s \sin^2\beta \quad (5)$$

Note that absorbance is used in equations 4 and 5 rather than transmittance, as seen in equation 1. This is because the two polarized rays inside the crystal (corresponding to n_1/n_2) are constrained by the optical anisotropy of the medium and cannot be further decomposed. (The assertion by Sambridge et al. [2008] that absorbance can be simply replaced by transmittance in all equations is incorrect, as transmittance is used if and only if there are multiple rays or components being attenuated independently.) Combining equations 3, 4, and 5 results in:

$$A(\alpha) = -\log(10^{-A_l \sin^2\beta - A_s \cos^2\beta} \sin^2\alpha + 10^{-A_l \cos^2\beta - A_s \sin^2\beta} \cos^2\alpha) \quad (6)$$

The orientation of the copper particles cannot be directly extracted from the angular absorption figures, as it is masked by the optical anisotropy of the feldspar. It also means the pleochroism of an anisotropic crystal is generally smaller than the anisotropy of the absorber (figure 7, B and D). The angle β determines the shape of the angular absorption figure but does not change its orientation. (To view how the angular absorption figure changes with β, go to www.gia.edu/gems-gemology/fall-2023-oregon-sunstone-effects and see videos 1 and 2.)

The "absorption ellipsoid" (Dowty, 1978; Sambridge et al., 2008) of a triclinic crystal is completely independent from its optical indicatrix, because there is no symmetrical constraint on either of them by the crystal structure. Although the optical indicatrix can be easily determined, the orientation of the absorber (absorption ellipsoid) cannot be independently measured due to the splitting and polarization of light rays inside the crystal (figure 7, C and D). In theory, the orientation of an anisotropic absorber in a triclinic medium can be determined by reconstructing the absorbance ellipsoid from the absorption coefficient of six independent directions (Dowty, 1978). In practice, however, such reconstruction is very difficult (if not impossible), as it requires complete deconvolution of the absorption spectra into independent absorption bands with accurate baseline corrections. Therefore, the absorber orientation (absorption ellipsoid) has never been quantified for any triclinic crystals. Moreover, the absorption spectra of copper particles cannot be simplified as combinations of several independent bands with fixed peak widths and positions, because the absorption/scattering peak continuously changes with different particle sizes and shapes. Nonetheless, it is still possible to determine the orientation of the copper particles in a strongly pleochroic Oregon sunstone, as the intense absorption peak at ~600–630 nm only occurs when light is polarized along (or at a slight angle with) the long direction of these particles.

The optical orientation (principal axes X, Y, and Z of the optical indicatrix) of the feldspar crystal needs to be determined first, because the polarized absorption spectrum is only meaningful when measured along special optical directions. This can be achieved by locating the two optic axes using an optical orienting device (Thomas et al., 2014). The Y-axis is perpendicular to the optical plane (a plane containing two optic axes), whereas the X- and Z-axes are the bisectors of the two optic axes. Sample SB-001 mounted on a dop along the Z-axis of the optical indicatrix (with the X-axis facing downward) is shown in figure 8A, along with the relative orientation between the optical indicatrix (white ellipsoid) and the crystallographic axes of the feldspar (figure 8, C and D). The orientation of the optical indicatrix agrees with the composition following the stereographic plot by Smith and Brown (1988, p. 200). Similar to most Oregon sunstone crystals, sample SB-001 is tabular shaped, with the table face parallel to the (010) cleavage/twin plane (Stewart et al., 1966). The (001) cleavage is relatively poorly developed but still recognizable on one side of the crystal (figure 8A). Note that even with the two cleavage planes (010) and (001) correctly identified, though they are not always obvious, the direction of the *a*-axis still cannot be unambiguously determined (there are two possibilities for positive and negative direction) without any developed crystal faces (other than the cleavages). Without using X-ray diffraction, measuring the optical orientation of the crystal is necessary to determine its crystallographic axes.

When the polarization plane of the incident light (red plane in figure 9A) is perpendicular to the X-axis (vertical blue line), the polarization will remain unchanged inside the crystal (immersed in an index-matching liquid to avoid irregular surface refraction). This property allows the absorbance to be measured along any direction perpendicular to the X-axis. Here we define the longest axis of the copper particles as P (black line in figure 9A), the angle between P and the X-axis as γ, and the angle between the P-X plane (yellow plane) and the plane normal to the incident light (green plane) as φ. As the crystal is rotated around the X-axis (perpendicular to the polarization plane), the projection of the copper particle along the horizontal direction (polarization direction marked as red arrow in figure 9B) is dependent on the angle φ, which is maximized at $\varphi = 0°$ and minimized at $\varphi =$

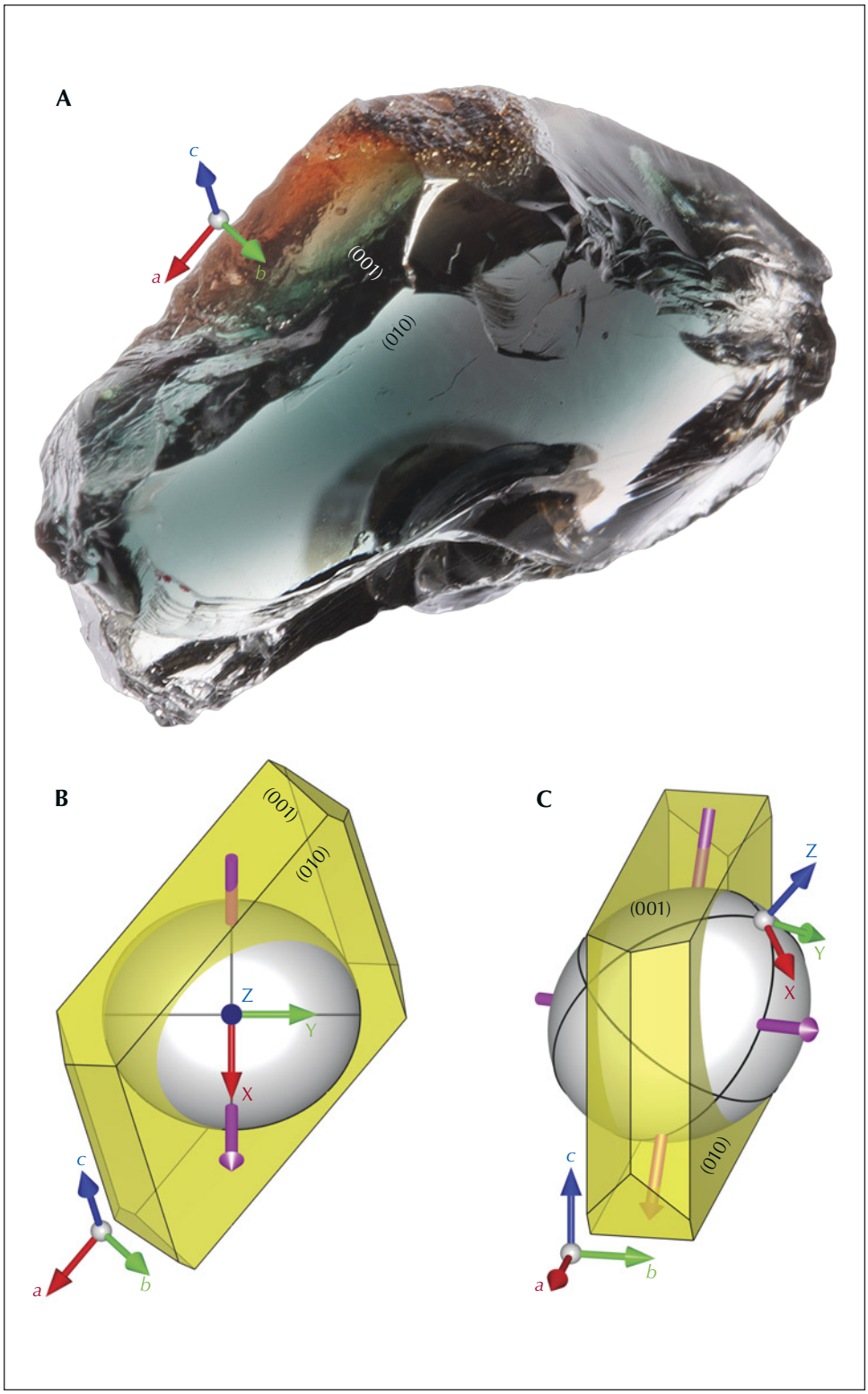

Figure 8. A: Sample SB-001 mounted on a dop (behind the sample) along the Z-axis of the optical indicatrix (with the X-axis facing downward). The crystallographic axes of the crystal and the two cleavage planes are labeled. Photo by Shiyun Jin. B: Diagram of the feldspar crystal (with ideal crystal habit) in the same orientation as in A, showing the orientation relation between the crystallographic axes and the optical indicatrix of sample SB-001. C: The same orientation relation as in B but viewed from a more general direction, similar to figure 8.8 in Smith and Brown (1988).

90°. (To view the full rotation around the X-axis, along with the corresponding particle projection, see video 3.) The color change during the rotation is more dramatic when P is closer to the horizontal plane (γ angle closer to 90°). The images in figures 9C and 9D show the two extreme colors (green at $\varphi \approx 0°$ and red

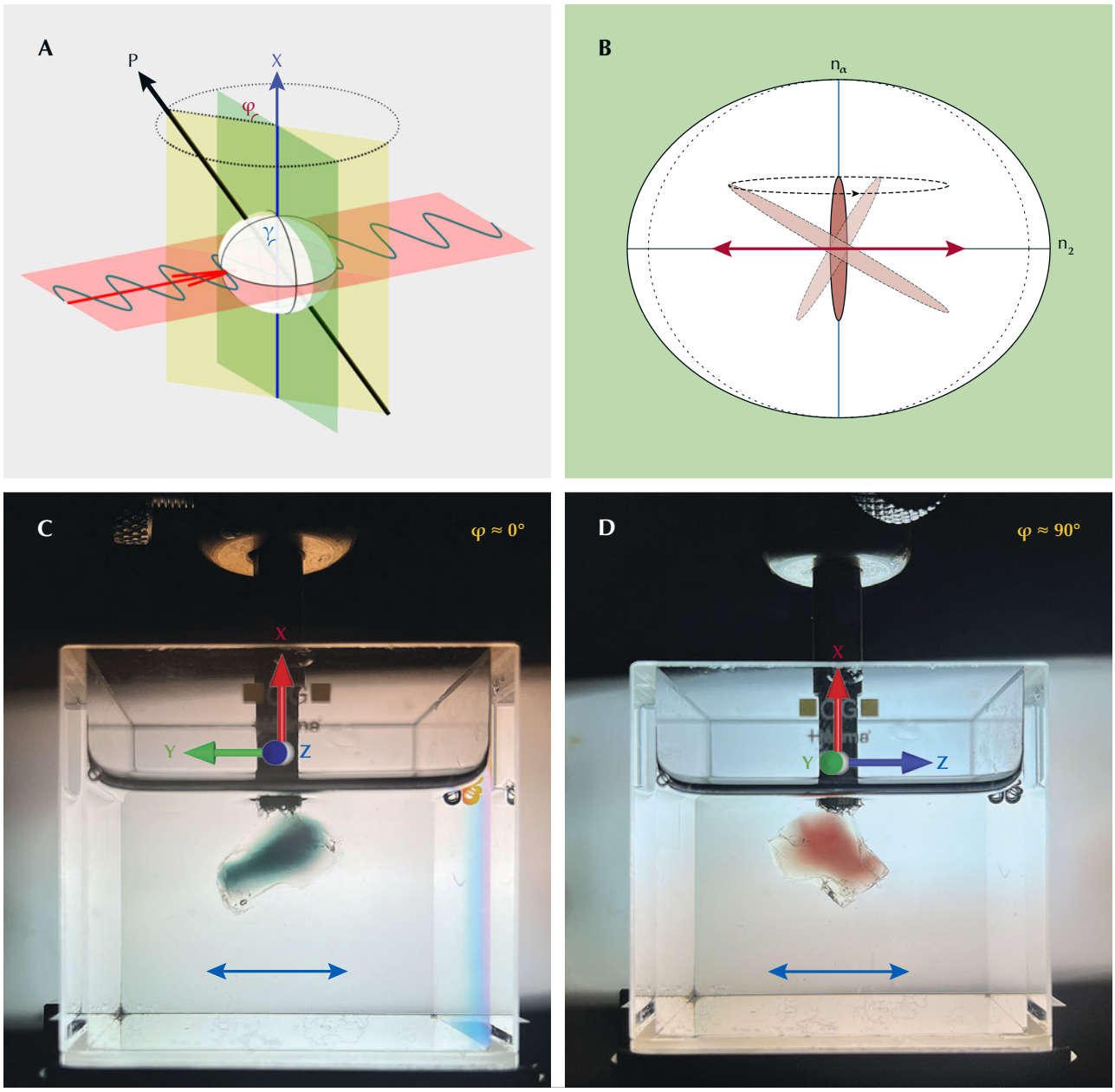

Figure 9. A: When the feldspar crystal is rotated around the X-axis, the horizontally polarized incident light (red plane perpendicular to the X-axis) does not change polarization inside the crystal, while the longest axis of the copper particle (P-axis) would revolve around the X-axis. The angle between P and the X-axis is defined as γ, and the angle between the P-X plane (yellow plane) and the plane normal to the incident light (green plane) is defined as φ. B: Diagram showing the projection of a copper particle along the incident light direction as it revolves around the X-axis (vertical) during the rotation. The absorbance for the horizontally polarized light (red arrow) is determined by the projection of the copper particle along the horizontal direction, which is maximized at φ = 0° and minimized at φ = 90°. C: Photo of sample SB-001 with maximum absorption at φ ≈ 0° showing deep bluish green color under horizontally polarized light. D: Sample SB-001 rotated 90° and showing red color with minimum absorption. Photos by Shiyun Jin.

at $\varphi \approx 90°$) during the rotation around the X-axis under horizontally polarized light (to see the color change during the full rotation, see video 4). The P-X plane can thus be determined by the position of maximum ($\varphi = 0°$) and minimum ($\varphi = 90°$) absorption. The same measurement can be performed by

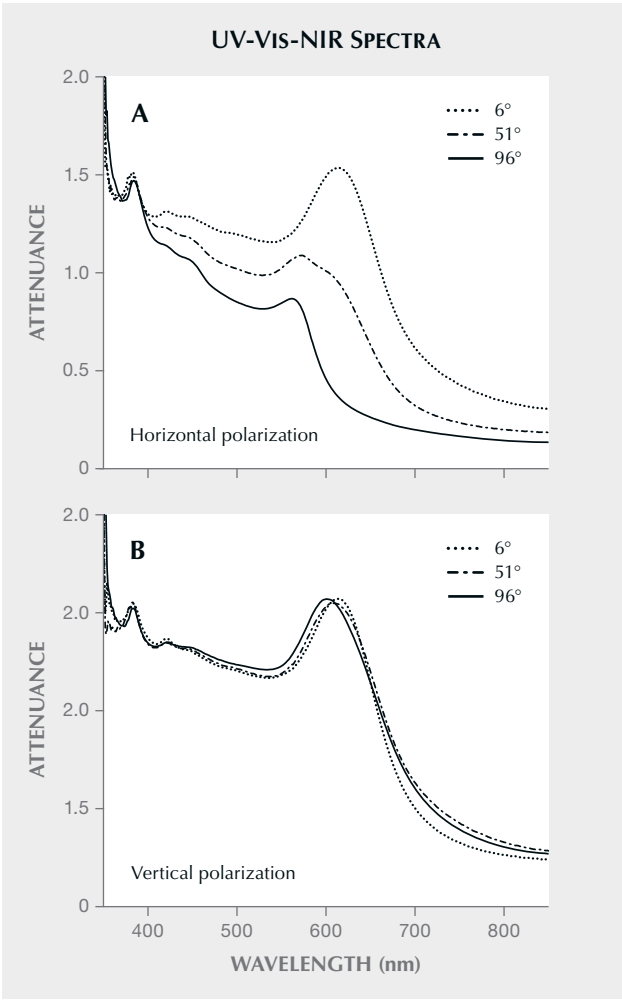

Figure 10. A: UV-Vis-NIR absorption spectra of sample SB-001 under horizontally polarized light corresponding to the positions in figures 9C (maximum absorption, 6°), 9D (minimum absorption, 96°), and halfway in between (intermediate absorption, 51°). The angles 6°, 51°, and 96° indicate the angle between the incident light and the Z-axis for each spectrum. B: Absorption spectra of sample SB-001 under vertical polarization at the same positions as in A. Note that the intermediate absorption spectrum (51°) is a direct average of the maximum (6°) and minimum (96°) absorption spectra, instead of the negative logarithm of averaged transmittance.

rotation around the Z-axis to determine the P-Z plane, and the orientation of the copper particles P can be determined as the intersection of the P-X and P-Z planes. It should be noted that measurement with rotation around the Y-axis should be avoided because incident light at a slight angle with the optic axis may result in incompletely polarized rays and irregular refraction (Sambridge et al., 2008).

The absorption spectra of sample SB-001 with polarization perpendicular and parallel to the X-axis (at three different angles between the incident direction and the Z-axis) are shown in figure 10, measured using the same configuration in figures 9C and 9D. The maximum and minimum absorption occur when the incident light is at an angle of 6(±3)° and 96(±3)° with the Z-axis, indicating the P-X plane (red plane in figure 11) is at an angle of ~6° with the X-Y plane (~96° with the X-Z optical plane). Note that the spectra with polarization parallel to the X-axis barely change with rotation of the crystal; this is expected because the projection of the copper particles along the vertical direction does not change during rotation of the crystal (figure 9B and video 3). It should also be noted that the minimum absorption spectrum in figure 10A (96°) does not show any shoulders at ~610 nm, agreeing with the computational results by Jin et al. (2022). This indicates that the shoulder of the absorption spectrum in figure 6C is contributed by the long direction of the copper particles (A_l) resulting from a small β angle in equation 6. The spectrum under vertical polarization is also very similar to the 6° spectrum under horizontal polarization (figure 10A), indicating the γ angle (figure 9A) between P and X is close to 45° ($\beta = \gamma$ when $\varphi = 0°$). Performing the same measurements around the Z-axis results in an angle of ~135° between the P-Z (blue plane in figure 11) and X-Z planes. The intersection of the P-X and P-Z planes aligns well with the *a*-axis of the feldspar crystal (figure 11). This makes sense because the (010) and (001) cleavage planes have the weakest connections (chemical bonds) in the feldspar structure, which means the copper particles encounter the least resistance when growing along the intersection of these two planes (*a*-axis). It is also possible that a faster copper diffusion rate along the *a*-axis contributes to the particle elongation. As the particles get larger, one of the cleavage planes dominates the growth, resulting in flaky inclusions that create the schiller effect (figure 5).

If the crystal is viewed along P (see figure 9A), which has the smallest projection of the copper particles, only red color would be observed (no pleochroism) because the absorption is always minimal no matter the polarization of the incident light. On the other hand, viewing perpendicular to P does not guarantee maximum absorption or pleochroism because the polarization of light inside the crystal is controlled by the optical anisotropy of the feldspar matrix (figure 7). The maximum pleochroism occurs only when the polarization of light inside the

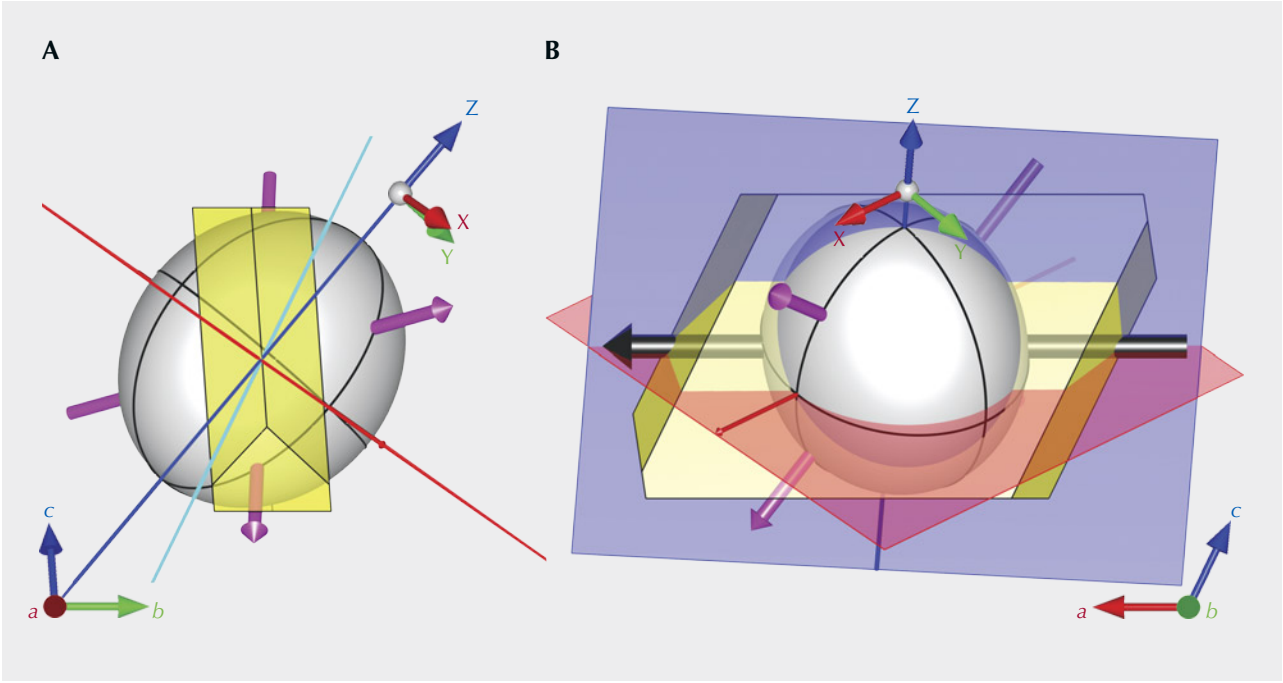

Figure 11. The orientations of the P-X (red) and P-Z (blue) planes of sample SB-001 relative to its crystallographic and optic axes, viewed down the crystal's a*-axis (A) and* b*-axis (B). The intersection of the P-X and P-Z planes (P, thick black arrow in B) aligns perfectly with the* a*-axis, which is also the intersection of the two cleavage planes. The cyan plane in A marks the direction of maximum pleochroism, with the elliptical section perfectly aligned with the copper particles.*

feldspar crystal is perfectly parallel or perpendicular to P (β = 0°/90° in equation 6 and figure 7C). This special optical direction can be found easily by total optical extinction between crossed polarizers, because the incident light (horizontal plane in figure 12A) polarized perpendicular to P would be completely extinguished by the analyzer (gray plane in figure 12A, with vertical polarization parallel to P) after the crystal only when the elliptical optical section is aligned with P. Images of sample SB-001 mounted on a dop along the *a*-axis (particle orientation P) between cross polarizers at two different positions are shown in figure 12, B and C, along with the schematic relations between the particle orientation and the optical sections. (To view the crystal going in and out of complete extinction during the full rotation, see video 5.) The orientation of the optical section that creates complete extinction in figure 12D is marked as the cyan plane in figure 11A, which is at an angle of ~30° with the (010) cleavage. This is the orientation with the strongest pleochroism, as shown by the polarized extinction spectra in figure 12D. This method can be used to maximize (or minimize) the pleochroism while faceting Oregon sunstone crystals, as the copper particles should mostly elongate along the *a*-axis (the easiest direction to identify in a rough feldspar crystal), even though the exact orientation of the section with maximum pleochroism may vary depending on the composition of the feldspar.

COLOR ZONING IN OREGON SUNSTONE

Another special feature commonly observed in Oregon sunstone is color zoning. Unlike most colored stones, in which the color intensity is directly proportional to chromophore concentration, the colors and color intensities of copper feldspars are strongly dependent on the density, size, and shape of the copper particles (Jin et al., 2022), which are not simply correlated with the concentration of copper in the crystal. The treated (copper-diffused) feldspars from China (e.g., sample A110) contain much more copper than natural Oregon sunstone of similar (if not stronger) colors (table 1) (Jin et al., 2022). This means the color zoning in Oregon sunstone, controlled by multiple factors (copper concentration, defects, temperature/cooling rate, and oxygen fugacity), is much more complicated than the zoning in other gemstones.

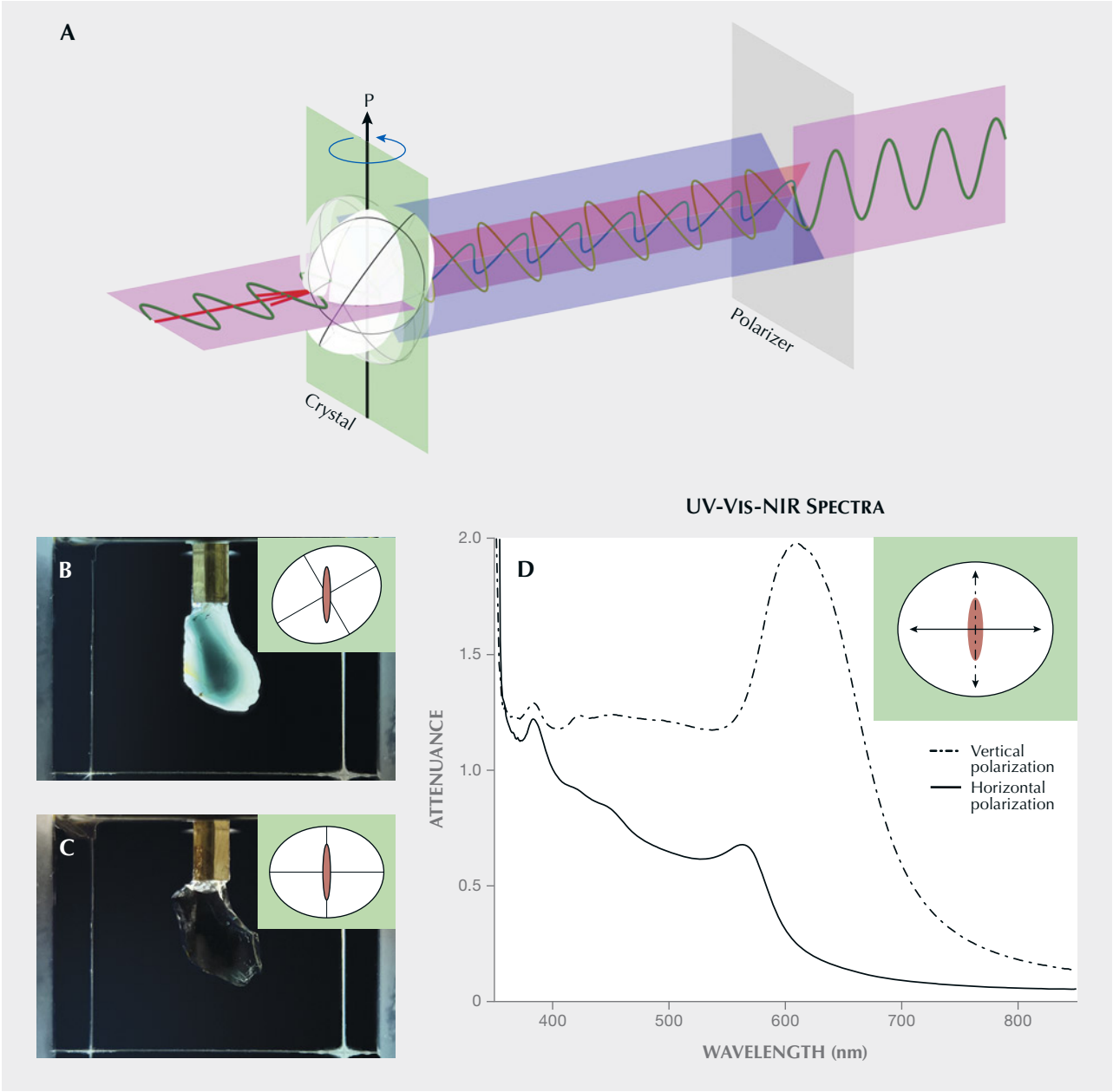

Figure 12. In A, an arbitrarily oriented feldspar crystal splits the horizontally polarized incident light into two perpendicularly polarized beams of light (traveling at different speeds inside the crystal); the phase shift due to the speed difference allows the light to partially pass through the vertical polarizer positioned after the crystal (gray plane). However, if the optical section of the feldspar is aligned with the horizontal and/or vertical direction, the incident light remains horizontally polarized inside the crystal (as in figure 9), which would be completely extinguished by the vertical polarizer. Images of sample SB-001 between cross polarizers (horizontal and vertical), rotated around P (a-axis) at two different positions (non-extinction and extinction), are shown in B and C, respectively, along with the schematic relations between the copper particles and the optical sections. Polarized (vertical and horizontal) UV-Vis-NIR absorption spectra corresponding to the extinction position in C are shown in D, which represents the maximum possible pleochroism that can be observed in sample SB-001.

The most recognizable zoning pattern of Oregon sunstone is the "watermelon" color, with a red-colored core followed by a thin green-colored (pleochroic) rim, before turning near-colorless close to the surface of the crystal. Images of Oregon sunstone crystals with typical "watermelon" colors under transmitted

light (brightfield illumination) are shown in figure 13. The color zones in Oregon sunstone have smooth transitions and curved boundaries (e.g., Rossman, 2011; Xu et al., 2017), with the shape roughly following the irregular shape of the feldspar crystal (or cracks inside the crystal; e.g., sample A319 in figure 13). The colorless zone near the surface of the crystal is often wider than the colored zone.

The color zoning in almost all other gemstones, such as ametrine or "watermelon" tourmaline, is a direct reflection of the changes in chemical composition (chromophore concentration) of the crystal across the different zones, which are controlled by either the conditions (chemistry, temperature, pressure) during crystal growth (i.e., growth zoning), or the crystal chemistry of the zoned mineral itself (i.e., sector zoning). The light-absorbing elements (e.g., iron, titanium, chromium, vanadium, or manganese) typically diffuse very slowly in crystals, and thus any abrupt changes in their concentrations (sharp color zone boundaries) can only be created during crystal growth. Gradual changes in the chemistry of the fluid that feeds the crystal growth would create the smooth color changes that are often observed in some elongated crystals (e.g., bicolor tourmaline). Slow diffusion of the chromophores after crystallization can gradually smooth out some of the initially sharp boundaries over thousands or millions of years in certain geological settings, which is often used to estimate the cooling rate or annealing time of chemically zoned minerals. Whether sharp or smooth, the color zoning in gemstones other than Oregon sunstone almost always follows the crystal habit of the mineral (i.e., concentric/radial hexagonal zones with sharp corners or along the *c*-axis in elongated crystal form).

Figure 13. Three Oregon sunstone crystals show typical "watermelon" colors from two different directions. The third direction of each sample only displays a light red color with no obvious zoning and is therefore not shown in the figure. The cracks in sample A314 were accidentally created during sample preparation (which is why it did not affect the color zoning as in sample A319). The dashed line on sample A314 indicates the position of the LA-ICP-MS analysis traverse. Photos by Shiyun Jin.

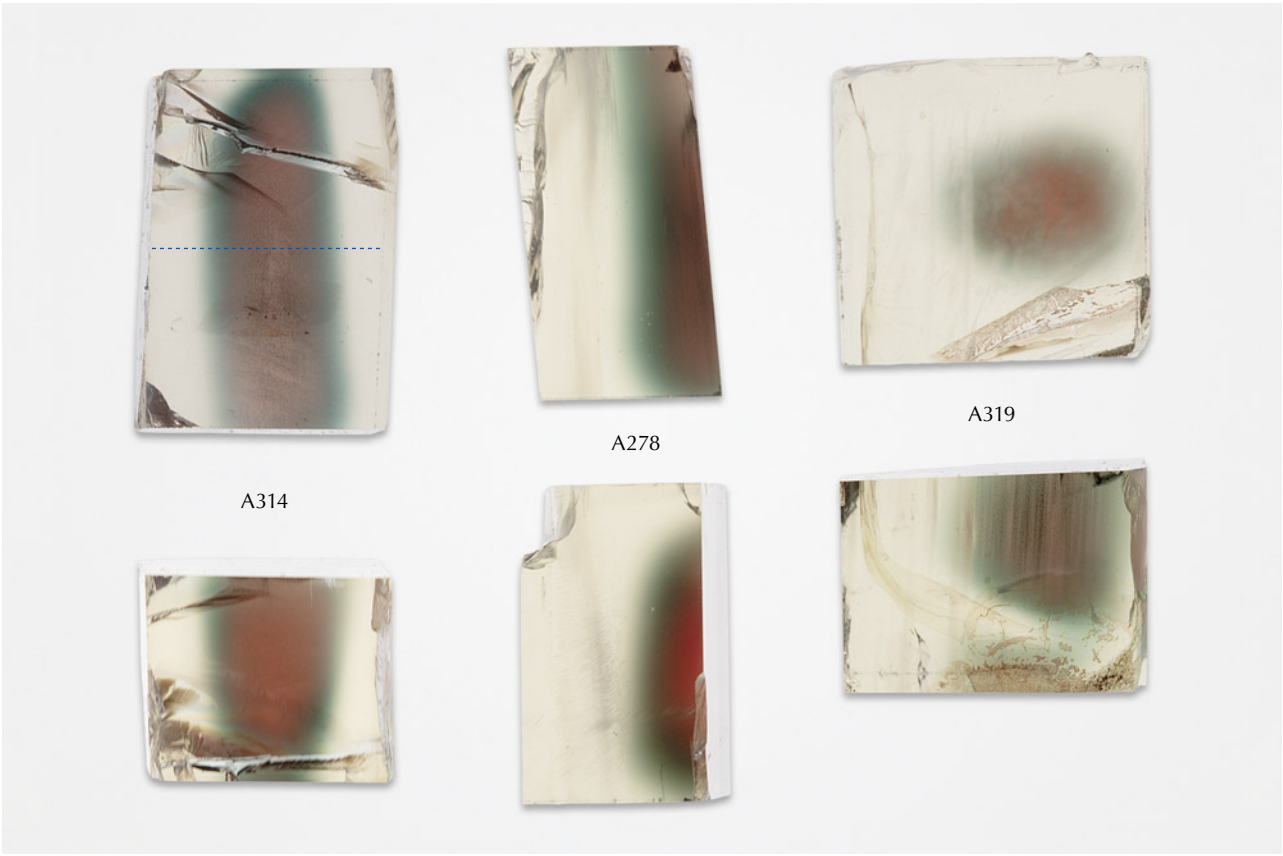

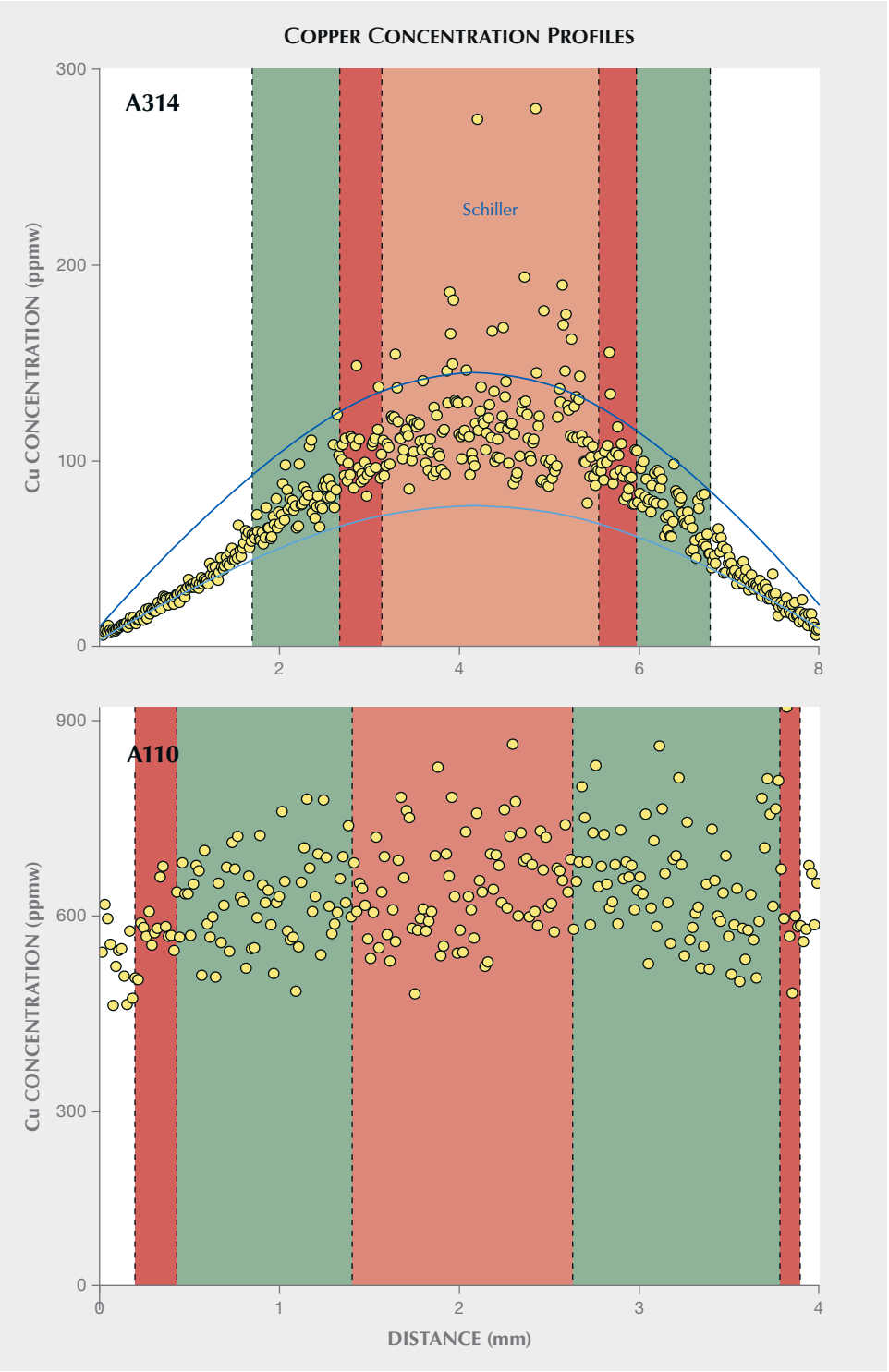

Figure 14. Copper concentration profiles across the different color zones in natural Oregon sunstone (top, sample A314) and diffused sunstone (bottom, sample A110) from LA-ICP-MS analyses. The corresponding color changes along the profiles are drawn in the background. The position of the line analysis on sample A314 is marked in figure 13 with the dotted line.

The unique zoning characteristics of Oregon sunstone are clearly not growth controlled, with no correlation to the common crystal habit of feldspar. Copper has been shown to diffuse in feldspar extraordinarily rapidly (Emmett and Douthit, 2009; Audétat et al., 2018; Zhou et al., 2021, 2022), which means the concentration profile of copper in feldspar may change noticeably within weeks or even days at magmatic temperatures. The "watermelon"-colored Oregon sunstones have most of their copper near the core of

the crystal and almost no copper at the surface, as shown by the LA-ICP-MS analysis results for sample A314 in figure 14. However, the color zoning appears to contradict the copper concentration profile, as the red color corresponds to a smaller copper particle size than the green color, as shown in figure 2. This apparent anomaly can be resolved with a closer look at the "watermelon"-colored Oregon sunstone, revealing the larger micron-scaled particles with schiller effect in the red-colored cores (figure 15). The copper would precipitate first at the core of the crystal with higher copper concentrations, which had longer growth time to form larger particles than the zones closer to the surface with lower copper concentrations. Most of the copper particles in the green zone stopped growing at intermediate sizes (~100 nm in diameter) before they became large enough to produce schiller. Smaller particles that produce a red color (<80 nm in diameter) would precipitate at a later stage, presumably due to further cooling. The larger particles with

Figure 15. "Watermelon"-colored Oregon sunstone crystals all show larger flakes of copper inclusions at the core, creating the schiller effect at certain orientations that is most obvious under an optical microscope. A: Sample A314 in transmitted light (brightfield illumination). B: The same area of sample A314 under reflected light; the red-colored core shows much stronger reflection (schiller) than the green-colored rim. C: The copper flakes in sample A195 noticeably decrease in size from the red core to the green rim before disappearing in the clear edge. D: The flaky copper inclusions align along the cleavage planes in sample A319. Photomicrographs by Shiyun Jin; fields of view 8.76 mm (A–C) and 4.38 mm (D).

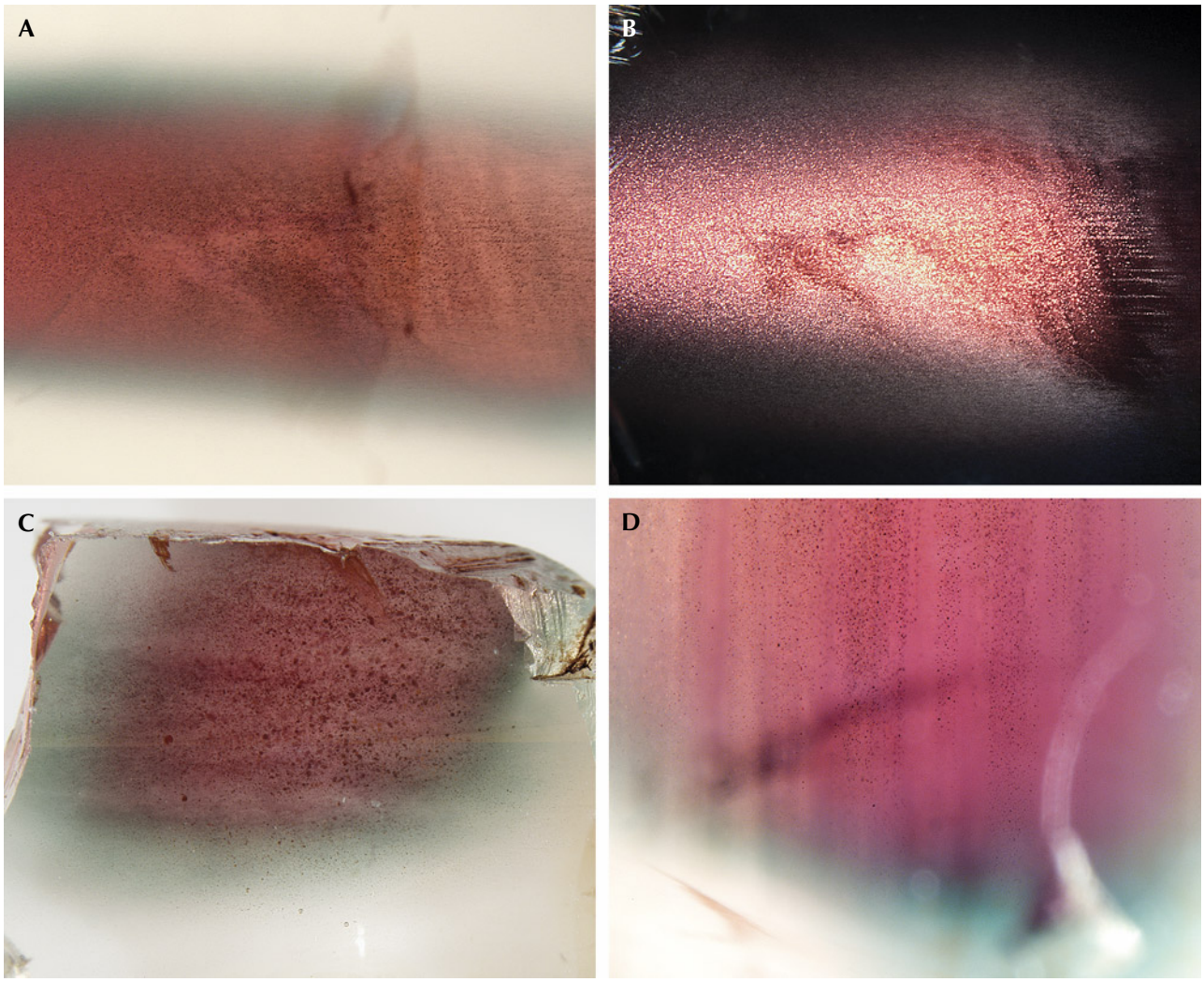

schiller effect have a flat extinction spectrum (figure 5) and therefore cannot mask the red color from the small particles in transmitted light. The intermediate particles that generate a green color, on the other hand, have the strongest extinction power (Jin et al., 2022) and would overshadow the red color from any small particles (figures 6, 11, and 13). The copper profile (figure 14) in the artificially diffused sample A110 (figure A-2), in contrast, is mostly flat with dips near the very edge, showing no obvious correlation between the color zones and copper concentration.

Copper could partition into the feldspar phenocrysts during their growth from the basaltic magma at depth. It has been hypothesized that copper in natural sunstone may have been introduced through diffusion after crystallization (Rossman, 2011). Because of the extraordinarily rapid diffusion rate of copper in feldspar crystals, the original copper distribution during crystal growth would be erased by diffusion during cooling. Some theoretical inward and outward diffusion profiles are illustrated in figure 16. With a long enough diffusion time, the two initially independent diffusion profiles from opposite surfaces (figure 16, A and D) would meet at the center of the crystal (figure 16, B and E), after which the profile would slowly approach a perfect sine function with decreasing amplitude (half a wavelength; figure 16C). The concentration profile of sample A314 (figure 14) and other Oregon sunstones with "watermelon" color is most certainly created by prolonged outward diffusion (figure 16E), starting from a more or less homogeneous copper concentration throughout the crystal. It should be noted that once the copper in the feldspar starts to precipitate as nanoparticles, they cannot move anymore, but can only grow by absorbing the copper dissolved in the feldspar lattice around it. This is why the copper profile of sample A314 in figure 14 follows a sine function (cyan curve) in the clear zone but deviates from it in the colored zones.

Using the diffusion coefficients of copper in plagioclase feldspar measured by Audétat et al. (2018), it can be roughly estimated that at least 100 days of outward diffusion at 1000°C are required to create the profile in sample A314. The real time to create the color zoning in sample A314 would be significantly longer, considering the time needed for copper to diffuse (or partition) into the feldspar crystal, as well as the significantly lower average temperature (and slower diffusion) during cooling. This is why the typical "watermelon" colors seen in figure 13, showing a wide clear zone near the entire surface of the stone and a red-colored core with schiller, have only been found in natural feldspar. It is likely that the extraordinarily strong pleochroism of sample SB-001 (figures 6, 9, and 12), indicating a higher aspect ratio of the copper particles, is also caused by slow cooling in natural basaltic lava flow.

In contrast, the copper profile of sample A110 indicates a complete inward diffusion of copper at high temperature (homogeneous copper concentration throughout the crystal) followed by a rapid cooling period, resulting in the precipitation of a small number of copper particles (color zones) and a very shallow outward diffusion profile near the surface (clear rim). This is the case for most artificially copper-diffused feldspars, with a concentration profile similar to the one in figure 16D. (The diffusion depth of sample A110 is comparable to the size of the laser beam and therefore not resolved in figure 14.) The copper particles would precipitate slightly later near the edge, which explains the "reverse-watermelon" color commonly observed in copper-treated feldspars with red rims outside green cores (McClure, 2009; Rossman, 2011). Rossman (2011) reported unusual "watermelon" color (red core and green rim; figure 15) in some artificially diffused feldspars, characterized by thin clear edges at the surface, often followed by thin red rims outside the green rings (similar to sample A110 in figure A-2, right), which are distinctively different from the natural "watermelon" Oregon sunstone. Incomplete inward diffusion (figure 16C) followed by rapid cooling (figure 16D), which would create a ring of peak copper concentration with less copper at both the core and the edge (figure 16F), may explain the color profile of the treated "watermelon" feldspars. The red core in sample A110 might be caused by the temperature or the oxygen fugacity gradient inside the crystal during copper diffusion and precipitation, since no obvious difference in copper concentration is detected relative to the green zone. Further study is needed to understand the detailed chemical reactions involved in the copper diffusion and exsolution processes. Schiller at the center of feldspar crystals (e.g., figures 5 and 15) has never been observed in artificially diffused feldspar, likely due to the much longer time it would take for the larger copper particles to form. Even if it were possible, producing these less desirable colors rather than vivid red and green colors would not be economically sound. Some copper-treated feldspars showing a pinkish sheen at the surface are probably the result of failed diffusion experiments.

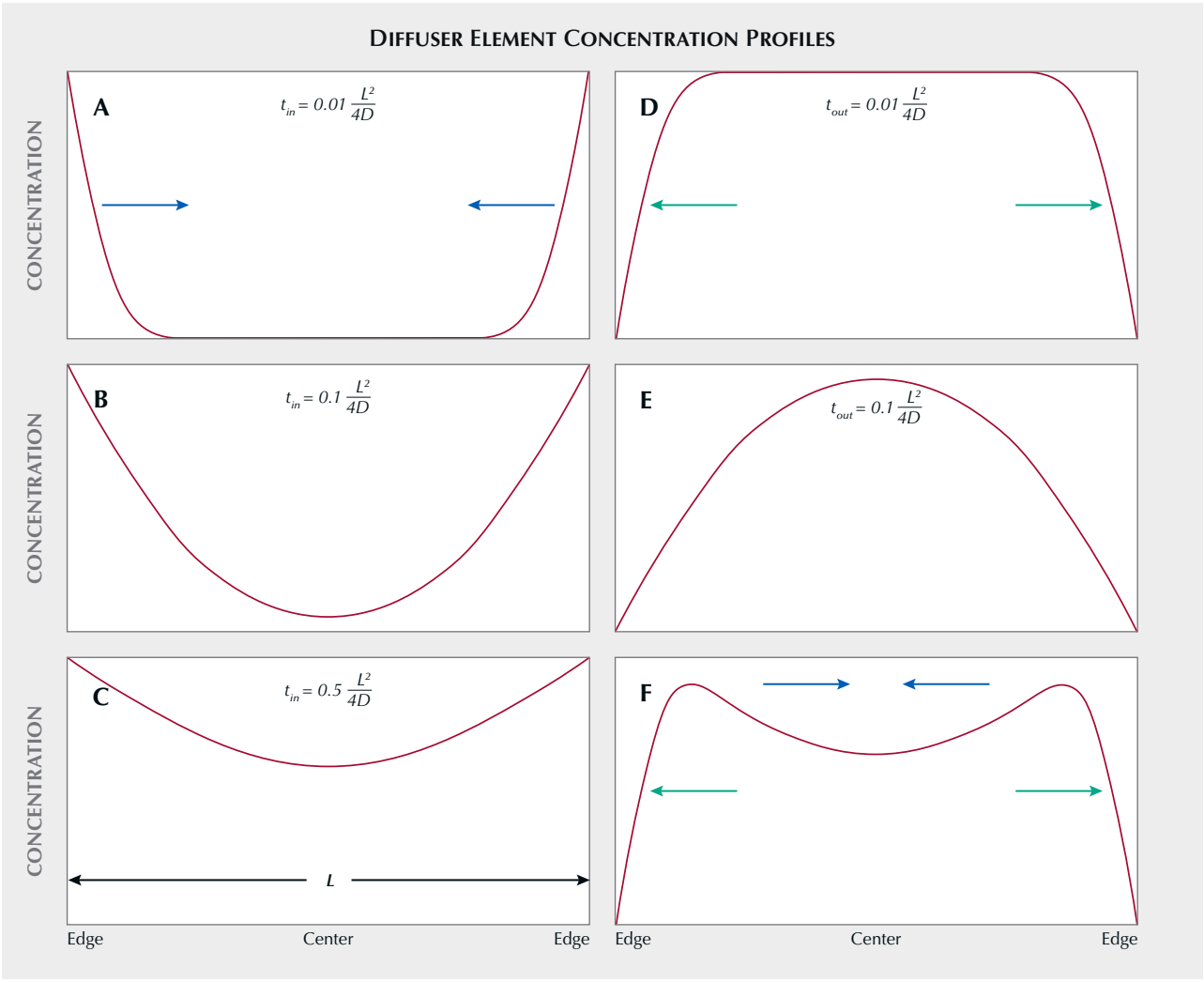

Figure 16. Schematic concentration profiles of a diffuser element (with a diffusion coefficient of D*) in a crystal (with a thickness of* L*) after various diffusion processes with different directions and times. A, B, and C show typical inward diffusion profiles (initial concentration in the crystal is zero) with increasing times (at* $t = 0.01L^2/4D$, $t = 0.1L^2/4D$ *and* $t = 0.5L^2/4D$, *respectively). D and E show outward diffusion profiles starting from a homogeneous concentration (at* $t = 0.01L^2/4D$ *and* $t = 0.1L^2/4D$, *respectively). Note that inward diffusion and outward diffusion are exactly inverse processes. The profile in F can result from an incomplete inward diffusion followed by a short period of outward diffusion (C + D).*

CONCLUSIONS

This paper has described and discussed in detail the special color effects observed in Oregon sunstone (figure 17), including aventurescence (schiller), pleochroism, and color zoning. All the special optical effects of Oregon sunstone can be explained as combinations of the properties described here. The scattering power of the colloidal copper particles in Oregon sunstone is quantified for the first time. The strong scattering peak at ~625 nm agrees with the computed optical properties of copper nanoparticles in feldspar (Jin et al., 2022). The long axis of the particle is measured to be aligned along the *a*-axis in strongly pleochroic Oregon sunstones, which is expected from the weak connections along the (010) and (001) cleavage planes in the feldspar structure. To our knowledge, this is also the first time the anisotropic absorption (extinction) property has been quantified (oriented) in any triclinic mineral. The accurate orientation of the copper particles along with the optical indicatrix of the host feldspar would allow gem cutters to optimize the color and optical effects while faceting Oregon sunstones. The pleochroism in natural Oregon sunstone appears much stronger than in copper-treated feldspars, indi-

Figure 17. A 31.12 ct Oregon sunstone carving by Larry Woods. Photo by Robert Weldon; courtesy of John D. Woodmark, Desert Sun Mining & Gems.

cating higher aspect ratios of the copper particles, likely due to a slower cooling rate. More specimens need to be tested to confirm this as a universal characteristic of natural pleochroic Oregon sunstone, which could be used to identify natural stones without schiller. The concentration of copper in natural Oregon sunstones with "watermelon" color shows an outward diffusion profile that takes at least a few months (most likely years) to form, distinctly separating them from the artificially copper-diffused feldspars with no obvious correlation between color and copper content. The schiller at the core of the feldspar crys-

tals, created by copper flakes a few micrometers in size or larger, has been found exclusively in natural stones. Further study on the dissolution and diffusion mechanisms of copper in feldspar is necessary to create a comprehensive method of separating treated copper-colored feldspars from natural ones.

ABOUT THE AUTHORS

Dr. Shiyun Jin is a research scientist, Dr. Aaron Palke is senior manager of research, Nathan Renfro is senior manager of colored stone identification, and Ziyin Sun is a senior research associate, at GIA in Carlsbad, California.

ACKNOWLEDGMENTS

The authors would like to thank Shane F. McClure, Mariana Photiou, Gabriela A. Farfan, Huifang Xu, and M.P. Gem Corp for providing the samples used in this study, along with their locality information. We also thank Christopher M. Breeding for his assistance with the UV-Vis spectrometer.

REFERENCES

Abduriyim A., McClure S.F., Rossman G.R., Leelawatanasuk T., Hughes R.W., Laurs B.M., Lu R., Isatelle F., Scarratt K., Dubinsky E.V., Douthit T.R., Emmett J.L. (2011) Research on gem feldspar from the Shigatse region of Tibet. *G&G*, Vol. 47, No. 2, pp. 167–180.

Andersen O. (1915) On aventurine feldspar. *American Journal of Science*, Vol. s4-40, No. 238, pp. 351–399, http://dx.doi.org/10.2475/ajs.s4-40.238.351

——— (1917) Aventurine labradorite from California. *American Mineralogist*, Vol. 2, No. 7, p. 91.

Audétat A., Zhang L., Ni H. (2018) Copper and Li diffusion in plagioclase, pyroxenes, olivine and apatite, and consequences for the composition of melt inclusions. *Geochimica et Cosmochimica Acta*, Vol. 243, pp. 99–115, http://dx.doi.org/10.1016/j.gca.2018.09.016

Dowty E. (1978) Absorption optics of low-symmetry crystals—Application to titanian clinopyroxene spectra. *Physics and Chemistry of Minerals*, Vol. 3, No. 2, pp. 173–181, http://dx.doi.org/10.1007/BF00308120

Elterman P. (1970) Integrating cavity spectroscopy. *Applied Optics*, Vol. 9, No. 9, pp. 2140–2142, http://dx.doi.org/10.1364/AO.9.002140

Emmett J.L., Douthit T.R. (2009) Copper diffusion in plagioclase. *GIA News from Research*, www.gia.edu/doc/Cu-diffusion-Emmett.pdf, April 22.

Farfan G., Xu H. (2008) Pleochroism in calcic labradorite from Oregon: Effects from size and orientation of nano- and micro-precipitates of copper and pyroxene. *Geochimica et Cosmochimica Acta*, Vol. 72, p. A256. Presented at the Goldschmidt Conference, Vancouver, British Columbia, Canada. http://dx.doi.org/10.1016/j.gca.2008.05.009

Freestone I., Meeks N., Sax M., Higgitt C. (2007) The Lycurgus Cup—A Roman nanotechnology. *Gold Bulletin*, Vol. 40, No. 4, pp. 270–277, http://dx.doi.org/10.1007/BF03215599

Fry E.S., Kattawar G.W., Pope R.M. (1992) Integrating cavity absorption meter. *Applied Optics*, Vol. 31, No. 12, pp. 2055–2065, http://dx.doi.org/10.1364/AO.31.002055

He S., Cui Y., Ye Y., Zhang P., Jin Y. (2009) Optical nano-antennas and metamaterials. *Materials Today*, Vol. 12, No. 12, pp. 16–24, http://dx.doi.org/10.1016/S1369-7021(09)70313-X

Hofmeister A.M., Rossman G.R. (1983) Color in feldspars. In P.H. Ribbe, Ed., *Feldspar Mineralogy*. Mineralogical Society of America, Washington, D.C., pp. 271–280.

——— (1985) Exsolution of metallic copper from Lake County labradorite. *Geology*, Vol. 13, No. 9, pp. 644–647, http://dx.doi.org/10.1130/0091-7613(1985)13<644:EOMCFL>2.0.CO;2

Hossain M.K., Kitahama Y., Huang G.G., Han X., Ozaki Y. (2009) Surface-enhanced Raman scattering: Realization of localized surface plasmon resonance using unique substrates and methods. *Analytical and Bioanalytical Chemistry*, Vol. 394, No. 7, pp. 1747–1760, http://dx.doi.org/10.1007/s00216-009-2762-4

Jin S., Wang X., Xu H. (2018) Revisiting the $I\bar{1}$ structures of high-temperature Ca-rich plagioclase feldspar — a single-crystal neutron and X-ray diffraction study. *Acta Crystallographica Section B: Structural Science, Crystal Engineering and Materials*, Vol. 74, No. 2, pp. 152–164, http://dx.doi.org/10.1107/S2052520618003219

Jin S., Xu H., Wang X., Zhang D., Jacobs R., Morgan D. (2019) The incommensurately modulated structures of volcanic plagioclase: Displacement, ordering and phase transition. *Acta Crystallographica Section B: Structural Science, Crystal Engineering and Materials*, Vol. 75, No. 4, pp. 643–656, http://dx.doi.org/10.1107/S2052520619006243

Jin S., Sun Z., Palke A.C. (2022) Color effects of Cu nanoparticles in Cu-bearing plagioclase feldspars. *American Mineralogist*, Vol. 107, No. 12, pp. 2188–2200, http://dx.doi.org/10.2138/am-2022-8325

Kiefert L., Wang C., Sintayehu T., Link K. (2019) Sunstone labradorite-bytownite from Ethiopia. *Journal of Gemmology*, Vol. 36, No. 8, pp. 694–696.

Libowitzky E., Rossman G.R. (1996) Principles of quantitative absorbance measurements in anisotropic crystals. *Physics and Chemistry of Minerals*, Vol. 23, No. 6, pp. 319–327, http://dx.doi.org/10.1007/BF00199497

McClure S.F. (2009) Observations on identification of treated feldspar. *GIA News from Research*, GIA. https://www.gia.edu/doc/identification-treated-feldspar.pdf, August 22.

Mignani A.G., Ciaccheri L., Cacciari I., Ottevaere H., Thienpont H., Parriaux O., Johnson M. (2009) Innovative spectroscopy of liquids: A fiber optic supercontinuum source and an integrating sphere for scattering-free absorption measurements. In *2009 IEEE SENSORS*, pp. 131–135, http://dx.doi.org/10.1109/ICSENS.2009.5398218

Nakai I., Numako C., Hosono H., Yamasaki K. (1999) Origin of the red color of Satsuma copper-ruby glass as determined by EXAFS and optical absorption spectroscopy. *Journal of the American Ceramic Society*, Vol. 82, No. 3, pp. 689–695, http://dx.doi.org/10.1111/j.1151-2916.1999.tb01818.x

Nelson N.B., Prézelin B.B. (1993) Calibration of an integrating sphere for determining the absorption coefficient of scattering suspensions. *Applied Optics*, Vol. 32, No. 33, pp. 6710–6717, http://dx.doi.org/10.1364/AO.32.006710

Palásti D.J., Albrycht P., Janovszky P., Paszkowska K., Geretovszky Z., Galbács G. (2020) Nanoparticle enhanced laser induced breakdown spectroscopy of liquid samples by using modified

surface-enhanced Raman scattering substrates. *Spectrochimica Acta Part B: Atomic Spectroscopy*, Vol. 166, article no. 105793, http://dx.doi.org/10.1016/j.sab.2020.105793
Petryayeva E., Krull U.J. (2011) Localized surface plasmon resonance: Nanostructures, bioassays and biosensing—A review. *Analytica Chimica Acta*, Vol. 706, No. 1, pp. 8–24, http://dx.doi.org/10.1016/j.aca.2011.08.020
Rossman G.R. (2011) The Chinese red feldspar controversy: Chronology of research through July 2009. *G&G*, Vol. 47, No. 1, pp. 16–30, http://dx.doi.org/10.5741/GEMS.47.1.16
Ruivo A., Gomes C., Lima A., Botelho M.L., Melo R., Belchior A., Pires de Matos A. (2008) Gold nanoparticles in ancient and contemporary ruby glass. *Journal of Cultural Heritage*, Vol. 9, pp. e134–e137, http://dx.doi.org/10.1016/j.culher.2008.08.003
Sambridge M., Gerald J.F., Kovács I., O'Neill H.St.C., Hermann J. (2008) Quantitative absorbance spectroscopy with unpolarized light: Part I. Physical and mathematical development. *American Mineralogist*, Vol. 93, No. 5-6, pp. 751–764, http://dx.doi.org/10.2138/am.2008.2657
Smith J.V., Brown W.L. (1988) *Feldspar Minerals: Volume 1 Crystal Structures, Physical, Chemical, and Microtextural Properties*. Springer-Verlag, Berlin, Heidelberg, http://dx.doi.org/10.1007/978-3-642-72594-4
Stewart D.B., Walker G.W., Wright T.L., Fahey J.J. (1966) Physical properties of calcic labradorite from Lake County, Oregon. *American Mineralogist*, Vol. 51, No. 1-2, pp. 177–197.
Sullivan J.M., Twardowski M.S. (2009) Angular shape of the oceanic particulate volume scattering function in the backward direction. *Applied Optics*, Vol. 48, No. 35, pp. 6811–6819, http://dx.doi.org/10.1364/AO.48.006811
Sun Z., Renfro N.D., Palke A.C., Breitzmann H., Muyal J., Hand D., Hain M., McClure S.F., Katsurada Y., Miura M., Rossman G.R. (2020) Gem News International: Sunstone plagioclase feldspar from Ethiopia. *G&G*, Vol. 56, No. 1, pp. 184–188.
Thomas T., Rossman G.R., Sandstrom M. (2014) Device and method of optically orienting biaxial crystals for sample preparation. *Review of Scientific Instruments*, Vol. 85, No. 9, article no. 093105, http://dx.doi.org/10.1063/1.4894555
Wang C., Shen A.H., Palke A.C., Heaney P.J. (2019) Color origin of the Oregon sunstone. Presented at the *36th International Gemmological Conference IGC*, Nantes, France, pp. 71–74.
Xu H., Hill T.R., Konishi H., Farfan G. (2017) Protoenstatite: A new mineral in Oregon sunstones with "watermelon" colors. *American Mineralogist*, Vol. 102, No. 10, pp. 2146–2149, http://dx.doi.org/10.2138/am-2017-6186
Zhou Q., Wang C., Shen A.H. (2021) Copper nanoparticles embedded in natural plagioclase mineral crystals: In situ formation and third-order nonlinearity. *Journal of Physical Chemistry C*, Vol. 126, No. 1, pp. 387–395, http://dx.doi.org/10.1021/acs.jpcc.1c09145
——— (2022) Application of high-temperature copper diffusion in surface recoloring of faceted labradorites. *Minerals*, Vol. 12, No. 8, article no. 920, http://dx.doi.org/10.3390/min12080920

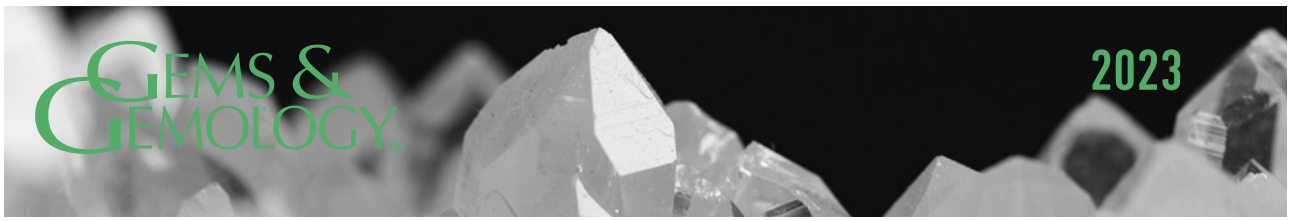

CONGRATULATIONS

This year, readers from all over the world took the 2023 *Gems & Gemology* Challenge. Participants tested their knowledge by answering questions listed in the Spring 2023 issue. Those who earned a score of 75% or higher received a GIA Certificate of Completion. Participants who earned a perfect score are listed below.

G&G Challenge Winners

Australia
Barbara Wodecki

India
Raju Jain

Israel
Maria Machevariani

Malaysia
Arnold Cheong

Myanmar
Thuzar Aung

Ukraine
Nataliya Vovk

United Kingdom
Ana Lucia Tres

United States
Lo Combs
Martin Harmon
Thaïs Anne Lumpp-Lamkie
Michele Mejia
Jana Miyahira-Smith
Klinton Pipes
Tim Richardson
Adam Shor
Samantha Shor
Lee Steele
Kate Waterman
Elly Wedge
Danielle Yamamoto
Clifton Young

Answers

See pages 92–93 of the Spring 2023 issue for the questions.

1 (a), 2 (b), 3 (d), 4 (a), 5 (d), 6 (b), 7 (d), 8 (d), 9 (b), 10 (c), 11 (b), 12 (a), 13 (b), 14 (c), 15 (a), 16 (d), 17 (a), 18 (c), 19 (a), 20 (a), 21 (c), 22 (c), 23 (b), 24 (d), 25 (b)

The Science of Colored Stone Identification and Origin.

GIA

GIA research and reports are the benchmark of colored stone analysis. Those who buy, sell, or curate the world's most important gems rely on GIA's expertise, precision, objectivity, and integrity.

GIA.edu/ColoredStones

Etch Pits in Heliodor and Green Beryl From the Volyn Pegmatites, Northwest Ukraine: A Diagnostic Feature

Gerhard Franz, Oleksii A. Vyshnevskyi, Volodymyr M. Khomenko, Peter Lyckberg, and Ulrich Gernert

Green beryl and the yellow beryl variety heliodor are well known from the Volyn pegmatite field in Ukraine, and this study presents details of their morphological characteristics. Visible etch pits are characteristic of beryl from this locality. In addition, they may contain an organic matter called kerite. Formation of the etch pits is associated with a fluorine-rich, late-stage fluid phase. Etch pits on the pinacoidal face have a hexagonal outline and a pointed bottom (originating at linear defects) transitioning to etch pits with very steep walls, and they occur in three different orders of magnitude: ≤500 µm, ≤50 µm, and 1–3 µm. On the first-order prismatic faces, etch pits with a flat bottom (originating from point defects) or pointed bottom are square to rectangular, the latter oriented parallel or perpendicular to the beryl's *c*-axis. Flat bottom etch pits are more abundant than pointed bottom and also occur in three different orders of magnitude. In addition, small etch pits with a canoe shape and porosity on the nanometer scale were observed. Scanning electron microscopy of these etch pits was used to distinguish uncut stones from other pegmatitic beryls, but these phenomena are also visible with an optical microscope or even with a loupe.

Paleoproterozoic pegmatites near Khoroshiv (formerly Volodarsk-Volynskyi) in northwest Ukraine are known as a source of high-quality green beryl and the yellow beryl variety heliodor (e.g., Koshil et al., 1991; Simmons, 2014, and references therein). The green beryl's color can be very intense but never reaches the typical emerald color. Aquamarine is also claimed from the Volyn pegmatite field, but very rarely, and emerald from southeast Ukraine (Franz et al., 2020) is the country's only other important gem beryl occurrence. The finest specimens of Volyn beryl with color between green and yellow (figure 1) and size of up to 140 cm in length are displayed in the Museum of Precious and Decorative Stones in Khoroshiv (Vasylyshyn et al., 2001), while gem-quality crystals up to 55 cm have been sold abroad.

Since 1931, the pegmatites have been mined extensively for piezo quartz, which occurs in exceptionally large crystals from one to two meters (Lyckberg, 2005; Lyckberg et al., 2009, 2019). In addition to beryl, which is present in ~2% of the pegmatites, approximately 10% of these pegmatites contain gem-quality topaz. Among the first gem findings was topaz in 1931–1933, and later gem beryl was recovered as a byproduct.

In Brief

- Gem-quality crystals of green beryl and heliodor from the Volyn pegmatite field in Ukraine show spectacular dissolution features.
- Etch pits resulting from the dissolution are rectangular on prismatic faces and hexagonal on pinacoidal faces.
- The etch pits occur in different sizes and overlap each other, indicating different stages of dissolution that are diagnostic for uncut stones.
- Fossil organic matter known as kerite can be attached to the beryl crystals.

Mining for heliodor continued after World War II, but this material was only available in Eastern Europe. The first crystals reached the Western European market in 1980, and in 1987 Volyn beryl finally emerged

See end of article for About the Authors and Acknowledgments.
Gems & Gemology, Vol. 59, No. 3, pp. 324–339,
http://dx.doi.org/10.5741/GEMS.59.3.324

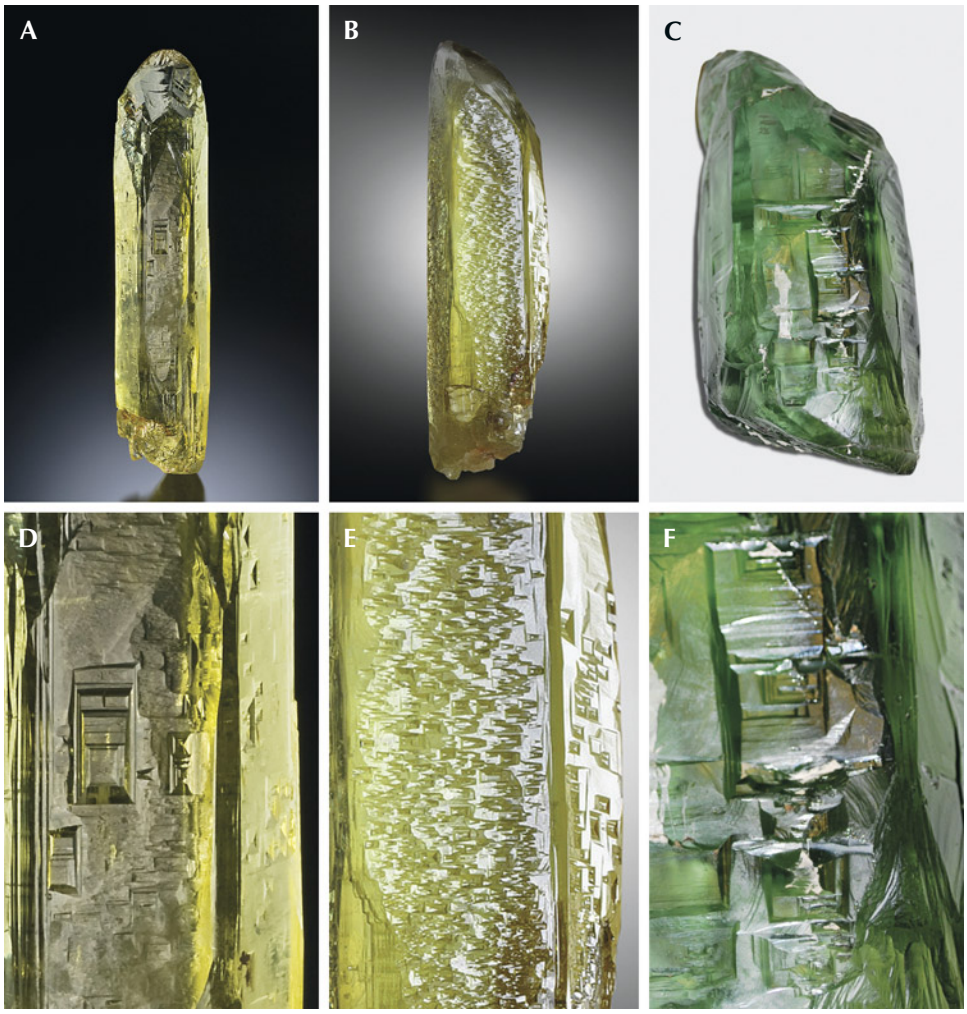

Figure 1. Yellowish green heliodor and green beryl from Volyn, oriented with the c*-axis vertical (top row) and detail views of the prismatic faces (bottom row). A and D: An 8.5 cm crystal with well-developed prismatic faces and strongly sculptured end faces; the detail view shows F-type etch pits elongated parallel to the* c*-axis. B and E: Transition from prismatic face (1.8 cm wide) to sculptured pyramidal face with triangular hillocks (compare with the SEM image in figure 10); the detail view shows dominantly asymmetrical P-type etch pits. C and F: A 2.683 kg deep green crystal measuring 18 × 10 × 9 cm with rectangular F-type etch pits, mostly oriented perpendicular to the* c*-axis. The samples in A and B are from the collection of Peter Lyckberg. The sample in C, named "Professor Pavlyshyn," is from the Museum of Precious and Decorative Stones in Khoroshiv. Photos by Peter Lyckberg (A and B) and Gerhard Franz (C).*

at the gem shows in Tucson. Many of these were used for cutting (figure 2), but a large number of fine mineral specimens were also preserved.

Since the early 1990s, the Volyn Quartz Samotsvety Company has conducted mining for beryl and topaz. Lyckberg et al. (2009) reviewed the mining and collecting history, the geology, and the formation of chambers within the pegmatites. That article also contains a list of accompanying minerals in the pegmatite and several photos showing the etch pits.

A characteristic feature of Volyn beryl crystals is their morphology, with exceptionally large dissolution features (etch pits), described on the basis of light microscopy by Bartoshinskiy et al. (1969) and Lazarenko et al. (1973). The prism faces show rectangular cavities with negative crystal faces, while the basal planes show negative, hexagonally shaped crystal faces. Al-

Figure 2. Rectangular step-cut green beryl from the Volyn pegmatite, 190.00 ct and 28.55 × 39.02 × 21.71 mm, with a rough unpolished table containing etch pits. Faceting and photo by Konstantyn Zalizko.

Figure 3. Map of the major tectonic units of Ukraine (based on the geological map in Shestopalov et al., 2020, and from Wikimedia Commons) with the Ukrainian Precambrian Shield, part of the East European Platform. Ukraine's two gem beryl occurrences: heliodor in the Volyn pegmatite field in the southwest of the Korosten Pluton and emerald at Kruta Balka, are each indicated with a star.

though dissolution of early precipitated minerals during a later stage is frequently observed in pegmatites (Černý, 2002; London, 2008), these features together with the yellow-green color and their size are diagnostic for Volyn beryl. In large crystals, they are visible without magnification, and in smaller crystals they can be seen with the aid of a loupe or optical microscope.

This study presents an investigation of the morphology of the etch pits on prismatic and basal faces in a number of beryl specimens from Volyn by means of scanning electron microscopy (SEM), which helped to identify the origin of uncut stones, extending the work of Kurumathoor and Franz (2018) on etch pits as a provenance indicator. The nomenclature for etch pits follows from that work: F-type = flat bottom, which originate at point defects; P-type = pointed bottom, which originate at linear defects (i.e., edge and screw dislocations); H-type = hollow, with walls almost perpendicular to a face and bottom that is not visible; and C-type = canoe-shaped.

GEOLOGICAL SETTING

The Volyn pegmatites are genetically and spatially connected with granites of the Korosten plutonic complex in the northwest Ukrainian shield. This pluton crops out over an area of approximately 15,000 km^2 and has intrusion ages of 1800–1760 Ma (figure 3; Shumlyanskyy et al., 2017, 2021). Its country rocks are high-grade migmatic gneisses. In the Khoroshiv region at its western margin, pegmatites are found in a contact zone between granite and gabbroic rocks over a distance of 22 km and a width of 300 to 1500 m (e.g., Lazarenko et al., 1973; Koshil et al., 1991; Ivanovich and Alekseevich, 2007). Miarolitic cavities, produced during the late-stage crystallization by fluids, occur all along the edges of the pluton. The southern and eastern sides have been test-mined for quartz.

The pegmatites belong to the category of shallow pegmatites, fully differentiated, and are irregularly distributed in the granites (Ivanovich and Alekseevich, 2007). According to the nomenclature of Černý and Ercit (2005) and Linnen et al. (2012), they belong to the

miarolitic interior-type of the niobium-, yttrium-, and fluorine-enriched family. They reach a size of several tens of meters; individual pegmatite bodies are typically about 30 m by 40 to 45 m wide (Kalyuzhnyi et al., 1971; Lyckberg, 2005; Ivanovich and Alekseevich, 2007). The pegmatites contain large miarolitic pockets and are referred to in the Ukrainian literature as "chamber pegmatites." They are zoned around an open cavity, which can reach a volume of approximately 40 m^3 and in extreme cases up to 4000 m^3 (Lyckberg et al., 2009).

A cross section of a pegmatite is shown in figure 4. Quartz crystals one or two meters in size, most often as smoky quartz, grew from the hanging wall into the chamber. The floor is covered with quartz that has fallen down, as well as smaller crystals of mica, topaz, beryl, and albite. Chambers in which beryl and topaz occur together as large crystals are the exception in these deposits, because during the multistage crystallization conditions they can replace each other. The footwall of the chambers consists of a strongly leached feldspar-rich horizon up to 36 m deep (Lyckberg et al., 2009) where quartz was dissolved, and further down lies a zone of broken-up pegmatite. New mineral formations in this zone include albite, siderite, topaz, fluorite, beryl (rarely), and phenakite. The zones around the chamber are a quartz core above the chamber, then a more or less concentric feldspar zone, a blocky quartz-feldspar zone with large pegmatitic crystals, and next to the granite a zone with graphic-textured quartz-feldspar intergrowths.

Some of the chambers were destroyed forming a breccia, which consists of broken crystals and rock fragments, cemented by quartz, opal, chalcedony,

Figure 4. Cross section of pegmatite number 487 from the Volyn pegmatite field, showing the different zones. The strongly leached feldspar-rich horizon below the chamber is typical, as is a quartz core above the chamber. The pegmatite measures approximately 12 m × 7.5 m, and the chamber is approximately 5 m × 2 m wide. The vertical scale on the far left represents depth in meters. Modified by D. Lyckberg after © Volyn Quartz Samotsvety Company.

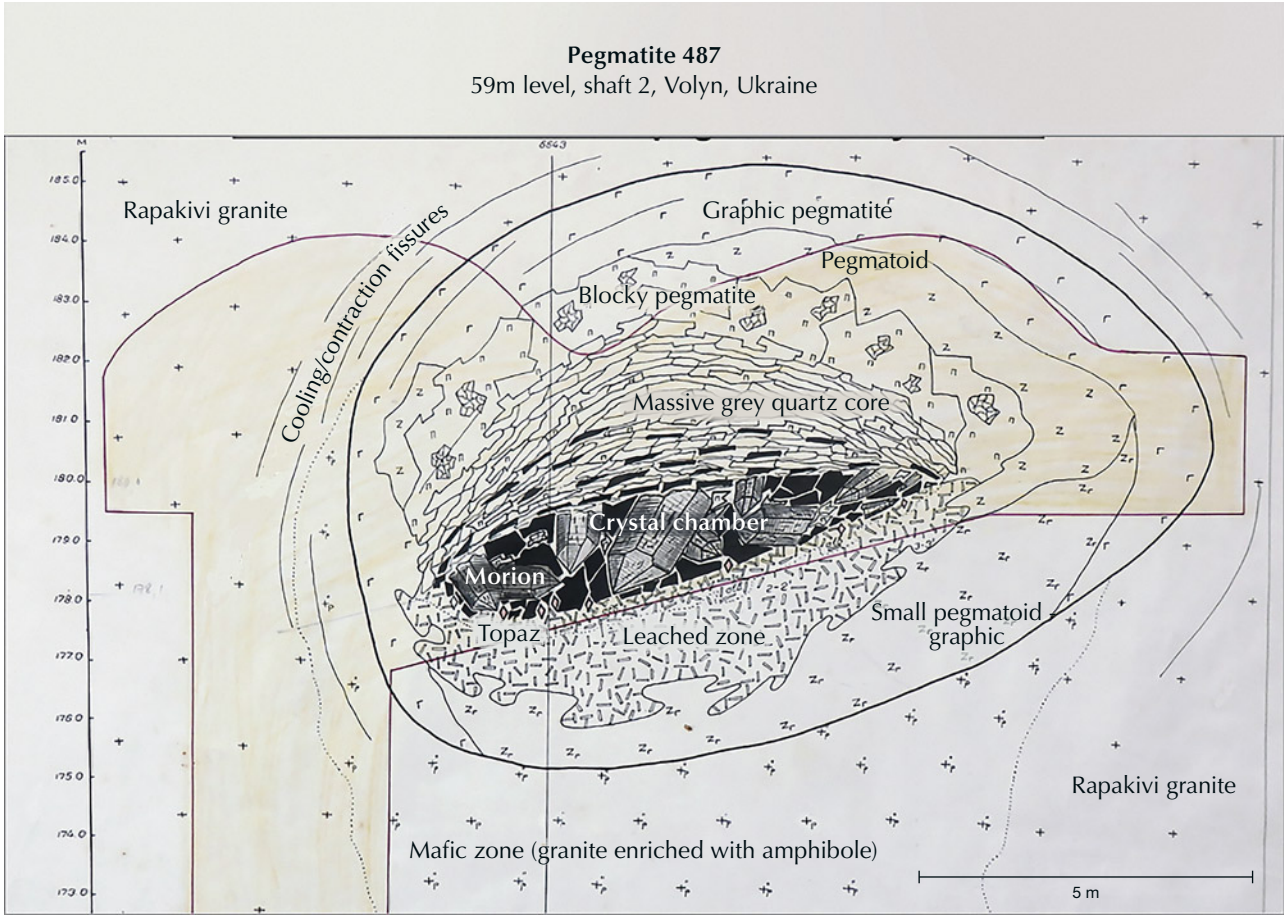

and clay minerals. Pseudomorph replacements of beryl, which now consist of opal, muscovite, bertrandite, buddingtonite, and minor amounts of euclase, albite, potassium feldspar, columbite, pyrite, barite, rare earth element minerals, and organic matter, occur in the breccia (Bartoshinskiy et al., 1969; Franz et al., 2017). The authors recently obtained another sample of a beryl pseudomorph, which contains siderite next to the beryllium minerals bertrandite and euclase, pointing to a variable fluid composition during the latest alteration stages. We also obtained a sample with a pseudomorph of white mica replacing topaz, which again shows the importance of a late alteration stage for the gemstones.

Based on fluid inclusion studies, the pegmatites crystallized at a high fluid pressure, first in a closed system (from 600° to 390°C) and then during cooling in an open system (at 365° ± 15°C) at a depth of 2.0 to 2.5 km (Lukashev, 1976; Kalyuzhnyi et al., 1971; Voznyak, 2007; Voznyak et al., 2012).

Another very special feature of these pegmatites is the occurrence of an organic matter called kerite. It is found within the cavities, attached to feldspar and topaz. It was interpreted as an example of abiogenic (of inorganic origin) formation (Ginzburg et al., 1987; Luk'yanova et al., 1992)—in other words, inorganic synthesis of fibrous carbon hydrates in the cooling stage of the pegmatites. They were later reinterpreted as fossil cyanobacteria (Gorlenko et al., 2000; Zhmur, 2003) from a geyser-type deposit. Recent investigations (Franz et al., 2022, 2023) have also identified a number of different fossils, some of them fungi-like. Filamentous fossils and remnants of former biofilms were also identified in etch pits of beryl.

PREVIOUS WORK ON VOLYN BERYL

Beryl is an accessory mineral found in 2% of the approximately 1500 pegmatite bodies at Volyn. It is present in small amounts in cavity areas, found in clay primarily in the lower sections of the pocket where they once grew on albite (Lyckberg et al., 2009), but their initial location is mostly lost. Beryl crystals are usually sitting in a clay-mica-quartz rock matrix or in a soft clay mass of dominantly kaolinite, as variably oriented individual crystals. Anhedral crystals, measuring no more than 0.5 cm in cross section, also occur in the leached zone under the chamber, where beryl fills cracks and leaching voids in albite.

The Vickers hardness of the Volyn beryl as measured on prismatic faces ranges from 1380 to 1395 kg/mm^2 (Lazarenko et al., 1973), corresponding to 7–8 on the Mohs scale. Volyn beryl is characterized by a relatively low density of 2.65 to 2.75 g/cm^3 (Gurskyi et al., 2006) and low refractive indices of n_o = 1.568–1.570 and n_ε = 1.566–1.567 (Lazarenko et al., 1973).

TABLE 1. Morphological characteristics of Volyn beryl (Lazarenko et al., 1973).

Morphological types	Type 1	Type 2	Type 3	Type 4	Type 5
Color	Brownish green	Light yellow, yellowish green	Greenish yellow, yellowish green	Light green to light blue	Brownish green to yellow
Shape	Prismatic	Long-prismatic, columnar	Needle-shaped, prismatic	Prismatic	Irregular
Other faces, etch pits	Rarely developed {0001} and {11$\bar{2}$1} faces	Deep etch pits; only remants of edges	Curved {11$\bar{2}$1}	Microporous dissolution	Only relics of original faces
External features (rough crystals)	All types: Rectangular and nearly square etch pits on {10$\bar{1}$0} prismatic faces, hexagonal etch pits on {0001} basal planes, and triangular hillocks between prismatic faces and on transition from prismatic faces to pyramidal faces				

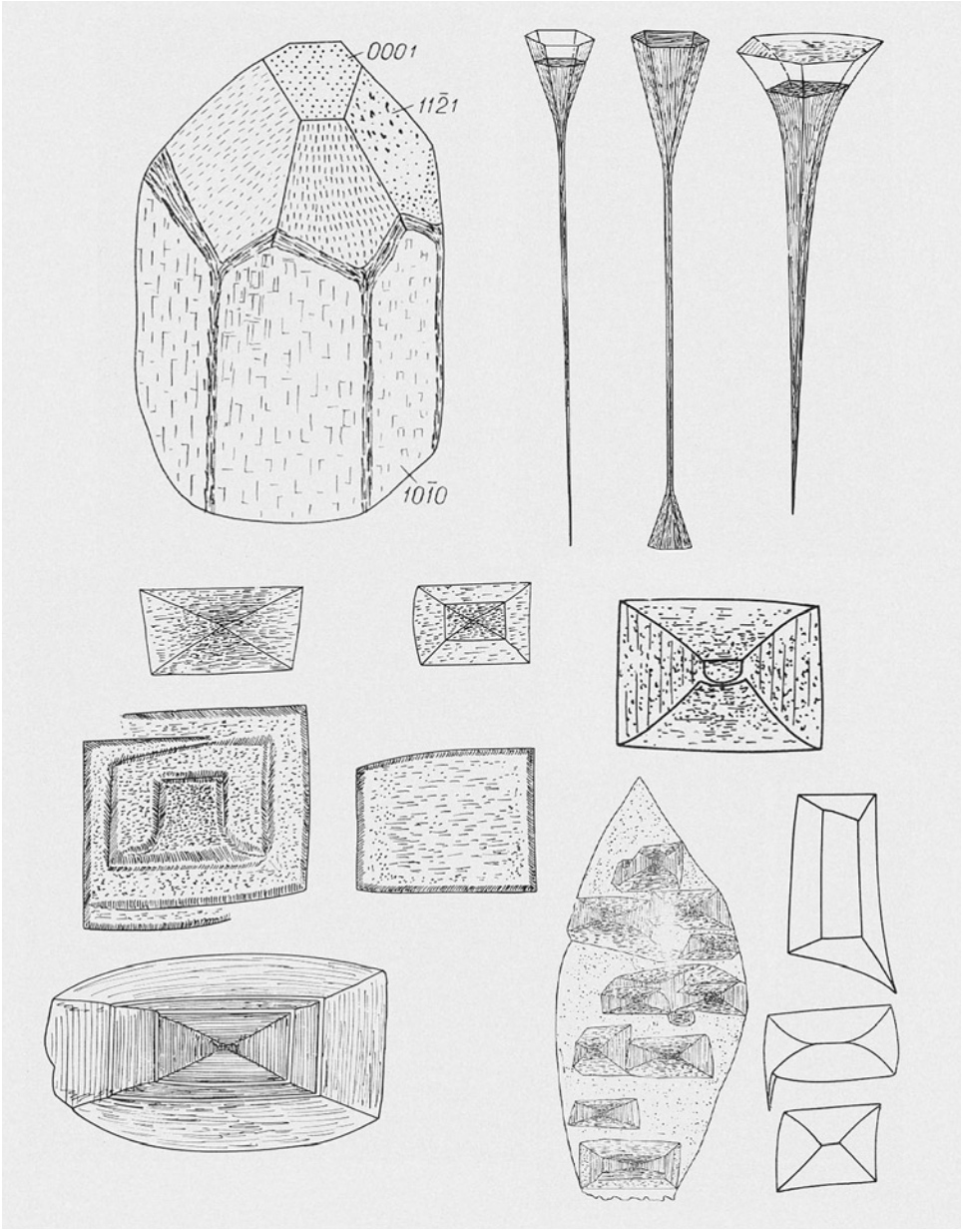

Figure 5. Crystal drawings, reproduced from Bartoshinskiy et al. (1969), showing the typical crystal habit with Miller indices of the common faces (top left), spectacular long funnel-shaped etch pits (ending in thin tubes) on the pinacoidal face (top right) and the typical P-type and F-type etch pits on the first-order prismatic face. The outline can be symmetrical or asymmetrical, and F-types can overlap each other. No scale was given in the original publication.

Only a few chemical analyses of Volyn beryl are available in the literature (Lazarenko et al., 1973; Khomenko et al., 2007; Voznyak et al., 2012). The low contents of sodium (≤0.10 wt.%), lithium (≤0.02 wt.%), cesium (≤0.24 wt.%), iron(II) (≤0.29 wt.%), and magnesium (≤0.03 wt.%), as well as the relatively high Fe^{3+}/Fe^{2+} ratios (on average near 7:1), are characteristic for Volyn beryl. Titanium, manganese, chromium, vanadium, potassium, calcium, gallium, niobium, molybdenum, and barium were reported as minor elements, mostly below or near 0.01 wt.%.

Lazarenko et al. (1973) described different stages of the dissolution of beryl, which produced five morphological types of columnar-prismatic, occasionally spicular beryl crystals (table 1), with characteristically sculptured crystal faces as well as systems of dissolution cones (so-called etch channels). Basal faces are rare. Bartoshinskiy et al. (1969) showed rectangular F- and P-type etch pits with a partly curved outline on the first-order prismatic face and spectacular long, tubular etch pits on the pinacoidal face (figure 5).

The nature of the typical color for Volyn heliodor was studied by Khomenko et al. (2007, 2010) using optical spectroscopy. Variations in the color of Volyn beryl are due to the intensity of the absorption seen in the slope from 28000 to 22000 cm^{-1} of the strong

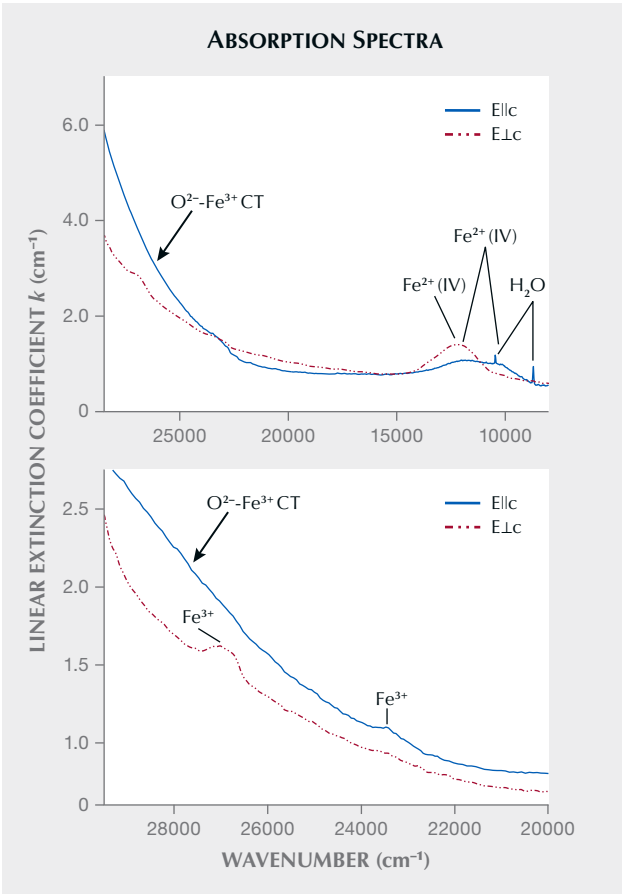

Figure 6. A: Representative polarized optical absorption spectra of a weakly colored yellow-green beryl from Volyn. Linear extinction coefficient k *(cm^{-1}) is the absorption coefficient of a sample 1 cm thick. Arrows point to a strong long-wave tail of the O^{2-}-Fe^{3+} charge transfer (CT) in the UV region and the weak Fe^{2+} and H_2O bands in the NIR region. B: Absorption along the long-wavelength slope of a strong O^{2-}-Fe^{3+} charge transfer band that causes yellow color in the polarized spectra of heliodor. Spin-forbidden absorption bands of Fe^{3+} ions are labeled with arrows; modified from Khomenko et al. (2007, 2010).*

UV absorption, caused by the O^{2-}-Fe^{3+} charge transfer in structural or interstitial positions near the cationic vacancies (figure 6). This slope covers the blue absorption at approximately 450–470 nm (22222–21276 cm^{-1}). Fe^{2+} ions do not affect the color of Volyn heliodors, confirming results of previous spectroscopic investigations by Wood and Nassau (1968), Schmetzer et al. (1975), and Platonov et al. (1984, 2016).

Volyn beryl's color varies from saturated brownish green to light yellow-green (figures 1 and 2). Most of the gem-quality crystals can be regarded as typical heliodor with a yellowish shade of variable intensity (rare greenish blue crystals are displayed in the Museum of Precious and Decorative Stones; Vasylyshyn et al., 2001). Although some reproductions of crystals from Volyn show an intense green color resembling that of emerald, this is purely a matter of color reproduction: Typical emerald color is not reported from Volyn crystals, in line with the absence of chromium and vanadium. Ukraine's only emerald occurrence is Kruta Balka (Franz et al., 2020), and the attribution of emerald to Volyn in Grundmann and Giuliani (2002) is probably erroneous. Morganite has not been reported from Ukraine, either.

MATERIALS AND METHODS

For SEM investigation of the etch pits, nine light yellowish green beryl crystals were selected from the collection of the Institute of Geochemistry, Mineralogy and Ore Formation of the National Academy of Sciences of Ukraine (IGMOF NASU) in Kyiv, along with three nearly colorless prismatic crystals (collected by author GF from the mine tailings in 2008) with a partly developed pinacoidal face.

SEM and energy-dispersive X-ray spectroscopy (EDS) were performed using a JEOL JSM-6700F field emission scanning electron microscope equipped with a JED-2300 EDS spectrometer at IGMOF NASU. The spectra were collected with an accelerating voltage of 15 kV and a beam current of 0.65 nA. Operating conditions for each analysis were identical. The samples were cleaned in an ultrasonic bath and then sputtered with a platinum layer of 15 nm thickness. The three nearly colorless crystals were carbon coated and investigated at the Central Facility for Electron Microscopy (ZELMI), Technical University Berlin, using a Hitachi SU8030 cold field emission SEM equipped with an EDAX Octane-A Plus 30 mm^2 silicon drift detector for qualitative EDS analysis. Some images were obtained in combination with a backscattered electron (BSE) and SE detector.

Standard gemological properties were investigated on another 16 rough beryl crystals (mineralogical collection of IGMOF NASU) and 20 faceted beryls (private collection of O. Vyshnevskyi) from the Volyn pegmatite field. For refractive index and birefringence measurements, we used an Eickhorst GemLED refractometer. Sartorius CP 224 S analytical lab balances equipped with a hydrostatic attachment were used for specific gravity (YDK01MS Density Determination Kit), using distilled water as fluid. The color of the samples was graded using a GIA GemSet in strong, diffuse daylight.

TABLE 2. Gemological characteristics of Volyn beryl.

Color	Very light to medium yellowish green	Very light to strongly yellowish green	Very light to medium green-yellow
Refractive index	n_ω = 1.569–1.570 n_ε = 1.562–1.564	n_ω = 1.568–1.571 n_ε = 1.562–1.566	n_ω = 1.568–1.571 n_ε = 1.562–1.566
Birefringence	0.006–0.008	0.005–0.006	0.005–0.006
Specific gravity			
Rough crystals (16)		2.62–2.70	
Faceted stones (20)		2.66–2.70	
Internal features	Crystals, liquid (fluid) inclusions, fingerprints, etch tubes, fractures		

RESULTS

Gemological Characteristics. The standard gemological properties of the 16 rough and 20 faceted samples are summarized in table 2. All were transparent to translucent, and none showed fluorescence under short- and long-wave UV light. Their refractive indices of 1.568–1.571 (n_ω) and 1.562–1.566 (n_ε) and birefringence values of 0.005–0.008 were typical for natural beryl. Samples with stronger yellowish hue showed slightly lower birefringence. Eye-clean rough crystals, as well as all faceted stones, had a specific gravity in the range of 2.66–2.70. Translucent rough beryl had a lower specific gravity range of 2.62–2.65, which may be due to numerous fluid inclusions. Solid inclusions with a size of tens to hundreds of micrometers, brought to the surface in polished sections, were identified by EDS analysis as albite, microcline, muscovite, columbite, iron sulfide, titanium oxide, and iron oxide/hydroxide (possibly goethite).

Morphology of Etch Pits. In general, the "negative faces" of an etch pit follow the symmetry pattern of the crystal. The nomenclature for the description is outlined in figure 7. Faces of the etch pits can be

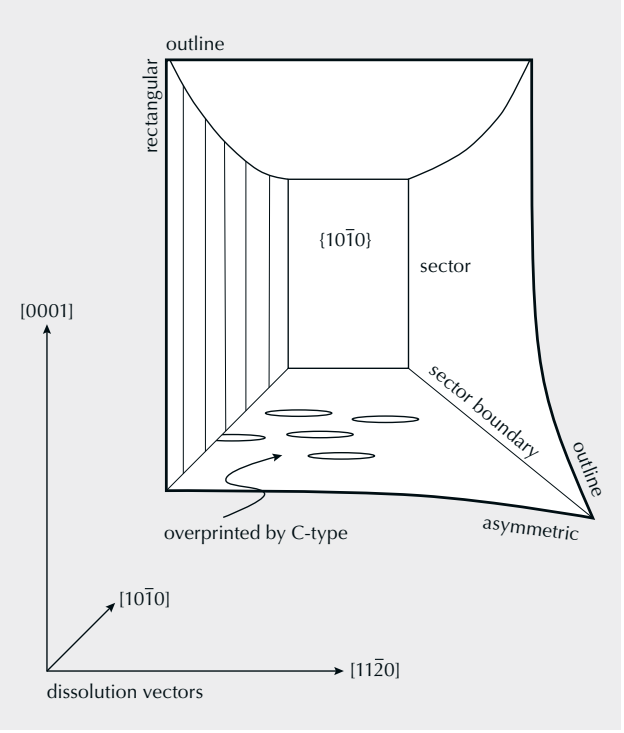

Figure 7. Nomenclature for the description of etch pits, shown for F-type (flat bottom, originating from point defects) on the first-order prism. P-type etch pits show the same features, except that the bottom is pointed. The outline of the etch pit indicates the relative dissolution vectors in the directions parallel and perpendicular to the c*-axis. If the vectors do not change with increasing depth, sectors with straight boundaries are formed. If the dissolution vectors change relative to each other, sector boundaries become curved toward an hourglass shape. Stepped sectors indicate discontinuities in the dissolution velocity. An asymmetric outline indicates heterogeneous dissolution within a growing etch pit. Etch pits of one kind or one generation can be overprinted by another type.*

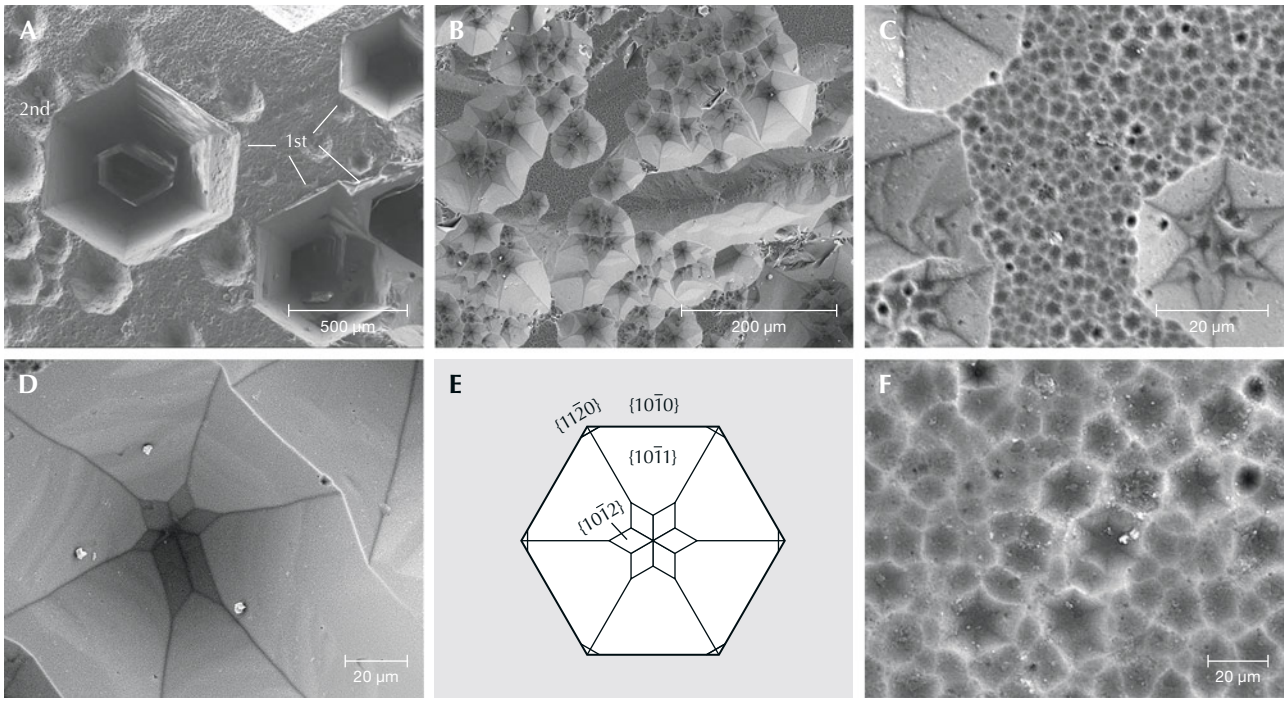

Figure 8. SEM images of Volyn beryl crystals with etch pits on {0001}. A: Deep first-order P-type etch pits (transitional to H-type) with no steps, straight, regular in outline, and up to 500 µm in diameter together with irregular second-order P-type etch pits approximately 50 µm in diameter. B: Second-order P-type etch pits overlapping each other. C: Second- and third-order P-type etch pits. D: Star-like bottom in a second-order P-type etch pit, produced by dissolution following first the {10$\bar{1}$0} first-order prismatic face, then in the deep part the {11$\bar{2}$0} second-order prismatic face. E: Diagram of a P-type etch pit; the negative crystal produced by dissolution shows the {10$\bar{1}$0} first-order prismatic face with the {10$\bar{1}$1} in the upper part and at the bottom the {10$\bar{1}$2} first-order hexagonal dipyramidal faces. This indicates a change in the relative dissolution velocity with increasing depth. F: Third-order P-type etch pits, with about 1 to 3 µm diameter.

even or stepped; outlines of an etch pit on the crystal face can be straight or curved, symmetrical or asymmetrical.

Rectangular etch pits on first-order prismatic faces {10$\bar{1}$0} and hexagonal etch pits on the basal planes {0001} were formed by dissolution. Pyramidal faces are rarely developed on the investigated crystals. Etch pits on {0001} are P-type; however, some with very steep faces are transitional to H-type (figure 8). We observe three orders of magnitude: First-order etch pits are up to 500 µm in diameter and have a mostly straight hexagonal outline (figure 8A). Second-order etch pits are on the order of 50 µm wide, with a less regular outline, partly overlapping each other (figure 8, B and C). Many of these show at their bottom a star-like pattern (figure 8D), produced by a change from dissolution parallel to the first-order prismatic face {10$\bar{1}$0} to dissolution parallel to the second-order prismatic face {11$\bar{2}$1} (figure 8E). The negative crystal produced by dissolution shows the {10$\bar{1}$0} first-order prismatic face with the {10$\bar{1}$2} and {10$\bar{1}$1} first-order hexagonal dipyramidal faces. Third-order etch pits are 1 to 3 µm wide, irregular in outline and very abundant, covering all of {0001} (figure 8, C and F).

Figure 9 shows etch pits on the first-order prism {10$\bar{1}$0} of the beryl crystals. These etch pits are rectangular, with their long side parallel to the *c*-axis (figure 9A), perpendicular (figure 9B), or nearly square (figure 9C). Similar to {0001}, F-type etch pits were observed in three orders of magnitude; however, P-types are much rarer and only observed in first-order, whereas F-types dominate and there is a more or less continuous spectrum for second- and third-order types. In addition, there are small C-type etch pits, which can be oriented perpendicular to the *c*-axis (figure 9, D and E) or parallel to the *c*-axis (figure 9, F and G). First-order P-types with stepped sides can be strongly elongated parallel to the *c*-axis (figure 9, D and E). F-type etch pits show a smooth curvature of the edges (figure 9G), which was also observed in P-types (figure 9B).

Edges between two first-order prisms are characterized by the presence of triangular hillocks, formed by dissolution of the prismatic faces (figure 1B and figure 10). Pyramidal faces were only observed in one

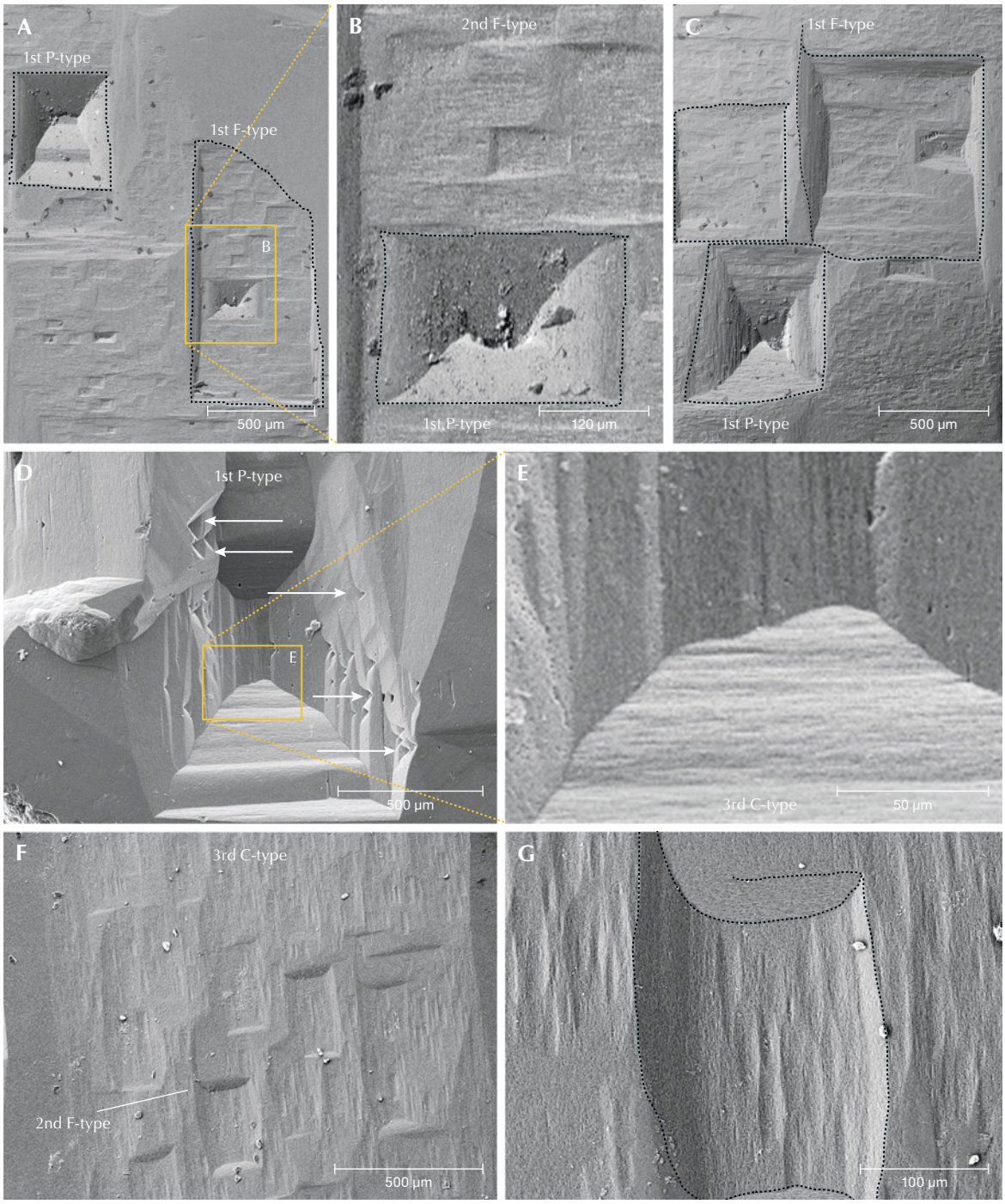

Figure 9. SEM images of Volyn beryl crystals with etch pits on first-order prismatic faces {10$\bar{1}$0}, with the orientation of the c*-axis nearly vertical. Some etch pits are outlined (black dotted lines). A: Rectangular first-order P-type etch pit and asymmetric first-order (1st) F-type etch pit (approximately 500 µm × 1000 µm) with long edge parallel to the* c*-axis. Note the second-order (2nd) approximately 50 µm × 100 µm wide F-type etch pits within first-order F-type etch pit. B: Rectangular symmetric first-order P-type etch pit with smoothly curved, hourglass-shaped sector boundaries. C: Two large first-order F-type etch pits, and an asymmetrical first-order P-type etch pit, overprinted by very flat second- to third-order F-type etch pits. D: Stepped first-order P-type etch pit with bottom elongated into a line. Note the small triangular etch pits in the left and right sector walls (arrows). E: Lower sector wall with third-order C-type etch pit, oriented perpendicular to the* c*-axis. F: Second-order F-type etch pits with large, asymmetric third-order C-type etch pits oriented parallel to the* c*-axis (magnified in G).*

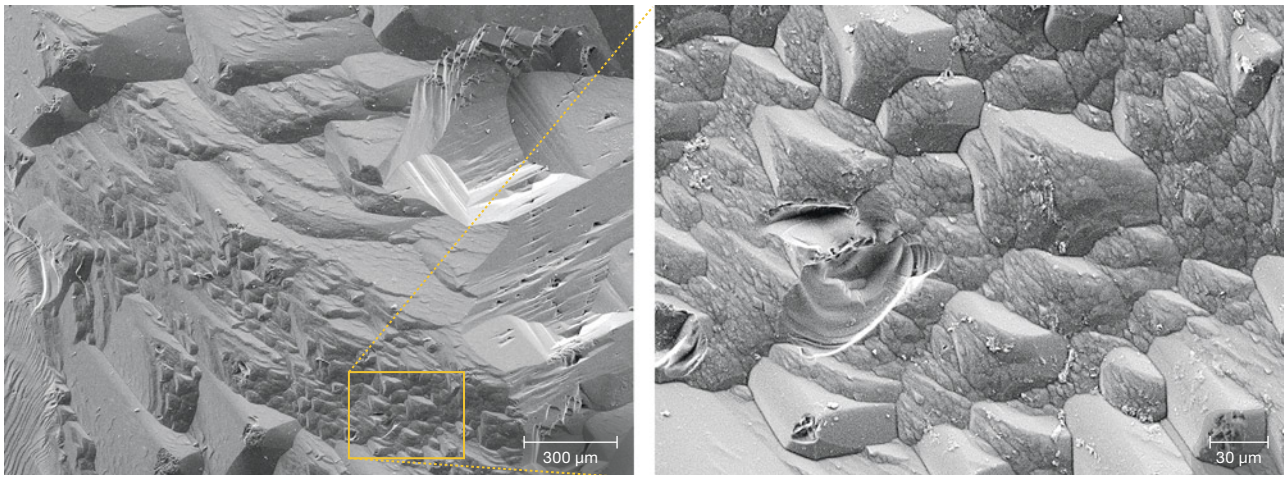

Figure 10. SEM image (left) of the edge between two prism faces, forming triangular hillocks, magnified on the right.

crystal and contained triangular steps (figure 11). On the steps, small third-order F-type etch pits developed.

Analysis of the crystals' surfaces yielded more information about the dissolution process and the components in the dissolving fluid. The faces show a porosity, both outside and inside the etch pits (figure 12) and also within the small C-type etch pits. Individual pores show no crystallographic outline and are on the order of several hundred nanometers, mostly elongated parallel to the *c*-axis. Very small grains of a titanium dioxide polymorph and gold (with minor contents of silver, copper, and iron as determined by EDS) were observed (figure 12D), as well as particles consisting of a mixture of chloride and sulfate crystals and a particle with light rare earth elements and phosphorous.

DISCUSSION

On a crystal face, the distinction between growth features and dissolution features is based mainly on the observation that growth features, such as growth hillocks, are positive (on the basal plane with a hexagonal shape), rising up on top of each other in stepwise fashion (Sahama, 1966), whereas pits that extend down into the crystal are negative and indicate dissolution. Flamini et al. (1983) showed SEM images of growth features on red (manganese-bearing) beryl from Utah. The features described above on the pinacoid and the prism of Volyn beryl are all interpreted as dissolution features. Phenomena observed at crystal edges and the transition from the prism to the pinacoid are less clear, and we propose that for a provenance study

Figure 11. Left: SEM image of dissolution features on the transition from prismatic face (lower part, with rectangular F-type etch pits) to pyramidal face (upper right), with the formation of triangular hillocks. Right: Small etch pits (indicated by arrows) formed parallel to the larger F-type etch pits on the prismatic face.

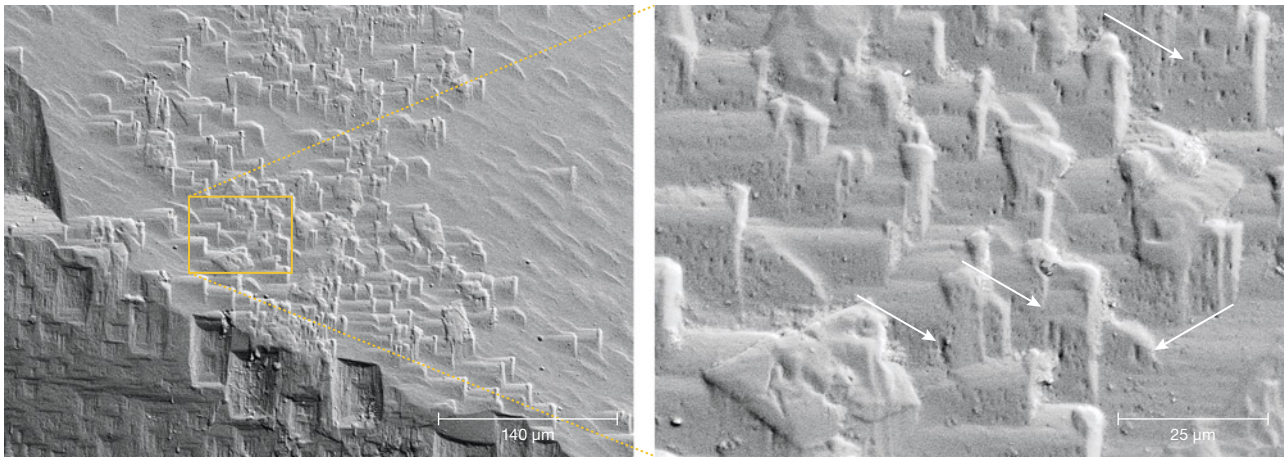

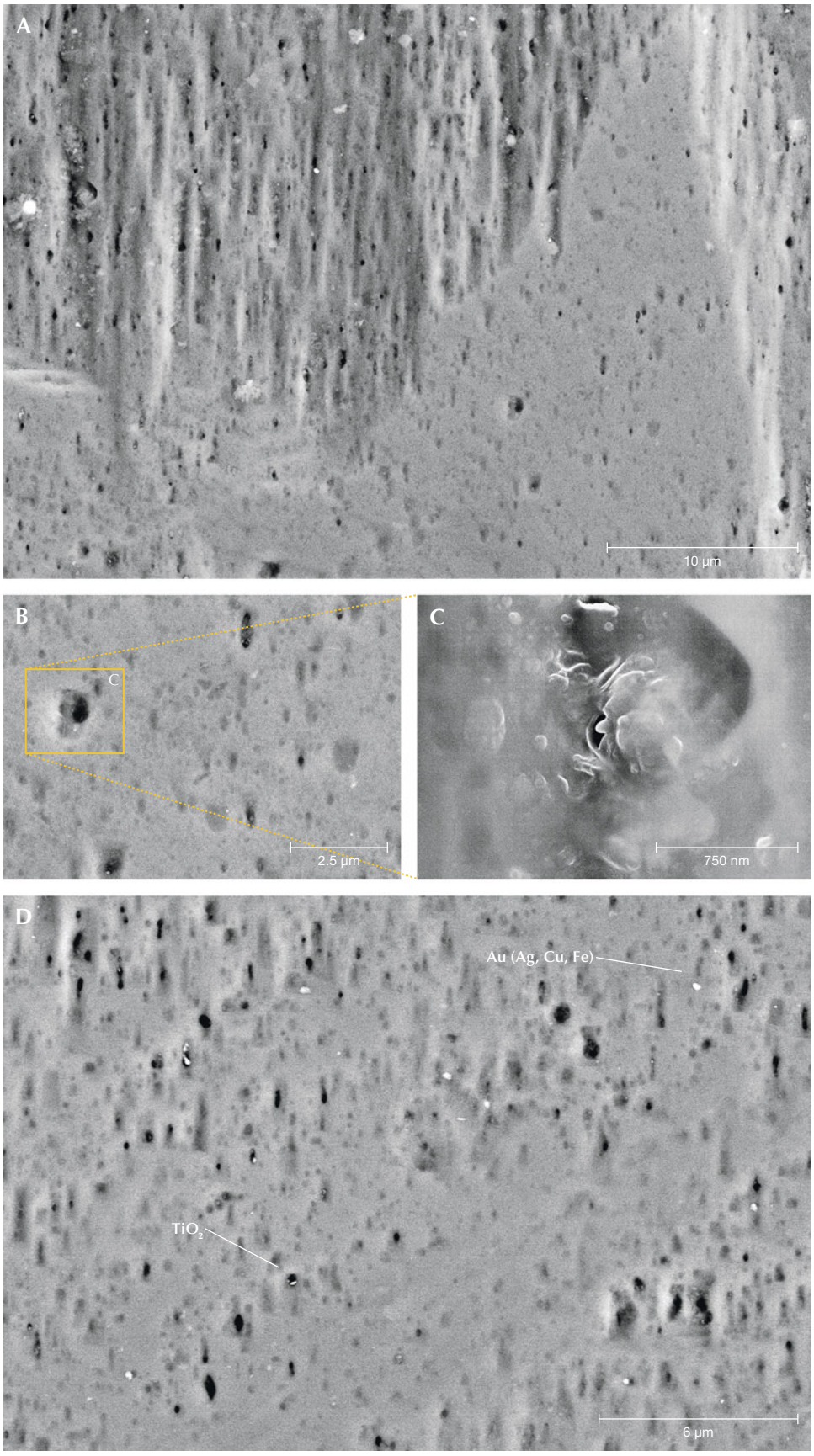

Figure 12. Combined SEM-BSE images of enlarged areas of a prism face, showing small-scale porosity. A: The edge of an etch pit with elongated C-type etch pits. The smooth surface is a prism face near the etch pit. B and C: Enlarged part of the prism face, showing anhedral pores measuring several hundred nanometers. D: A surface with very small grains of gold with silver, copper, and iron impurities, as well as titanium dioxide (chemical composition determined by EDS).

only the pinacoid and the first-order prism should be used.

Dissolution of a mineral can be considered as "negative growth." As growth is generally described by growth laws (e.g., Philpotts and Ague, 2022), similarly we can describe dissolution by "negative growth laws." On a crystal face, dissolution is first dominated by the number of defects (i.e., dislocation-controlled). Removal of atoms is energetically favored at defects compared to an ideal surface. At point defects, the defect disappears and removal of atoms produces steps on the crystal's face in two directions. On a linear defect, the defect extends in the third dimension into the crystal and removal of atoms continues in three dimensions. Once a deep etch pit has formed, dissolution can be rate-determined by diffusion of the components in solution out of the etch pit, and it is then diffusion-controlled. This is what is seen on the pinacoidal face. There are a few first-order etch pits, due to a small number of large screw dislocation bundles, which were formed parallel to the *c*-axis during growth of the crystal. They can probably extend deep into the crystal as etch channels (Bartoshinskiy et al., 1969).

We interpret the second-order etch pits as due to smaller screw dislocations, which are more frequent (figure 8A) and formed a negative first-order prism. When these etch pits became deep, the dislocation-controlled dissolution was followed by a diffusion-controlled dissolution, and the negative crystal ends with the $\{10\bar{1}2\}$ and $\{10\bar{1}1\}$ first-order hexagonal dipyramidal faces. Relative dissolution velocity is—as estimated from the shape and depth of the etch pits—in the sequence of the directions [0001] > $[11\bar{2}0]$ > $[10\bar{1}0]$. The deep channels (figure 5) shown by Bartoshinskiy et al. (1969) demonstrate that [0001] is a preferred direction for dissolution. Very deep P-type etch pits are also shown in figure 8A, where the bottom is no longer visible. In the diagram in figure 8E, the negative crystal produced by dissolution is shown in the upper part the outline of the $\{10\bar{1}0\}$ first-order prismatic face with the $\{10\bar{1}1\}$ hexagonal dipyramidal faces. This indicates faster dissolution in $[11\bar{2}0]$ compared to $[10\bar{1}0]$, leaving traces of the first-order prismatic faces. At the bottom (i.e., with increasing depth), a change is seen from the $\{10\bar{1}1\}$ first-order hexagonal dipyramidal faces to the $\{10\bar{1}2\}$ hexagonal dipyramidal faces (figure 8, C and D). This indicates a change in the relative dissolution velocity with increasing depth. Therefore, at the end of the etch pit, the sequence of relative velocities is [0001] > $[10\bar{1}0]$ > $[11\bar{2}0]$, which also implies that dissolution in $[11\bar{2}0]$ is not very different from that in $[10\bar{1}0]$.

Third-order etch pits are very abundant, covering the basal plane completely and also occurring within second-order etch pits (figure 8, C and F). Such a high number of growth dislocations seems unlikely, and we propose that dissolution on these faces is controlled by the crystal structure of beryl with its pronounced channels parallel to the *c*-axis. Demianets et al. (2006) determined by atomic force microscopy that experimentally produced hydrothermal beryl shows growth hills on the pinacoidal face, with a separation distance of approximately 0.2 µm. The cavities around such growth hills might be correlated with the sites where dissolution is effective in the absence of dislocations, producing the third-order etch pits (figure 8F). The centers of the Si_6O_{18} rings within the beryl structure aligned with the basal planes are sites of preferential removal of atoms, supported by the fact that first-order etch pits are very deep and can extend into the long, funnel-shaped tubes (figure 5; Bartoshinskiy et al., 1969; Lazarenko et al., 1973) perpendicular to the Si_6O_{18} rings. This is also in line with the sodium-poor composition of Volyn beryl. Sodium would be situated within the channels, generally bound to a tetrahedral site with a stronger bond than water and could thus prevent strong dissolution in [0001].

On the first-order prismatic faces, P-type etch pits are rare and most are large, first-order P-types (figure 9), indicating relatively few screw dislocations perpendicular to the *c*-axis. Prismatic faces are dominated by F-type etch pits, associated with point defects (substituting atoms, vacancies, and interstitial atoms). These etch pits are very abundant, often covering the whole face and overlapping each other (figure 1). They range in size from a centimeter down to several micrometers (figure 9), and though we classified them as first- and second-order etch pits, there is more or less a continuum in size. The outline is rectangular, elongated perpendicular or parallel to the *c*-axis, or nearly square, indicating essentially equal dissolution velocities in both directions. The sector boundaries are mostly straight, with equal dissolution velocities in both directions, but some show curved boundaries, indicating continuously changing dissolution velocities, also observed in P-type etch pits (figure 9B). First-order etch pits can also be asymmetrical.

Our investigations also yielded some information about the fluid phase, which caused the dissolution. This fluid must have been able to transport elements

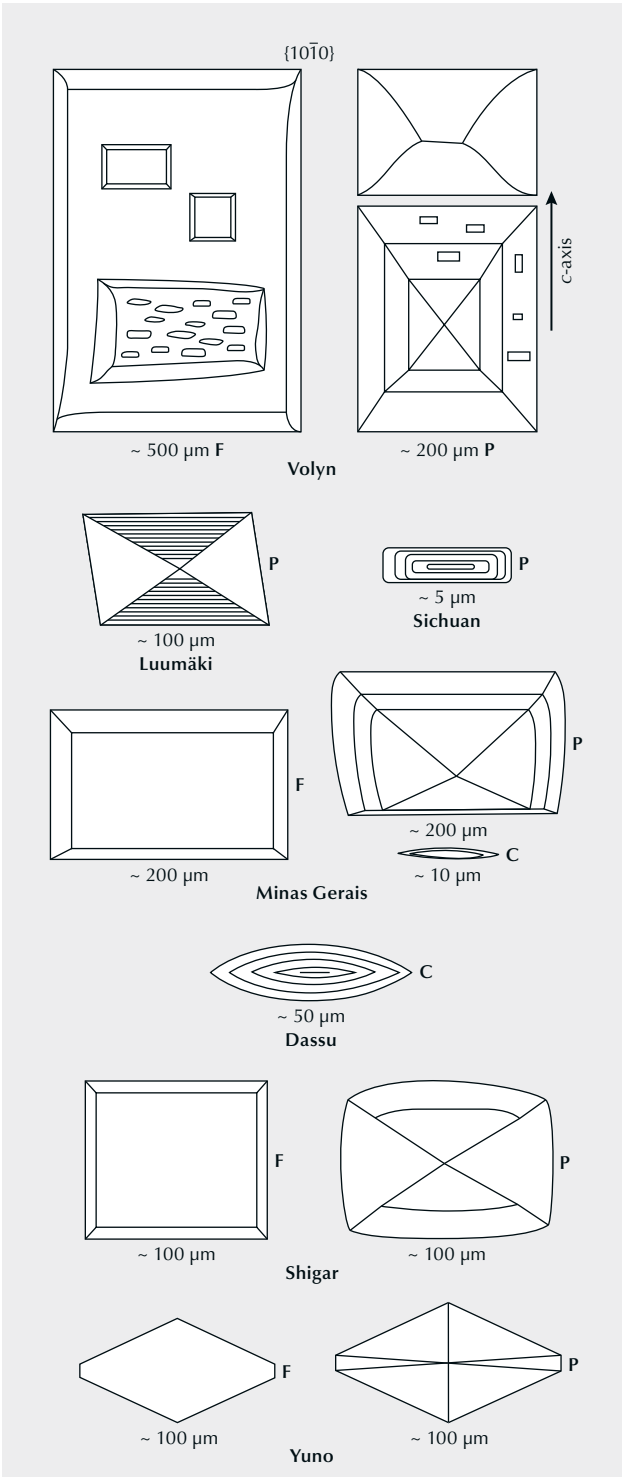

Figure 13. Diagrams of etch pits on {10$\bar{1}$0} of heliodor from Volyn compared to heliodor from Luumäki (Finland) and aquamarine from Sichuan (China), Minas Gerais (Brazil), Dassu, Shigar, and Yuno (Himalayas), from Kurumathoor and Franz (2018). F- and P-type etch pits are larger on crystals from Volyn and overlap each other, but note that they can also be asymmetrical. Within F-type etch pits, C-type etch pits oriented perpendicular to the c*-axis are larger and more irregular in outline than on crystals from Minas Gerais. In P-type etch pits on crystals from Luumäki, abundant steps were identified, whereas the steps in crystals from Volyn are less frequent or missing, and sector boundaries can be curved.*

such as titanium, rare earth elements, and even gold (figure 12D). Furthermore, we know from the locality that in these niobium-, yttrium-, and fluorine-rich pegmatites, fluorine is a major component, as shown by the abundance of topaz as a typical gemstone, by fluorite as an accessory mineral, and by the occurrence of fluorine-rich muscovite (Franz et al., 2017). Beryl and topaz can be related to each other by the chemical equilibrium

$$Be_3Al_2Si_6O_{18} + 28\ HF \rightleftharpoons Al_2F_2SiO_4 + 3\ BeF_2^{fluid} + 5\ SiF_4^{fluid}\ 14\ H_2O$$

where beryllium fluoride and silicon fluoride are fluid species. This chemical equilibrium might explain why either beryl or topaz crystallized in the chambers, but rarely both, and it also hints toward a fluorine-rich fluid phase for the late-stage dissolution of the beryl. Lyckberg et al. (2009) noted that when topaz and beryl occur together, one grows at the expense of the other, which supports the interpretation inferred from the chemical equilibrium above.

The large gem-quality crystals with their dissolution phenomena on the surfaces show that possible products of newly formed minerals during incongruent dissolution have been transported away. In other words, we are dealing with an open system. Possible remnants of beryl dissolution as clay-like material are observed in some etch pits, but it is not yet clear whether this material is a product of the dissolution of the beryl or contamination from a late-stage hydrothermal process of other minerals such as feldspar.

The shape and size of the etch pits on Volyn beryl are different from those of other pegmatitic beryls (figure 13; Kurumathoor and Franz, 2018) and may well help to identify uncut crystals. A characteristic feature in particular is that F-type etch pits are much larger (figures 8 and 9) compared to beryl from most other localities. They frequently overlap each other (figures 1, 8, and 9), which is rarely observed in beryl from other localities. The different dissolution stages of the Volyn beryl with varying acidity-alkalinity described in the literature (Barthoshinskiy et al., 1969;

Lazarenko et al., 1973) might be correlated with our observation of first-, second-, and third-order etch pits. The degree of etching is quite variable on different crystals, and it even varies from pegmatite to pegmatite (Lyckberg et al., 2009).

The crystal from Minas Gerais in figure 13 shows similarly large F- and P-type etch pits and also small third-order C-type etch pits within F-type etch pits. At Volyn, however, the C-type etch pits are much larger, more abundant, and less regular in outline (figure 13A). C- and P-type etch pits measuring from 5 up to 50 µm, as observed in crystals from Dassu (Himalayas) and China, were not found in Volyn beryl, nor was the orthorhombic outline of F- and P-type etch pits in crystals from Yuno (Himalayas). Aquamarine from Shigar (Himalayas) shows P-type etch pits with a curved outline, which is not observed in the Volyn crystals, but its flat F-type etch pits are similar. Although the geological background of Volyn beryl is most similar to that from Luumäki, Finland (Lahti and Kinnunen, 1993; Lyckberg, 2004), with a similar heliodor color and a similar relation to a Precambrian anorthosite pluton, the etch pits on the prism faces are quite different (figure 13). On the crystals from Luumäki, only P-type etch pits were observed in Kurumathoor and Franz (2018), with an oblique outline and frequent steps. It must be noted, however, that for Kurumathoor and Franz (2018) only a small fragment from one crystal was available, which might not be representative for the occurrence. Furthermore, it must be kept in mind that up to now only a few crystals from the different localities could be investigated using SEM. Future research should be concentrated on more crystals from the same localities and on other beryl varieties with different composition (e.g., rich in sodium-magnesium, lithium-cesium, or manganese) that are also from non-pegmatitic environments.

CONCLUSIONS

Beryl crystals from Volyn are associated with the Korosten pluton in the Precambrian Ukrainian Shield. These crystals are of gem quality, exceptional in size, and have excellent color—both the yellow heliodor and the green beryl. They are found in chambers of pegmatites that formed in the cooling and crystallization stages of the pegmatite melt. A special feature of these beryl crystals is the appearance of dissolution features known as etch pits. On the prismatic face, these etch pits are very pronounced and often cover the whole crystal. On the basal face, they form six-sided channels, ending with pyramidal faces or penetrating deep into the crystal. The shape and size of the etch pits are characteristic for the Volyn occurrence and easily distinguish them from beryl crystals from other localities.

ABOUT THE AUTHORS

Dr. Gerhard Franz is a retired professor of mineralogy and petrology at the Institute for Applied Geosciences, Technical University Berlin. Dr. Oleksii Vyshnevskyi and Dr. Volodymyr Khomenko are senior researchers at the Institute of Geochemistry, Mineralogy and Ore Formation of the National Academy of Sciences of Ukraine. Dr. Peter Lyckberg is a researcher and scientific collaborator with the National Museum of Natural History in Luxembourg. Ulrich Gernert is a physics engineer at the Central Facility for Electron Microscopy (ZELMI), Technical University Berlin.

ACKNOWLEDGMENTS

The Alexander von Humboldt Foundation financially supported author V. Khomenko's stay in Berlin in 2022–2023. The Museum for Precious and Decorative Stones in Khoroshiv is thanked for the permission to use the photograph of a beryl crystal in figure 1. We also thank the peer reviewers and editors for handling the manuscript, as well V. Chournousenko for stimulating discussions and for sharing his knowledge about the Volyn pegmatite field.

REFERENCES

Bartoshinskiy Z.V., Matkovskiy O.I., Srebrodolskiy B.I. (1969) Accessory beryl from chamber pegmatites of Ukraine. *Mineralogical Sbornik*, Vol. 23, No. 4, pp. 382–397 [in Russian].

Černý P. (2002) Mineralogy of beryllium in granitic pegmatites. *Reviews in Mineralogy and Geochemistry*, Vol. 50, No. 1, pp. 405–444, http://dx.doi.org/10.2138/rmg.2002.50.10

Černý P., Ercit T.S. (2005) The classification of granitic pegmatites revisited. *Canadian Mineralogist*, Vol. 43, No. 6, pp. 2005–2026, http://dx.doi.org/10.2113/gscanmin.43.6.2005

Demianets L.N., Ivanov-Shitz A.K., Gainutdinov R.V. (2006) Hydrothermal growth of beryl single crystals and morphology of their singular faces. *Inorganic Materials*, Vol. 42, No. 9, pp. 989–995, http://dx.doi.org/10.1134/S0020168506090111

Flamini A., Gastaldi L., Grubessi O., Viticoli S. (1983) Sulle caratteristiche particolari del berillo rosso dell'Utah. *La Gemmologia*, Vol. 9, No. 1/2, pp. 12–20 [in Italian].

Franz G., Khomenko V., Vishnyevskyy A., Wirth R., Struck U., Nissen J., Gernert U., Rocholl A. (2017) Biologically mediated crystallization of buddingtonite in the Paleoproterozoic: Organic-igneous interactions from the Volyn pegmatite, Ukraine. *American Mineralogist*, Vol. 102, No. 10, pp. 2119–2135, http://dx.doi.org/10.2138/am-2017-6055

Franz G., Vyshnevskyi O., Taran M., Khomenko V., Wiedenbeck M., Schiperski F., Nissen J. (2020) A new emerald occurrence from Kruta Balka, Western Peri-Azovian region, Ukraine: Implications for understanding the crystal chemistry of emerald. *American Mineralogist*, Vol. 105, No. 2, pp. 162–181, http://dx.doi.org/10.2138/am-2020-7010

Franz G., Lyckberg P., Khomenko V., Chournousenko V., Schulz H.-M., Mahlstedt N., Wirth R., Glodny J., Gernert U., Nissen J. (2022) Fossilization of Precambrian microfossils in the Volyn pegmatite, Ukraine. *Biogeosciences*, Vol. 19, No. 6, pp. 1795–1811, http://dx.doi.org/10.5194/bg-19-1795-2022

Franz G., Khomenko V., Lyckberg P., Chournousenko V., Struck U., Gernert U., Nissen J. (2023) The Volyn biota (Ukraine) – 1.5 Ga old (micro)fossils in 3D-preservation, a spotlight on the 'boring billion'. *Biogeosciences*, Vol. 20, pp. 1901–1924, http://dx.doi.org/10.5194/egusphere-2022-1116

Ginzburg A.I., Bulgacov V.S., Vasilishin I.S., Luk'yanova V.T., Solntseva L.S., Urmanova A.M., Uspensky V.A. (1987) Kerite from pegmatites of Volyn. *Doklady Akademii Nauk SSSR*, Vol. 292, pp. 188–191 [in Russian].

Gorlenko V.M., Zhmur S.I., Duda V.I., Suzina N.E., Osipov G.A., Dmitriev V.V. (2000) Fine structure of fossilized bacteria in Volyn kerite. *Origin of Life and Evolution of the Biosphere*, Vol. 30, pp. 567–577.

Grundmann G., Giuliani G. (2002) Emeralds of the World. *extraLapis English*, No. 2, pp. 24–35.

Gurskyi D.S., Esypchuk K.Yu., Kalinin V.I. (2006) *Mineral Deposits of Ukraine. Vol. II: Industrial Mineral Deposits*. Centre of Europe Publishing House, Kyiv-Lviv, 552 pp. [in Ukrainian].

Ivanovich P.V., Alekseevich D.S. (2007) *Mineralogy of the Volynian Chamber Pegmatites, Ukraine*. EKOST Association, Moscow, 128 pp.

Kalyuzhnyi V.A., Voznyak D.K., Gigashvili G.M. (1971) *Mineral Forming Fluids and Mineral Paragenesis of Chamber Pegmatites of Ukraine*. Naukova Dumka, Kyiv, 216 pp. [in Ukrainian].

Khomenko V.M., Vyshnevskyi O.A., Gnelytska Z.T., Kamenchuk V.K. (2007) Crystal chemistry of beryl from Volyn deposit on the basis of microprobe analyses, optical and IR spectroscopic data. *Mineralogical Journal (Ukraine)*, Vol. 29, No. 3, pp. 26–38 [in Ukrainian].

Khomenko V.M., Savchuk Ye.O., Vyshnevskyi O.A., Dovbnya N.A. (2010) Influence of irradiation on state of Fe-ions in Volyn beryl. *Proceedings of the Ukrainian Mineralogical Society*, Vol. 7, pp. 64–71.

Koshil I.M., Vasilishin I.S., Pavlishin V.I., Panchenko V.I. (1991) Geologischer Aufbau und Mineralogie der Pegmatite in Wolynien, Ukraine. *Lapis*, Vol. 10, pp. 28–41.

Kurumathoor R., Franz G. (2018) Etch pits on beryl as indicators of dissolution behaviour. *European Journal of Mineralogy*, Vol. 30, No. 1, pp. 107–124, http://dx.doi.org/10.1127/ejm/2018/0030-2703

Lahti S.I., Kinnunen K.A. (1993) A new gem beryl locality: Luumäki, Finland. *G&G*, Vol. 29, No. 1, pp. 30–37, http://dx.doi.org/10.5741/GEMS.29.1.30

Lazarenko E.K., Pavlishin V.I., Latysh V.T., Sorokin Ju G. (1973) Mineralogy and genesis of the chamber pegmatites of Volyn Lvov. *Vysshaja shkola*, 360 pp. [in Russian].

Linnen R.L., Van Lichtervelde M., Černý P. (2012) Granitic pegmatites as sources of strategic metals. *Elements*, Vol. 8, No. 4, pp. 275–280, http://dx.doi.org/10.2113/gselements.8.4.275

London D. (2008) *Pegmatites*. Canadian Mineralogist, Special Publication No. 10, Mineralogical Association of Canada, Québec, 347 pp.

Lukashev A.N. (1976) *Depth of Pegmatite Formation*. Nedra, Moscow, 152 pp. [in Russian].

Lu'kyanova, V.T., Lobzova, R.V., and Popov, V.T. (1992) Filaceous kerite in pegmatites of Volyn. *Izvestiya Ross. Akademii Nauk Ser. Geologicheskaya, 5*, pp. 102–118 [in Russian].

Lyckberg P. (2004) Ein Neufund phantastischer grüner Edelberylle aus Luumäki, Karelien, Finnland. *Mineralien-Welt*, Vol. 6, pp. 38–45 [in German].

——— (2005) Gem beryl from Russia and Ukraine. In *Beryl and Its Color Varieties*. Lapis Intl., East Hampton, Connecticut, pp. 49–57.

Lyckberg P., Chornousenko V., Wilson W.E. (2009) Famous mineral localities: Volodarsk-Volynski, Zhitomir Oblast, Ukraine. *Mineralogical Record*, Vol. 40, pp. 473–506.

Lyckberg P., Chournousenko V., Chournousenko O. (2019) Giant heliodor and topaz pockets of the Volodarsk chamber pegmatites, Korosten pluton, Ukraine. In *Proceedings of the 36th International Gemmological Conference*, Nantes, France, August 27–31, pp. 78–83.

Philpotts A.R., Ague J.J. (2022) *Principles of Igneous and Metamorphic Petrology*, 3rd ed. Cambridge University Press, Cambridge, UK.

Platonov A.N., Taran M.N., Balitsky V.S. (1984) *The Nature of the Color of Gems*. Nedra, Moscow, 196 pp. [in Russian].

Platonov A.N., Khomenko V.M., Taran M.N. (2016) Crystal chemistry, optical spectra and color of beryl. I. Heliodor and golden beryl - two varieties of natural yellow beryl. *Mineralogical Journal (Ukraine)*, Vol. 38, No. 2, pp. 3–14 [in Russian].

Sahama T.G. (1966) Polygonal growth of beryl. *Bulletin of the Geological Society of Finland*, Vol. 222, pp. 31–42.

Schmetzer K., Berdesinski W., Bank H. (1975) Farbveränderungen von Edelsteinen der Beryllgruppe. *Zeitschrift der Deutschen Gemmologischen Gesellschaft*, Vol. 24, No. 2, pp. 81–87.

Shestopalov V., Shybetskyi I., Pochtarenko V., Shymkiv L., Kolaibina I., Shurpach N., Petrenko L., Rudenko Yu., Borysova T. (2020) *Screening of Ukraine for Geological Disposal of Radioactive Waste*. Novyi Druk, Kyiv, 134 pp. [in Ukrainian].

Shumlyanskyy L., Belousova E., Petrenko O. (2017) Geochemistry of zircons from basic rocks of the Korosten anorthosite-mangerite-charnockite-granite complex, north-western region of the Ukrainian Shield. *Mineralogy and Petrology*, Vol. 111, No. 4, pp. 459–466, http://dx.doi.org/10.1007/s00710-017-0514-2

Shumlyanskyy L., Franz G., Glynn S., Mytrokhyn O., Voznyak D., Bilan O. (2021) Geochronology of granites of the western Korosten AMCG complex (Ukrainian Shield): Implications for the emplacement history and origin of miarolitic pegmatites. *European Journal of Mineralogy*, Vol. 33, No. 6, pp. 703–716, http://dx.doi.org/10.5194/ejm-33-703-2021

Simmons W.B. (2014) Gem-bearing pegmatites. In L.A. Groat, Ed., *Geology of Gem Deposits*, Mineralogical Association of Canada, Short Course Series, Vol. 44, pp. 257–304.

Vasylyshyn I.S., Indutny V.V., Pavlyshyn V.I. (2001) Museum of Precious and Decorative Stones. State Gemmological Centre of Ukraine, Kyiv, 100 pp. [in Ukrainian].

Voznyak D.K. (2007) *Microinclusions and Reconstruction of Conditions of Endogenous Mineralogenesis*. Naukova Dumka, Kyiv, 279 pp. [in Ukrainian].

Voznyak D.K., Khomenko V.M., Franz G., Wiedenbeck M. (2012) Physico-chemical conditions of the late stage Volyn pegmatite evolution: Fluid inclusions in beryl studied by thermobarometry and IR-spectroscopy methods. *Mineralogical Journal (Ukraine)*, Vol. 34, pp. 26–38 [in Ukrainian].

Wood D.L., Nassau K. (1968) The characterization of beryl and emerald by visible and infrared absorption spectroscopy. *American Mineralogist*, Vol. 53, No. 5-6, pp. 777–800.

Zhmur S.I. (2003) Origin of Cambrian fibrous kerites of the Volyn region. *Lithology and Mineral Resources*, Vol. 38, pp. 55–73, http://dx.doi.org/10.1023/A:1021827724818

Iolite from the Thor-Odin Dome, British Columbia, Canada: Geology, Chemical Composition, Inclusions, and Cause of Chatoyancy

Philippe M. Belley

The Blue Arrow and Blue Bear iolite (gem cordierite) claims located in the Thor-Odin dome (near Revelstoke in British Columbia, Canada) are two new examples of iolite occurrences hosted in hydrothermally altered mafic volcanic rocks metamorphosed at upper amphibolite to granulite facies, in which cordierite (X_{Mg} = 0.81–0.90) occurs in association with gedrite, iron-rich phlogopite, quartz, almandine-pyrope garnet, and various trace minerals. Strongly pleochroic, gem-quality cordierite rough from these claims produced dark violet-blue faceted stones generally smaller than 2 ct (both localities) and light grayish blue to dark slightly grayish violet-blue chatoyant cabochons up to approximately 12 ct (Blue Bear only). Coarse-grained cordierite-rich rocks are widespread in the Thor-Odin dome, which indicates good potential for future iolite discoveries in the region. Primary mineral inclusions in Blue Bear iolite include iron-rich phlogopite, muscovite, zircon, xenotime-(Y), hematite, and apatite. Where cordierite is traversed by rehealed fractures, mica inclusions are altered to unidentified hydrous aluminosilicates rarely containing trace pyrrhotite or barite. Three types of fluid inclusions occur in Thor-Odin iolite: (1) primary blocky fluid inclusions; (2) primary acicular fluid inclusions oriented parallel to the *a*-axis of cordierite, which cause chatoyancy when present in high concentrations (at Blue Bear only); and (3) secondary subequant fluid inclusions occurring along rehealed subconchoidal fractures.

Two gem-quality cordierite (iolite) localities, the Blue Arrow and Blue Bear occurrences, were recently discovered (in 2016 and 2021, respectively) in the mountainous Thor-Odin dome, southwest of Revelstoke in British Columbia, Canada (figure 1). They have so far produced small quantities of faceted stones (generally <2 ct, though the author has seen faceted windowed stones up to 4.76 ct from Blue Bear) and attractive cat's-eye cabochons (up to 12.02 ct, Blue Bear only). The present study seeks to gain new insights into: (1) the geological origin of the occurrences in a regional context and how they compare to the geology of other iolite deposits, (2) the nature of iolite mineralization at the Blue Arrow and Blue Bear localities, (3) the chemical composition and inclusions of Thor-Odin dome iolite, and (4) the nature of the inclusions responsible for chatoyancy.

See end of article for About the Author and Acknowledgments.
Gems & Gemology, Vol. 59, No. 3, pp. 340–355,
http://dx.doi.org/10.5741/GEMS.59.3.340

GEOLOGY OF IOLITE DEPOSITS

Deposits of iolite (gem-quality cordierite) occur in magnesium- and aluminum-rich metamorphic rocks formed at amphibolite to granulite facies conditions. Many iolite occurrences are found around the world, but relatively few have been comprehensively characterized from a geological (i.e., petrological, geochemical, and geochronological) perspective.

Significant deposits occur in the Bandarguha and Orabahala areas of Kalahandi District, India, where gem cordierite (with X_{Mg} = [Mg]/[Mg + Fe] = 0.82–0.88) is hosted in granulite facies cordierite-biotite schists and gneisses, which can contain the following accessory minerals: quartz, potassium feldspar, plagioclase, sillimanite, corundum, and orthopyroxene (Das and Mohanty, 2017).

Figure 1. Location map of the Thor-Odin dome near Revelstoke in British Columbia, Canada.

At the Geco copper-zinc mine—a volcanogenic massive sulfide deposit in Manitouwadge, Ontario, Canada—cordierite ($X_{Mg} \approx 0.80$; Fox and Yakymchuk, 2017) occurs in amphibolite facies (650° ± 30°C, 6 ± 1 kbar; Petersen, 1984) rocks consisting of a metamorphosed hydrothermally altered (calcium- and sodium-depleted) basalt and a cordierite-rich dike possibly representing an altered synvolcanic dike (Pan and Fleet, 1995). The typical cordierite host rock at the Geco mine is a cordierite-gedrite gneiss often containing quartz, sulfides (generally chalcopyrite), and garnet; but it is also found in quartz-rich segregations (Pan and Fleet, 1995; P. Belley, hand sample observations). The Geco mine is a significant iolite occurrence that did not produce much gem rough due to the exclusive focus on copper and zinc mining (B. Wilson, pers. comm., 2018). Wilson (2014) noted beautiful violet-blue faceted stones of 2.00 and 2.20 ct from the Geco deposit, as well as an overly dark 6.10 ct stone.

Gem cordierite occurs in magnesium- and aluminum-rich, orthoamphibole-bearing rocks (similar to those at the Geco mine but not associated with sulfide deposits) at Palmer Canyon in the Laramie Range of Wyoming, United States (Patel et al., 1999; Hausel, 2002), and in the Passmore area, Shuswap metamorphic complex, southern British Columbia (Simandl et al., 2000). In the Passmore area, the gem cordierite mineralization occurs in contact metasomatic deposits that are in contact with anthophyllite-rich granulite facies metamorphic rocks (1) between more siliceous intrusive or crosscutting rocks such as quartz veins and pegmatites and (2) in biotite-rich rocks (Simandl et al., 2000).

In Brief

- Violet-blue faceted iolite gems (usually <2 ct) and chatoyant cabochons (up to 12 ct) are described from occurrences in the Thor-Odin dome in British Columbia, Canada.
- The occurrences are hosted in gedrite-cordierite rocks consisting of altered mafic volcanic rocks metamorphosed under granulite facies conditions.
- Chatoyancy is caused by an abundance of acicular fluid inclusions parallel to the *a*-axis of cordierite.
- Mineral inclusions include biotite, muscovite, zircon, xenotime-(Y), hematite, and apatite.

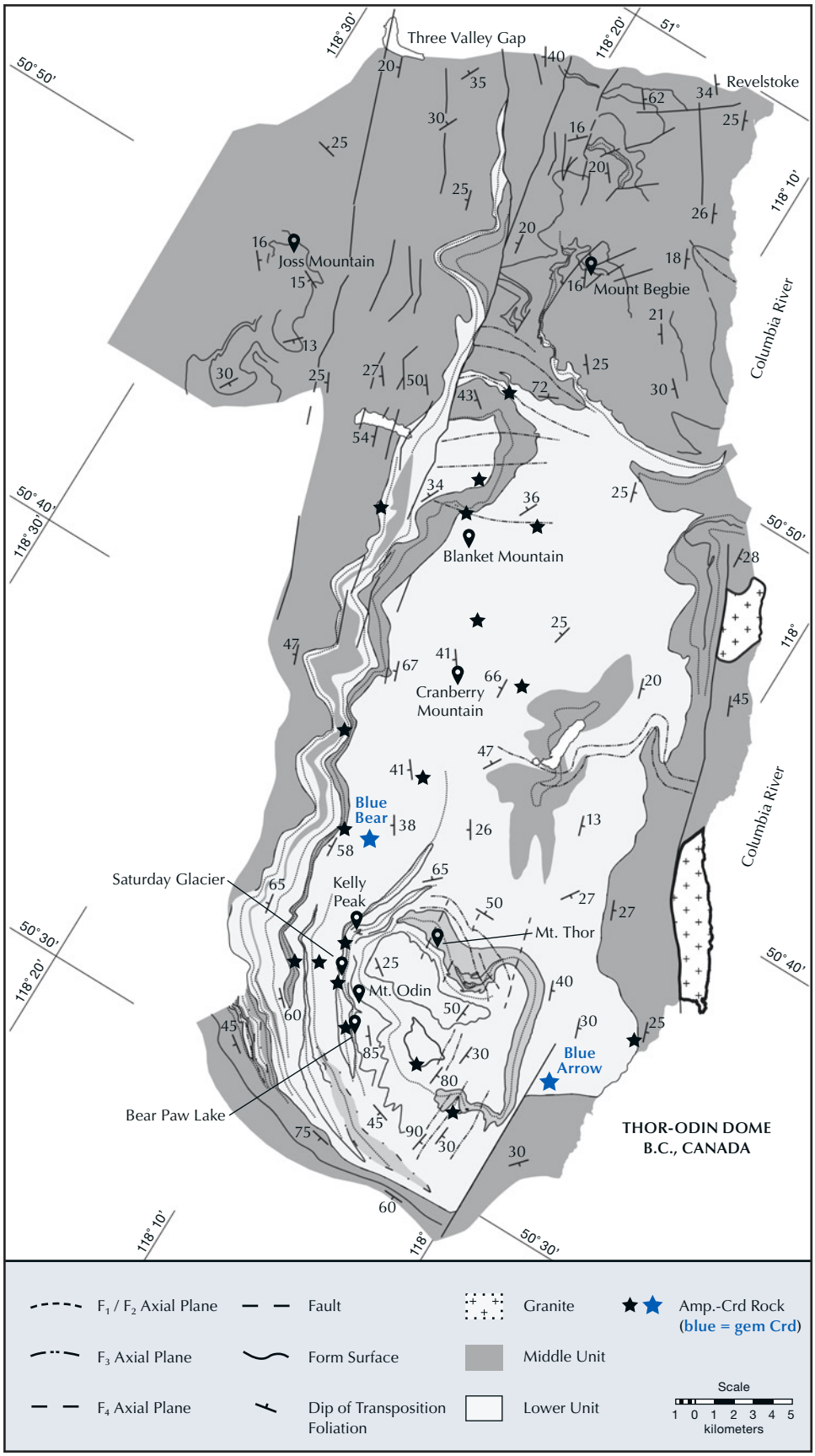

Figure 2. Simplified geological map of the Thor-Odin dome showing the location of known cordierite-orthoamphibole rock occurrences, including the Blue Bear and Blue Arrow gem cordierite occurrences. Modified after Goergen and Whitney (2012), reproduced with permission from SNCSC (© 2011 Springer-Verlag. Contrib. Mineral. Petrol., *Volume 163).*

Figure 3. View of Arrow Lake from the talus at the Blue Arrow iolite occurrence. Photo by D.J. Lake.

HISTORY AND ACCESSIBILITY

While gem-quality cordierite was not discovered in the Thor-Odin dome until 2016, it has been known to occur in a nearby geological terrane, the Valhalla metamorphic core complex, since the 1990s. In 1998, exploration near Passmore in British Columbia (within the Valhalla complex) by Anglo Swiss Resources Inc. generated about 50 kg of high-grade rough iolite, which yielded less than 100 carats of finished gems (Wight, 1999; Laird, 2002). Passmore produced both "bright and lively [faceted stones] with a blue-violet color and excellent clarity" up to 0.6 ct (Simandl et al., 2000; Wilson, 2014) and cabochons up to 1.5 ct (Simandl et al., 2000), some of which display asterism (Wight, 1999).

Cordierite-orthoamphibole rocks have been documented from 20 localities within the Thor-Odin dome (Duncan, 1984; Norlander et al., 2002; Hinchey and Carr, 2007; Goergen and Whitney, 2012; see figure 2 of the present study), although as many as 30 cordierite localities are known to local prospectors (H. Hyder, pers. comm., 2022). In 2016, prospector Herb Hyder discovered the Blue Arrow iolite occurrence in talus overlooking Arrow Lake (figures 3 and 4), and in 2021 he discovered the Blue Bear iolite occurrence (currently under claim) in outcrop at high elevation (approximately 2000–2400 m above mean sea level) 1–2 km south of Dickinson Lake and west of Horsefly

Figure 4. Aerial image of the Blue Arrow iolite occurrence, which consists of cordierite-bearing boulders near the forest's edge. Photo by Philippe Belley.

Figure 5. Cordierite-gedrite-biotite-garnet boulder at the Blue Arrow occurrence. Photo by D.J. Lake.

Peak. The iolite occurrences are located on relatively steep slopes (see figures 4 and 5) and very difficult terrain. Both localities can be accessed by hiking from the nearest logging road, but the Blue Bear claim is most easily accessed via helicopter since it is a substantially difficult hike with considerable elevation gain. Due to its high elevation, the Blue Bear locality is covered by snow except for one or two summer months (generally in August). At the time of this writing, collecting is not permitted at either claim and the mineral exploration rights are privately owned.

GEOLOGICAL SETTING

Regional Geology. The study area is located in the Thor-Odin dome, which forms the southern portion of the Monashee complex—the deepest structural level of the Shuswap metamorphic core complex in the Omineca Belt of southern British Columbia. The Thor-Odin dome consists of Paleoproterozoic basement rocks (primarily migmatitic paragneiss and orthogneiss) and Paleoproterozoic to possibly Paleozoic supracrustal metasedimentary cover rocks, both of which experienced high-grade (granulite facies; 750°–800°C) metamorphism concomitant with decompression from above 8–10 kbar to below 5 kbar during exhumation, resulting in anatexis.[1] Partial melting occurred approximately 60 to 54 Ma, possibly continuing until 51 Ma (Vanderhaeghe et al., 1999; Norlander et al., 2002; Hinchey et al., 2006).

Cordierite-bearing gedrite-rich gneisses occur at regional scale and exclusively within the paragneiss in the basement sequence of the Thor-Odin dome (the "Lower Unit," also containing orthogneiss), which consists mostly of cordierite-biotite-quartz-feldspar gneiss, migmatitic garnet-sillimanite-quartz-feldspar gneiss, with local calc-silicate rock, marble, and quartzite (Norlander et al., 2002; Hinchey and Carr, 2007). The only previously reported gem materials found within the basement sequence of the Thor-Odin dome are large crystals, averaging 5 cm across and up to 10 cm, of opaque to rarely translucent, internally fractured, zoned dark blue and dark grayish brown corundum (the latter being star sapphire). These corundum are reported from a single locality, where they occur within restite boudins[2] in leucosome[3] of metapelitic[4] origin, having formed as a result of muscovite breakdown and partial melting along the prograde *P-T* path at or before 60 Ma, near peak granulite facies metamorphic conditions (Abdale et al., 2023).

[1]Anatexis: The partial melting of crustal rocks.

[2]Restite: Residual material left at the site of partial melting, such as in a migmatite. Boudin: A sausage-like pinch-and-swell structure formed by extension of originally continuous rock layers.

[3]Leucosome: The light-colored portion of migmatite, which is a product of partial melting.

[4]Metapelitic: Sourced from or related to metapelites (metamorphosed pelitic rock such as shale or mudstone).

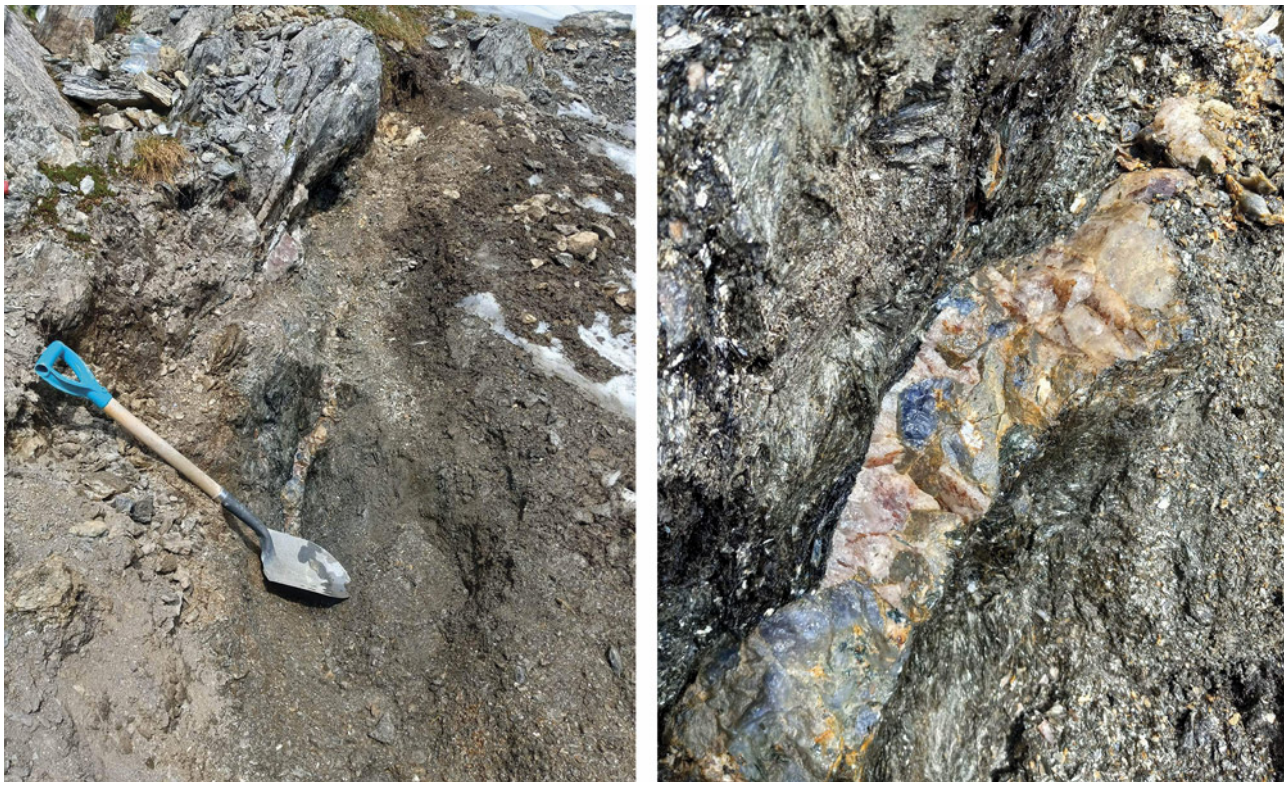

Figure 6. Cordierite-bearing quartz vein (approximately 10 cm wide) cutting gedrite-cordierite rocks at the Blue Bear occurrence. Photos by Herb Hyder.

Gedrite-Cordierite Rocks. Gedrite-cordierite-rich rocks are widespread in the Thor-Odin dome (Goergen and Whitney, 2012; figure 2), where they occur as elongated boudins up to 500 m in length (Norlander et al., 2002). Two variants of this rock are known: one containing almandine-pyrope garnet porphyroblasts[5] averaging 5 cm across and another containing sapphirine (Norlander et al., 2002). The mineral assemblage is variable but always includes gedrite (2–25 cm long and the most abundant mineral, comprising >30–40% of the rock), cordierite (usually as interstitial masses between gedrite blades), and biotite (phlogopite, with $X_{Mg} \approx 0.8$). Other minerals observed in rock samples include garnet (up to 15 cm in diameter, where present), quartz, sillimanite, kyanite, sapphirine, corundum, and/or staurolite. Minerals occurring in trace amounts include ilmenite, rutile, apatite, magnesium-rich hercynite, plagioclase, and monazite (Norlander et al., 2002; Hinchey and Carr, 2007).

Gedrite-cordierite rocks in the Thor-Odin dome have a distinctive bulk chemical composition that is characterized by a relative depletion in alkali elements, calcium, and low field strength minor and trace elements, along with enrichment in aluminum, magnesium, iron, and high field strength trace elements. The rocks are interpreted to consist of Paleoproterozoic mafic volcanic rocks that underwent hydrothermal alteration, likely by seawater, and were subsequently metamorphosed in the Cordilleran orogeny (Hinchey and Carr, 2007). Hinchey and Carr's genetic model is based on a combination of whole rock major and trace element chemical composition (including rare earth element patterns) and neodymium isotopic systematics.

DESCRIPTION OF THE IOLITE OCCURRENCES

Blue Arrow Occurrence. Violet-blue, strongly pleochroic cordierite occurs in approximately half a dozen large boulders (up to 2.5 m across; figure 5) on the northern side of an east-facing talus overlooking Arrow Lake. The talus measures approximately 1.0 by 0.7 km. The cordierite host rock consists of very coarse-grained (average 1–4 cm grain size) gedrite-rich gneiss consisting of the following minerals in rock-forming amounts (highest to lowest abundance): gedrite, anhedral cordierite (often occurring in the in-

[5]Porphyroblast: In metamorphic rocks, a larger mineral grain that occurs in a groundmass composed of relatively smaller grains.

Figure 7. Large, euhedral cordierite crystal containing facetable and cabochon-quality sections. Note the deformation-induced fractures visible on prism faces in the photo on the right. The crystal measures 11.3 cm wide. Photos by Philippe Belley.

terstices of gedrite crystals), biotite, subhedral garnet porphyroblasts, and quartz. The cordierite occurs as translucent to transparent, dark blue masses up to approximately 8 cm. Cordierite porphyroblasts are highly fractured, with facetable gem rough that could produce finished stones 0.5 ct or larger coming only from small zones in a minority of the porphyroblasts.

Figure 8. Freshly recovered rough chatoyant cordierite from the Thor-Odin dome. Note the lighter color and abundant acicular inclusions in the smaller fragments. Photo by Herb Hyder.

Blue Bear Occurrence. Violet-blue, strongly pleochroic cordierite occurs as subhedral to euhedral porphyroblasts in gedrite-cordierite-biotite-(±quartz) gneiss, and in quartz-cordierite veins (<10 cm thick) cutting these rocks (figure 6). The geographic extent of cordierite mineralization is currently unknown, and exploration in this steep, high-elevation terrain is ongoing. Cordierite crystals shown to the author averaged 5 cm across, and the largest crystal measured 11.3 cm long (figure 7). Cordierite crystals vary from anhedral to euhedral. Most large euhedral crystals are enveloped by biotite. The cordierite is highly fractured, translucent to transparent, and locally contains zones suitable for production of polished gemstones. Higher-quality material is shown in figures 7 and 8, and representative cordierite, quartz, and gedrite are shown in figure 9. In some crystals (in part or in whole), the cordierite is moderately to heavily included by parallel acicular inclusions. Cordierite

Figure 9. Representative cordierite (top left), quartz with cordierite (top right), and gedrite (bottom) from Blue Bear. As is common in metamorphic gem deposits, only a small fraction of the mineral occurs in gem quality. The gedrite fragment measures 65 mm across. Photo by Philippe Belley.

Figure 10. Cordierite-bearing biotite-quartzofeldspathic gneiss near the Blue Bear occurrence. This lithology is not known to contain gem-quality cordierite. Photo by Herb Hyder.

that is not of gem quality occurs in biotite-rich quartzofeldspathic gneiss in the area (figure 10).

MATERIALS AND METHODS

Samples. The cordierite samples examined consist of ~4 kg of unprocessed rough from the Blue Bear claim and ~100 g from the Blue Arrow claim, both provided by Herb Hyder, an independent prospector. A 1.15 ct faceted stone from Blue Arrow was acquired from local gem cutter Russell Crick, who visited the locality. Additional samples were recovered by D.J. Lake and the author on a site visit to the Blue Arrow locality; however, none of this material was of sufficient quality to facet into stones larger than 0.3 ct. Rough samples provided by Herb Hyder were processed by the author, and the highest-quality material was sent for cutting and polishing, resulting in the production of faceted stones. The largest stones described in this study are a 1.15 ct faceted stone from Blue Arrow (figure 11), a 1.24 ct faceted stone from Blue Bear (figure 12), and chatoyant cabochons up to 12.02 ct from Blue Bear (figure 13). The largest faceted gemstones reported to the author from each locality consist of a very dark, included 2.0 ct stone

Figure 11. Rough and cut iolite from the Blue Arrow occurrence. The faceted stones weigh up to 1.15 ct, with the two matching triangular stones weighing approximately 0.8 ct in total. Photo by Michael Bainbridge.

Figure 12. Rough and cut iolite from Blue Bear. From left to right, the faceted stones weigh 1.24, 0.48, 0.48, and 0.88 ct. Photo by Philippe Belley.

from Blue Arrow and a dark 4.46 ct windowed stone from Blue Bear. The specific gravity of the largest stone of each variety and locality was obtained hydrostatically, and the refractive indices of Blue Arrow and Blue Bear faceted iolites were measured with a Kruss professional refractometer with a monochromatic sodium light source.

Figure 13. Chatoyant iolite cabochons from Blue Bear. The three largest stones weigh 12.02, 8.52, and 7.24 ct. The remainder weigh between 0.96 to 3.71 ct. Note the variation in color, where lighter-colored cabochons have a higher concentration of acicular inclusions. Photo by Philippe Belley.

Sample Examination and Preparation. Rock samples were examined to characterize the mineralogy and mineral habits. Selected samples of individual minerals and rock fragments were polished into 25 mm sections, carbon coated (coating thickness 5–10 nm), and examined using Memorial University of Newfoundland's FEI Quanta 650 SEG scanning electron microscope (SEM). The SEM was equipped with two Bruker XFlash 5030 energy-dispersive X-ray spectrometers (EDS) for mineral identification, with a 30 s X-ray acquisition time, and a secondary electron detector (SE) for acicular inclusion examination, using an operating voltage of 25 kV. Gem-quality rough was cut and polished (faceted stones and cabochons) and examined using a binocular gemological microscope.

Chemical Analysis. Five spots, each spread out over a ~1 cm^2 area, were analyzed each on two representative gem-quality pieces from each locality. Chemical compositions of cordierite were obtained with a JEOL JXA-8230 electron microprobe at Memorial University of Newfoundland. Operating voltage was 15 kV with 20 nA beam current and 3 µm beam diameter. Count times were 40 s (except 20 s for sodium, potassium, and silicon, and 30 s for calcium) with background collection times equal to half of the count times. The following standards were used: orthoclase (potassium), albite (sodium), diopside (calcium, magnesium, and silicon), almandine (aluminum and iron), rhodonite (manganese), and sphalerite (zinc). Matrix correction calculations were done using the eponymous "PAP" method (Pouchou and Pichoir, 1985).

RESULTS

Properties of Rough. More than 90% of the cordierite at both Thor-Odin localities is not of gem quality, owing mostly to extensive post-formation fracturing, a common feature in metamorphic gem deposits, and less commonly owing to an abundance of primary mineral or secondary fluid inclusions. Gem-quality cordierite is present only in portions of single crystals, with a fairly random distribution, and the best gem rough generally comes from the largest crystals. The cordierite crystal in figure 7 illustrates deformation-controlled fracturing where the dominant fractures show some degree of preferential orientation. This crystal also contains facetable rough in an area where fracturing is less pervasive.

At the Blue Bear locality, cordierite contains a variable degree of parallel acicular inclusions ranging from nearly absent (not visible in a hand sample) to extremely abundant, often varying from both extremes within a single crystal. The portions richest in these inclusions are light slightly grayish blue and show strong chatoyancy (see the smaller rough fragments in figure 8).

Standard Gemological Properties. Cordierite from both localities is very strongly pleochroic, showing three different colors in different orientations: dark saturated violet-blue, medium-light blue-gray, and light gray-yellow with low color saturation. Specific gravity values for the three largest iolite gemstones from each locality and variety were 2.61 (Blue Arrow, faceted), 2.60 (Blue Bear, faceted), and 2.59 (Blue Bear, chatoyant cabochon). Refractive indices were measured on one faceted stone from each locality. These refractive index values were 1.610–1.620 for Blue Arrow and 1.538–1.548 for Blue Bear.

Properties of Cut Stones. *Faceted Stones*. When correctly oriented to maximize the violet-blue color, faceted iolite stones show a beautiful, saturated violet-blue color that is of medium lightness in stones in the half-carat range, while dark in stones of approximately 1 ct (figures 11 and 12). In similarly sized examples, faceted gems from Blue Arrow are darker than those from Blue Bear.

Cabochons. Cat's-eye cabochon samples were from the Blue Bear locality only, and all of this material consists of translucent cordierite containing abundant parallel acicular inclusions. They were cut with the base perpendicular to the grayish yellow axis of the cordierite. The stones are therefore grayish yellow if backlit through the base. They display a distinct chatoyant band perpendicular to the long axis of the acicular inclusions (described below) that is visible even in diffuse indoor and outdoor lighting conditions. The cabochons occur in two color varieties: dark grayish blue-violet with a light gray cat's-eye, and light gray-blue with a very light gray cat's-eye (see figure 13). Darker cabochons contain a lesser amount of acicular inclusions and are more transparent than the lighter, more heavily included cabochons. The strength and sharpness of the cat's-eye is identical in the dark and light varieties.

Chemical Composition. Gem cordierite from the Thor-Odin dome, which was analyzed using electron probe microanalysis (EPMA), is strongly cordierite-dominant, with only a minor component (<20 mol.%) of sekaninaite, the Fe^{2+} end member of the cordierite-sekaninaite solid solution series. The Blue Bear cordierite sample analyzed has a higher X_{Mg} value than the sample from Blue Arrow, with values of 0.90 and 0.81, respectively (table 1). The higher iron concentration in Blue Arrow cordierite correlates with a darker color in larger stones (compare figures 11 and 12). The analyzed sample of Blue Bear cordierite is richer in manganese, zinc, and sodium than the Blue Arrow cordierite sample.

Mineral Associations and Inclusions. At both localities, inclusions observed in rough crystals include millimeter- to centimeter-scale grains and clusters of biotite (likely iron-rich phlogopite), gedrite, and quartz. These minerals form a stable assemblage with cordierite in the gneiss. Muscovite occurs locally in Blue Bear gneiss and, based on grain boundary relationships, appears to form a stable assemblage with gedrite and cordierite. A 1.5 mm yellow hexagonal prismatic apatite crystal was observed in cordierite from Blue Bear.

Rehealed fractures, indicated by the presence of secondary fluid inclusions along subconchoidal fractures, are common in iolite from the two localities. Relatively few gem-quality samples were available from Blue Arrow, so the following inclusion descriptions focus on Blue Bear iolite, where a combination of optical microscope and SEM-EDS was used to examine faceted stones and flat-polished samples. Some subconchoidal fractures in iolite are filled with a translucent white unidentified hydrous aluminosilicate phase containing equal molar proportions of alu-

TABLE 1. Average chemical composition (in wt.%), measured with EPMA, of two representative samples of gem cordierite (iolite) from the Thor-Odin dome, Canada.

	Blue Arrow (5 analyses)	Standard deviation	Blue Bear (5 analyses)	Standard deviation	Detection limit
SiO_2	49.39	0.13	49.55	0.18	0.01
TiO_2	bdl[a]	—	bdl	—	0.01
Al_2O_3	33.79	0.08	33.93	0.06	0.01
FeO	4.60	0.12	2.35	0.06	0.01
MnO	0.03	0.01	0.07	0.01	0.01
ZnO	0.02	0.02	0.03	0.01	0.01
MgO	10.96	0.04	12.17	0.13	0.01
CaO	0.02	<0.01	0.01	<0.01	0.01
Na_2O	0.26	0.02	0.47	0.01	0.01
K_2O	0.01	<0.01	0.01	<0.01	0.01
Total[b]	98.55	0.41	98.13	0.18	
X_{Mg}	0.81		0.90		

[a]*bdl = below detection limit*
[b]*The slightly low total weight % indicates the presence of volatiles in structural channels (i.e., H_2O and CO_2; Vry et al., 1990) in the cordierite.*

minum and silicon, and 0.5–2.2 mol.% of iron, magnesium, calcium, and potassium (figure 14). This mineral may be impure halloysite, a common alteration mineral of cordierite (Layman, 1963). The most common inclusions observed in Blue Bear iolite are fluid inclusions (both primary blocky fluid inclusions and secondary subequant rounded inclusions along rehealed subconchoidal fractures), acicular inclusions (causing chatoyancy when abundant; described below), euhedral platy brown iron-rich phlogopite (figure 15), tabular to equant white muscovite (commonly altered to hydrous aluminosilicates containing aluminum and silicon in similar molar abundances, and possibly consisting of clay minerals; figures 16 and 17), zircon (figure 17), anhedral uranium-bearing xenotime-(Y) (figure 18), and platy hematite (≤20 µm crystals). Zircon is fairly common in cordierite as groupings of closely

Figure 14. Unidentified aluminosilicate (possibly halloysite or another clay mineral) filling a fracture in cordierite from Blue Bear. Backscattered electron SEM image; field of view 650 µm.

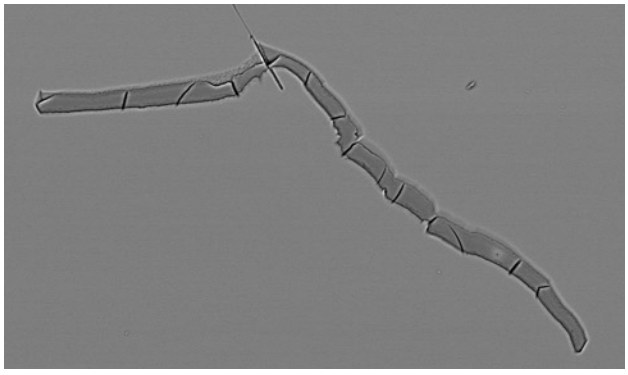

Figure 15. Light brown iron-rich phlogopite, a white unidentified mineral (possibly muscovite), and acicular fluid inclusions in a faceted iolite from Blue Bear. Photomicrograph by Philippe Belley; field of view 2.4 mm.

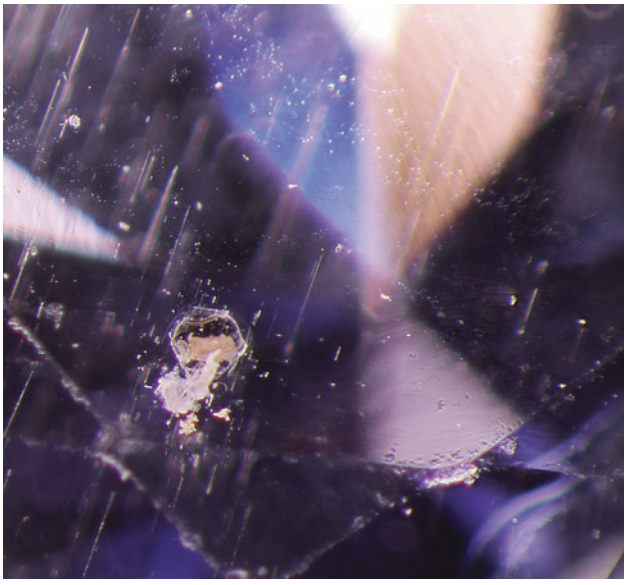

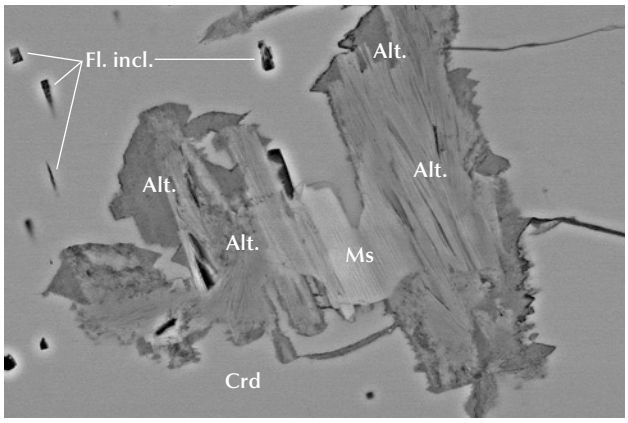

Figure 16. Inclusion of primary muscovite (Ms), which is partly altered to unidentified aluminosilicates (Alt.), and blocky fluid inclusions (Fl. incl.) in cordierite (Crd) from Blue Bear. Note the fractures leading to the partly altered muscovite. Backscattered electron SEM image; field of view 165 µm.

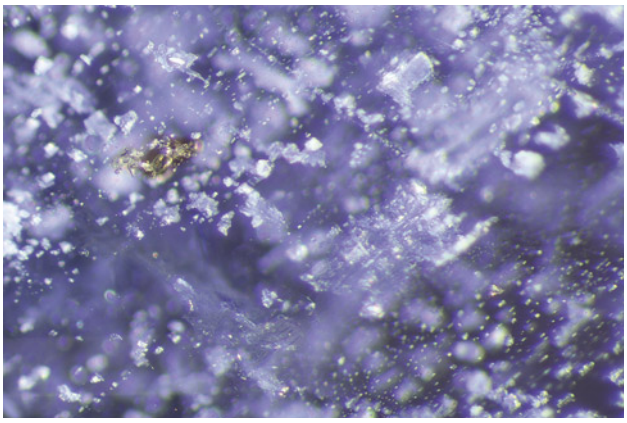

Figure 17. Densely included cordierite from Blue Bear containing a grouping of zircon crystals with yellowish radiohalos, white muscovite, and small colorless fluid inclusions. The fluid inclusions proximal to the zircon group appear primary, while those in the lower right corner occur on a rehealed fracture and are thus secondary. Photomicrograph by Philippe Belley; field of view 1.88 mm.

spaced, euhedral to subhedral, light-colored or colorless prismatic crystals associated with biotite (figures 17 and 19). The zircons appear yellowish due to the presence of radiation damage in cordierite proximal to these grains, making their true color difficult to assess. Partly to wholly altered muscovite and less commonly biotite, which are replaced by hydrous aluminosilicates, occur in close proximity to fluid inclusions that indicate the presence of rehealed fractures. Unaltered mica-species grains occur in areas not traversed by such features. This hydrous aluminosilicate alteration rarely contains very small (approximately 5–10 µm) inclusions of pyrrhotite or barite.

Chatoyancy-Causing Inclusions. Acicular inclusions are common in cordierite from the Blue Bear claim. They are less abundant in facetable material (figure 15) and more abundant (to the point of decreasing transparency) in chatoyant material. The inclusions are straight and oriented parallel to the direction of greatest light absorption in cordierite (the dark violet-blue axis). Even in single cabochons, these inclusions vary in concentration, forming bands of slightly higher or lower inclusion density (figure 20, left). The inclusions vary in length and, to a lesser degree, diameter (figures 15 and 20, right). A polished section of chatoyant cordierite, cut at an oblique angle to the

Figure 18. Zircon (Zrn) and xenotime-(Y) (Xtm-Y) inclusions in gem cordierite (Crd) from Blue Bear. Backscattered electron SEM image; field of view 150 µm.

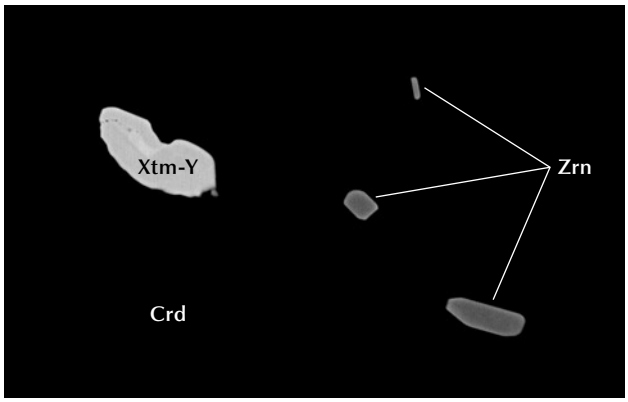

Figure 19. Zircon (white) associated with biotite (Bt; iron-rich phlogopite) in gem-quality cordierite from Blue Bear. Backscattered electron SEM image; field of view 120 µm.

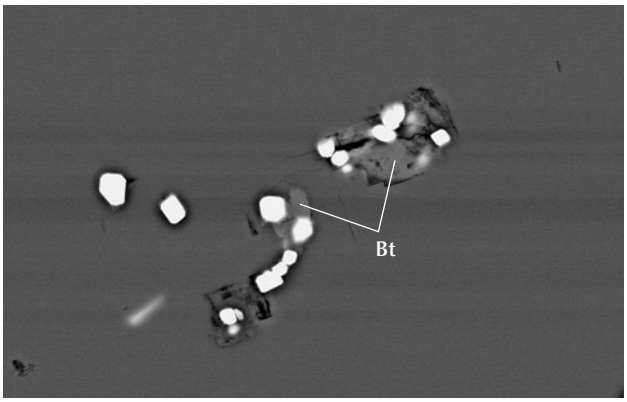

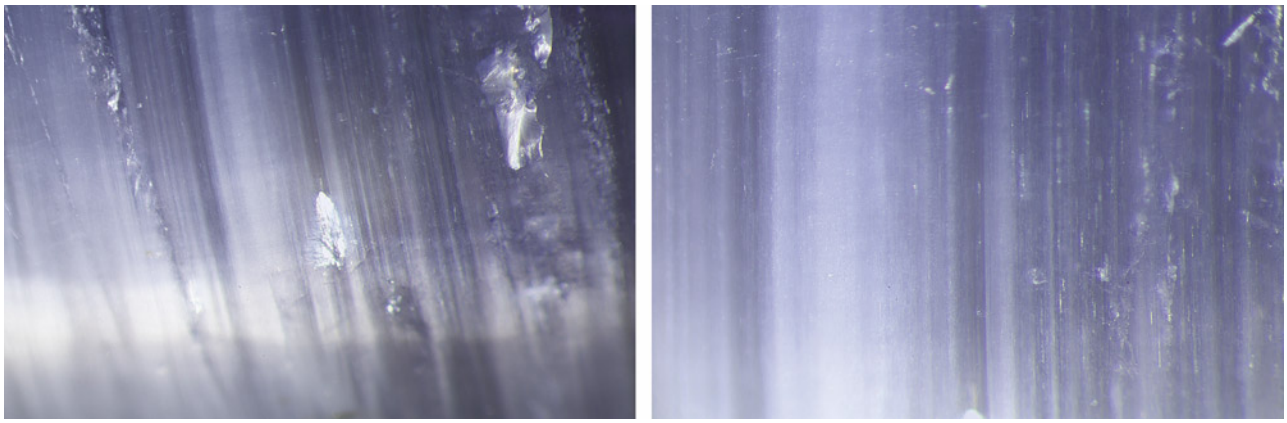

Figure 20. Magnified view of the 12.02 ct cat's-eye iolite cabochon from Blue Bear. Note the variable inclusion density within the stone and the variable length of the acicular inclusions. Photomicrographs by Philippe Belley; fields of view 5.57 mm (left) and 2.81 mm (right).

acicular inclusions, was examined using SEM in secondary electron mode. This revealed that the exposed inclusions (≤2 µm in diameter) are hollow and thus do not consist of solid inclusions (figure 21).

DISCUSSION

Deposit Geology. The iolite occurrences in the Thor-Odin dome of British Columbia bear many resemblances to other deposits and occurrences worldwide: They all occur within, or contiguous to, upper amphibolite to granulite facies magnesium- and aluminum-rich metamorphic rocks. Cordierite-bearing rocks in the Thor-Odin dome, like those in most other localities, are associated with rock-forming amounts of orthoamphibole (gedrite, though some localities contain anthophyllite). These rocks differ from those reported in the Bandarguha and Orabahala areas of India, which are principally composed of cordierite and biotite (Das and Mohanty, 2017). Iolite localities that have been subject to more extensive petrological and geochemical research, such as Thor-Odin (Hinchey and Carr, 2007) and the Geco mine (Pan and Fleet, 1995) consist of alkali- and calcium-depleted, magnesium- and aluminum-enriched metamorphic rocks with hydrothermally altered mafic volcanic (i.e., basaltic) protoliths.

Gem cordierite mineralization at Blue Arrow is similar in habit to another locality in the Thor-Odin dome, where cordierite occurs as anhedral crystals in the interstices of large gedrite crystals (Hinchey and Carr, 2007). While the Blue Bear locality occurs in a comparable geological setting—cordierite-gedrite rocks—the nature of the mineralization differs from that at Blue Arrow: Cordierite crystals are anhedral

Figure 21. Secondary electron images of a chatoyant Blue Bear iolite that was polished to crosscut the acicular inclusions. The images clearly show that the elongated cylindrical inclusions consist of fluid inclusions and are not filled with any solid material. Fields of view 200 µm (left) and 15 µm (right).

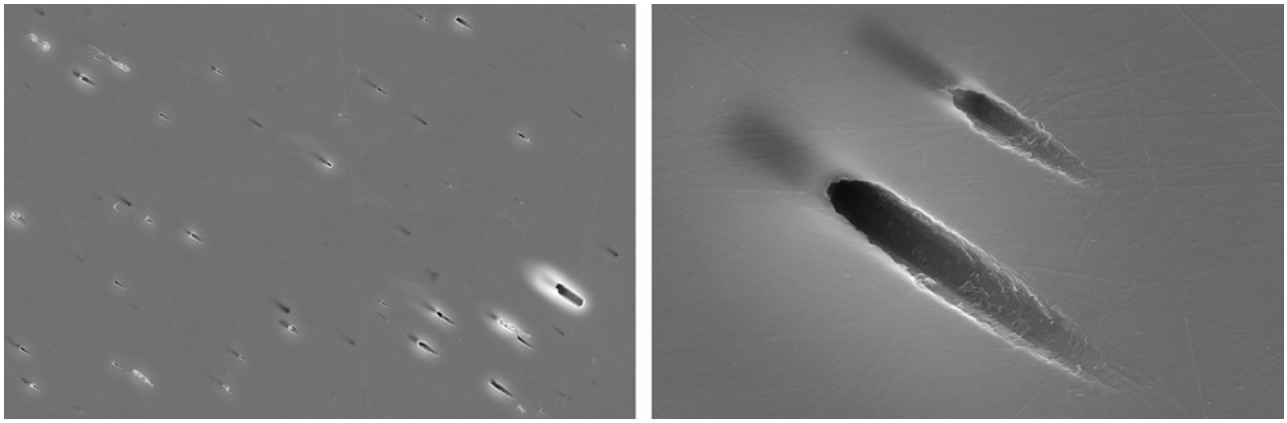

TABLE 2. Summary of inclusions occurring in gem-quality cordierite.

	Thor-Odin, Canada (present study)	India (Kammerling and Koivula, 1991; Das and Mohanty, 2017; Muyal and Mattlin, 2019)	Madagascar (Graziani and Guidi, 1978)	Wyoming, United States (Hausel, 2003)
Biotite	x	x		x
Hematite	x	x		
Rutile		x	x	
Zircon	x	x		
Apatite	x		x	
Quartz		x		
Muscovite	x			
Orthopyroxene		x		
Xenotime-(Y)	x			
Monazite		x		
Dolomite			x	
Pyrite		x		
White acicular inclusions	x	x		x

to euhedral and occur both within the gedrite-rich rock (where they are sometimes enveloped by a layer of biotite) and in quartz veins cutting this rock. The occurrence of cordierite within crosscutting quartz segregations is reported from the Thor-Odin dome for the first time in the present study, but similar mineralization is known at the nearby localities in Passmore, British Columbia (Simandl et al., 2000), and at the Geco mine in Ontario (Pan and Fleet, 1995).

Potential for Future Production. Beautiful faceted stones, generally smaller than 2 ct, have been produced in very small quantities from the Blue Arrow and Blue Bear localities, and attractive cat's-eye cabochons to ~12 ct have come from Blue Bear. The original bedrock source for the iolite-bearing boulders at Blue Arrow has yet to be discovered. Iolite was only discovered recently at Blue Bear, and the area has been minimally explored. Further exploration at both sites has the potential to yield new iolite-producing zones.

Extremely coarse-grained cordierite-bearing metamorphic rocks are widespread throughout the Thor-Odin dome (Duncan, 1984; Norlander et al., 2002; Hinchey and Carr, 2007; Goergen and Whitney, 2012; present study). Potential targets for gem cordierite exploration are therefore numerous, and prospectors may discover new iolite deposits in the future. Exploration in this region is not without its challenges. The rugged terrain and remoteness of most of the metamorphic dome make exploration difficult, time-consuming, costly, and sometimes dangerous. These factors would also present challenges to gem mining, should a significant deposit be discovered.

Inclusions. Inclusions reported in gem-quality cordierite include a variety of silicates, oxides, sulfides, and phosphates (table 2), with the most common being hematite and biotite. Hematite occurs in the "bloodshot" iolite variety (India and Sri Lanka; Kammerling and Koivula, 1991; Muyal and Mattlin, 2019) as oriented crystals causing asterism (Bui et al., 2022) or as small isolated inclusions (Thor-Odin dome; present study). Iron-rich phlogopite (biotite) inclusions are reported from Wyoming (Hausel, 2003), India (Das and Mohanty, 2017), and Thor-Odin (present study). Rutile is reported in iolite from Madagascar (Graziani and Guidi, 2018) and India (Das and Mohanty, 2017) but was not observed in Thor-Odin samples. Quartz was observed as inclusions in iolite from India (Das and Mohanty, 2017); at the Thor-Odin dome, quartz was found as large inclusions on the edge of large fractured crystals but was absent in rough and faceted stones. Zircon inclusions were noted from both India (Das and Mohanty, 2017) and Thor-Odin. In the present study, zircon generally occurred in small groupings of numerous crystals associated with iron-rich phlogopite inclusions. Apatite inclusions have only been reported from Madagascar (hydroxyl end member; Graziani and Guidi, 1978) and from Thor-Odin (present study). Mineral inclusions reported only from a single locality are the following: dolomite (Madagascar; Graziani

and Guidi, 1978); monazite, orthopyroxene, quartz, and pyrite (India; Das and Mohanty, 2017); and muscovite, xenotime-(Y), and secondary alteration products from mica inclusion breakdown, which include an unidentified hydrous aluminosilicate (possibly clay minerals) and rare pyrrhotite and barite (Thor-Odin; present study). Muscovite is commonly associated with cordierite, where it is a retrograde metamorphic alteration product of the latter (e.g., Layman, 1963). Muscovite inclusions—which, based on grain boundary relationships, form a stable assemblage with gem cordierite at the Blue Bear occurrence—are to the author's knowledge, reported here as primary inclusions for the first time.

Primary blocky fluid inclusions and secondary fluid inclusions, the latter occurring on rehealed subconchoidal fractures, are common in Thor-Odin iolite. While they have not been reported from other iolite localities worldwide, such inclusions are likely to occur at most if not all of these localities due to the prevalence of similar fluid inclusions in most metamorphic gem minerals.

White acicular inclusions in cordierite, described as possibly being sillimanite, are reported by Hausel (2003) in gemstones from Wyoming. Parallel acicular inclusions are also reported from an iolite cabochon of Indian origin, where these inclusions are the cause of chatoyancy (Kammerling and Koivula, 1991). Acicular inclusions resembling those from the Indian iolite cabochon occur abundantly in Blue Bear cordierite. These are discussed next.

Cause of Chatoyancy. Chatoyancy in iolite is rare, caused by fine acicular inclusions (Kammerling and Koivula, 1991). In the cat's-eye iolites from Blue Bear, the orientation of the fine acicular inclusions is parallel to the direction of strongest visible light absorption (dark violet-blue) and perpendicular to the other pleochroic colors (light grayish yellow and light blue gray). In iron-bearing cordierite, the strongest absorption occurs parallel to the direction of highest refractive index (γ), which is the Z vibration axis, where light is absorbed by intervalence charge-transfer (IVCT) between Fe^{2+} in the octahedral site and Fe^{3+} at the T_1 tetrahedral site of the cordierite structure—and to a much greater extent than absorption by IVCT occurring along the Y axis (Goldman et al., 1977). The γ-axis, along which visible light is most strongly absorbed, is oriented parallel to the *a*-axis of cordierite (see figure 4 of Fritsch and Rossman, 1988). The Blue Bear chatoyancy-causing inclusions occur in the same orientation as similar colorless acicular inclusions previously reported in chatoyant iolite from South India (Kammerling and Koivula, 1991), as well as colored acicular hematite inclusions causing chatoyancy in iolite cabochons from an unknown country of origin (Bui et al., 2022). The nature and composition of the colorless acicular inclusions reported by Kammerling and Koivula (1991) were not identified. In the present study, the secondary electron images of a chatoyant cordierite polished at an oblique angle to the long axis of the acicular inclusions reveal that they consist of "empty" depressions. Thus, the inclusions in Blue Bear chatoyant iolite, and likely that in iolite reported by Kammerling and Koivula (1991), consist of fluid inclusions.

CONCLUSIONS

The Blue Arrow and Blue Bear gem cordierite claims at the Thor-Odin dome near Revelstoke in British Columbia, Canada, are two new examples of iolite occurrences hosted in hydrothermally altered mafic rocks metamorphosed at upper amphibolite to granulite facies. At these occurrences, cordierite (X_{Mg} = 0.81–0.90) occurs in association with gedrite, iron-rich phlogopite (biotite), quartz, almandine-pyrope garnet, and various accessory and trace minerals. Test sampling on the claims yielded strongly pleochroic, gem-quality rough that produced dark violet-blue faceted stones generally smaller than 2 ct (both localities), as well as light grayish blue to dark slightly grayish violet-blue chatoyant cabochons up to 12.02 ct (Blue Bear only). Coarse-grained cordierite-rich rocks are widespread in the Thor-Odin dome, which indicates good potential for future iolite discoveries in the region.

Primary mineral inclusions in gem-quality Blue Bear cordierite include iron-rich phlogopite, muscovite, zircon, xenotime-(Y), hematite, and apatite. Muscovite and xenotime-(Y) are, to the author's knowledge, the first reported examples of these minerals as primary inclusions in iolite. Where cordierite is traversed by rehealed fractures, mica inclusions are altered to unidentified hydrous aluminosilicates rarely containing trace pyrrhotite or barite.

Three types of fluid inclusions occur in Thor-Odin iolite: (1) primary blocky fluid inclusions; (2) primary acicular fluid inclusions oriented parallel to the *a*-axis of cordierite, which cause chatoyancy when present in high concentrations (at Blue Bear only); and (3) secondary, generally subequant, fluid inclusions occurring along rehealed subconchoidal fractures.

ABOUT THE AUTHOR

Dr. Philippe Belley manages the Gem Science Research Group in his role as assistant professor in the Department of Earth Sciences, Memorial University of Newfoundland in St. John's, Canada.

ACKNOWLEDGMENTS

The author thanks Herb Hyder for providing samples, information, and photographs; D.J. Lake for help in the field and for providing additional field photographs; Dylan Goudie for support with SEM-EDS and sample preparation; and Dr. Wanda Aylward for support with EPMA. The manuscript was improved thanks to detailed comments from three anonymous reviewers.

REFERENCES

Abdale L., Belley P.M., Groat L.A., Cempírek J., Škoda R., Wall C. (2023) Corundum genesis at the Blue Jay Sapphire occurrence (British Columbia, Canada) as a record of metamorphism and partial melting in the Monashee complex. *Lithos*, Vol. 438-439, article no. 106992, http://dx.doi.org/10.1016/j.lithos.2022.106992

Bui T.N., Delaunay A., Hennebois U., Steinbach M.P., Gauthier J.-P. (2022) Origin of asterism and chatoyancy in rare six-rayed star iolite. *Journal of Gemmology*, Vol. 37, No. 7, pp. 670–672.

Das S.K., Mohanty J.K. (2017) Characteristics of cordierite (iolite) of Bandarguha-Orabahala Area, Kalahandi District, Odisha, India. *Journal of Geology & Geophysics*, Vol. 6, article no. 1000294.

Duncan I.J. (1984) Structural evolution of the Thor-Odin gneiss dome. *Tectonophysics*, Vol. 101, No. 1-2, pp. 87–130, http://dx.doi.org/10.1016/0040-1951(84)90044-1

Fox K.E., Yakymchuk C. (2017) Canadian gem-grade cordierite. *Proceedings of the 35th International Gemmological Conference*, October 8–19, 2017, Windhoek, Namibia, pp. 129–131.

Fritsch E., Rossman G.R. (1988) An update on color in gems. Part 2: Colors involving multiple atoms and color centers. *G&G*, Vol. 24, No. 1, pp. 3–15, http://dx.doi.org/10.5741/GEMS.24.1.3

Goergen E.T., Whitney D.L. (2012) Long length scales of element transport during reaction texture development in orthoamphibole-cordierite gneiss: Thor-Odin dome, British Columbia, Canada. *Contributions to Mineralogy and Petrology*, Vol. 163, No. 2, pp. 337–352, http://dx.doi.org/10.1007/s00410-011-0671-y

Goldman D.S., Rossman G.R., Dollase W.A. (1977) Channel constituents in cordierite. *American Mineralogist*, Vol. 62, pp. 1144–1157.

Graziani G., Guidi G. (2018) Hydrous gem magnesian cordierite with inclusions of hydroxyapatite, dolomite, and rutile. *Mineralogical Magazine*, Vol. 42, No. 324, pp. 481–485, http://dx.doi.org/10.1180/minmag.1978.042.324.10

Hausel W.D. (2002) A new source of gem-quality cordierite and corundum in the Laramie Range of southeastern Wyoming. *Rocks & Minerals*, Vol. 77, No. 5, pp. 334–339, http://dx.doi.org/10.1080/00357529.2002.9925657

——— (2003) Cordierite (iolite) and corundum (sapphire-ruby): Potential Wyoming gemstones. *Proceedings of the 39th Forum on the Geology of Industrial Minerals* (Reno, Nevada), Nevada Bureau of Mines and Geology, Special Publication 33, pp. 130–138.

Hinchey A.M., Carr S.D. (2007) Protolith composition of cordierite-gedrite basement rocks and garnet amphibolite of the Bearpaw Lake area of the Thor-Odin dome, Monashee complex, British Columbia, Canada. *Canadian Mineralogist*, Vol. 45, No. 3, pp. 607–629, http://dx.doi.org/10.2113/gscanmin.45.3.607

Hinchey A.M., Carr S.D., McNeill P.D., Rayner N. (2006) Paleocene-Eocene high-grade metamorphism, anatexis, and deformation in the Thor-Odin dome, Monashee complex, southeastern British Columbia. *Canadian Journal of Earth Sciences*, Vol. 43, No. 9, pp. 1341–1365, http://dx.doi.org/10.1139/e06-028

Kammerling R.C., Koivula J.I. (1991) Two strongly pleochroic chatoyant gems. *Journal of Gemmology*, Vol. 22, No. 7, pp. 395–398.

Laird J. (2002) Garnets and gemstones of the Slocan Valley. *British Columbia Rockhounder*, Vol. 5, pp. 5–7.

Layman F.G. (1963) Cordierite alteration. *Proceedings of the Pennsylvania Academy of Science*, Vol. 37, pp. 169–174.

Muyal J., Mattlin P. (2019) *G&G* Micro-World: Iolite-sunstone intergrowth and inclusions. *G&G*, Vol. 55, No. 3, pp. 427–428.

Norlander B.H., Whitney D.L., Teyssier C., Vanderhaeghe O. (2002) Partial melting and decompression of the Thor-Odin dome, Shuswap metamorphic core complex, Canadian Cordillera. *Lithos*, Vol. 61, No. 3-4, pp. 103–125, http://dx.doi.org/10.1016/S0024-4937(02)00075-0

Pan Y., Fleet M.E. (1995) Geochemistry and origin of cordierite-orthoamphibole gneiss and associated rocks at an Archean volcanogenic massive sulphide camp: Manitouwadge, Ontario, Canada. *Precambrian Research*, Vol. 74, No. 1-2, pp. 73–89, http://dx.doi.org/10.1016/0301-9268(95)00010-3

Patel S.C., Frost B.R., Chamberlain K.R., Snyder G.L. (1999) Proterozoic metamorphism and uplift history of the north-central Laramie Mountains, Wyoming, USA. *Journal of Metamorphic Geology*, Vol. 17, No. 3, pp. 243–258, http://dx.doi.org/10.1046/j.1525-1314.1999.00201.x

Petersen E.U. (1984) Metamorphism and geochemistry of the Geco Massive Sulfide Deposit and its enclosing wall-rocks. PhD thesis, University of Michigan, Ann Arbor, Michigan, USA.

Pouchou J.L., Pichoir F. (1985) "PAP" $\phi(\rho Z)$ procedure for improved quantitative microanalysis. In J.T. Armstrong, Ed., *Microbeam Analysis Proceedings*. San Francisco Press, San Francisco, California, pp. 104–106.

Simandl G.J., Marshall D., Laird J. (2000) Gem-quality cordierite deposits, Slocan Valley, British Columbia (NTS 82F/12E). In *British Columbia Geological Survey—Geological Fieldwork 1999*, British Columbia Ministry of Energy and Mines, Paper 2000-1, pp. 349–358.

Vanderhaeghe O., Teyssier C., Wysoczanski R. (1999) Structural and geochronological constraints on the role of partial melting during the formation of the Shuswap metamorphic core complex at the latitude of the Thor-Odin dome, British Columbia. *Canadian Journal of Earth Sciences*, Vol. 36, No. 6, pp. 917–943, http://dx.doi.org/10.1139/e99-023

Vry J.K., Brown P.E., Valley J.W. (1990) Cordierite volatile content and the role of CO_2 in high-grade metamorphism. *American Mineralogist*, Vol. 75, No. 1-2, pp. 71–88.

Wight W. (1999) Garnet and iolite gems in the Slocan Valley, British Columbia. *Canadian Gemmologist*, Vol. 20, No. 1, p. 18.

Wilson B.S. (2014) Colored gemstones from Canada. In L.A. Groat, Ed., *Geology of Gem Deposits*, 2nd ed., Mineralogical Association of Canada, Short Course Series 44, pp. 375–405.

Lab Notes

Editors
Thomas M. Moses | Shane F. McClure | Sally Eaton-Magaña

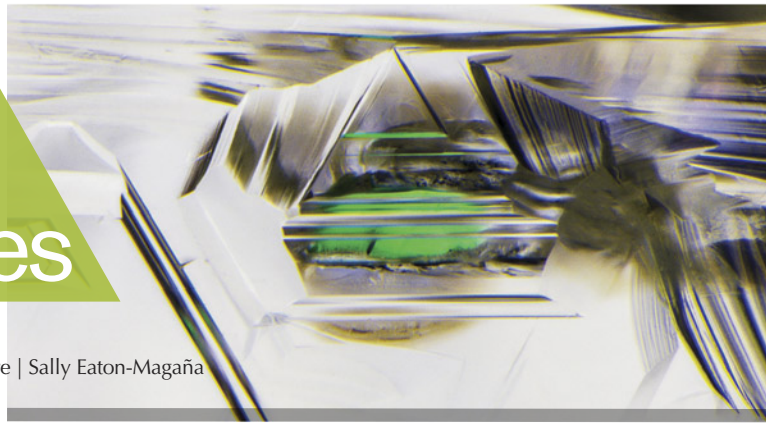

DIAMOND

Etch Features Reveal the Morphology of Diamond

Natural monocrystalline diamonds formed in the earth's mantle have two major growth forms: octahedron and cube. It has been suggested that diamond growth habit depends on multiple factors, including crystallization temperature, growth rate, and the degree of carbon supersaturation in the diamond-forming fluids (J.W. Harris et al., "Morphology of monocrystalline diamond and its inclusions," *Reviews in Mineralogy and Geochemistry*, Vol. 88, No. 1, 2022, pp. 119–166). If a diamond forms under changing conditions, it might not have a regular octahedral or cubic morphology but a combination of both. In some cases, diamonds grow without any well-defined crystal faces and are referred to as "irregular diamonds" (see examples in R. Tappert and M.C. Tappert, *Diamonds in Nature: A Guide to Rough Diamonds*, Springer-Verlag, Berlin, 2011, p. 28). While octahedral or cubic faces cannot always be identified visually in irregular diamonds, the morphology can be inferred by etch features left on the diamond by fluids in the mantle or during kimberlite eruption. Trigons and tetragons are the most common of these etch features—restricted to octahedral and cubic crystal faces, respectively.

Figure 1. Table (left) and pavilion (right) views of a chameleon diamond with visible trigons and tetragons. The trigons and tetragons are shown in more detail in figures 2 and 3. The diamond measures 1.28 cm in length.

The Carlsbad laboratory recently examined a 2.00 ct Fancy brown-greenish yellow diamond with both trigons and tetragons on its surface (figure 1). The trigons were located within a small indented natural near the table facet, while the tetragons were preserved within an indented natural at the culet (figures 2 and 3). Co-occurring trigons and tetragons are very uncommon and indicate an irregular morphology, characterized by both octahedral and cubic growth.

This stone was identified as a chameleon diamond. For such a classification, the diamond must include a green color component, show phosphorescence to short-wave UV, and change from a greenish color to a yellow or orange color with gentle heating or when kept in the dark for an extended period (C.M. Breeding et al., "Natural-color green diamonds: A beautiful conundrum," Spring 2018 *G&G*, pp. 2–27). These diamonds typically have a broad visible absorption band centered at approximately 480 nm and are referred to as "480 nm band diamonds." A study on rough yellow diamonds from Canada showed that all of those colored by the 480 nm absorption band have irregular morphology (M.Y. Lai et al., "Yellow diamonds with colourless cores – evidence for episodic diamond growth beneath Chidliak and the Ekati mine, Canada," *Mineralogy and Petrology*, Vol. 114, 2020, pp. 91–103), suggesting

Editors' note: All items were written by staff members of GIA laboratories.

Gems & Gemology, Vol. 59, No. 3, pp. 356–369.

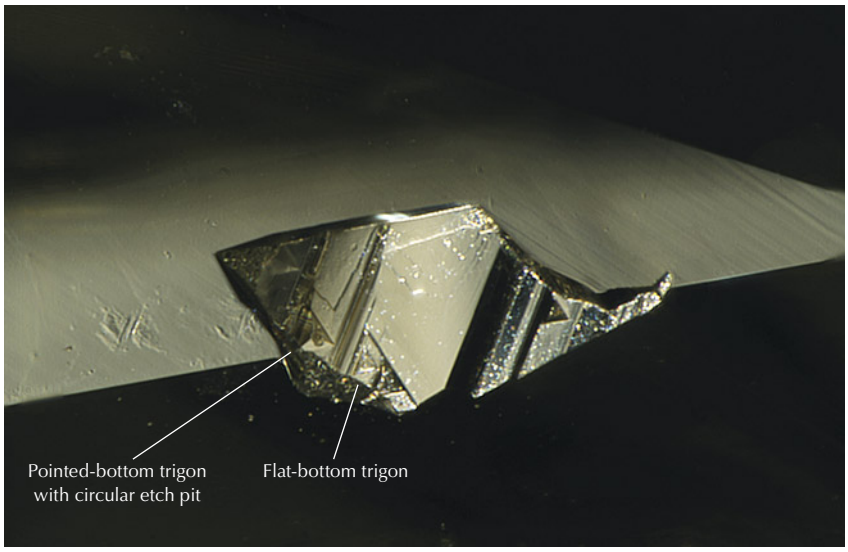

Figure 2. Flat-bottom and pointed-bottom trigons (surface features restricted to an octahedral crystal face) preserved on an unpolished portion of the diamond. A circular etch pit overprinting a pointed-bottom trigon indicates a late-stage diamond dissolution event that postdated the formation of the trigon. Field of view 1.26 mm.

that diamonds with the 480 nm absorption band may form under changing conditions in the mantle.

Trigons on diamond have two major morphologies: either a flat bottom or a pointed bottom (pyramidal). The type of trigon is primarily dependent on the temperature and pressure at the position where diamond dissolution occurs, as well as on the carbon dioxide and water contents in the fluid that etches diamonds. Experimental work indicates that fluids with higher carbon dioxide content tend to produce pointed-bottom rather than flat-bottom trigons (Y. Fedortchouk, "A new approach to understanding diamond surface features based on a review of experimental and natural diamond studies," *Earth-Science Reviews*, Vol. 193, 2019, pp. 45–65). Both forms of trigons were observed on the chameleon diamond we examined, as well as a circular etch pit overprinting a pointed-bottom trigon (figure 2). Unlike pointed-bottom trigons, circular pits are typically created by fluids with low carbon dioxide contents, indicating a late-stage etching event after the formation of the trigon.

The combination of surface features provides clues for the morphology of diamonds in rough form, as well as the interactions between diamonds and fluids throughout their journey from mantle residence to the earth's surface.

Mei Yan Lai and Matthew Hardman

Figure 3. Tetragons (surface features restricted to the cubic crystal face) preserved at the culet of the diamond. Field of view 1.26 mm.

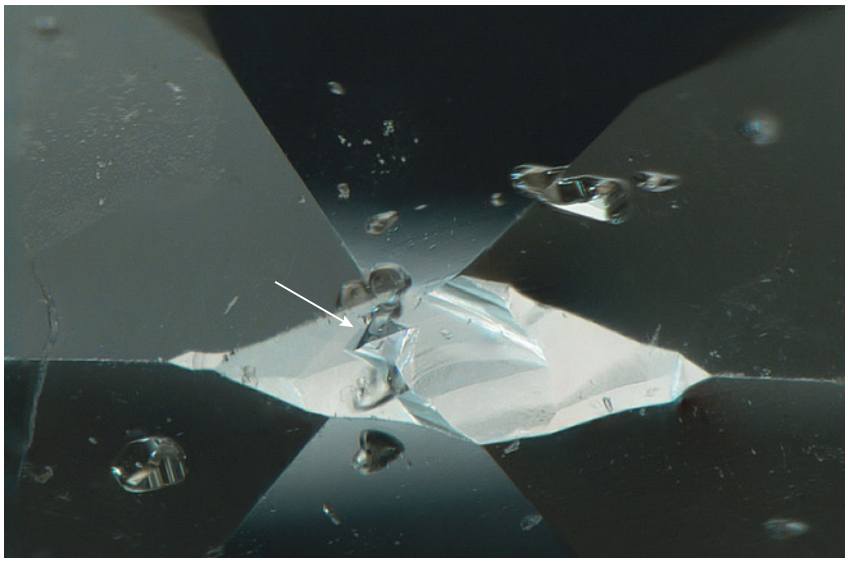

Natural Diamond with Unusual Phosphorescence

Phosphorescence spectroscopy shows that natural type IIb diamonds can have two broad phosphorescence bands: one centered at 500 nm that appears greenish blue and one centered at 660 nm that appears red. Generally, one of these phosphorescence bands is dominant. In the Hope diamond, for example, the phosphorescence initially appears orangy red and transitions to red as the subordinate greenish blue phosphorescence fades away (S. Eaton-Magaña et al., "Using phosphorescence as a fingerprint for the Hope and other blue diamonds," *Geology*, Vol. 36, No. 1, 2008, pp. 83–86). Occasionally, the faster-decaying greenish blue phosphorescence band will transition to the slower-decaying red band (Spring 2007 Lab Notes, pp. 47–48).

Recently, a 0.90 ct diamond with D color and I_1 clarity was submitted to GIA's laboratory in Ramat Gan, Israel, for a diamond dossier report. Infrared (IR) absorption spectroscopy indicated that the natural diamond was nominally type IIa. However, photoluminescence (PL) spectroscopy revealed that the diamond contained boron-related features, including the 648.2 nm peak attributed to a boron interstitial (B. Green, "Optical and

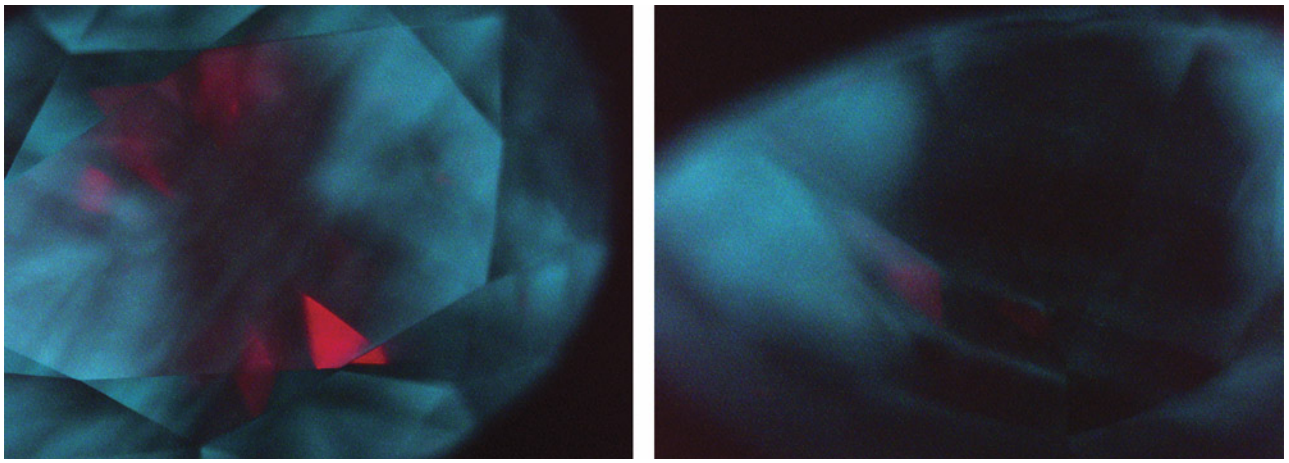

Figure 4. These deep-UV (<225 nm) phosphorescence images of the table (left) and pavilion (right) in a 0.90 ct D-color natural diamond with very low boron showed localized areas of the 500 nm (greenish blue) and 660 nm (red) bands.

magnetic resonance studies of point defects in single crystal diamond," PhD thesis, University of Warwick, 2013), along with the observed phosphorescence. These features indicated that the diamond did contain boron, but below the detection level of IR absorption spectroscopy. The distinctive aspect was that both the red and greenish blue phosphorescence were localized and visible within the same image (figure 4).

The phosphorescence is attributed to donor-acceptor pair recombination. For the 500 nm band, this recombination has been identified as interactions between boron acceptors and isolated nitrogen donors (J. Zhao, "Fluorescence, phosphorescence, thermoluminescence and charge transfer in synthetic diamond," PhD thesis, University of Warwick, 2022), while the 660 nm band is attributed to boron acceptors and unknown donors that are likely related to plastic deformation (S. Eaton-Magaña and R. Lu, "Phosphorescence in type IIb diamonds," *Diamond and Related Materials*, Vol. 20, No. 7, 2011, pp. 983–989). PL maps were collected on the table and pavilion with 455, 532, and 785 nm excitation; only an undefined PL feature at 813 nm showed an apparent increase on the pavilion within the red-phosphorescing region (figure 4, right).

Type IIb diamonds grown by high-pressure, high-temperature (HPHT) methods almost always show the 500 nm phosphorescence and occasionally a separate orange phosphorescence band centered at 580 nm. In a few instances, HPHT-grown diamonds have shown the 500 and 580 nm bands simultaneously in different portions of the diamond (Eaton-Magaña and Lu, 2011; Spring 2023 Gem News International, pp. 155–156).

This is the first time the authors have seen spatially distinct observations of red and greenish blue phosphorescence in a natural diamond, an unusual find.

Sally Eaton-Magaña, Evelina Goldort, and Dani Binyamin

Natural Type IIa Diamond with Unusual Red Fluorescence Distribution

The Carlsbad laboratory received a natural type IIa diamond with some unusual characteristics. As part of the standard data collection, the diamond type was determined by Fourier-transform infrared (FTIR) spectroscopy and deep-UV fluorescence images collected using the DiamondView instrument. The DiamondView images revealed predominantly red fluorescence on one side of the diamond and blue fluorescence on the other. This 3.58 ct pear modified brilliant diamond had H color and received an SI_2 clarity grade due to cavities, chips, and a feather (figure 5).

Type IIa diamonds typically display a blue fluorescence pattern under deep UV as a result of "band A" fluorescence or the N3 defect in the stone (U.F.S. D'Haenens-Johansson et al., "Synthesis of diamonds and their identification," *Reviews in Mineralogy and Geochemistry*, Vol. 88, No. 1, 2022, pp. 689–753). High amounts of nitrogen vacancy (NV) centers can cause red fluorescence in diamonds;

Figure 5. This 3.58 ct natural type IIa diamond with H color and SI_2 clarity displayed a unique fluorescence pattern when exposed to deep-UV light.

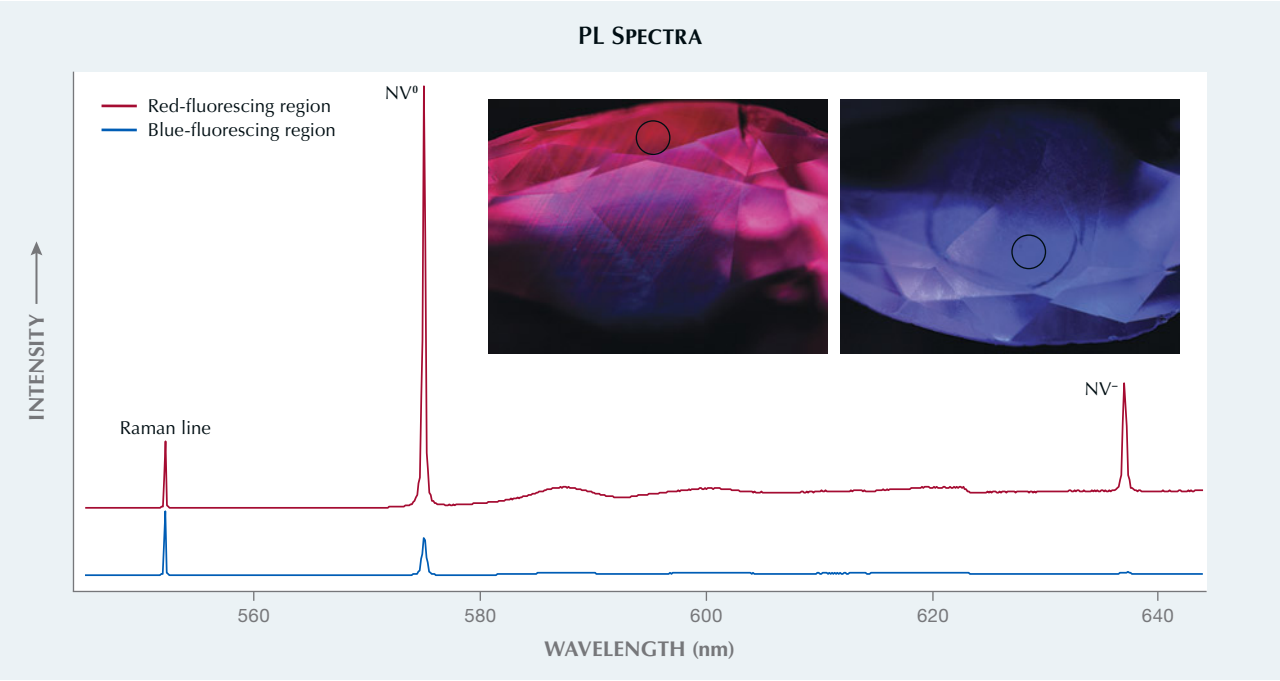

Figure 6. 514 nm PL spectra collected on the pavilion of opposite sides of the stone. The spectrum plotted in red corresponds with the red-fluorescing region, and the blue spectrum corresponds with the blue-fluorescing region, with Raman lines at 552 nm scaled as equal. Spectra are offset vertically for clarity. PL analysis spots are circled in the deep-UV fluorescence images.

however, this is rare in type IIa stones, as they are defined by nitrogen concentrations low enough to be undetectable by FTIR (Summer 2016 Lab Notes, pp. 189–190). The NV centers can be detected in a negative charge state (NV^-, zero-phonon line at 637 nm) or a neutral state (NV^0, zero-phonon line at 575 nm). Photoluminescence (PL) testing revealed much higher concentrations of both NV centers in the red-fluorescing region of the stone (figure 6). This distribution could have occurred if traces of isolated nitrogen were concentrated in one growth area of the stone.

PL mapping using 532 nm laser excitation (figure 7) displayed the relative intensities of these defects, demonstrating the wide distribution of the NV centers in opposite sides of the table and crown facets of this diamond. Analysis of this interesting fluorescence feature demonstrated that nitrogen could have been distributed unevenly in a relatively pure type IIa diamond when it initially formed.

Taryn Linzmeyer and Barbara Whalen

Figure 7. False-color 532 nm PL map showing the Raman-normalized peak area of NV^0 (left) and NV^- (right). The maps were compiled from 47,040 spectra. The pronounced gradient in NV centers across the diamond resulted in the different fluorescence color observations (see figure 6 insets).

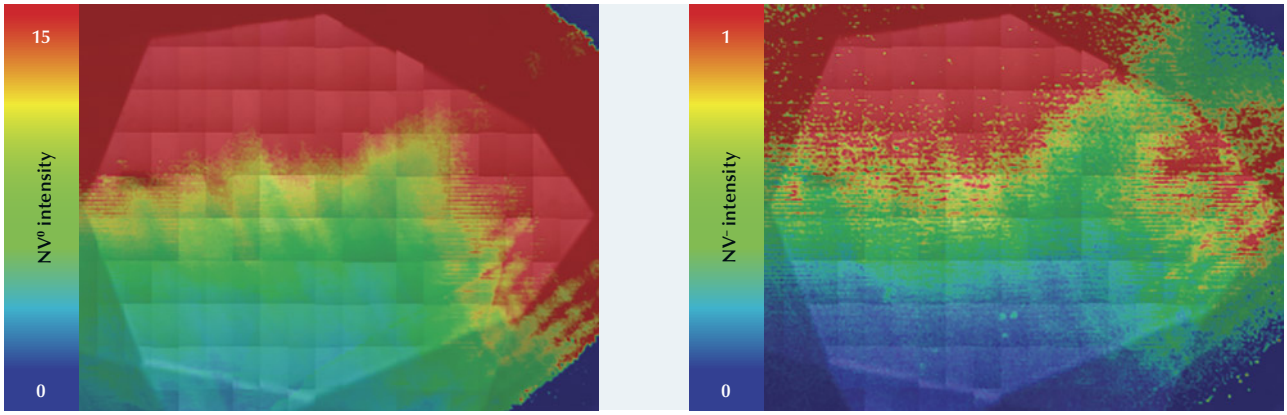

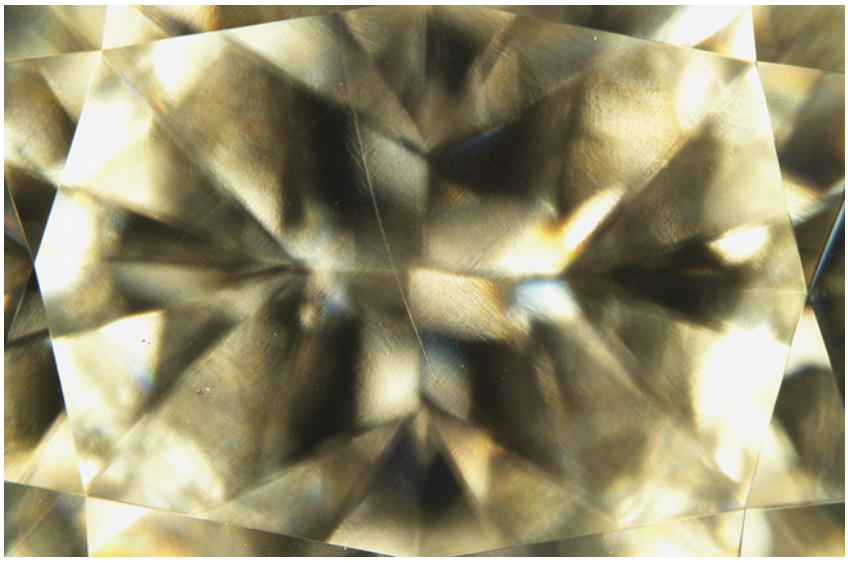

Figure 8. The etch channel in this CVD laboratory-grown diamond extends across the table facet into the crown. Field of view 7.19 mm.

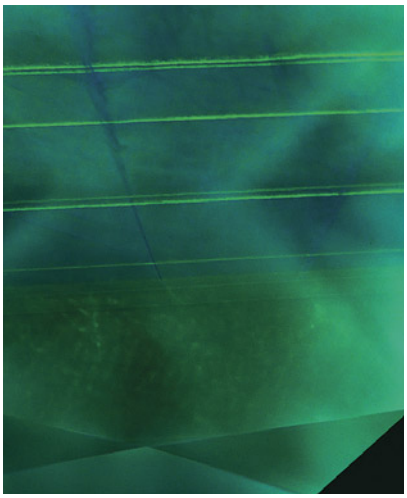

Figure 10. DiamondView imaging revealed that the channel was surrounded by blue-fluorescing dislocation bundles extending across the growth layers of the CVD diamond.

LABORATORY-GROWN DIAMOND

CVD "Etch" Channel

GIA's New York laboratory recently examined a diamond that had been grown via chemical vapor deposition (CVD) and processed using a high-pressure, high-temperature (HPHT) treatment. Standard grading procedures identified it as a 4.00 ct H-color cushion modified brilliant with SI_1 clarity. The diamond was identified as HPHT processed primarily due to the green fluorescence observed in the stone (see figure 10), while distinct fluorescent growth layers across the table and pavilion confirmed its CVD origin.

While GIA regularly receives CVD-grown diamonds submitted for laboratory-grown diamond reports, this particular example exhibited a unique characteristic. An etch channel–like structure was plainly visible across the table of the stone, a feature not observed in CVD laboratory-grown diamonds at GIA so far. The channel broke the surface of the table and extended across the stone, ending near a pavilion facet on the other side (figure 8). When viewed under high magnification, a dark residue (figure 9) was observed around parts of the channel. This residue was not present throughout the channel and appeared to be opaque. Close to the surface-reaching channel on the table facet were multiple smaller channels contained within the diamond. The surface-reaching opening of the channel was imaged with a scanning electron microscope (SEM), which revealed a jagged, slit-shaped entrance, suggesting that the shape of the channel extending throughout the diamond structure was similar in nature (figure 11). Some fragmentary material trapped just inside the entrance of the opening appeared to extend into the channel itself. This fragmentary material could have been the same type of opaque residue observed in some areas of the channel.

Fluorescence imaging with the DiamondView instrument also revealed the presence of this channel, which could be discerned by the blue-fluorescing line of dislocation bundles following the channel's path (figure 10). These dislocation bundles appeared almost perpendicular to the green-fluorescing growth layer boundaries, suggesting the channel was

Figure 9. Dark residue is visible in some parts of the channel, as seen through the pavilion. The appearance of the residue is similar to that of graphitized carbon but could also be attributed to non-diamond carbon. Field of view 1.99 mm.

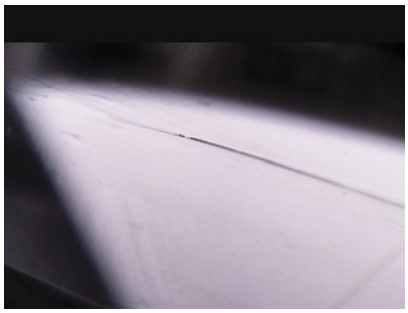

Figure 11. A secondary electron SEM image showed the finer structure of the channel opening, revealing a jagged, slit-like feature. Field of view 16 µm.

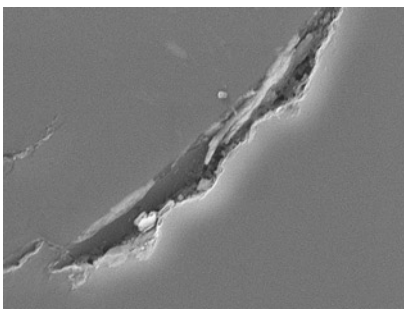

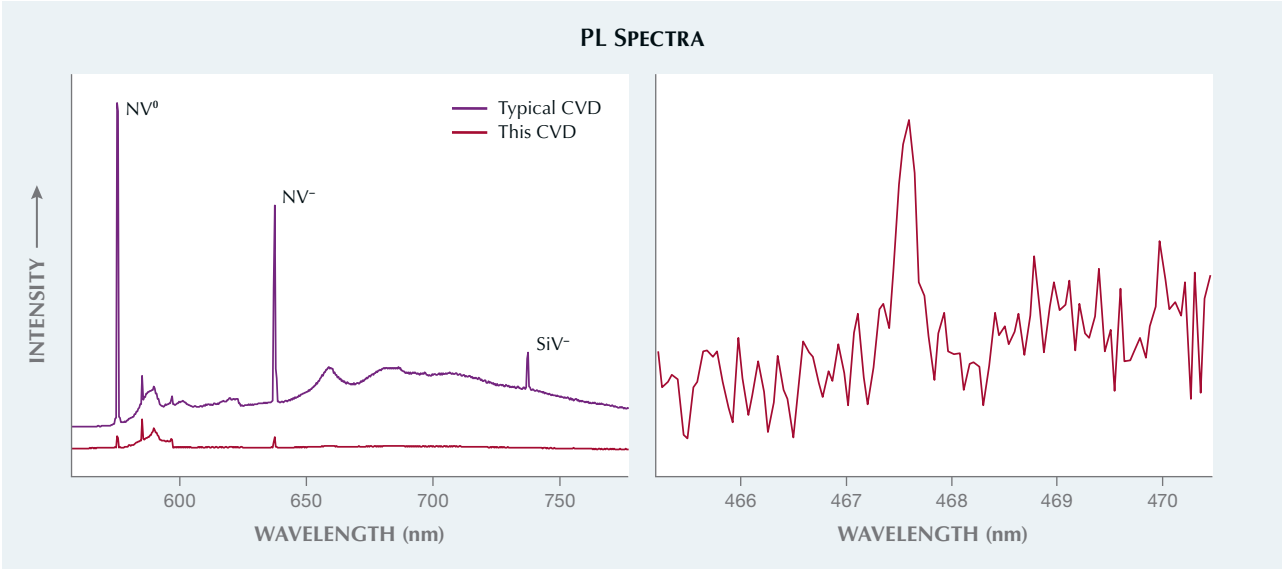

Figure 12. The PL spectra for a 1.40 ct CVD-grown diamond are shown in red. Left: The 514 nm PL spectrum reveals relatively weak NV centers and no detectable silicon. For comparison, the 514 nm PL spectrum for a more commonly observed as-grown CVD (purple) shows much stronger NV centers and detectable silicon. The Raman lines (not shown) are scaled as equal. Spectra are offset vertically for clarity. Right: Many locations on the CVD-grown diamond were analyzed with 457 and 633 nm excitation to verify whether the 468 nm center or the SiV^- center could be detected; this very weak peak of the 468 nm center was only detected at the culet.

created by exploiting weaker dislocation bundles that propagated through the diamond during CVD growth.

The presence of this channel in a CVD laboratory-grown diamond and the shape of the channel opening were unlike any natural etch channel opening or laser drill hole opening previously seen. It is unclear whether this channel was created during initial CVD growth or during HPHT processing. The opaque residue visible in some parts of the channel as well as the material visible at the channel surface could point to the presence of graphitized carbon, suggesting the channel was a byproduct of HPHT treatment, or it might indicate the presence of non-diamond carbon, which is a common feature found in untreated CVD laboratory-grown diamonds. In summary, the residue may arise from either the CVD growth process or post-growth treatment. Because this feature has not previously been documented at GIA, future studies may help determine the mechanism of action that could create channels in CVD-grown diamonds.

Elina Myagkaya

CVD-Grown Diamond with Few Diagnostic Features

Diamonds grown by chemical vapor deposition (CVD) have evolved rapidly in the last two decades. However, the vast majority submitted to GIA for reports still show several diagnostic features such as the silicon vacancy or SiV^- defect (a doublet at 736.6 and 736.9 nm) and/or the 468 nm peak when analyzed by photoluminescence (PL) spectroscopy. Additionally, most CVD diamonds have distinctive fluorescence images when analyzed by deep UV with the DiamondView instrument.

Therefore, it was interesting to analyze a 1.40 ct E-color, VVS_2 type IIa diamond submitted for a laboratory-grown diamond report. Initial PL data collection did not show either the SiV^- center or the 468 nm peak. The features observed were a 3H peak at 503.5 nm using 455 nm excitation and relatively weak nitrogen vacancy (NV) centers at 575 (NV^0) and 637 (NV^-) nm using 514 nm excitation (figure 12, left). The stone showed weak anomalous birefringence indicating strain; while this observation is helpful in confirming whether a diamond is grown by high-temperature, high-pressure (HPHT) methods, such birefringence cannot distinguish between natural and CVD origins. The deep-UV fluorescence image showed only deep blue coloration, which appeared generally comparable with the vast majority of natural type IIa diamonds (figure 13, left). Therefore, many of the standard markers of CVD origin were not present even when examined using advanced methods. Careful analysis of the fluorescence image revealed some distinct differences from the majority of natural diamonds, namely the patchiness of the fluorescence with some inert regions.

Many models of the DiamondView instrument include a series of filters that permit fluorescence imaging in which portions of the visible spectrum are blocked out. Using these filters, the blue portion of the visible spectrum was blocked in order to observe weaker underlying fluorescence features. With the orange long-pass filter blocking wavelengths less than 550 nm, NV-related fluorescence clearly showed the striations indicative of

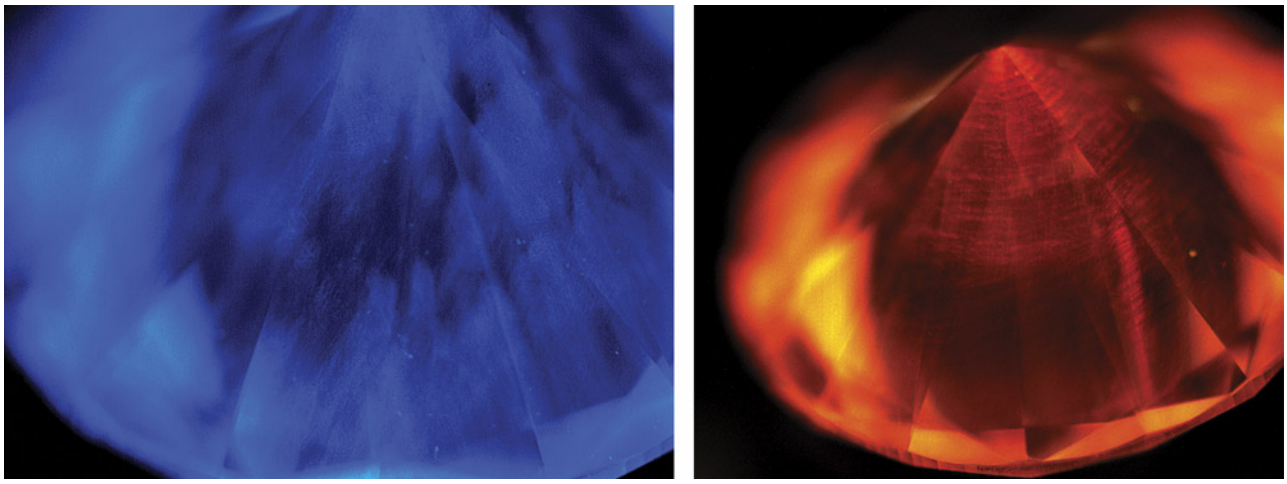

Figure 13. Left: The deep-UV (<230 nm) fluorescence image showed blue coloration (due to the presence of dislocation bundles) that appeared nominally similar to DiamondView images of natural type IIa diamonds. Right: When the fluorescence was filtered by an orange long-pass filter that blocked wavelengths below 550 nm, the NV-related fluorescence and the striations indicative of CVD growth became apparent.

CVD growth (figure 13, right). Also, several locations of the diamond were analyzed with PL spectroscopy to determine if either the 468 nm center or the SiV^- could be detected. Only at the culet was a small 468 nm feature observed (figure 12, right).

The author concluded that this was a CVD-grown diamond with no evidence of post-growth treatment. This example is a noteworthy indicator that as CVD growth methods improve, telltale defects are being minimized or eliminated entirely. Careful examination of all data, both spectroscopic and fluorescence imaging, is needed to provide accurate origins for diamond.

Sally Eaton-Magaña

Solid Laboratory-Grown Single-Crystal Diamond Ring

Carved single-crystal diamond rings are rare, with few examples to reference (see Spring 2020 Lab Notes, pp. 132–133). But with advancing technology in the laboratory-grown diamond industry, the creation of solid faceted diamond rings is now a reality. Recently submitted to the New York laboratory was a 4.04 ct single-crystal laboratory-grown diamond ring (figure 14). The 3.03 mm thick band had an inner diameter of 16.35–16.40 mm and an outer diameter of 20.32–20.40 mm. The ring was produced by Dutch Diamond Technologies in collaboration with the Belgian jewelry store Heursel, established in 1745.

This laboratory-grown diamond ring was cut from an 8.54 ct plate grown by chemical vapor deposition (CVD). Laser cutting produced a near-perfect circular ring, as demonstrated using digital imaging analysis to measure its inner and outer circumferences (figure 15).

The manufacture of a solid single-crystal diamond ring is a complex and challenging process. Once material is removed from the crystal, very fine fractures and imbalanced strain can have severe consequences, and the ring can shatter. Processing can take more

Figure 14. The 4.04 ct ring fashioned from a single-crystal CVD-grown diamond.

Figure 15. OpenCV software was used to draw perfect circles from the center of the ring, marked by a green dot.

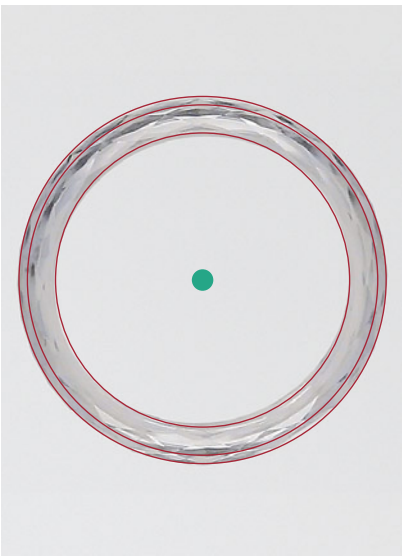

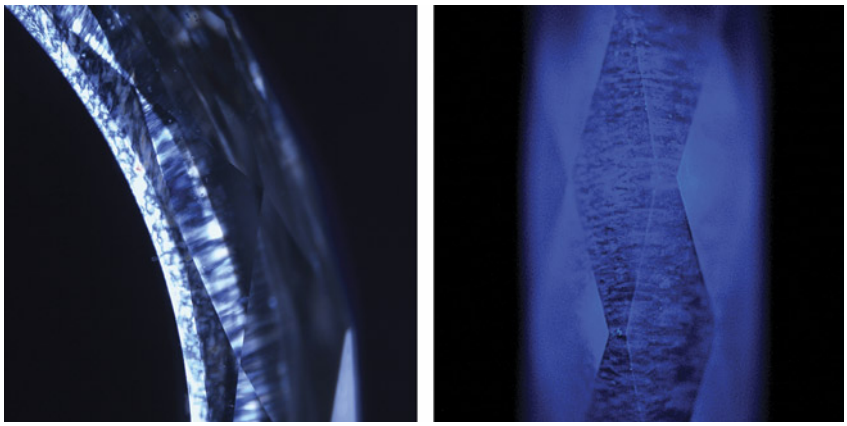

Figure 16. Strong birefringence observed under cross-polarized light (left) and blue fluorescence observed in the DiamondView (right).

than six months. Creating the ring from a single-crystal laboratory-grown diamond involved about 1,131 hours of processing (including pre-grinding) in the Dutch town of Cuijk, followed by 751 hours of polishing in Belgium.

Infrared absorption analysis revealed it was a type IIa diamond (no detectable nitrogen), and no hydrogen-related peaks were detected at 3107 or 3123 cm^{-1}. Photoluminescence spectroscopy showed interesting vacancy-related defects indicative of a multi-step growth process. A very strong emission from the silicon vacancy (SiV^-) defect was observed with 633 nm laser excitation; this is a common feature used to identify CVD-grown diamond. The conclusion was that this ring had not undergone post-growth treatment; nevertheless, it was notable that the ring showed relatively low nitrogen-related defects such as NV centers, along with no detectable 468 nm peak or the 596/597 nm doublet. P. Martineau et al. ("Identification of synthetic diamond grown using chemical vapor deposition (CVD)," Spring 2004 *G&G*, pp. 2–25) observed the 596/597 doublet with a 514 nm laser. Also of note, there were no H3 or 468 nm centers detected with 457 nm laser excitation.

Strong birefringence was observed using cross-polarized light under microscopic analysis, with an unusual radial pattern (figure 16, left) signifying unique growth conditions compared to typical CVD diamonds available in the market today. The deep ultraviolet illumination of the DiamondView (figure 16, right) confirmed these unusual growth features with a lack of post-growth fluorescence colors such as green produced by the H3 center.

The solid laboratory-grown diamond ring was studied by GIA and determined to have VVS_2 clarity based on dark non-diamond carbon pinpoint inclusions (growth remnants typical of CVD-grown diamonds) with Good polish (polishing on the interior surface of the ring precluded Very Good). Although the ring was a near-perfect circle (figure 15), symmetry was considered not applicable. The diamond had an E color specification based on GIA's color grading scale. The ring was laser inscribed "Laboratory-Grown" on a side facet.

The quality and size of this solid diamond ring (see the video clip at www.gia.edu/gems-gemology/fall-2023-lab-notes-solid-CVD-ring) provide a great example of the advancing technology in laboratory-grown diamonds and changing trends in the jewelry industry. This is the first time a GIA laboratory has examined a colorless diamond ring fashioned entirely from a laboratory-grown diamond.

Paul Johnson, Stephanie Persaud, and Madelyn Dragone

PEARLS

A Traditional Bombay Pearl Bunch

During the era when the maharajahs and maharanis ruled much of India, natural pearls were in great demand. In the nineteenth and early twentieth centuries, many merchants from the Middle East relocated to Bombay (now Mumbai) to benefit from this demand (R. Carter, *Sea of Pearls*, Arabian Publishing, London, 2012, pp. 169–175). Thus, it is no surprise that India has been a significant center of pearl manufacturing, processing, and trading for centuries. To showcase their high-quality pearls, traders and artisans in Bombay would sort the pearls, string them with silk threads, and tie them together at both ends using decorative metallic cords of various colors. These bunches were in great demand in the heyday of the natural pearl market and were sold as "Bombay bunches" (M. Manutchehr-Danai, *Dictionary of Gems and Gemology*, Springer, Berlin and Heidelberg, 2008, p. 101).

Recently, GIA's Mumbai laboratory had the opportunity to examine an 80-year-old Bombay bunch inherited by one of the city's established pearl families. The bunch consisted of 553 light cream round and near-round drilled pearls, strung in nine hanks, each containing four strands, with the exception of one hank with seven strands. The hanks were tied at both ends with white metal wires, together with silver and blue cords and tassels (figure 17). The pearls ranged from 3.83 to 5.72 mm, and the total weight of the bunch was approximately 80.51 g. The owner stated that the total weight of the pearls was approximately 130 chow (equivalent to 331.8 ct or 66.35 g). Chow is a system of converting weight into volume (*The Pearl Blue Book*, CIBJO, 2020).

The strung pearls were perfectly matched in color and exhibited smooth surfaces with high luster. When viewed under 40× magnification, they all exhibited typical nacreous overlapping aragonite platelets. Their internal structures were examined by real-time microradiogra-

Figure 17. A Bombay bunch consisting of nine hanks and 553 high-quality natural pearls ranging from 3.83 to 5.72 mm.

phy. The majority revealed fine growth arcs and concentric ringed structures, while others revealed tight or minimal structures, some with small faint cores or light organic-rich cores (figure 18). It was evident that these were natural pearls from *Pinctada*-species mollusks, as their internal structures were very similar to those observed in *Pinctada radiata* pearls from the Arabian (Persian) Gulf when compared to GIA's research database.

All pearls showed an inert reaction when exposed to optical X-ray fluorescence analysis. Energy-dispersive X-ray fluorescence spectrometry on a few samples revealed manganese values ranging from below detection limits to 30.7 ppm and strontium values of 1215 to 1989 ppm, consistent with a saltwater growth environment. Raman analysis using 514 nm excitation was also carried out on the surface of selected pearls showing a doublet at 702/705 cm^{-1} as well as a peak at 1085 cm^{-1}, indicative of aragonite. Very weak polyenic pigment-related peaks at 1130 and 1530 cm^{-1} were also observed in a few of the pearls, likely associated with their light cream coloration (A. Al-Alawi et al., "Saltwater cultured pearls from *Pinctada radiata* in Abu Dhabi (United Arab Emirates)," *Journal of Gemmology*, Vol. 37, No. 2, 2020, pp. 164–179). The photoluminescence spectra under 514 nm excitation were also consistent with the Raman results and displayed high fluorescence together with the aragonite peaks, typical of most nacreous pearls. When exposed to long-wave ultraviolet light, the pearls showed a moderate blue reaction.

Figure 18. Real-time microradiography images of eight pearls from the Bombay bunch revealing fine growth arcs and concentric ringed structures typical of those internal structures observed in Pinctada radiata *pearls.*

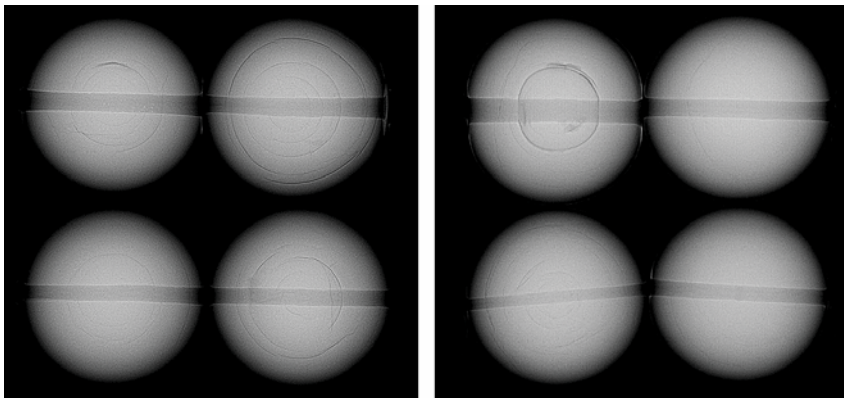

Historically, Bombay bunches were known to contain high-quality *Pinctada radiata* pearls fished from the Arabian (Persian) Gulf, commonly referred to as "Basra pearls" in the trade. Records indicate that the proportion of round pearls found in each natural pearl harvest today is less than 5% (H. Bari and D. Lam, *Pearls*, Skira, Milan, 2010, p. 43). Natural pearls are rare to find, and it can take decades to match a round pair of similar size, color, and luster. Encountering Bombay bunches in today's

Figure 19. A white button-shaped atypical bead cultured pearl weighing 8.15 ct and measuring 11.73 × 11.35 × 9.03 mm.

market is a rarity, and it was a great opportunity for GIA Mumbai to examine such an interesting and memorable pearl submission.

Pfokreni Nipuni, Abeer Al-Alawi, and Roxane Bhot Jain

Flame-Like Surface Structure in a Nacreous Atypical Bead Cultured Pearl

GIA's Mumbai laboratory recently received an atypical bead cultured pearl with a unique surface appearance. The white button-shaped pearl weighed 8.15 ct and measured 11.73 × 11.35 × 9.03 mm (figure 19).

Viewed under 40× magnification, the surface exhibited typical fine nacreous overlapping aragonite platelets, but a distinct pattern similar to the flame structures observed in some porcelaneous pearls was also noted (Summer 2021 Lab Notes, pp. 152–153). These flame-like features were formed due to the presence of relatively opaque, frosty white rounded depressions on the pearl's surface. Although rounded, they seemed to be oriented longitudinally and were more tapered toward the base and apex and broader along the sides of the pearl (figure 20). Also observed on the surface were small white spots with slightly elongated comet tails that flowed tangentially to the circumference of the button. The base and apex of the pearl lacked the whitish subsurface opaque features that produced the flame structure effect, and these two areas appeared more translucent than the other parts of the pearl.

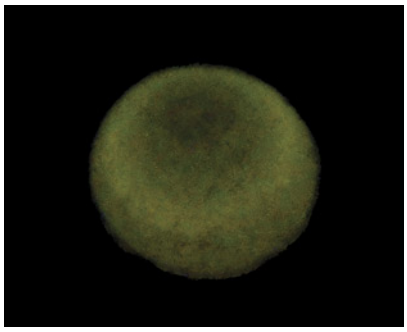

Figure 21. XRF reaction of the pearl, with the sides appearing brighter than the base and apex.

Under long-wave ultraviolet radiation, the pearl showed a strong yellowish green reaction, and a similar but weaker reaction was noted under short-wave ultraviolet radiation. The deep-UV (<230 nm) radiation of the DiamondView instrument revealed a clear bluish reaction, with the surface showing a chalky white flame-like structure extending from the apex center across the pearl. Raman analysis of the pearl's surface using a 514 nm excitation showed a doublet at 701/704 cm^{-1} as well as peaks at 1086 and 1464 cm^{-1} characteristic of aragonite. The photoluminescence spectra revealed high fluorescence, with a maximum centered at approximately 620 nm.

Energy-dispersive X-ray fluorescence spectrometry revealed a low manganese level of 16.9 ppm and a higher strontium level of 1577 ppm, indicative of a saltwater environment. However, when exposed to X-ray fluorescence (XRF) analysis, the pearl exhibited a moderate yellowish green fluorescence with a higher intensity toward the sides but a weaker reaction on the base and apex (figure 21). Saltwater pearls are usually inert when tested by this method, while freshwater pearls and saltwater bead cultured pearls with freshwater shell nuclei tend to fluoresce weak to strong yellowish green. In the case of bead cultured pearls, a thinner nacre usually produces a stronger reaction; conversely, the thicker the nacre, the weaker the reaction.

Real-time microradiography imaging (RTX) revealed a long, complex linear feature in the center typically associated with non-bead cultured pearls (figure 22, left). When viewed under X-ray computed microtomo-

Figure 20. Rounded depressions forming the flame-like structure. Field of view 0.4 mm.

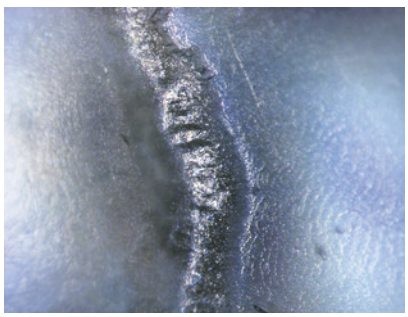

Figure 22. Left: RTX image of the pearl's internal structure with a large linear feature. Right: μ-CT image showing a freshwater-type linear feature in the center and a faint boundary (arrow).

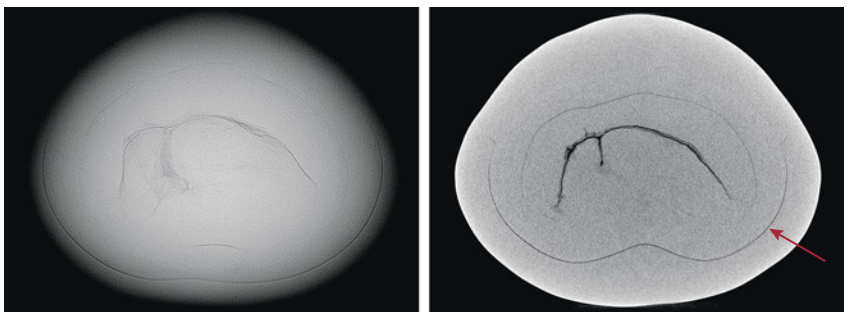

graphy (μ-CT), the linear feature looked very similar to those often observed in freshwater non-bead cultured pearls. A faint boundary was also seen around the central linear feature (figure 22, right) and other growth rings. All these observations, together with the XRF reaction of the pearl and the saltwater chemistry, were indicative of an atypical bead cultured saltwater pearl with a freshwater pearl used as its nucleus (P. Kessrapong and K. Lawanwong, "Atypical bead cultured *Pinctada maxima* pearls nucleated with freshwater non-bead cultured pearls," *GIA Research News*, April 6, 2020). The nacre thickness overlying the freshwater non-bead cultured pearl nucleus ranged from approximately 1.09 to 1.90 mm. The thicker nacre was positioned near the base and apex and the thinner nacre toward the sides. This aligned with the XRF reaction observed, as a thinner saltwater nacre will allow more fluorescence from the freshwater pearl nucleus to pass through the nacre layers, while thicker nacre masks the reaction.

Over the years, GIA has encountered similar atypical bead cultured pearls with sizeable freshwater non-bead cultured pearls used as a nucleus (Spring 2023 Lab Notes, pp. 74–76). However, the presence of flame-like structures seen on nacreous pearls is a very rare phenomenon. This combination of interesting culturing along with the unique surface features make this pearl noteworthy.

Prasad Mane, Nishka Vaz, and Abeer Al-Alawi

*Figure 23. Two traditional Indian-style pearl nose rings (*nath*) set with colored gemstones and pearls measuring approximately 6.63 × 6.09 mm to 8.42 mm (left) and 5.38 mm to 8.02 × 7.61 mm (right).*

Pearls in Traditional Indian Nose Rings

The beauty of Indian jewelry lies in the artisanship involved in creating intricate, unique designs. One example is the classic Indian nose ring (known as the *nath*). It is typically cashew shaped, with a chain to connect it to a hairpiece or earring. The nath exemplifies traditional Maharashtrian jewelry and is usually crafted in yellow gold. Made famous during the Peshwa rule, the nath has been crafted using diamonds, pearls, rubies, and emeralds. Today, the nath is worn mainly for weddings or special occasions, while everyday nose adornments take the form of smaller, simpler studs or rings made from gold or silver. Recently, GIA's Mumbai laboratory received two traditional nose rings for pearl identification.

Each was set with 17 drilled pearls, near-drop and button, ranging from light cream to cream in color. They were skillfully strung together with yellow metal wire and set with colored gemstones of various shapes and cutting styles. The pearls in the larger nose ring (figure 23, left) ranged from approximately 6.63 × 6.09 mm to 8.42 mm, and the item weighed a total of 13.96 g. Those in the smaller nose ring (figure 23, right) ranged from 5.38 mm to 8.02 × 7.61 mm, and this piece weighed 9.05 g overall. When viewed under 40× magnification, the pearl surfaces in both pieces showed typical nacreous overlapping aragonite platelets and a medium to high surface luster. Energy-dispersive X-ray fluorescence (EDXRF) spectrometry revealed manganese levels below the instrument's detection level and a strontium content averaging 950 ppm. In addition, the pearls were inert to X-ray fluorescence, indicative of saltwater origin. They showed a moderate greenish yellow reaction under long-wave ultraviolet light and a weaker reaction of similar color under short-wave UV. Real-time microradiography imaging revealed internal structures similar to those observed in natural pearl studies for various *Pinctada*-species mollusks (K. Scarratt et al., "Natural pearls from Australian *Pinctada maxima*," Winter

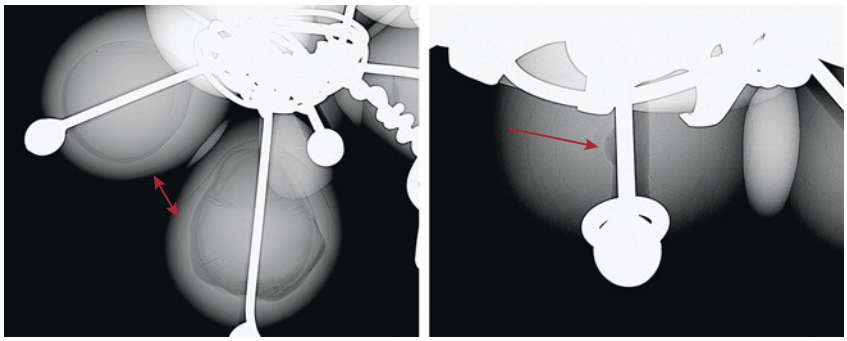

Figure 24. Real-time microradiography of the internal structures observed in the larger nose ring consisting of organic-rich acicular structures and growth arcs (left) and a "collapsed core" near the drill hole area surrounded by growth arcs (right).

2012 *G&G*, pp. 236–261; N. Nilpetploy et al., "The gemological characteristics of Pipi pearls reportedly from *Pinctada maculata*," Winter 2018 *G&G*, pp. 418–427). The radiopaque areas visible on the microradiographs of both items correspond to the yellow metal fittings and wire, since they are denser and prevent X-rays from passing through.

Five pearls from the larger nath revealed an organic-rich internal structure with varying patchy light and dark gray contrasting areas, along with an acicular structure radiating from their centers that occupied almost half of the internal structure (figure 24, left). Two pearls showed "collapsed cores" close to the drill holes (figure 24, right); the bulk of the cores, if any, were removed as a result of drilling. The remaining ten pearls displayed fine concentric rings and growth arcs, all proving their natural origin.

Microradiography of the pearls in the smaller nath revealed similar internal structures. While the majority of those pearls showed fine concentric rings and growth arcs, three of them (marked with arrows in figure 25) also possessed organic-rich and acicular cores that occupied varying degrees of their structure. The internal structures observed in both items contained classic natural pearl structures similar to those observed in known *Pinctada radiata* pearls in GIA's research database. The EDXRF results were also within the range expected for *Pinctada radiata* samples, with the lower levels of strontium (average of 950 ppm) and manganese (mostly below detection limits) consistent with that mollusk species and below those expected from *P. maxima* pearls (A. Homkrajae et al., "Internal structures of known *Pinctada maxima* pearls: Natural pearls from wild marine mollusks," Spring 2021 *G&G*, pp. 2–21).

The combinations of natural pearls made these two pieces very attractive. It is no easy task to create traditional nose ornaments with pearls of such size. These two unique pearl jewelry items provide an excellent example of Indian heritage.

Lubna Sahani, Abeer Al-Alawi, and Roxane Bhot Jain

Figure 25. The majority of the pearls in the smaller nose ring showed faint growth arcs and concentric ringed structures, while three of them showed organic-rich acicular cores (marked with arrows) typical of natural pearls.

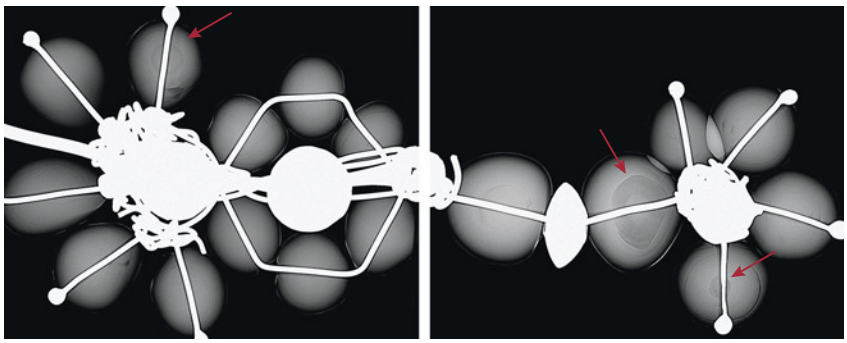

RUBY

"Nebula" Inclusion in Ruby Beryllium-Diffused to Heal Fractures

Recently the Carlsbad laboratory received a 4.12 ct purple-red stone measuring approximately 11.50 × 7.70 × 4.72 mm (figure 26) for identification services. It featured unusual veil-like reddish color zoning wafting throughout a purple bodycolor. The refractive index measured 1.760–1.770, identifying the stone as a ruby.

Figure 26. An unusual ruby with coloring reminiscent of a nebula found in the depths of outer space.

Figure 27. Fingerprints resulting from flux-assisted heating of a beryllium-rich flux. Field of view 7.19 mm.

Microscopic examination indicated that the reddish color zoning was associated with altered fingerprints that resembled a cosmic nebula due to a flux-rich residue (figure 27). These fingerprints appeared to be consistent with fractures that had been healed using a flux-assisted heating process in a high-heat environment.

Due to the indications of high heat, laser ablation–inductively coupled plasma–mass spectrometry (LA-ICP-MS) chemical analysis was performed to check for the presence of beryllium diffusion. Initially, LA-ICP-MS conducted on two spots revealed beryllium concentrations of <0.019 ppma and 60.87 ppma. This significant discrepancy prompted additional LA-ICP-MS testing in three spots, revealing beryllium concentrations of <0.19 ppma, 1780 ppma, and <0.19 ppma. Microscopic observation of the testing spots showed areas of high beryllium on or near the reddish color zones, while areas of very low beryllium were associated with testing areas on the purple areas of the stone.

Therefore, it was concluded that a beryllium-rich flux was used to heal the fractures naturally present in the stone. The ruby was likely heated in this flux at temperatures high enough to allow the beryllium to seep from the flux into the stone, but not long enough for the beryllium to infiltrate its entirety.

Michaela Damba

Translucent Ruby Filled with Zinc Glass

Recently the Carlsbad laboratory received an 8.57 ct translucent purplish red heart-shaped mixed-cut stone for identification service (figure 28). Standard gemological testing revealed a refractive index of 1.760–1.769, and a ruby spectrum was obtained with a handheld spectroscope. The stone showed a medium to strong red fluorescence to long-wave UV radiation and a very weak red fluorescence to short-wave UV radiation. During microscopic analysis, several fractures containing a whitish filler and air pockets were seen using fiber-optic lighting (figure 29). Using reflected light, fractures with a lower luster than the host corundum were also observed, which confirmed the presence of a filling material.

The stone did not show the blue flash effect typically observed in rubies filled with lead glass (S.F. McClure et al., "Identification and durability of lead glass–filled rubies," Spring 2006 *G&G*, pp. 22–36). Although the filler improved the durability, it did not appear to improve the clarity.

Glass filling treatment has been used on heavily fractured rubies to increase their clarity and durability since the early 1980s, and cavity filling was noted and described as early as 1984. The original filler was silica glass, which was easily visible since its refractive index (~1.5) is significantly lower than corundum (R.E.

Figure 28. An 8.57 ct heart-shaped fracture-filled ruby treated with a zinc glass filling.

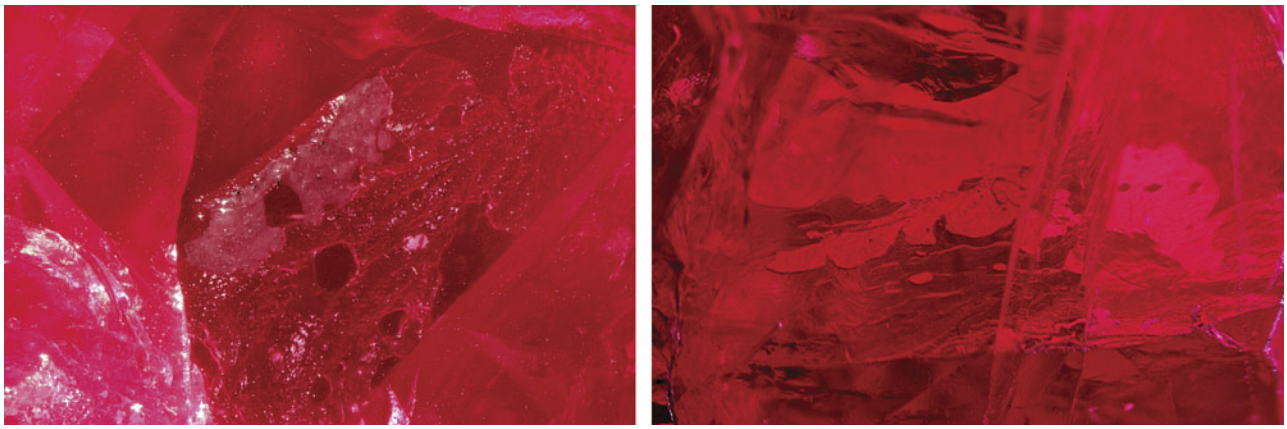

Figure 29. A fracture with whitish filler (left) and trapped air pockets (right). Fields of view 1.58 mm (left) and 2.90 mm (right).

Kane, "Natural rubies with glass-filled cavities," Winter 1984 *G&G*, pp. 187–199). In early 2004, gemologists discovered a new type of glass filler with high lead content and a much better clarity enhancement due to its higher reflective index (~1.70) (GAAJ Research Laboratory, "Lead-glass impregnated ruby," March 15, 2004). Since then, lead glass fillers have become the most popular filler for rubies, although other glass types such as bismuth and cobalt have also been used (T. Leelawatanasuk et al., "Cobalt-doped glass-filled sapphire: An update," *Australian Gemmologist*, Vol. 25, No. 1, 2013, pp. 14–20; Spring 2020 Lab Notes, p. 139).

In the heart-shaped ruby submitted to the laboratory, energy-dispersive X-ray fluorescence spectroscopy did not detect lead or bismuth but did show chromium, iron, and zinc. Additional chemical analysis was performed with laser ablation–inductively coupled plasma–mass spectrometry on two spots of one larger fracture with a substantial amount of filler in order to quantitatively measure the elements in the glass filler. The averages of the two analysis spots were 28750 ppmw silicon, 1091 ppmw zinc, and 108 ppmw lead.

Chemical results and gemological properties revealed that this glass filler was not the lead or bismuth glass the authors first suspected, but rather a silica-based glass doped with zinc. While this type of filler had visual properties similar to those of other glass fillers in corundum, it did not show a flash effect. This is the first time the authors have encountered a ruby filled with zinc glass.

Shiva Sohrabi and Amy Cooper

PHOTO CREDITS
Adriana Robinson—1, 26, 28; Matthew Hardman—2, 3; Evelina Goldort—4; Diego Sanchez—5; Barbara Whalen—6; Elina Myagkaya—8–10; Sally Eaton-Magaña—13 (right); Towfiq Ahmed—14, 15; Paul Johnson—16 (left); Madelyn Dragone—16 (right); Gaurav Bera—17, 19, 23; Nishka Vaz—20; Nathan Renfro—27; Shiva Sohrabi—29

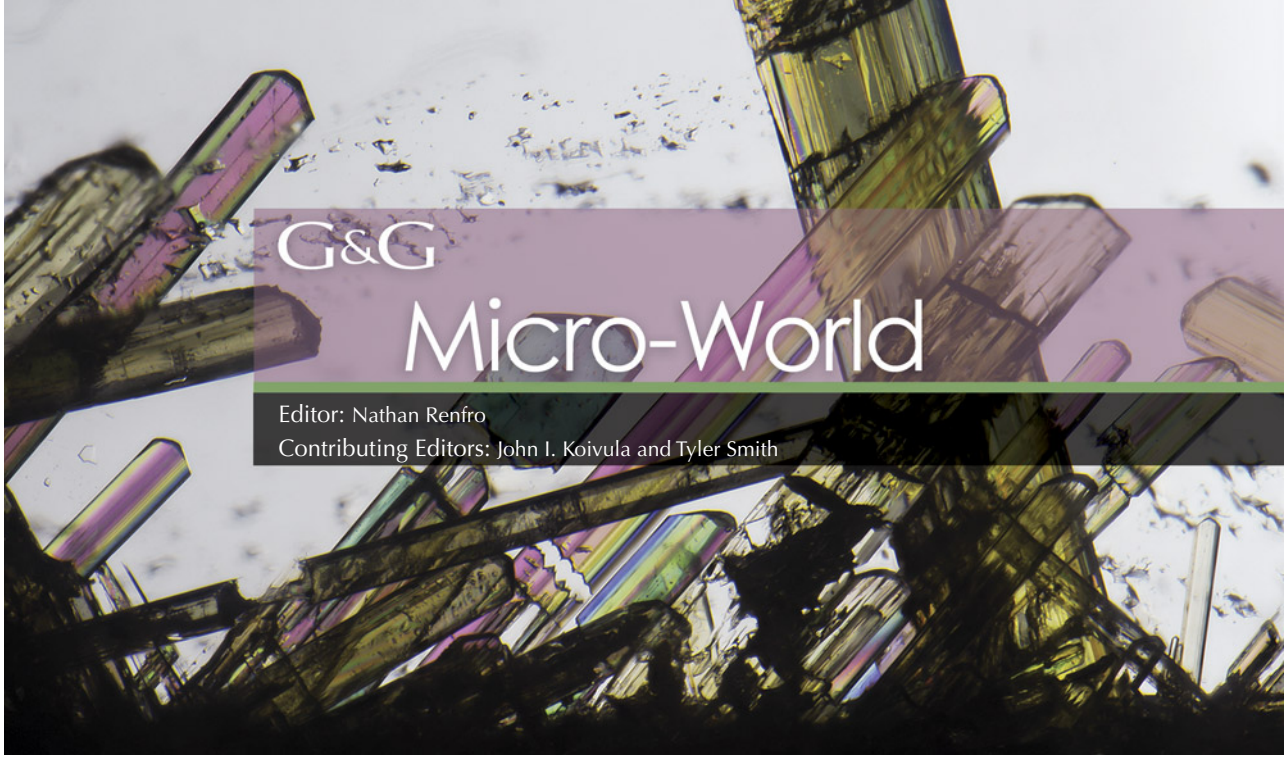

Breyite in Diamond

The author recently examined a 0.71 ct, D-color, type IaB diamond with an interesting inclusion reminiscent of a stone splashing in water (figure 1). Raman analysis identified the well-formed colorless transparent crystal as breyite ($CaSiO_3$), a calcium-rich silicate mineral commonly found in sublithospheric or superdeep diamonds. It was hypothesized that this diamond formed in the lower part of the transition zone or the lower mantle beneath the earth's crust.

Since the majority of diamonds in the jewelry industry come from the lithosphere, each one provides a window into Earth's intricate geology. Inclusions such as this one serve as a reminder that beauty and flaws may coexist peacefully, whether they add to a diamond's charm or provide scientific insight.

Aprisara Semapongpan
GIA, Bangkok

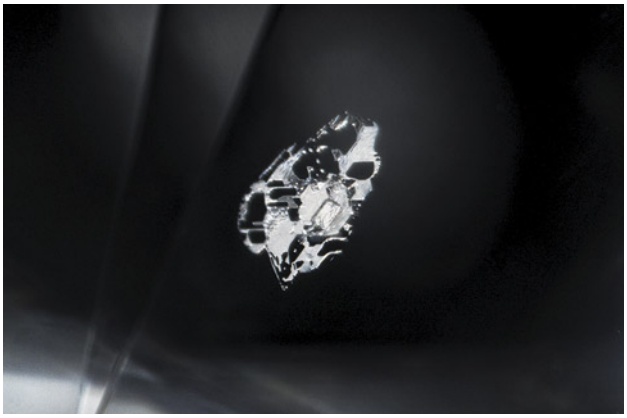

Figure 1. A well-formed colorless breyite crystal reminiscent of a stone making a splash in water. Photomicrograph by Aprisara Semapongpan; field of view 1.07 mm.

Spray of Columbite Crystals in Topaz

A probable columbite inclusion in beryl was featured in a recent Quarterly Crystal, demonstrating the striking form these minerals can display (Spring 2023 *G&G* Micro-World, pp. 90–91). It was only fitting to follow up with a look at the same inclusion hosted by a different mineral.

The cluster of bladed columbite crystals in figure 2, identified via Raman spectroscopy, was found in an 8.91 ct colorless topaz. The thinner crystals allowed the brown bodycolor to show through, while the thicker, sword-like center crystal appeared black and opaque. Thin-film interference was observed between the host and inclusion when illuminated with oblique lighting, adding some welcome color to an otherwise featureless crystal face. While columbite has been previously described in topaz (Fall 2009 *G&G*

About the banner: Numerous epidote crystals show colorful birefringence in plane-polarized light within their rock crystal quartz host. Photomicrograph by Nathan Renfro; field of view 5.75 mm.

Gems & Gemology, Vol. 59, No. 3, pp. 370–379.

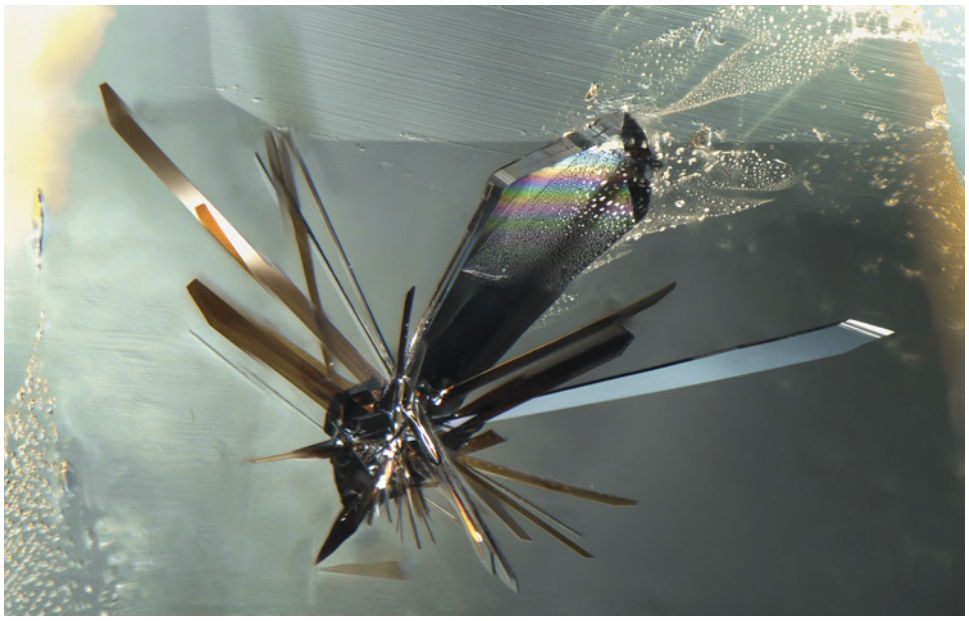

Figure 2. Bladed crystals of columbite radiate from a central point in colorless topaz. The mirror-like surfaces allow for reflections of neighboring blades, as seen in the top left crystal. Photomicrograph by Tyler Smith; field of view 2.90 mm.

Lab Notes, pp. 212–213; E.J. Gübelin and J.I. Koivula, *Photoatlas of Inclusions in Gemstones, Volume 2*, Opinio Publishers, Basel, Switzerland, 2005, pp. 263, 738), this is the most dramatic example observed by the author.

Tyler Smith
GIA, New York

Inclusion Resembling a *Gada* in Diamond

Recently, the authors observed an interesting etch channel (figure 3) in a 1.00 ct L-color type Ia round brilliant diamond with SI_1 clarity. It resembled a *gada*, a mace-like weapon belonging to the Hindu god Hanuman. This etch channel was the only one observed in the diamond; these features are often created by dissolution processes (T. Lu et al., "Observation of etch channels in several natural diamonds," *Diamond and Related Materials*, Vol. 10, No. 1, 2001, pp. 68–75).

This unusual clarity characteristic showcases the variety that is possible within the natural world.

Rujal Kapadia and Bhavya Maniar
GIA, Surat

Sally Eaton-Magaña
GIA, Carlsbad

Figure 3. This etch channel seen in the crown facets of a 1.00 ct diamond with SI_1 clarity (left) resembled a gada *(right), a mace-like weapon wielded by the Hindu god Hanuman. Photomicrograph (left) by Deepak Raj; field of view 0.80 mm. Photo (right) courtesy of the Metropolitan Museum of Art.*

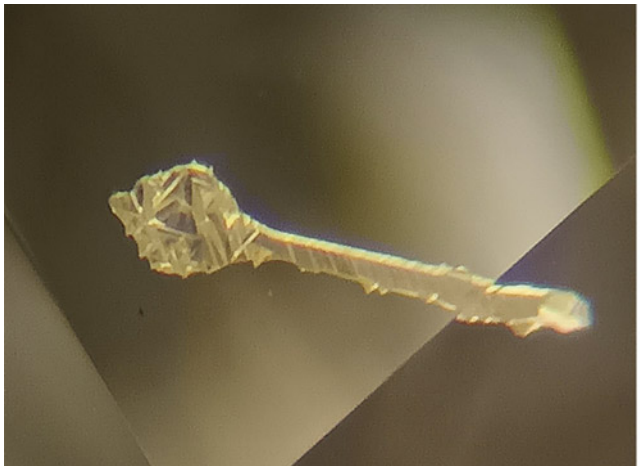

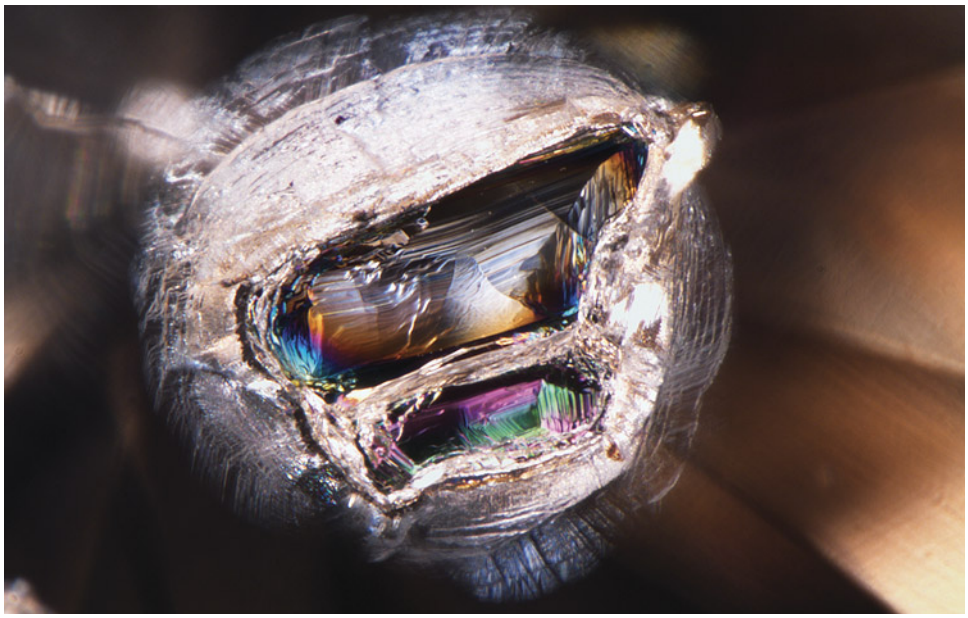

Figure 4. This iridescent ferropericlase crystal with a stress halo measuring approximately 0.7 mm was trapped inside a light brown diamond. Photomicrograph by Kyaw Soe Moe; field of view 1.58 mm.

Iridescent Inclusion in Brown Diamond

The iridescent crystal inclusion in the 1.07 ct light brown type IIa diamond in figure 4 was identified by Raman spectroscopy as ferropericlase. Ferropericlase, (Mg,Fe)O, can originate from either shallow (lithospheric) or deep (sublithospheric) depths within the earth. A stress halo was developed around the crystal by temperature and pressure changes during the ascent to the earth's surface. The colorful iridescence may have been caused by light interference at a thin film trapped between the inclusion and the host diamond. It is rare to see ferropericlase as an inclusion in diamond, especially such a large crystal.

Kyaw Soe Moe
GIA, New York

Natural Diamond with Twinning Wisps Resembling a Whale

The authors recently examined a 0.46 ct type Ia round brilliant diamond with SI_1 clarity that had surprisingly patterned twinning wisps. When viewed through the table, the twinning wisps resembled a whale (figure 5). Twin planes can form in diamond when the orientation of the crystal structure changes during growth in the earth's mantle. Twinning wisps are atomic defects along this plane, found in ~10% of type Ia diamonds (S. Eaton-Magaña et al., "Natural-color D-to-Z diamonds: A crystal-clear perspective," Fall 2020 *G&G*, pp. 318–335).

A termination of one of these features just below the pavilion was examined using photoluminescence (PL) mapping at various excitation wavelengths to examine the distribution of atomic-level defects in the crystal lattice. The PL mapping with 455 nm excitation revealed a relative increase in the defect concentrations of the nitrogen-related centers of H3 (NVN^0) with zero-phonon line (ZPL) at 503.2 nm and H4 (4N+2V) with ZPL at 495.9 nm; a weak radiation-related defect, the TR12 with ZPL at 469.9 nm was also detected (A.M. Zaitsev, *Optical Properties of Diamond*, Springer-Verlag, Berlin and Heidelberg, 2001, and references therein). PL mapping using 633 nm excitation revealed that the GR1 (V^0; ZPL at 741.2 nm) had a higher Raman-normalized peak area corresponding to the termination of the twinning wisp compared to diamond adjacent to the wisp. The GR1 defect is typically formed by radiation damage of a diamond lattice. Although the GR1 was elevated, we did not observe radiation stains around the twinning wisps. Furthermore, there were no visible changes to the color of the diamond's fluorescence when exposed to deep ultraviolet luminescence, which can occur with significant radiation exposure.

Figure 5. This round brilliant diamond displays twinning wisps that resemble a whale. Photomicrograph by Nathan Renfro; field of view 2.62 mm.

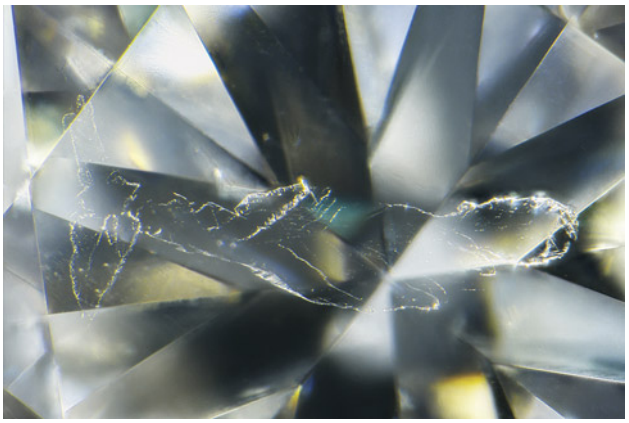

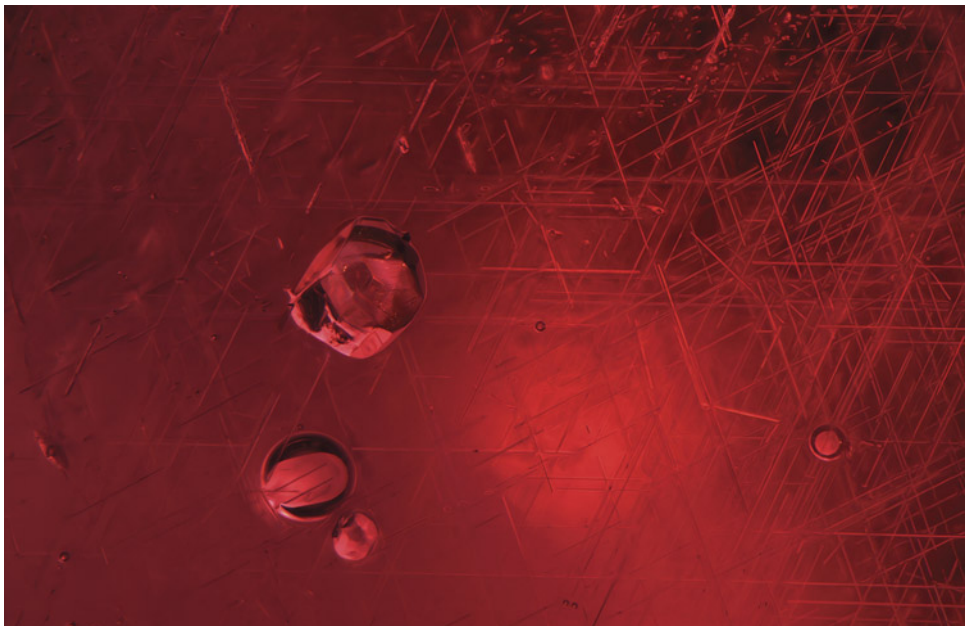

Figure 6. Gas bubbles hide just beneath natural crystal inclusions in this garnet and glass doublet. Photomicrograph by Emily Jones; field of view 1.58 mm.

This stone offers an example of how natural growth processes in diamond can result in microscopic features that occasionally form delightful patterns.

Taryn Linzmeyer and Roy Bassoo
GIA, Carlsbad

Jaldeep Sojitra
GIA, Surat

A Red Herring in a Red Garnet

At first glance, a 2.54 ct round mixed-cut stone examined by the author presented itself as a natural red garnet. Microscopic inspection revealed a host of transparent crystals and widespread epitaxial needles, both typical inclusions for garnet. Upon closer inspection, however, some of the apparent "crystals" were recognized as gas bubbles, betrayed by their smooth spherical forms (figure 6). This distinction can be easily missed without careful examination under high magnification. Additional observations and testing conclusively identified the material as pyrope-almandine garnet fused with manufactured glass. As with most garnet-topped doublets, the garnet portion was cut to occupy the crown while the glass made up most of the pavilion so that the natural inclusions of the garnet top masked the telltale signs of manufactured glass beneath.

Emily Jones
GIA, New York

Heliodor with a Large Schorl Inclusion

An 8.33 ct long rectangular heliodor, the yellow variety of beryl (ideally $Be_3Al_2Si_6O_{18}$), was examined by the author. It was reportedly from the Zelatoya Vada mine in Murgab, Tajikistan; however, it was likely from Pakistan (J.S. White, "Let's get it right: Tajikistan heliodor," *Rocks and Minerals*, Vol. 80, No. 4, 2005, pp. 285–286). The heliodor had a large schorl tourmaline inclusion prominently under the table facet (figure 7) and a small schorl tourmaline near one corner. A thin band of fine fluid inclusions ran parallel to the length of the stone adjacent to the tourmaline. The stone was clearly cut to highlight the interesting inclusion rather than hide or remove it; aside from the two tourmaline inclusions and the thin band of fluids, the beryl had high clarity.

Figure 7. Morphological features of the tourmaline crystal included in the heliodor are visible; striations and triangular growth marks are present. A band of fluid inclusions is visible near the tip of the schorl tourmaline. Photomicrograph by Rhiana Elizabeth Henry; field of view 2.90 mm. Gift of Mark Mauthner, GIA Museum no. 37772.

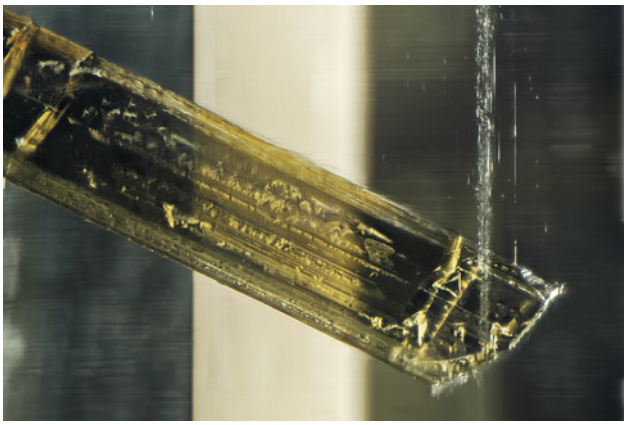

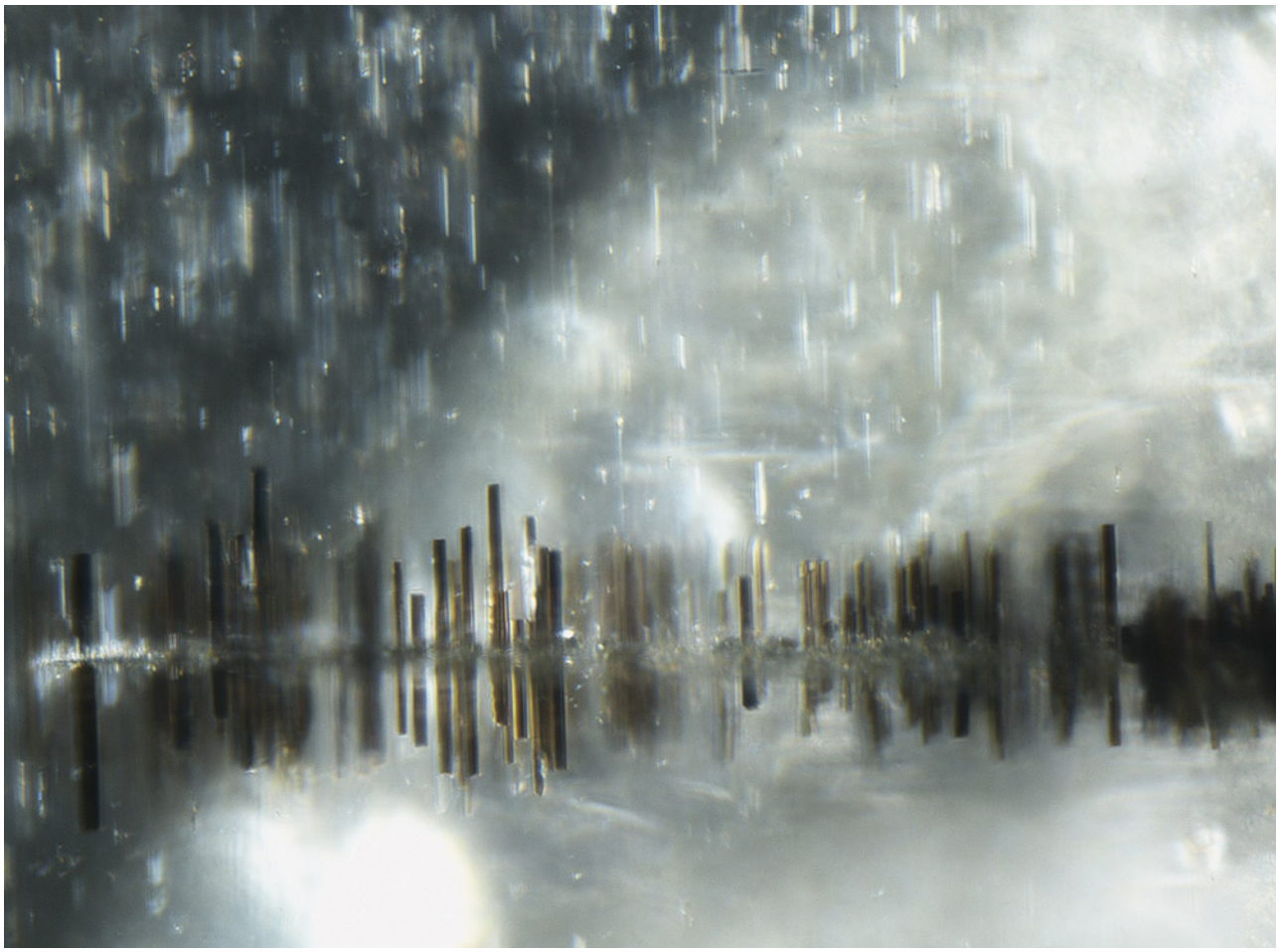

Figure 8. Blade-like magnetite inclusions developed from a healed fracture in a 2.08 ct Burmese peridot resemble a rainy lakeside city. Photomicrograph by Makoto Miura; field of view 1.06 mm.

Both the heliodor and the tourmaline were analyzed by Raman spectroscopy and laser ablation–inductively coupled plasma–mass spectrometry (LA-ICP-MS) to better understand the structure and chemistry of the minerals. Analyses were conducted on the girdle of the heliodor and on the back end of the tourmaline inclusion where it intersected a pavilion facet. The heliodor had low-moderate water bound in its structural channels, as determined qualitatively by Raman spectroscopy, which is expected for heliodor with low sodium content (R.E. Henry et al., "Crystal-chemical observations and the relation between sodium and H_2O in different beryl varieties," *Canadian Mineralogist*, Vol. 60, No. 4, 2022, pp. 625–675). The heliodor fit well within the expected chemistry; it had low overall cation substitutions, with minor or trace iron, magnesium, lithium, sodium, and cesium content. The tourmaline was confirmed to be schorl dominant due to its predominant sodium and iron content; however, due to high vacancy at the X structural site, the tourmaline had a high foitite component (D.J. Henry et al., "Nomenclature of the tourmaline-supergroup minerals," *American Mineralogist*, Vol. 96, 2011, pp. 895–913).

After data collection for research, this stone will be used in the GIA GemKids program as an educational piece for young students at the Carlsbad campus. It will represent the heliodor variety of beryl, showing fascinating inclusions as well as evidence of LA-ICP-MS laser pits on the girdle of the stone (not shown in the photomicrograph).

Rhiana Elizabeth Henry
GIA, Carlsbad

Rainy Lakeside City in Peridot

Inclusions in gemstones provide useful information regarding their geological origin. A 2.08 ct Burmese peridot containing unique black blade-like inclusions developed from healed fractures (fingerprints), as shown in figure 8. Raman spectroscopy identified these blade-like inclusions as magnetite. Tiny raindrop-like magnetite lamellae were also ob-

served throughout the stone. Such inclusions in Burmese peridot sometimes create four-rayed asterism. According to previous studies, the presence of magnetite lamellae suggests the oxidation or dehydration of olivine by geological processes. This image resembles a rainy lakeside city landscape.

Makoto Miura
GIA, Tokyo

Zigzag Fingerprint in Sri Lankan Sapphire

The author recently examined a 3.21 ct oval mixed-cut blue sapphire. Chemical analysis and gemological observation of internal fissures suggested a Sri Lankan origin. Under fiber-optic illumination, the fingerprints showed rectilinear zigzag-patterned films with vibrant colors that resulted from thin-film interference (figure 9). The rectilinear structure of this fingerprint was caused by the natural healing process of a fracture oriented parallel to the *c*-axis.

These zigzag-patterned fingerprints often indicate a Sri Lankan origin, but they can also be found in sapphires from Myanmar and Madagascar. The undamaged rectilinear pattern could indicate that the stone is unheated.

Yuxiao Li
GIA, Tokyo

Fissure with Moiré Pattern in Spinel

Surface-reaching fissures commonly host precipitates of epigenetic minerals, as was the case with a 4.22 ct purple spinel recently examined by the author. "Islands" of unidentified birefringent inclusions occupied a near-planar fissure. These inclusions were inert to Raman spectroscopy. Delicate depositions radiating from these islands interacted to create a complex moiré pattern (figure 10).

Figure 9. The rectilinear zigzag-patterned fingerprint in this 3.21 ct blue sapphire shows beautiful vibrant colors, indicating a Sri Lankan origin. Photomicrograph by Yuxiao Li; field of view 4.45 mm.

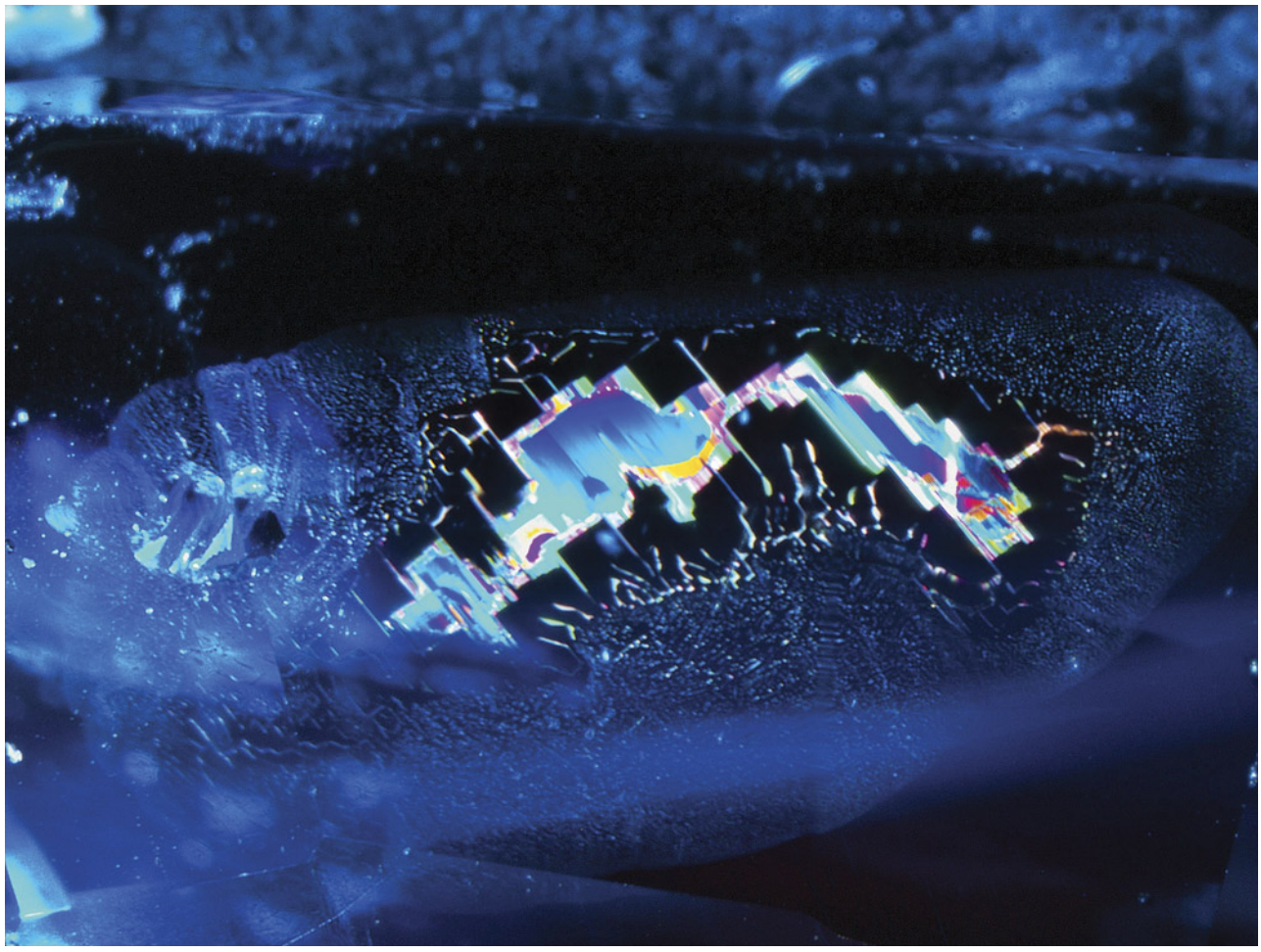

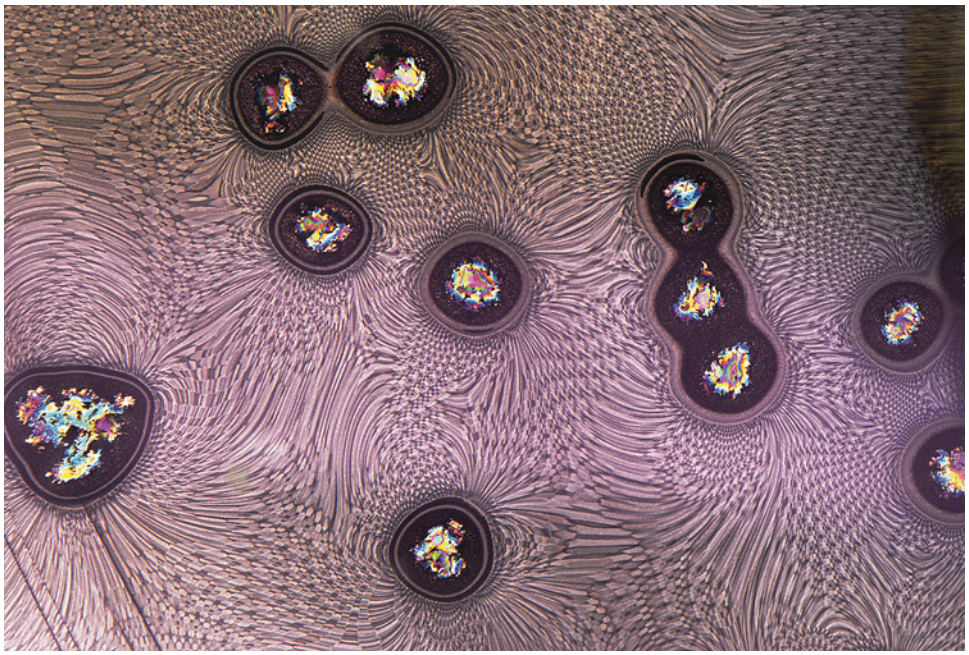

Figure 10. A precipitation of an unidentified mineral in a fissure of a purple spinel creates this highly intricate moiré pattern. A combination of oblique fiber-optic and darkfield illumination was used. Photomicrograph by Tyler Smith; field of view 2.90 mm.

Moiré patterns, named after their resemblance to a type of fabric, form when parallel or concentric lines overlap. It is unclear whether the islands formed first and were partially dissolved in a secondary event, or if they formed simultaneously with the spinel. Although moiré patterns have been observed in partially healed fluid fingerprints and surface-reaching fissures, it is rare to see them expressed in such a spectacular form.

Tyler Smith

Large Stellate Dislocation in Spinel

The author recently examined a 4.49 ct greenish blue spinel exhibiting a prominent stellate inclusion characterized by a network of needle-like dislocations clustered in a six-rayed star pattern (figure 11). The inclusion was large enough to be readily observed without magnification.

Star-like needles have been previously documented in spinel originating from Vietnam. These findings contribute to our understanding of spinel and its origins, providing

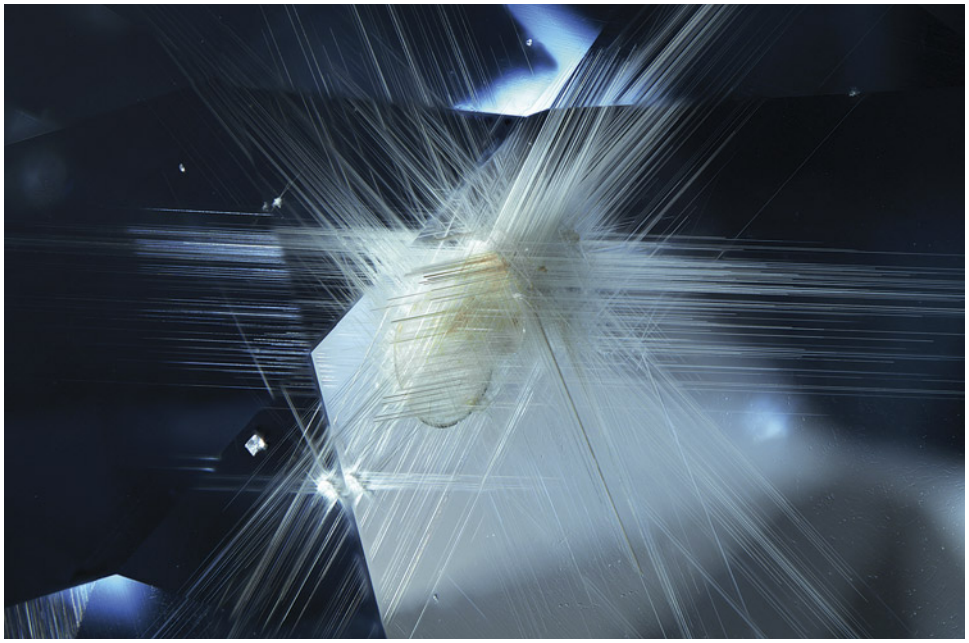

Figure 11. Stellate dislocations decorate the interior of a greenish blue spinel believed to be from Vietnam. Photomicrograph by Ezgi Kiyak; field of view 4.79 mm.

valuable information for gemologists. This is one of the most remarkable stellate inclusions the author has observed in a spinel.

Ezgi Kiyak
GIA, New York

Tourmaline in Emerald

The author recently examined a 3.80 ct emerald with well-formed black, opaque prismatic crystals (figure 12). The surface-reaching crystals were identified as tourmaline through the use of Raman spectroscopy. While tourmaline crystals are relatively uncommon inclusions, they have been documented in emeralds from Zambia, Pakistan, Russia, and Ethiopia, all of which are schist-hosted deposits. Laser ablation–inductively coupled plasma–mass spectrometry chemical analysis combined with inclusion observation revealed this emerald to be of Zambian origin.

Virginia Schneider
GIA, New York

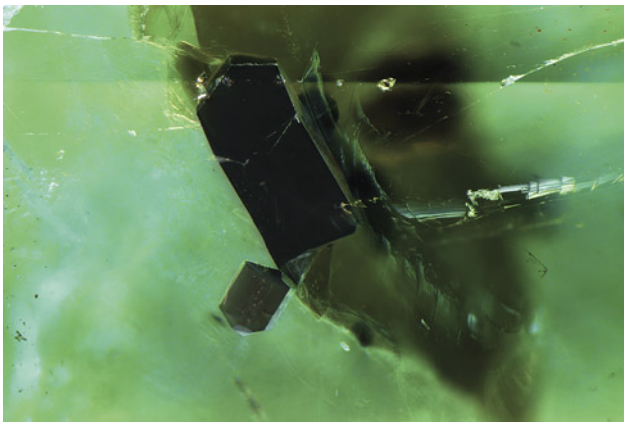

Figure 12. Prismatic black tourmaline in a Zambian emerald. Photomicrograph by Virginia Schneider; field of view 1.76 mm.

Turquoise Planet Earth

Armenia is not a widely known source of turquoise, but a recent donation to GIA's colored stone reference collection proved that the country can produce high-quality, aesthetically pleasing stones. One of them, cleverly cut into an 84.90 ct sphere measuring 23.70 × 23.88 × 23.91 mm, bore an astonishing resemblance to planet Earth (figure 13). The natural brown matrix material mimicked the continents, while the greenish blue turquoise represented the oceans. Infrared spectroscopy showed that, like most gem turquoise, the specimen had been polymer impregnated, a treatment that makes the stone more durable. Additionally,

Figure 13. An 84.90 ct sphere of Armenian turquoise measuring 23.70 × 23.88 × 23.91 mm displays a striking resemblance to planet Earth. Left: Diffuse fiber-optic lighting allows the face of the stone to be seen in full. Right: Pinpoint fiber-optic lighting creates an appearance of day and night cast onto Earth. Gifted to GIA's colored stone reference collection by Gemfab CJSC. Photos by Britni LeCroy.

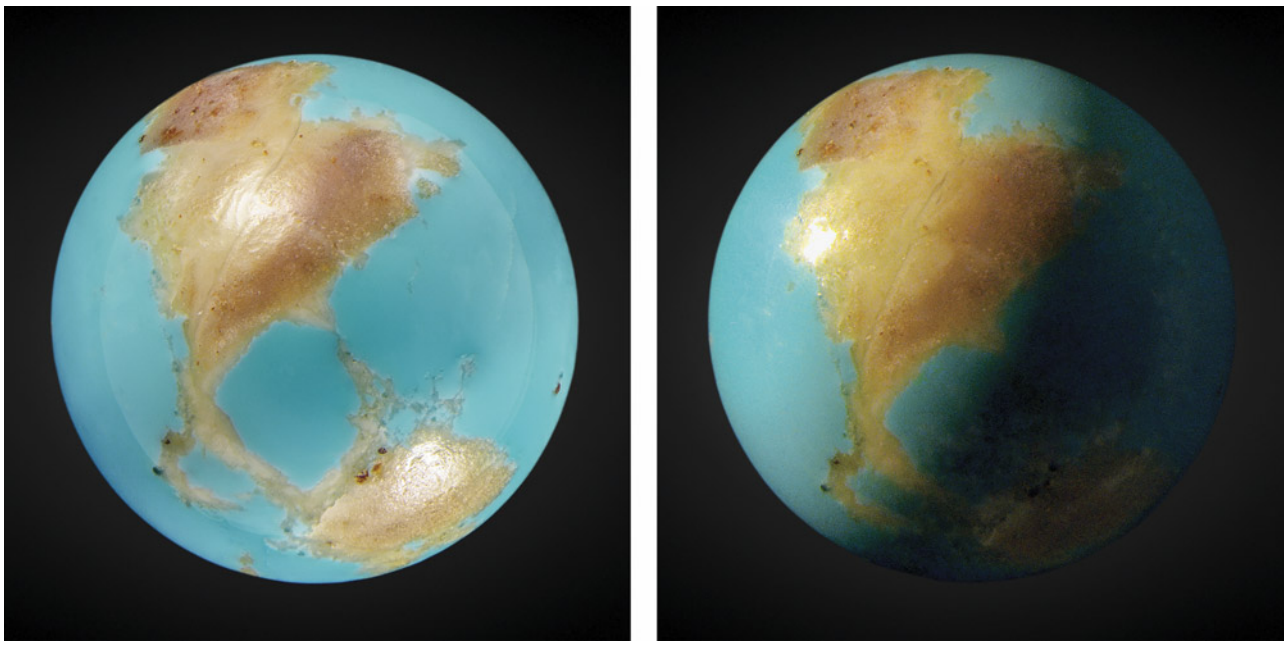

Figure 14. Dark yellowish to brownish green needle-like inclusions dominate the interior of this 21.36 ct Portuguese fluorapatite on siderite matrix. Photo by Adriana Robinson.

no dye was detected. To accentuate its likeness to our planet, the sphere was photographed against "Musou Black," marketed as the world's blackest fabric and advertised to absorb 99.905% of all light. Precise placements of pinpoint lighting created various appearances of a sunlit Earth suspended in space.

Britni LeCroy
GIA, Carlsbad

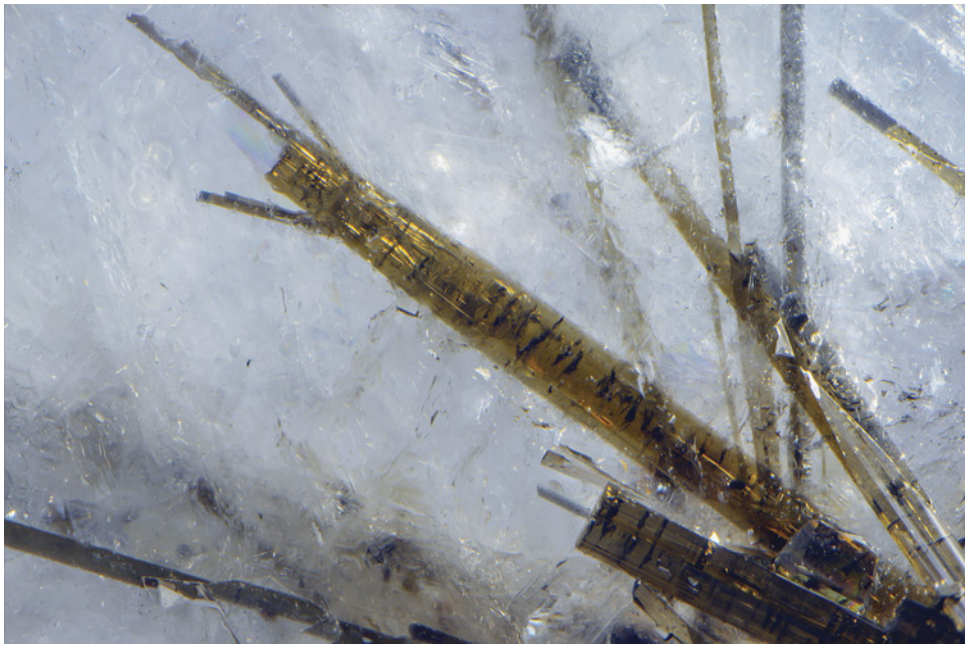

Figure 15. Raman analysis was used to identify the acicular inclusions in the fluorapatite host crystal as dravite tourmaline. Photomicrograph by Nathan Renfro; field of view 7.37 mm.

Quarterly Crystal: Dravite in Fluorapatite

Growing from an angular matrix plate of brown siderite, a doubly terminated hexagonal crystal weighing 21.36 ct with a very light purplish blue color (figure 14) was identified as fluorapatite by Raman analysis. As the photo shows, the semitransparent crystal clearly hosts a number of randomly arranged, eye-visible, translucent acicular inclusions. The fluorapatite thumbnail specimen, from the Panasqueira mine in the Castelo Branco district of Covilhã, Portugal, was acquired by author JIK from the collection of Dr. Vasco Trancoso at auction in June 2023. When the specimen was examined microscopically, the acicular morphology and dark yellowish to brownish green bodycolor of the inclusions, as well as their behavior in polarized light, suggested they might be tourmaline. Laser Raman microspectrometry was able to pinpoint their identity as dravite (figure 15), a member of the tourmaline group.

John I. Koivula, Nathan Renfro, and Maxwell Hain
GIA, Carlsbad

Editor: Evan M. Smith

Eclogite: Diamond-Encrusted Ancient Seafloor

Evan M. Smith and Matthew F. Hardman

The Link Between Eclogite and Diamonds

Earth's surface is divided into tectonic plates, and the ones that make up the ocean floor are destined to sink. Sheets of oceanic crust typically bend and sink down into Earth's interior at so-called subduction zones. Occasionally these banished slivers of ancient seafloor may become a sort of unexpected canvas to be painted with a sparkling sea of diamonds. In fact, ancient seafloor rocks that have been incorporated into old and thick parts of continents are one of the most important mantle substrates or "host rocks" for diamond growth (Stachel et al., 2022a). This particular host rock, known as eclogite, can be found as distinct fragments, called xenoliths, at some diamond mines and is also represented by mineral inclusions in diamonds (figure 1).

Our current understanding of where and how diamonds crystallize is largely based on mineral inclusions trapped inside them. The diamonds we mine were brought up to Earth's surface by kimberlites and related magmatic rocks, but they did not crystallize directly from this magma. Rather, the diamonds formed by independent processes and are usually millions or billions of years older than the kimberlitic magmas that inadvertently swept them up to the surface. Most diamonds (~98%) were formed at a depth of about 150–200 km within the continental lithosphere, essentially in old and thick parts of continents. Based on the relative abundance of mineral inclusions in a studied set of 2,844 diamonds, the three principal mantle host rocks here are peridotite (65%), eclogite (33%), and websterite (2%) (Stachel and Harris, 2008). Eclogitic diamonds constitute a significant portion of the gem diamond market, and their features embody the dynamic processes unique to Earth.

What Is Eclogite?

Typically, eclogite refers to a colorful red and green metamorphic rock that is made up of two key minerals: grossular-almandine-pyrope garnet and omphacitic clinopyroxene (figure 2) (Winter, 2010). Additional minerals sometimes present include rutile, coesite, kyanite, and iron-rich sulfides. All of these can be encountered as mineral inclusions in diamond. Eclogite can form in several ways, but the dominant process involves oceanic crust sinking down into the mantle (by subduction). The basalt and gabbro that make up oceanic

Figure 1. Mineral inclusions in diamond. This connected pair of green clinopyroxene and orange garnet indicates that diamond growth occurred within an eclogitic mantle host rock. Photomicrograph by Nathan Renfro; field of view 2 mm.

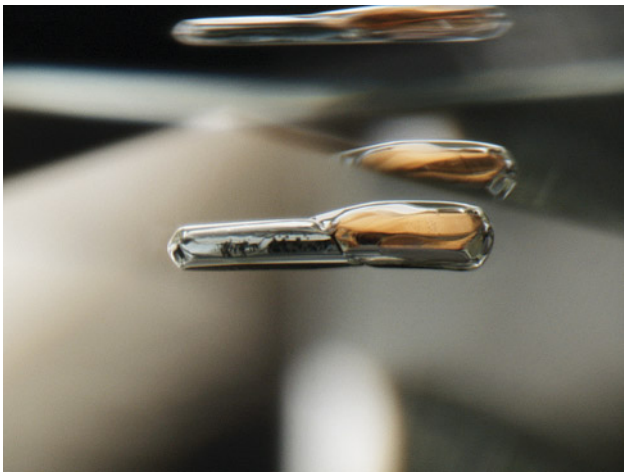

Editor's note: Questions or topics of interest should be directed to Evan Smith (evan.smith@gia.edu).

Gems & Gemology, Vol. 59, No. 3, pp. 380–386.

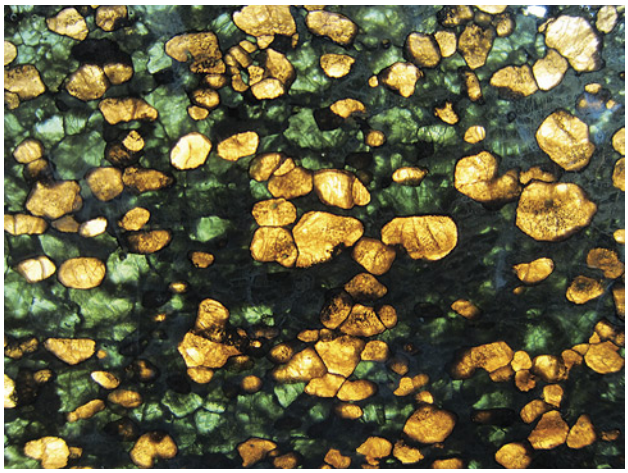

Figure 2. Polished slice of an eclogite xenolith. This backlit specimen shows the typical orange garnet and green clinopyroxene that make up eclogite. Recovered from the Roberts Victor mine in South Africa, this eclogite xenolith (sample JJG-243) is part of the Mantle Room collection curated by the University of Cape Town. Photomicrograph by Evan M. Smith; field of view approximately 5 cm.

crust undergo a transformation, known as metamorphism, as a result of changes in pressure and temperature that cause some minerals to break down and new ones to form.

Metamorphic rocks are sometimes classified into groups, called metamorphic facies, based on the pressure and temperature conditions at which they formed. One of these groups is known as eclogite facies. Any given metamorphic facies encompasses metamorphic rocks that form under the same range of pressure and temperature conditions, regardless of what the exact starting rock, or protolith, might have been. Figure 3 shows where the eclogite facies and other metamorphic facies fall within a pressure vs. temperature diagram. When basalt or gabbro from the oceanic crust get subducted, they metamorphose through zeolite and blueschist facies before transforming into eclogite at depths of about 50 km.

If the eclogite were carried deeper still, the clinopyroxene would begin to break down between 300 and 400 km, followed by the appearance of a new phase, stishovite (SiO_2) (Irifune and Ringwood, 1987). At this point, it would technically not be eclogite but could be described by the more general terms *metabasalt* or *metagabbro*. With varying pressure and temperature, the mineralogy can change drastically, even if the bulk composition of the rock remains unchanged.

Ancient Seafloor and the Process of Subduction

Inclusions (figure 1) and xenoliths (figure 2) show that eclogite has served as a host rock for diamond growth at depths of about 150–200 km. But that eclogite has actually

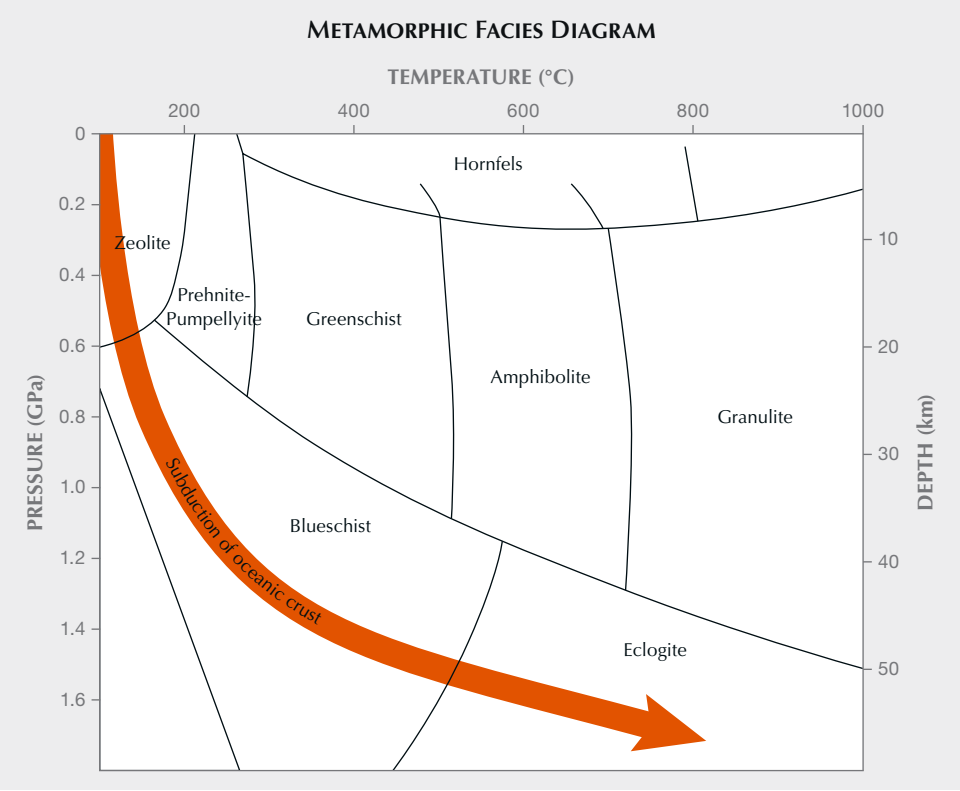

Figure 3. Metamorphic facies diagram. Each field in this pressure vs. temperature chart represents a group of metamorphic rocks that share similar characteristics. Eclogite is a high-pressure metamorphic facies as well as a rock name. The orange line gives a hypothetical pathway for the subduction of oceanic crust. Boundaries are gradational and do not actually exist as sharp divisions in P-T *space. Adapted from Winter (2010).*

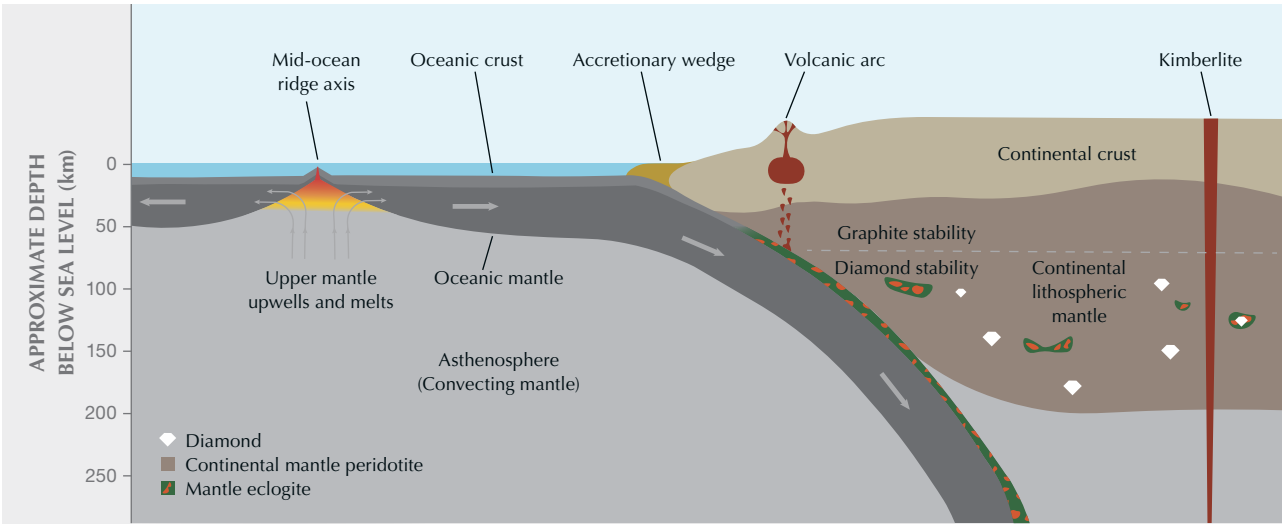

Figure 4. Diagram of a mid-ocean ridge and subduction zone. At mid-ocean ridges, the upper mantle upwells and melts, and the melts crystallize as oceanic crust. The oceanic crust spreads away from the ridge and subducts into the mantle beneath continental crust, which is more buoyant. Diamonds may be stable in the deep roots of continents, within the continental lithospheric mantle. They may form in association with mantle peridotite or eclogite. Kimberlite may rip diamond and mantle rocks from these deep roots as they erupt to the surface.

traveled a long way from its birthplace. Those same eclogitic inclusions and xenoliths have chemical and isotopic characteristics indicating that the protolith originated at Earth's surface as oceanic crust. Present-day ocean floors are composed of oceanic crust with an underlying layer of mantle peridotite, which together form a rigid plate called lithosphere that "floats" upon the convecting upper mantle because it is less dense (figure 4). Oceanic crust is generated at mid-ocean ridges, where the two plates on either side of the ridge spread apart from one another. The gap left between the diverging plates is filled by rock that flows up from beneath and partially melts, producing the magma that will make up newly formed crust. When these magmas erupt at the seafloor, they cool quickly and form a dark, fine-grained rock called basalt. At deeper levels within a mid-ocean ridge, the magma cools slowly and crystallizes as coarser-grained rocks, chiefly gabbro.

Oceanic crust is produced continuously at mid-ocean ridges on the ocean floor. Old crust is pushed farther from the ridge as new crust is produced. Old oceanic crust will cool, increasing its density. After millions of years, and driven by continual mid-ocean spreading, the oceanic crust will eventually collide with continental crust, which is generally much less dense due to its different mineralogy and elemental composition. When the oceanic crust collides with continental crust, the large difference in density leads the oceanic crust to subduct into the upper mantle beneath the continental crust (figure 4).

Subduction is the process by which a plate on the earth's surface moves beneath another and sinks into the mantle. During subduction, oceanic crust undergoes a progressive sequence of metamorphic reactions as pressure and temperature increase with depth (figure 3). This increases the density of the rock, which may continue to subduct until it transforms into eclogite. Occasionally, subducted eclogite is incorporated into the deep roots beneath continents, where the majority of diamond formation occurs, as shown by the green and orange lenses in figure 4.

Geoscientists can inspect aspects of eclogite geochemistry and isotopic composition to reconstruct its history. For example, when basalt forms at a mid-ocean ridge, it has an oxygen isotope composition that is similar to the upper mantle source region from which it was derived. When seawater interacts with oceanic crust, however, it can change the oxygen isotope composition of the rock, shifting it away from the original mantle-like value. Oxygen isotope compositions of minerals in eclogite that are outside the range of the typical ambient mantle are considered evidence that the eclogite had a protolith that was exposed to seawater prior to subduction (Jacob, 2004; Korolev et al., 2018, and references therein).

Eclogites also have relatively high concentrations of sodium compared to many other mantle rocks. This sodium comes from plagioclase in the oceanic protoliths, but during subduction the plagioclase becomes unstable and breaks down, with its constituent elements—including sodium—redistributed to new minerals formed during metamorphism.

With the proper analytical equipment, elements with extremely low abundance (e.g., concentrations at the parts per million or billion level) can be measured in eclogite minerals. Among these are the rare earth elements (REE), which are a group of 17 elements including the lanthanides (lanthanum, cerium, praseodymium, neodymium, promethium, samarium, europium, gadolinium, terbium, dyspro-

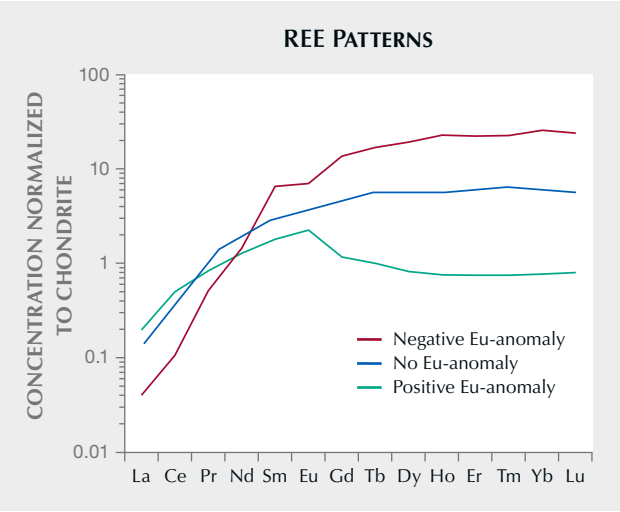

Figure 5. REE patterns for three eclogites with different europium anomalies. The concentrations of all elements are normalized to the elemental concentrations in chondritic meteorites (McDonough and Sun, 1995).

sium, holmium, erbium, thulium, ytterbium, and lutetium) plus scandium and yttrium. Slight differences in the behavior of these elements during geological processes can lead to changes in their relative concentrations, imparting a sort of chemical imprint of a rock's history. REE concentrations in igneous rocks can be inherited from their magmatic sources and subsequently modified by melting and other processes in the earth.

In many mantle rocks, REE patterns will have a smooth trend, with the concentration of europium being intermediate to the elements samarium and gadolinium (figure 5). Some eclogites, however, may have a positive or negative europium "anomaly" when compared to samarium and gadolinium (figure 5). The mineral plagioclase tends to have strong positive europium anomalies, as europium incorporates into plagioclase very strongly relative to other REE. Consequently, an igneous rock that accumulates plagioclase (such as gabbro in oceanic crust) may inherit a positive europium anomaly. A rock that forms from a magma that previously crystallized plagioclase (such as an oceanic lava) will have a negative europium anomaly. As plagioclase is only stable in the shallow portions of the earth (<30 km, approximately), eclogites with detectable europium anomalies are generally inferred to have protoliths that formed at shallow depths. Seeing this signature in mantle-derived rocks, such as eclogite xenoliths at a diamond mine, requires that those rocks formed near the surface and were carried down into the mantle by subduction (and in the case of xenoliths, these rocks have been brought back up again by kimberlites). Eclogite xenoliths really have come a long way.

Recycled Carbon and Its Contribution to Diamond Growth

Not all carbon atoms are identical. By paying close attention to differences in their mass (carbon isotopes), geologists have observed that diamonds formed in eclogite are distinguished by an unusual signature (figure 6). The signature suggests that eclogitic diamonds contain "recycled" carbon that was subducted from Earth's surface down into the mantle, where diamond growth occurred (figure 4).

A typical carbon atom has 6 protons and 6 neutrons in its nucleus, which sum to give its atomic mass, 12. Carbon-

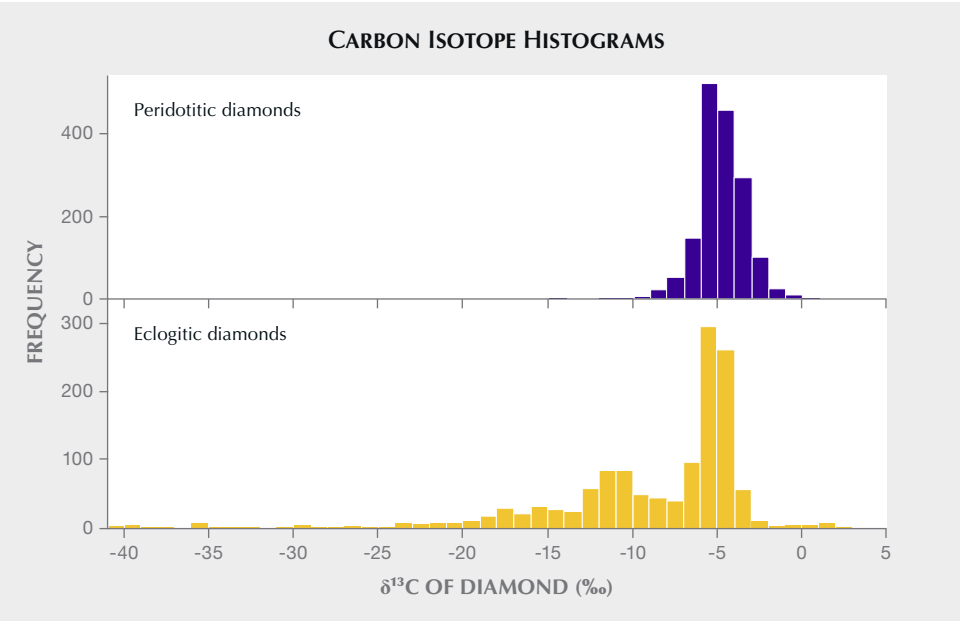

Figure 6. Carbon isotope histograms for peridotitic and eclogitic diamonds. While both histograms show a mode centered near –5‰ that corresponds to mantle carbon, eclogitic diamonds have a tail of negative values stretching beyond –40‰ that is thought to reflect subducted organic carbon. Data are from Stachel et al. (2022b).

12 (^{12}C) is the most common isotope of carbon. About 1% of naturally occurring carbon atoms have an extra neutron and therefore a mass of 13. Carbon-13 (^{13}C) is the second-most abundant isotope of carbon. Given that ^{12}C and ^{13}C have different masses, they behave slightly differently during chemical reactions. When plants grow, for example, photosynthesis favors ^{12}C. As a result, plants are enriched in ^{12}C (and depleted in ^{13}C) relative to the initial carbon dioxide in the atmosphere. Scientists can gain insight into many carbon-bearing materials by measuring the relative proportions of ^{12}C and ^{13}C. For any measurement, the $^{13}C/^{12}C$ ratio is reported in terms of how different it is from an agreed-upon standard (a reference known as the Vienna Pee Dee Belemnite). This deviation is written as $\delta^{13}C$ (pronounced "delta C thirteen") expressed in parts per thousand (per mille, ‰) and is calculated as $\delta^{13}C = [(^{13}C/^{12}C)_{sample}/(^{13}C/^{12}C)_{standard} - 1] \times 1000$.

Figure 6 shows $\delta^{13}C$ values for peridotitic and eclogitic diamonds. The histograms convey information about sources of carbon and potentially about the chemical process of diamond formation as well. In both histograms, the large peak centered at –5‰ corresponds to the average composition of carbon spread throughout the mantle (Cartigny, 2005). Eclogitic diamonds, however, possess a conspicuous tail of negative values or "light" isotopic compositions. These negative values are one of the most debated features of diamond geology, with no firm consensus on the exact processes at play (Cartigny, 2005).

The most accepted general view is that the negative isotopic trend of eclogitic diamonds stems from subducted carbon (Li et al., 2019; Stachel et al., 2022b). Subducted carbon is thought to mix with the ambient carbon already present in the mantle to give the range of observed carbon isotopic characteristics in eclogitic diamonds (figure 6). The recycled carbon could come in the form of sediments and altered oceanic crust containing organic matter and carbonates (biogenic and abiogenic) (Li et al., 2019). Taking into account the covariations in nitrogen concentration and isotopes suggests that eclogitic diamond formation involves multiple subducted ingredients that mix in complex ways during the process (Stachel et al., 2022b). Although there are unresolved details, the evidence is strong that a portion of the carbon in eclogitic diamonds is subducted. These diamonds are a physical manifestation of the deep and ancient geological carbon cycle.

Eclogitic Diamond Ages

Through the incredible phenomenon of radioactive decay, many rocks and minerals have a sort of built-in natural clock. Radioactive decay is the process whereby unstable radioactive elements break down over time, with different elements each having a predictable decay rate. Several decay systems apply to various types of inclusions in diamonds, and their analysis has led to our understanding that diamonds are millions to billions of years old (Smit and Shirey, 2019). The oldest diamonds are 3.5 billion years old, and diamonds have been forming episodically since that time, spanning three-quarters of Earth's history. Their antiquity combined with their deep mantle origin makes diamonds a unique record of large-scale geological evolution.

For example, diamond ages may provide a time stamp to mark the beginning of modern-style plate tectonics. Many of us are at least vaguely familiar with the notion that roughly 200 million years ago, the continents to the east and west of the Atlantic Ocean were nestled together in the supercontinent Pangaea. The Atlantic grew and opened up as Pangaea broke apart. The subduction zone and mid-ocean ridge spreading center depicted in figure 4 are integral mechanisms that explain how tectonic plates move, how new oceans form, and how old ones close and vanish. This dynamic surface structure is unique to Earth. Our planet did not always have plate tectonics, however, and at one point, its surface was a giant magma ocean. So when exactly did things change and the processes we observe today take hold?

Geologists have used several methods to constrain the timing of when plate tectonics began, including clues from diamonds. Comparing samples of different ages reveals that they are not all equal across time. Diamonds older than 3.0 billion years are exclusively peridotitic, whereas eclogitic diamonds only become prevalent among those younger than 3.0 billion years. This change arguably marked the first major episode of subduction of oceanic crust beneath a continent and the onset of the Wilson-cycle style of movements that characterize modern plate tectonics (Shirey and Richardson, 2011). Effectively, this model suggests there are no eclogitic diamonds older than 3.0 billion years because oceanic crust was not yet being subducted and incorporated as eclogite into the continental lithospheric mantle.

Economic Importance of Eclogitic Diamonds

Finding an economic diamond deposit is no trivial matter. Even after locating one or more kimberlites (figure 7) or lamproites, it is a challenging exercise to evaluate the quantity and quality of diamonds. A key variable that can make or break a potential mine is the presence of eclogitic diamonds. In some deposits, eclogitic diamonds are much more abundant than might be expected based on the relatively small amount of eclogite in the mantle.

Most of the continental lithospheric mantle is made up of peridotite (>95 vol.%; figure 4). Conversely, eclogite has a low global abundance (<5 vol.%) (Dawson and Stephens, 1975; Schulze, 1989), yet some mines can contain much higher abundances of eclogitic diamonds, to the point where they dominate the diamond population, such as at Koidu (Sierra Leone) and Orapa (Botswana). One in three diamonds have eclogitic vs. peridotitic mineral inclusions, indicating a relatively large proportion of diamonds are associated with eclogite (Stachel and Harris,

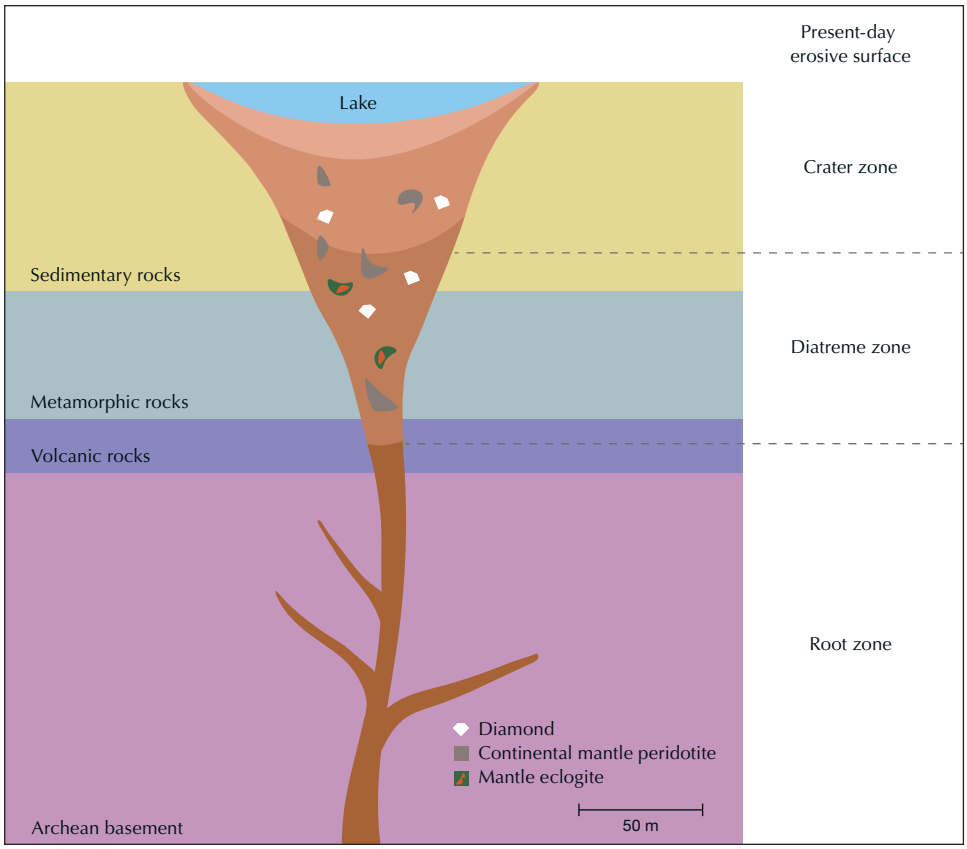

Figure 7. Diagram of a hypothetical kimberlite pipe. The kimberlite erupts through existing rocks and geologic formations ("country rock"). The shape, size, and distribution of rocks within a kimberlite pipe are highly variable from occurrence to occurrence. The country rock is arbitrary in this diagram and will vary based on the local geology into which the kimberlite erupts. The majority of kimberlites are not diamond-bearing (Kjarsgaard et al., 2022).

2008). While not all eclogites are associated with diamond, small volumes of eclogite in some kimberlites could be indicative of diamond-rich deposits.

Kimberlites can be very small (as small as 50 m across) and show very little topographic relief, making them difficult to find. Over millions of years, these sites may become completely covered by vegetation or water (forming lakes). In these cases, kimberlites can be located by exploiting their physical properties, as they erupt through existing rock and may have different magnetic or gravimetric properties from the surrounding material. Aerial surveys that passively examine the landscape, searching for gravitational or magnetic anomalies, could potentially identify a kimberlite.

A more direct approach is to use kimberlite indicator minerals (figure 8). Even in kimberlites that are diamond-bearing, diamonds may be present in abundances at the parts per million level. Conversely, rocks that are associated with diamonds are generally much more abundant and easier to locate. Minerals in these rocks commonly have elemental compositions that reflect the rock from which they derived and, occasionally, an association with

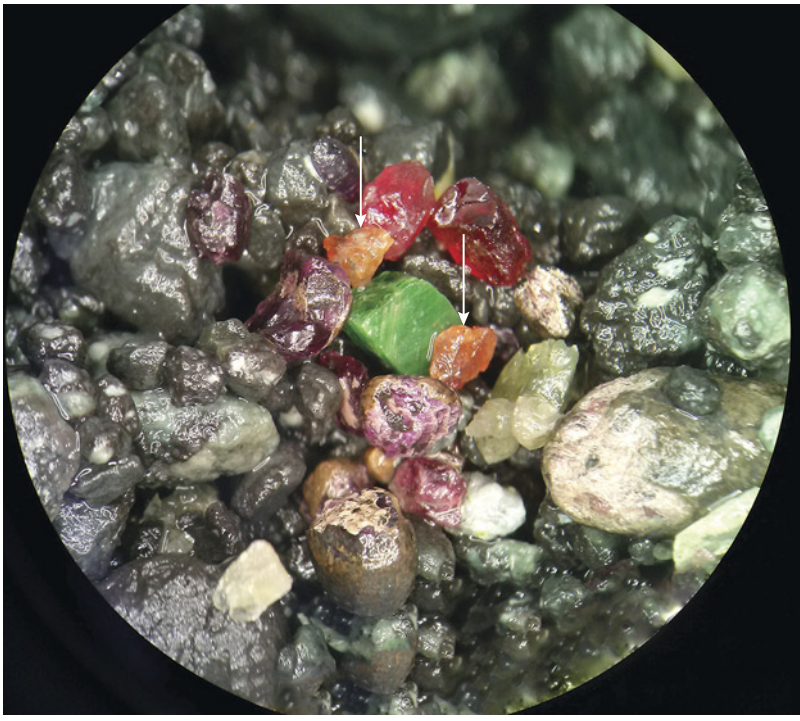

Figure 8. Broken-up sample of kimberlite from the Ekati diamond mine in northern Canada featuring colorful mantle indicator mineral grains. The bright green diopside and purple garnets are from peridotite, and the orange garnets (indicated by arrows) are from eclogite. Photo by Evan M. Smith; field of view approximately 2 cm.

diamond itself. For example, there is an observed association between diamond and mantle peridotites that are very chemically depleted (i.e., experienced substantial melting in the mantle, removing elemental components from their structure) (Gurney, 1984). The compositions of the garnets in these peridotites are characterized by low calcium contents and high chromium contents (Grütter et al., 2004). Garnets in eclogite are very different and instead have low chromium contents and variable calcium (Grütter et al., 2004). Given the disproportionate number of eclogitic diamonds compared to the global abundance of eclogite, even a small number of eclogitic garnets, such as the orange grains in figure 8, may indicate an economically valuable deposit. Minerals within kimberlite can be redistributed by rivers or glaciers, so if a garnet with composition similar to those associated with diamond is found in stream sediment or glacial till, this could indicate that a kimberlite deposit—possibly a diamond-bearing one—occurs upstream. When identified, a kimberlite deposit could one day be developed into an operating diamond mine.

ABOUT THE AUTHORS

Dr. Evan M. Smith is a senior research scientist with GIA in New York, and Dr. Matthew F. Hardman is a research scientist at GIA in Carlsbad, California.

REFERENCES

Cartigny P. (2005) Stable isotopes and the origin of diamond. *Elements*, Vol. 1, No. 2, pp. 79–84, http://dx.doi.org/10.2113/gselements.1.2.79

Dawson J.B., Stephens W.E. (1975) Statistical classification of garnets from kimberlite and associated xenoliths. *Journal of Geology*, Vol. 83, No. 5, pp. 589–607.

Grütter H.S., Gurney J.J., Menzies A.H., Winter F. (2004) An updated classification scheme for mantle-derived garnet, for use by diamond explorers. *Lithos*, Vol. 77, No. 1-4, pp. 841–857, http://dx.doi.org/10.1016/j.lithos.2004.04.012

Gurney J.J. (1984) A correlation between garnets and diamonds in kimberlite. In J.E. Glover and P.G. Harris, Eds., *Kimberlite Occurrence and Origin: A Basis for Conceptual Models in Exploration*, Volume Publication 8, Geology Department and University Extension, University of Western Australia, pp. 143–166.

Irifune T., Ringwood A.E. (1987) Phase transformations in primitive morb and pyrolite compositions to 25 Gpa and some geophysical implications. In M.H. Manghnani and Y. Syono, Eds., *High-Pressure Research in Mineral Physics.* Terra Scientific Publishing Company, Tokyo, and the American Geophysical Union, Washington DC, pp. 231–242, http://dx.doi.org/10.1029/GM039p0231

Jacob D.E. (2004) Nature and origin of eclogite xenoliths from kimberlites. *Lithos*, Vol. 77, No. 1-4, pp. 295–316, http://dx.doi.org/10.1016/j.lithos.2004.03.038

Kjarsgaard B.A., de Wit M., Heaman L.M., Pearson D.G., Stiefenhofer J., Janusczcak N., Shirey S.B. (2022) A review of the geology of global diamond mines and deposits. *Reviews in Mineralogy and Geochemistry*, Vol. 88, No. 1, pp. 1–117, http://dx.doi.org/10.2138/rmg.2022.88.01

Korolev N.M., Melnik A.E., Li X.-H., Skublov S.G. (2018) The oxygen isotope composition of mantle eclogites as a proxy of their origin and evolution: A review. *Earth-Science Reviews*, Vol. 185, pp. 288–300, http://dx.doi.org/ 10.1016/j.earscirev.2018.06.007

Li K., Li L., Pearson D.G., Stachel T. (2019) Diamond isotope compositions indicate altered igneous oceanic crust dominates deep carbon recycling. *Earth and Planetary Science Letters*, Vol. 516, pp. 190–201, http://dx.doi.org/10.1016/j.epsl.2019.03.041

McDonough W.F., Sun S.-S. (1995) The composition of the Earth. *Chemical Geology*, Vol. 120, No. 3-4, pp. 223–253, http://dx.doi.org/10.1016/0009-2541(94)00140-4

Schulze D.J. (1989) Constraints on the abundance of eclogite in the upper mantle. *Journal of Geophysical Research: Solid Earth*, Vol. 94, No. B4, pp. 4205–4212, http://dx.doi.org/10.1029/JB094iB04p04205

Shirey S.B., Richardson S.H. (2011) Start of the Wilson Cycle at 3 Ga shown by diamonds from subcontinental mantle. *Science*, Vol. 333, No. 6041, pp. 434–436, http://dx.doi.org/10.1126/science.1206275

Smit K.V. and Shirey S.B. (2019) Diamonds from the Deep: How old are diamonds? *Are* they forever? *G&G*, Vol. 55, No. 1, pp. 102–109.

Stachel T., Harris J.W. (2008) The origin of cratonic diamonds—Constraints from mineral inclusions. *Ore Geology Reviews*, Vol. 34, No. 1-2, pp. 5–32, http://dx.doi.org/10.1016/j.oregeorev.2007.05.002

Stachel T., Aulbach S., Harris J.W. (2022a) Mineral inclusions in lithospheric diamonds. *Reviews in Mineralogy and Geochemistry*, Vol. 88, No. 1, pp. 307–391, http://dx.doi.org/10.2138/rmg.2022.88.06

Stachel T., Cartigny P., Chacko T., Pearson D.G. (2022b) Carbon and nitrogen in mantle-derived diamonds. *Reviews in Mineralogy and Geochemistry*, Vol. 88, No. 1, pp. 809–875, http://dx.doi.org/10.2138/rmg.2022.88.15

Winter J.D. (2010) *Principles of Igneous and Metamorphic Petrology*, 2nd ed. Upper Saddle River, New Jersey, Pearson Education, 702 pp.

Knowledge and Skills for Today's Hot Topics

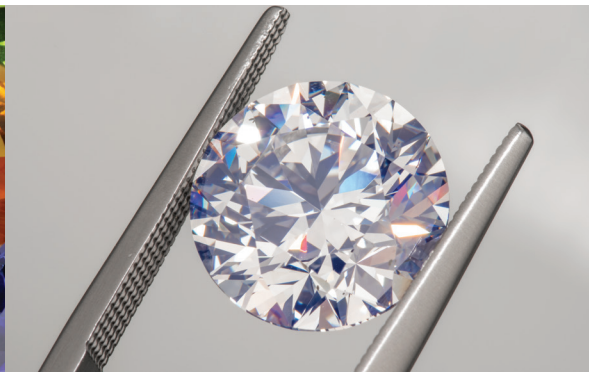

Online and In-Person Seminars Designed for Gem and Jewelry Professionals

- Natural and Laboratory-Grown Diamonds
- Jewelry Design
- Colored Stones
- Pearls
- Bench Skills

Visit **collective.gia.edu/seminars** for schedules and more information.

GIA Alumni receive a 10% discount. Seminars are open to all.

CONTINUING EDUCATION BY GIA Alumni Collective™

GEM NEWS INTERNATIONAL

Contributing Editors
Gagan Choudhary, *IIGJ-Research & Laboratories Centre, Jaipur, India* (gagan.choudhary@iigjrlc.org)
Christopher M. Breeding, *GIA, Carlsbad* (christopher.breeding@gia.edu)
Guanghai Shi, *School of Gemmology, China University of Geosciences, Beijing* (shigh@cugb.edu.cn)

COLORED STONES AND ORGANIC MATERIALS

The special color effect in "chameleon" amber. One special variety of Burmese amber is "chameleon" amber, named for the bluish green color that appears to float on its surface (figure 1). This material is found in the famous Tengchong market in Yunnan Province, China's largest Burmese amber market. Its bodycolor ranges from golden brown to brownish red or even red (figure 2A). When exposed to sunlight or strong white light against a black background, its surface shows a uniform green color (figure 2B). Chameleon amber is rare and expensive compared to regular Burmese golden or brownish amber, especially with the severe reduction of exports from Myanmar.

Until recently, few studies have been conducted on chameleon amber. X. Jiang et al. speculated that the green surface color might be caused by the superposition of its bodycolor and the fluorescence of amber ("Gemmological and spectroscopic characteristics of different varieties of amber from the Hukawng Valley, Myanmar," *Journal of Gemmology*, Vol. 37, No. 2, 2020, pp. 144–162). C.C. Shuai et al. proposed that the "light retention" effect was related to elevated sulfur and calcium contents ("The spectrum characteristic research of color change effect and 'light tarry effect' amber from Burma," *Spectroscopy and Spectral Analysis*, Vol. 40, 2020, pp. 1174–1178). Z. Shi et al. reported that the effect might be due to unique internal aromatic hydrocarbon structures ("Spectral characteristics of unique species of Burmese amber," *Minerals*, Vol. 13, No. 2, 2023, article no. 151).

Editors' note: Interested contributors should send information and illustrations to Stuart Overlin at soverlin@gia.edu.

Gems & Gemology, Vol. 59, No. 3, pp. 388–412.

For this study, three Burmese chameleon amber specimens were acquired from the Tengchong market (see figures 1, 2A, and 3A). All three displayed a translucent brownish red bodycolor, with a few bubbles and flow lines within them. The bluish green floating color was observed when the specimens were rotated. This phenomenon is most obvious with a black background. Standard gemological properties and Fourier-transform infrared spectroscopy data were consistent with those of regular Burmese amber. While the bluish green floating color might be related to fluorescence, no such effect is seen on other types of fluorescing Burmese amber (e.g., brownish amber). To further explore this, brownish Burmese amber beads with bodycolor similar to that of chameleon amber were selected as a reference (figures 2C and 3C). Their bodycolor was not as vivid as chameleon amber, and it did not display the bluish green floating fluorescence. Observation under a UV lamp showed

Figure 1. A good-quality 88.25 ct "chameleon" amber with a red bodycolor displaying a vivid green fluorescence color that appears to float on the surface. Photo by Yan Li.

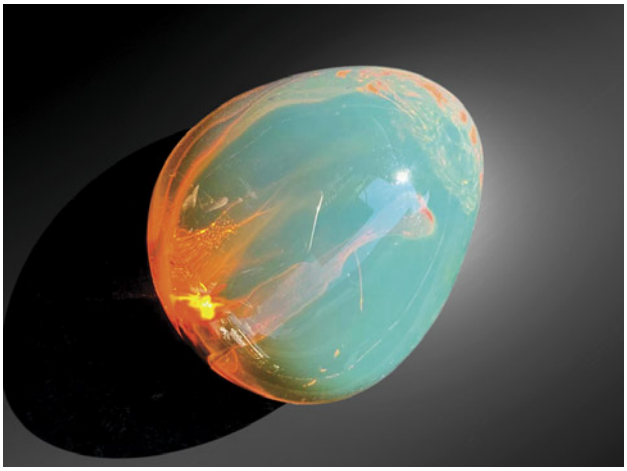

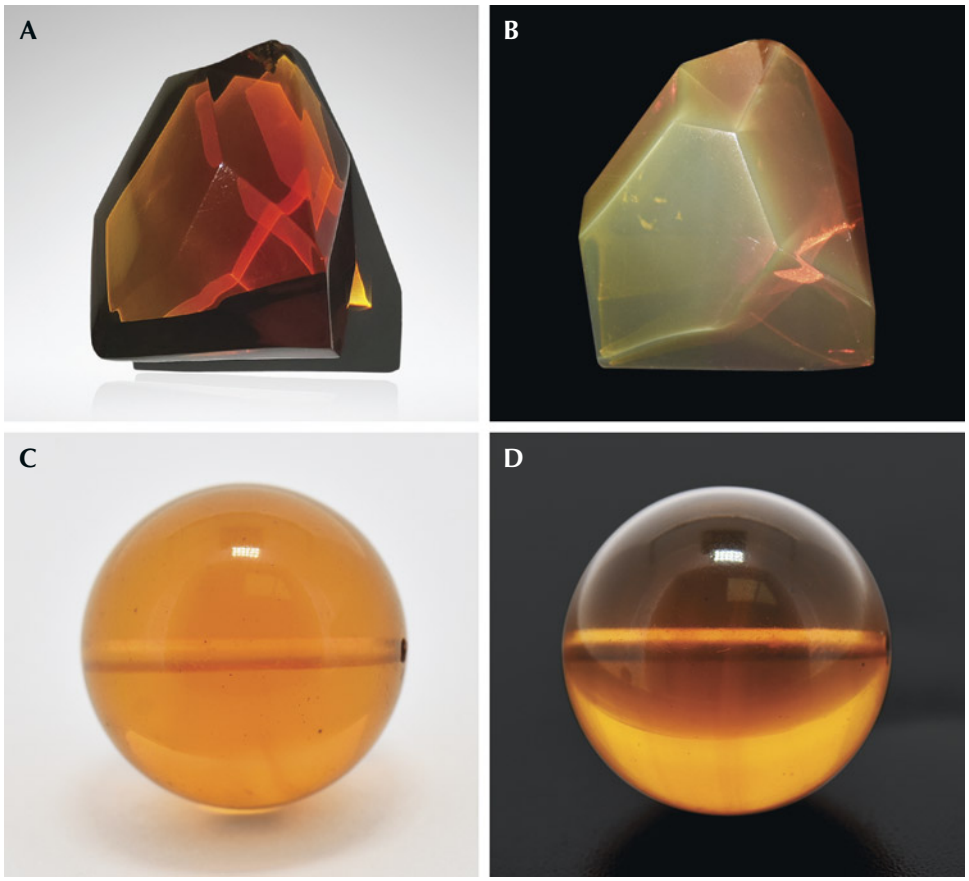

Figure 2. A and B: A 78.51 ct chameleon amber exposed to white light against white and black backgrounds. C and D: A 12.50 ct brownish reference sample exposed to similar lighting and backgrounds. Photos by Jinfeng Yang.

that the chameleon amber in figure 3A produced strong bluish white fluorescence (figure 3B) in long-wave UV (365 nm), while the brownish amber beads in figure 3C showed a weak bluish purple fluorescence (figure 3D).

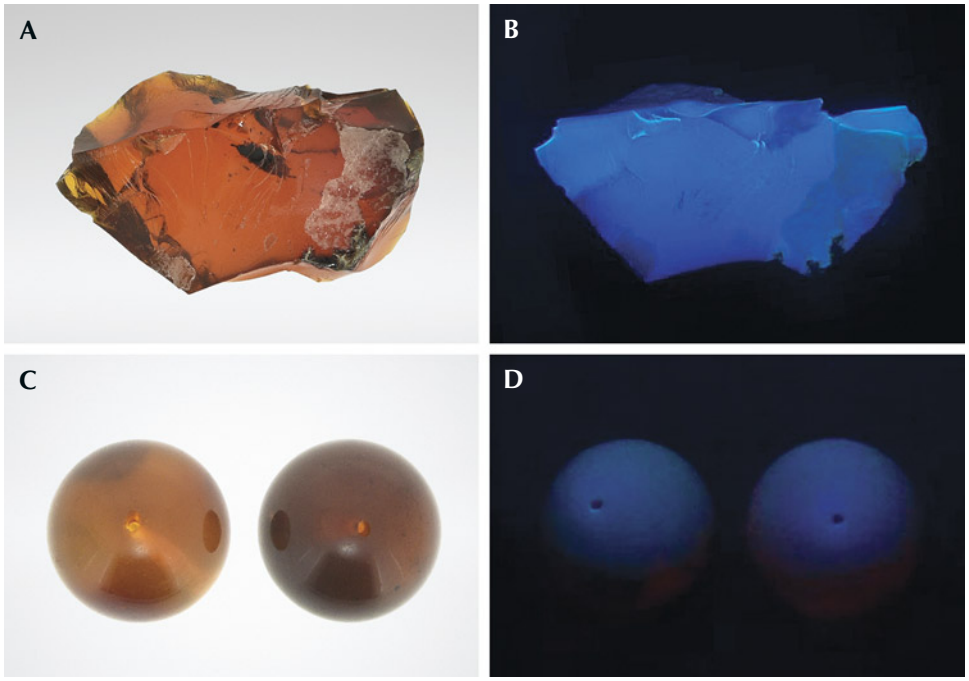

Figure 3. A and B: A 71.05 ct Burmese chameleon amber and its bluish white fluorescence under long-wave UV light. C and D: 16 mm brownish Burmese amber beads (12.60 ct on the left, 12.16 ct on the right) and their bluish purple fluorescence under long-wave UV. Photos by Jinfeng Yang.

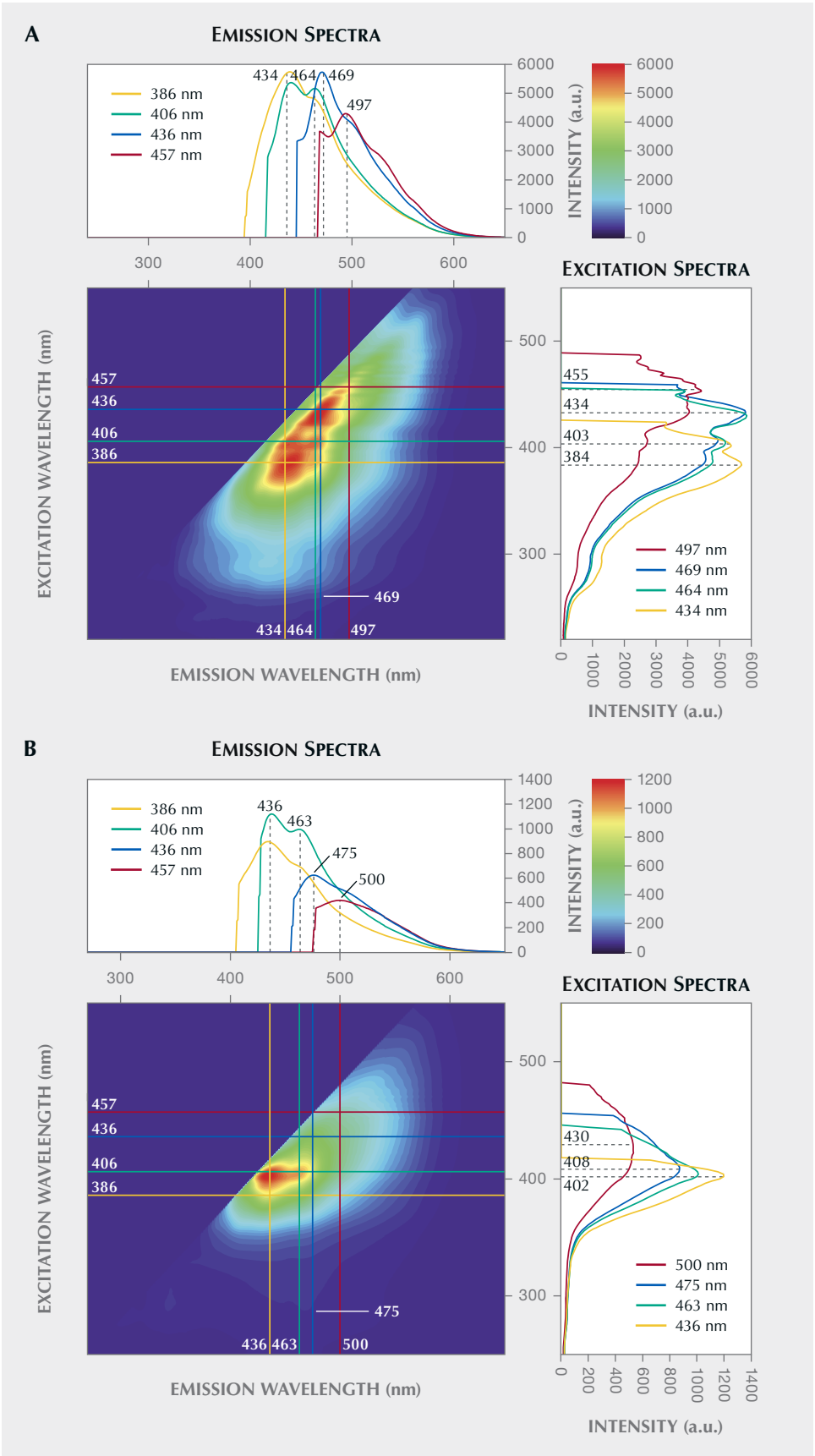

Figure 4. 3D fluorescence spectra of Burmese chameleon amber (A) and brownish amber (B).

The samples were then examined with 3D fluorescence spectroscopy (figure 4) under the excitation of a continuous-wavelength excitation light source. The fluorescence intensity of brownish amber was clearly much lower than that of chameleon amber. In addition, two peaks (455 and 384 nm) were absent in the excitation spectrum of brownish amber. A high degree of similarity was exhibited in the samples' emission spectra, with all the peaks positioned at approximately 434, 464, 469, and 497 nm. However, the biggest difference was in the fluorescence intensity, which was easily observed in chameleon amber.

The 3D fluorescence spectra of chameleon amber exhibited several fluorescence centers, mainly at 434, 464, 469, and 497 nm generated by excitation wavelengths of 386, 406, 436, and 457 nm. The fluorescence color could be calculated by the fluorescence centers, and the results showed that the spectral color was blue under 386 nm excitation and bluish green under 436 nm excitation. We believe that the bluish green floating color under sunlight is caused by the bluish green fluorescence center at 469 nm under 436 nm excitation. This is much more consistent with observations in daylight. Due to the low fluorescence intensity of brownish amber, its blue fluorescence color is very weak, and most light penetrates it without producing any special optical effect. The difference in fluorescence intensity between the 469 and 434 nm fluorescence centers corresponds with the relative spectral power distribution of the light source. Under the excitation of a xenon lamp, the fluorescence center at 434 nm is more intense than the light-emitting center at 469 nm. However, amber is usually observed in daylight. The optimal excitation wavelengths for the emission centers at 434 and 469 nm are 386 nm and 436 nm, respectively. From the relative spectral power distribution of the two light sources, it can be seen that the spectral density of the xenon lamp at 386 nm is greater than 436 nm, while the D65 daylight-equivalent source is the opposite. Against a dark background and under daylight, the fluorescence of chameleon amber should be dominated by the bluish green fluorescence emitted at 436 nm.

The fluorescence center at 469 nm is very common in Baltic, Dominican, Mexican, and Burmese amber. This fluorescence center in chameleon amber is unique for its high intensity and separation from other fluorescence colors. Only if the fluorescence intensity is high enough will it show as the dominant fluorescence color. The optimal excitation wavelength (436 nm) corresponding to the 469 nm fluorescence center is far removed from the optimal excitation wavelength of other strong fluorescence centers; therefore, the fluorescence color is not a mixture of multiple colors. Many varieties of amber can also produce strong fluorescence at 469 nm, but often mixed with other fluorescence colors of similar intensity. For example, the fluorescence peaks of 448 and 474 nm in Dominican blue amber always appear together, and their strong fluorescence peaks can be seen with exposure to the same excitation wavelength. In most cases, the fluorescence intensity of the former is slightly greater, which leads to the fluorescence of the blue amber being mainly blue, without a green modifier. Some Dominican blue amber with uneven fluorescence distribution can also show a mosaic pattern (X. Chenxing et al., "Characterisation of patchy blue and green colouration in Dominican blue amber," *Journal of Gemmology*, Vol. 37, No. 7, 2021, pp. 700–713). The fluorescence distribution of the chameleon amber tested in this study was uniform, with high intensity and good separation, producing a high-quality bluish green floating fluorescence effect.

Jinfeng Yang, Yan Li, and Youzhi Liang
Gemmological Institute
China University of Geosciences, Wuhan

A newly discovered iridescent andradite from Inner Mongolia, China. Iridescent garnet found in Chifeng City, Inner Mongolia, was recently encountered in the Chinese market. Iridescent garnet was first discovered in 1943 in the U.S. state of Nevada (E. Ingeron and J.D. Barksdale, "Iridescent garnet from the Adelaide Mining District, Nevada," *American Mineralogist*, Vol. 28, 1943, pp. 303–312), and it is also found in Mexico and Japan (M.A. Badar and M. Akizuki, "Iridescent andradite garnet from the Sierra Madre Mountains, Sonora, Mexico," *Neues Jahrbuch für Mineralogie - Monatshefte*, Vol. 1997, No. 12, pp. 529–539; T. Hainschwang and F. Notari, "The cause of iridescence in rainbow andradite from Nara, Japan," Winter 2006 *G&G*, pp. 248–258). To the authors' knowledge, this is the first report of iridescent garnet in China. Two rough samples were collected by the authors in the Lindong lead mining area (figure 5). The refractive index was over the limits of a conventional refractometer, and the hydrostatic specific gravity values were 3.85 and 3.84. Both showed an inert reaction to long- and short-wave ultraviolet fluorescence. These standard gemological testing results were consistent with garnet.

On the basis of energy-dispersive X-ray fluorescence, calcium, silicon, iron, aluminum, manganese, magnesium, titanium, and sodium were detected. The chemical composition of the larger sample was analyzed using electron probe microanalysis (EPMA). The composition was consistent with that of andradite, containing major elements of calcium, iron, aluminum, and silicon, with the derived chemical formula of $(Ca_{3.015}Mn_{0.031}Na_{0.006}Mg_{0.003}Ti_{0.002})(Fe_{1.846}Al_{0.138})[Si_{2.978}O_{12}]$. The backscattered electron image showed clear growth layers (figure 6, left). Aluminum in the darker zones was about 2 wt.% higher on average than in the lighter zones, and the iron content decreased with increasing aluminum. Raman spectroscopic analysis involved comparison with the RRUFF database (B. Lafuente et al., https://rruff.info/about/downloads/HMC1-30.pdf). The peak positions (figure 7) indicated that the samples were consistent with those of andradite, supporting the composition inferred from EPMA. Raman shifts within 300 to 400 cm^{-1} were assigned to SiO_4 rotational vibrations. Raman shifts within 400 to 700 cm^{-1} were caused by Si-O_{bend} (bridge oxy-

Figure 5. Iridescent andradite samples (25 ct and 125 ct) from the Lindong area of Inner Mongolia, China. As shown in the left photo, sample G-1 displays iridescence on the (211) plane but not on the (110) plane. Photos by Jiuchang Yang.

gen) bending and asymmetric stretching vibrations. Raman shifts at 800 to 1200 cm^{-1} were attributed to the characteristic absorption peak of Si-O_{str} stretching vibration (B.A. Kolesov and C.A. Geiger, "Raman spectra of silicate garnets," *Physics and Chemistry of Minerals*, Vol. 25, No. 2, 1998, pp. 142–151).

Figure 6. Left: Growth layers viewed normal to the (110) crystal face in a backscattered electron (BSE) image from a polished thin section. Right: The iron and aluminum contents corresponding to each spot in the BSE image.

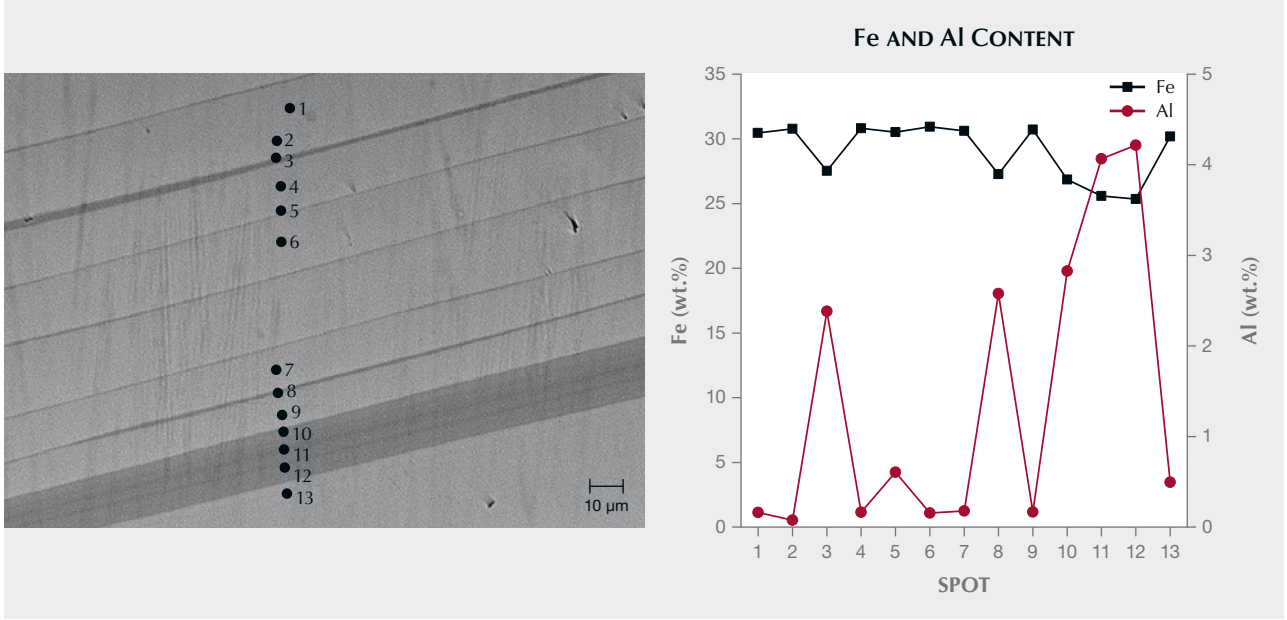

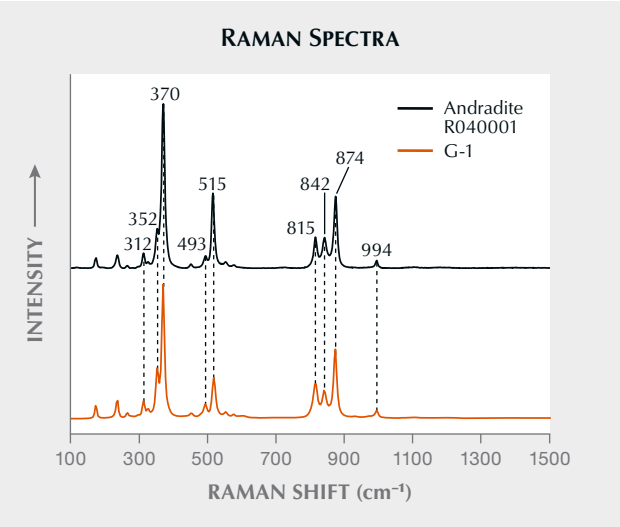

Figure 7. Sample G-1 was identified as andradite based on a comparison with a sample from the RRUFF database. Spectra are offset vertically for clarity.

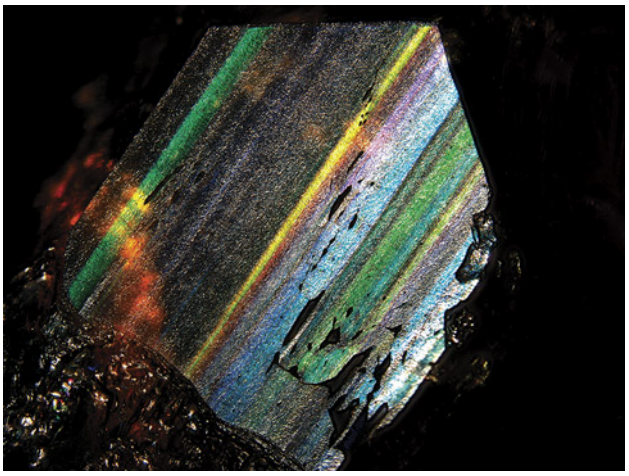

Figure 8. Sample G-1 displays strong iridescence with a full spectrum of colors. For certain bands, the color does not change as the viewing angle changes. This image is of a face parallel to (211). Photomicrograph by Jiuchang Yang; field of view 24.45 mm.

Microscopic observation revealed an attractive play-of-color with a complete visible spectrum of colors on the (211) crystal plane of sample G-1 (figure 8). We cut three polished thin sections from sample G-2 along the (110) and (211) crystallographic axes to observe the twinning structure and extinction phenomena under a polarizing microscope. The sample displayed angled layered growth structures and a strong grid-like pattern and abnormal birefringence (figure 9). A grid-like extinction phenomenon parallel to the growth layer (figure 9A) may have been caused by lattice-like twins, and figure 9C shows two areas with different extinction orientations. One study on Japanese andradite showed that the iridescence effect is caused by the alternate growth of iron-rich layers and aluminum-rich layers. These layers cause a thin-film interference phenomenon in the crystal struc-

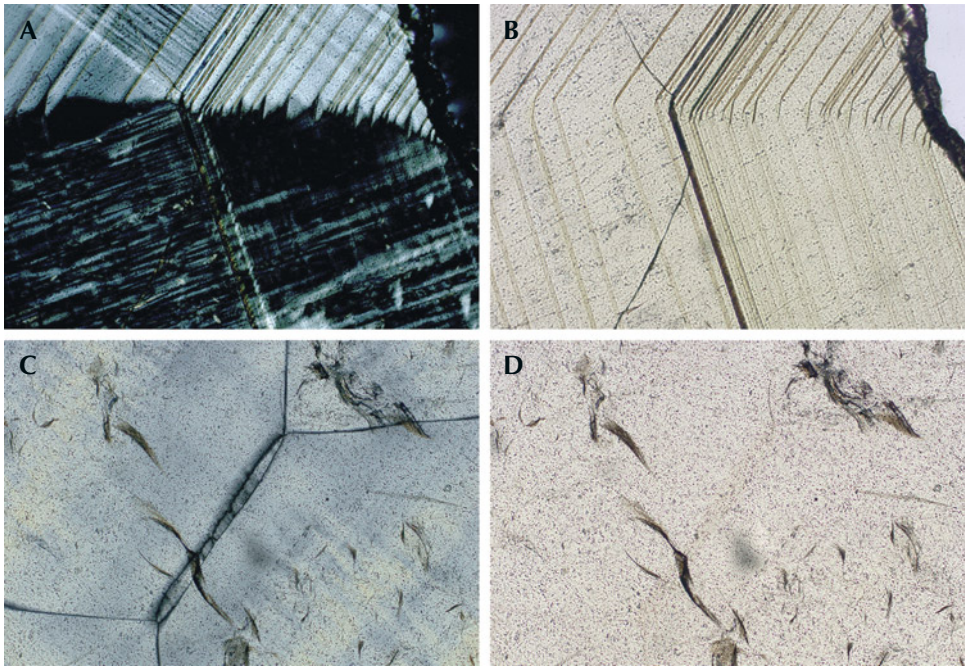

Figure 9. Top: The polished thin section in A and B was cut normal to the (110) crystal face. Observation under crossed polarizers (A) showed strong grid-like pattern, abnormal birefringence (possibly caused by lattice-like twinning), and angled growth bands. Bottom: The section in C and D was cut parallel to the (110) crystal face. Observation under crossed polarizers (C) showed partitioned abnormal birefringence caused by contact twinning and faint growth bands. Photomicrographs by Jiuchang Yang; field of view 25.05 mm.

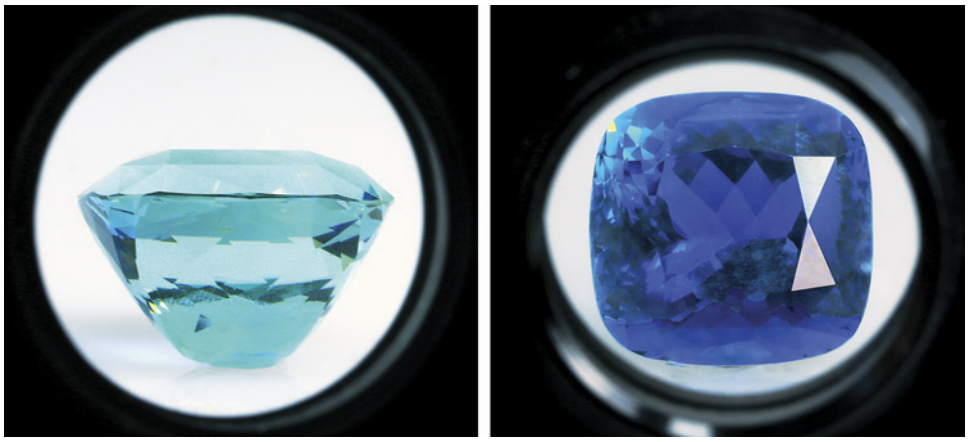

Figure 10. A 55 ct cushion-cut aquamarine exhibiting a distinct light bluish green and deep blue pleochroism using a dichroscope. Photos by Kaiyin Deng; courtesy of Farrugia Gem.

ture (Hainschwang and Notari, 2006). Therefore, we speculate that the iridescence of andradite from the Lindong lead mining area is not closely related to twinning but may be closely related to thin-film interference caused by its layered growth structure.

Jiuchang Yang, Quanli Chen (chenquanli@cug.edu.cn), Fengshun Xu, and Yan Li
Gemmological Institute
China University of Geosciences, Wuhan

Xianyu Liu
College of Jewelry, Shanghai Jian Qiao University

Aquamarine with zigzag growth line inclusions. A 55 ct cushion-cut aquamarine (figure 10, left) was recently submitted to Guild Gem Laboratories in Shenzhen for testing. This stone exhibited a very intense blue color accompanied by a subtle greenish secondary hue. A refractive index of 1.580–1.586 was obtained, together with a specific gravity of approximately of 2.71. Fourier-transform infrared (FTIR) and Raman spectroscopy confirmed its identity as beryl. The transmission FTIR spectrum exhibited distinct peaks at 2731, 2686, and 2641 cm^{-1} and a carbon dioxide–related signal at 2359 cm^{-1}. Peaks at 3235, 3162, 3111, and 3021 cm^{-1} were assigned to the presence of water (figure 11, left). This collection of FTIR peaks has been reported in natural aquamarine, but no synthetic counterpart has been reported to show this pattern (I. Adamo et al., "Aquamarine, Maxixe-type beryl, and hydrothermal synthetic blue beryl: Analysis and identification," Fall 2008 *G&G*, pp. 214–226). No organic-related peaks were found around the 2800–3200 cm^{-1} range, suggesting no clarity enhancement had been applied (L. Jianjun et al., "Polymer-filled aquamarine," Fall 2009 *G&G*, pp. 197–199). Strong deep blue and light bluish green pleochroism (figure 10) was observed using a dichroscope. Similar beryl materials with a deep blue color have been reported in previous studies (Fall 2014 GNI, pp. 244–245; Fall 2019 GNI, pp. 437–439). The ultraviolet/visible/near-infrared spectrum (figure 11, right) showed a broad Fe^{2+}-related band centered at around 835 nm and narrow absorption bands at 370 and 426 nm related to Fe^{3+} (D.S. Goldman et al., "Channel constituents in beryl," *Physics and Chemistry*

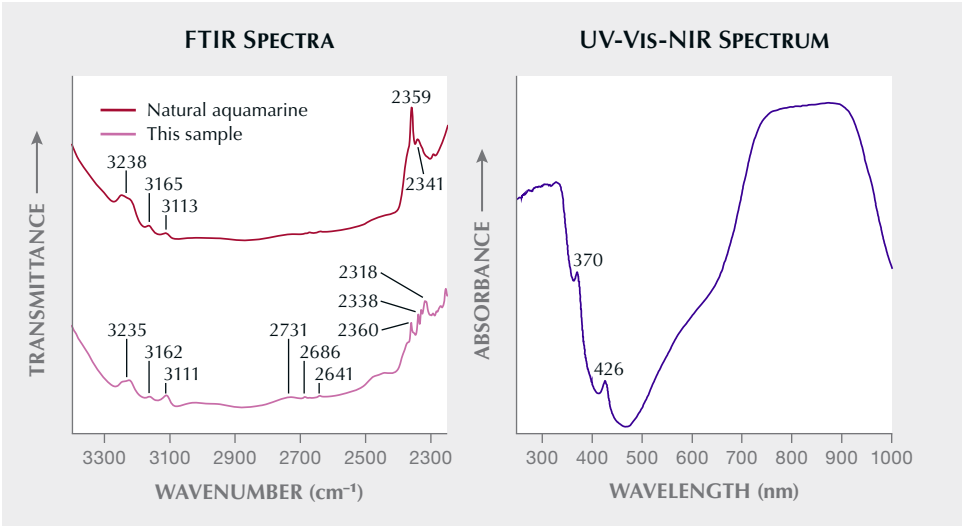

Figure 11. Infrared transmission spectra (left) and UV-Vis-NIR spectrum (right) of the aquamarine sample. The spectra on the left are offset vertically for clarity.

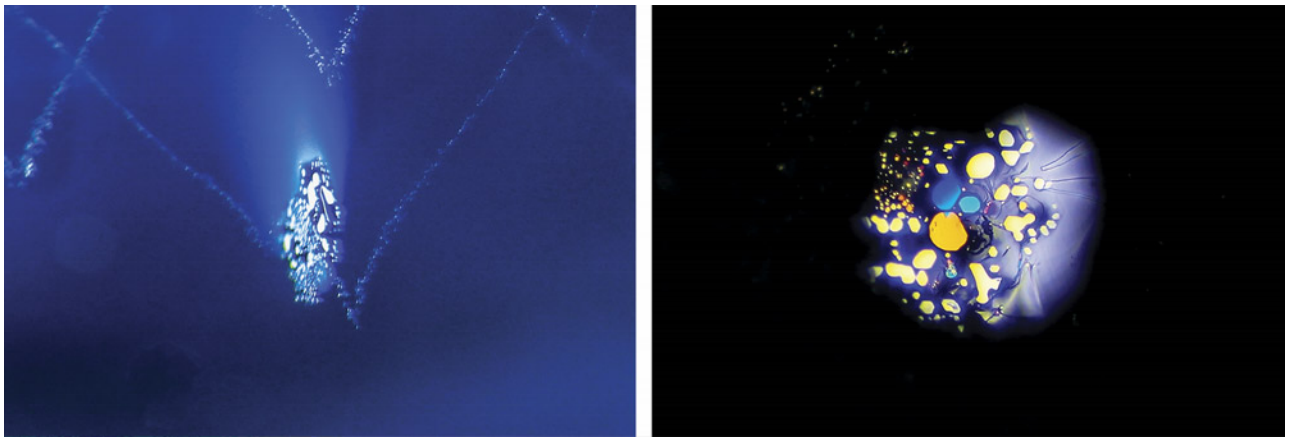

Figure 12. The thin film along the basal plane of the aquamarine under fiber-optic illumination. Photomicrographs by Yizhi Zhao; fields of view 3.45 mm (left) and 1.72 mm (right).

of Minerals, Vol. 3, No. 3, 1978, pp. 225–235; K. Schmetzer, "Hydrothermally grown synthetic aquamarine manufactured in Novosibirsk, USSR," Fall 1990 *G&G*, pp. 206–211; Adamo et al., 2008). Using a polariscope equipped with a conoscope, the optic axis was observed parallel to the table along the long axis of the cushion shape. Further chemical analysis by energy-dispersive X-ray fluorescence showed a high iron content (around 13000 ppmw), which likely contributed to the saturated blue color (Y. Shang et al., "Spectroscopy and chromaticity characterization of yellow to light-blue iron-containing beryl," *Scientific Reports*, Vol. 12, No. 1, 2022, article no. 10765).

Microscopic observation under darkfield illumination revealed fluid inclusions and minute voids. Under the table, a circular thin film with a strong light reflection was visible (figure 12). The image in figure 12 (left) was captured at an angle to the table of the aquamarine, since the thin film was easier to see under an oblique light source. Because beryl has imperfect cleavage along its basal plane {0001}, the space between the basal planes caused by initial cleavage was sufficient to form the thin film.

An interesting inclusion was observed only with oblique light: a distinct series of fluids resembling dots and broken lines. Higher magnification (figure 13) revealed that these zigzag lines consisted of discrete and minute fluid inclusions. Further observation along the optic axis confirmed that the planes were parallel to the *c*-axis of the aquamarine.

A previous study described similar inclusions in emeralds from Colombia as resembling a DNA double helix (Summer 2019 *G&G* Micro-World, p. 262). The authors have also encountered this type of inclusion before. Based on our observations, these helical inclusions spiral along the optic axis of the emerald. To our knowledge, this is the first time such helical inclusions have been reported in an aquamarine. This finding will help advance our understanding of the beryl family.

Yujie Gao, Xueying Sun (shirley.sun@guildgemlab.com), Yizhi Zhao, and Kaiyin Deng
Guild Gem Laboratories
Shenzhen, China

Figure 13. Zigzag lines were observed in the aquamarine using oblique light. Photomicrograph by Yizhi Zhao; field of view 4.52 mm.

Blackish green omphacite jade from Guatemala. In recent years, a new kind of Guatemalan jade has entered the Chinese jewelry market, where it is called *yongchuliao fei cui* (or *yongchuliao* for short). Prior to the availability of yongchuliao, Chinese consumers had a negative impression of Guatemalan material and preferred Burmese jade. However, the recent emergence of this new high-quality blackish green jade has attracted the attention of Chinese buyers.

The authors recently tested a rough stone and a carved pendant of yongchuliao (figure 14). Under reflected light, these samples appeared blackish green with a greasy luster similar to Burmese inky black jade. The rough stone was opaque and had numerous fine white inclusions measuring approximately 300 μm in diameter on its surface. The

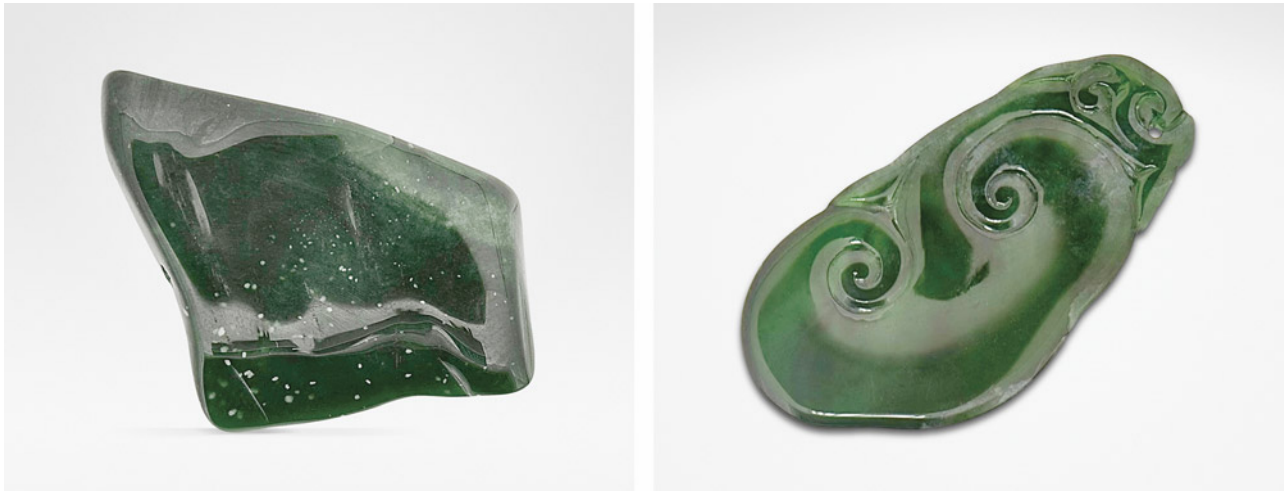

Figure 14. Yongchuliao *samples collected for testing. The rough sample on the left weighs 30.1 ct, and the carving on the right weighs 12.85 ct. Photos by Shilong Xu.*

carved sample was bright green with coarse texture and medium transparency under transmitted light (figure 15). The rough and carved samples had a refractive index of 1.67 and specific gravities of 3.342 and 3.332, respectively. These gemological characteristics are consistent with both jadeite-type jade and omphacite-type jade.

Qualitative analysis using energy-dispersive X-ray fluorescence spectrometry revealed magnesium, aluminum, silicon, calcium, chromium, manganese, and iron, among other elements. It should be noted that the ideal chemical formula of jadeite is $NaAlSi_2O_6$ and that of omphacite is $(Ca,Na)(Mg,Fe,Al)Si_2O_6$ (S.F. McClure, "The jadeite/omphacite nomenclature question," *GIA Research News*, April 12, 2012). Jadeite and omphacite can form a complete solid solution. The occurrence of calcium, magnesium, and other elements implies that the mineral composition of yongchuliao is not pure jadeite.

Raman shifts at 681, 514, 411, 378, 340, and 209 cm^{-1} were consistent with those of omphacite (figure 16). The Raman spectra of fibrous inclusions in the carved sample also matched those of omphacite rather than jadeite. The strongest Raman shift at 681 cm^{-1} was attributed to the symmetrical Si-O-Si stretching vibration (B. Xing et al., "Locality determination of inky black omphacite jades from Myanmar and Guatemala by nondestructive analysis," *Journal of Raman Spectroscopy*, Vol. 53, No. 11, 2022, pp. 2009–2018). Raman spectroscopy was used to compare the samples' mineral composition against the RRUFF database (B. Lafuente et al., https://rruff.info/about/downloads/HMC1-30.pdf), revealing that yongchuliao material

Figure 15. Left: Fibrous inclusions observed in the 12.85 ct carved sample; field of view 8.94 mm. Right: The carved sample appeared bright green rather than blackish green under transmitted light. Photos by Shilong Xu.

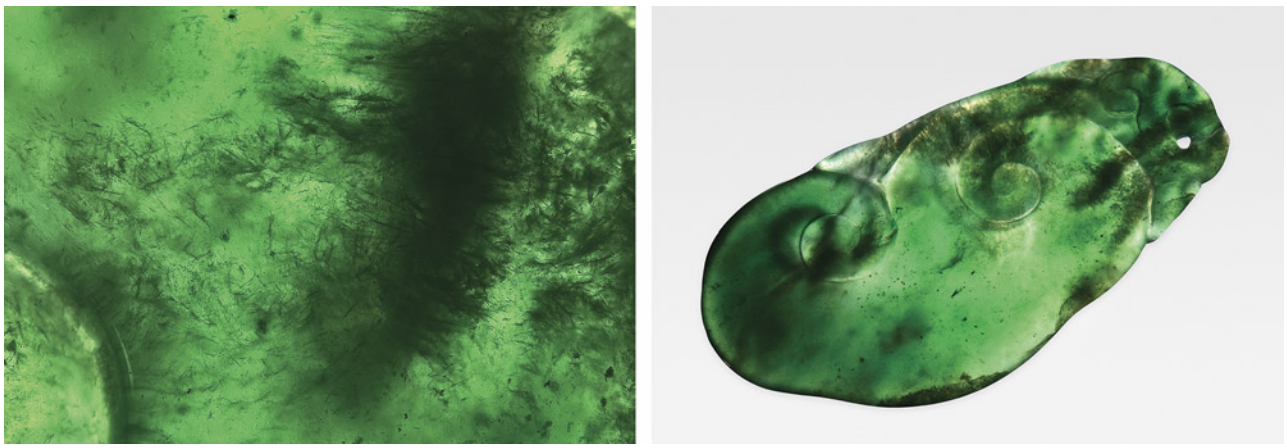

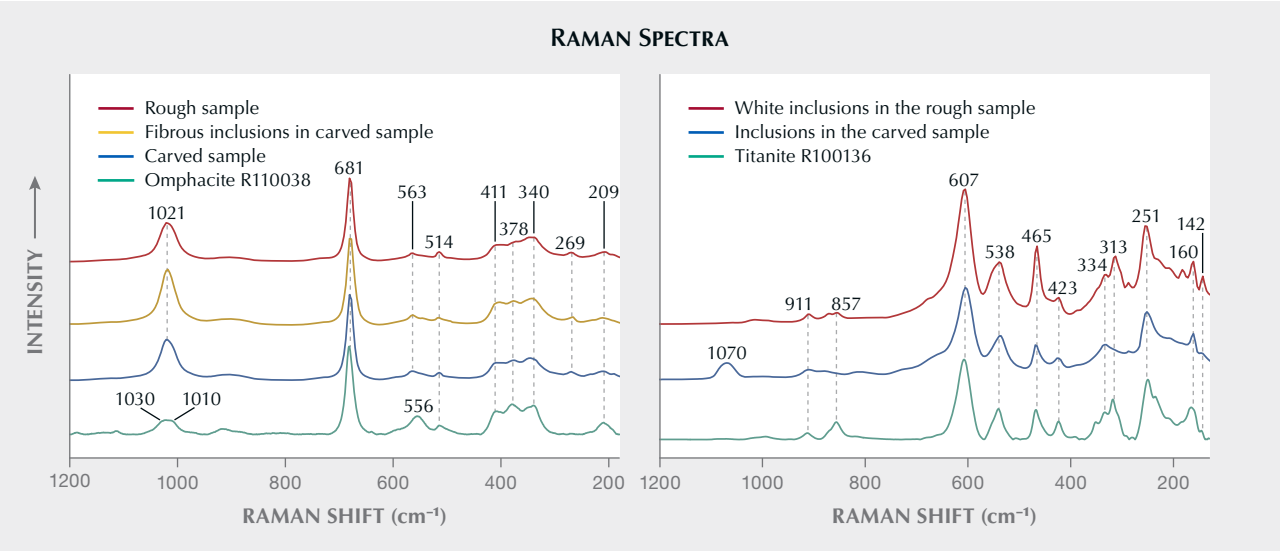

Figure 16. The mineral species were confirmed by comparison with samples from the RRUFF database. Spectra are offset vertically for clarity. Left: The host mineral and fibrous inclusions of the samples matched with omphacite. Right: The white dotted mineral inclusions in the rough sample matched with titanite. Titanite in the carved sample could also be observed in micro-Raman imaging.

consists almost entirely of omphacite. The fine white inclusions distributed evenly in the rough sample were coincident with titanite (figure 16). In addition, some of the sample was ground into powder for X-ray diffraction analysis to obtain the mineral composition of the whole rock. The results showed an omphacite content of about 98.49% (with a 5% margin of error), and the rest was magnesian calcite. The results from Fourier-transform infrared absorption spectroscopy were consistent with the Raman spectra, identifying the main mineral composition of the samples as omphacite.

A double-sided polished piece was cut from the rough sample for testing. Its ultraviolet/visible/near-infrared (UV-Vis-NIR) absorption spectrum (figure 17) showed an absorption peak at 437 nm, indicating the presence of Fe^{3+}. Absorption peaks at 637, 657, and 688 nm were also observed and attributed to Cr^{3+} (G.R. Rossman, "Color in gems: The new technologies," Summer 1981 *G&G*, pp. 61–62).

Based on testing, both samples were omphacite-type jade containing titanite inclusions. Since almost all of the yongchuliao we have observed exhibited nearly the same colors and textures as these samples, it is likely that other yongchuliao may also have similar mineral compositions.

Figure 17. In the UV-Vis-NIR spectrum of a piece cut from the rough sample, absorption peaks were observed within the visible range at 437, 637, 657, and 688 nm.

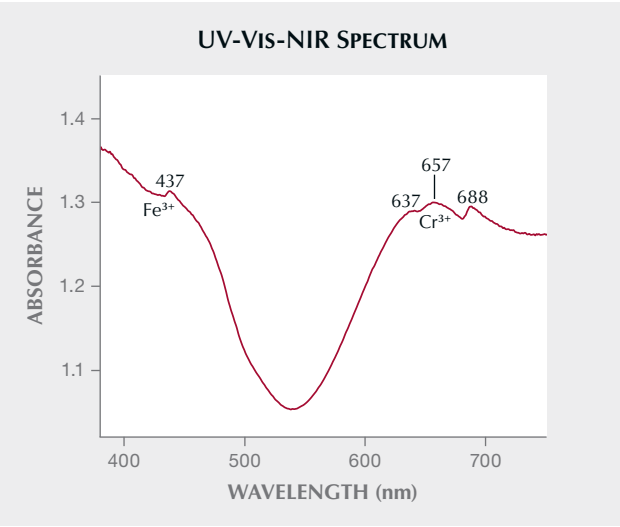

Shilong Xu, Quanli Chen (chenquanli@cug.edu.cn), and Yan Li
Gemmological Institute
China University of Geosciences, Wuhan

Xianyu Liu
College of Jewelry, Shanghai Jian Qiao University

Shell blister on an *Isognomon isognomon* shell. Theoretically, all mollusks are capable of producing pearls, but only a small number of them actually produce commercially traded nacreous pearls. Most come from the *Pinctada* and *Pteria* genera belonging to the *Pteridae* family. Species that produce the nacreous pearls regularly seen in the market, such as *Pinctada maxima*, *Pinctada radiata*, *Pteria sterna*, and *Pteria penguin*, are well known to aficionados. However, some unusual bivalve species can also produce pearls or shell blisters, and one example was recently submitted to GIA's Mumbai laboratory for scientific examination.

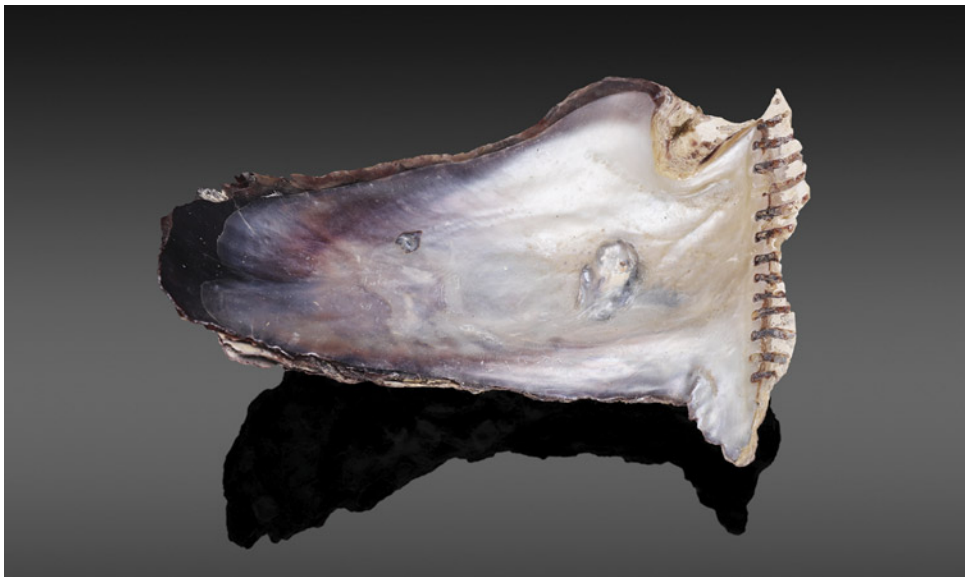

Figure 18. Isognomon isognomon *shell and blister. The shell measures approximately 107.76 × 72.39 mm. Photo by Gaurav Bera.*

The shell was from the *Isognomon isognomon* species, belonging to the *Isognomonidae* family and commonly known as the Pacific toothed oyster. It exhibited a blister feature that appeared as a folded section of nacre, located near the center, close to the posterior muscle scar and the hinge (figure 18). The shell weighed 46.88 g and measured approximately 107.76 × 72.39 mm, while the baroque-shaped silver to light gray blister measured approximately 8.80 × 4.21 mm. Not all instances of nacre growth on a shell are classified as pearls. While cyst pearls or whole pearls develop independently from the shell, blisters are nacreous concretions that appear to protrude from the shell (K. Lawanwong et al., "Natural shell blisters and blister pearls: What's the difference?" *GIA Research News*, August 26, 2019). According to the pearl classification established by CIBJO, the concretion observed on the shell in question would be categorized as a shell blister.

The shell itself displayed a narrow, elongated shape, featuring a straight hinge with distinct equidistant dark brown notches along its length (figure 19, left). These notches, also known as resilifers or ligament pits, resemble teeth, giving the species its common name; see I. Temkin and C. Printrakoon, "Morphology and taxonomy of *Isognomon spathulatus* (Reeve, 1858), a cryptic bivalve from the mangroves of Thailand," *Zootaxa*, Vol. 4107, No. 2, 2016, pp. 141–174.

The interior of the shell exhibited a predominantly nacreous aragonite surface, characterized by a discernible spiral platelet structure visible under microscopic exami-

Figure 19. Left: Dark brown rows of notch-like features observed on the hinge of the shell. Right: A whitish subsurface dendritic network of parasite channels. Photomicrographs by Prasad Mane; fields of view 16.3 mm (left) and 6.1 mm (right).

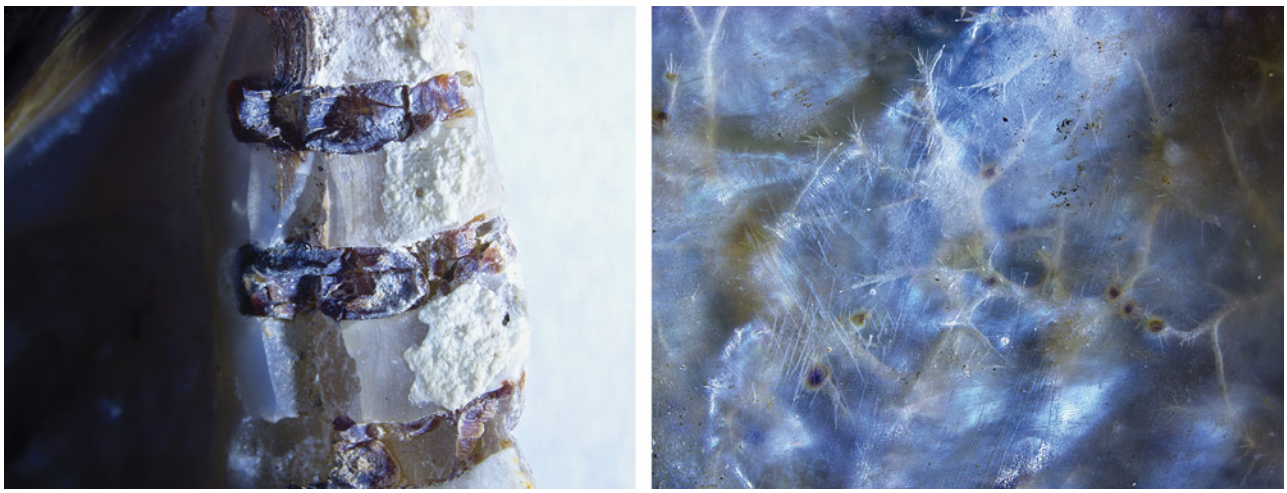

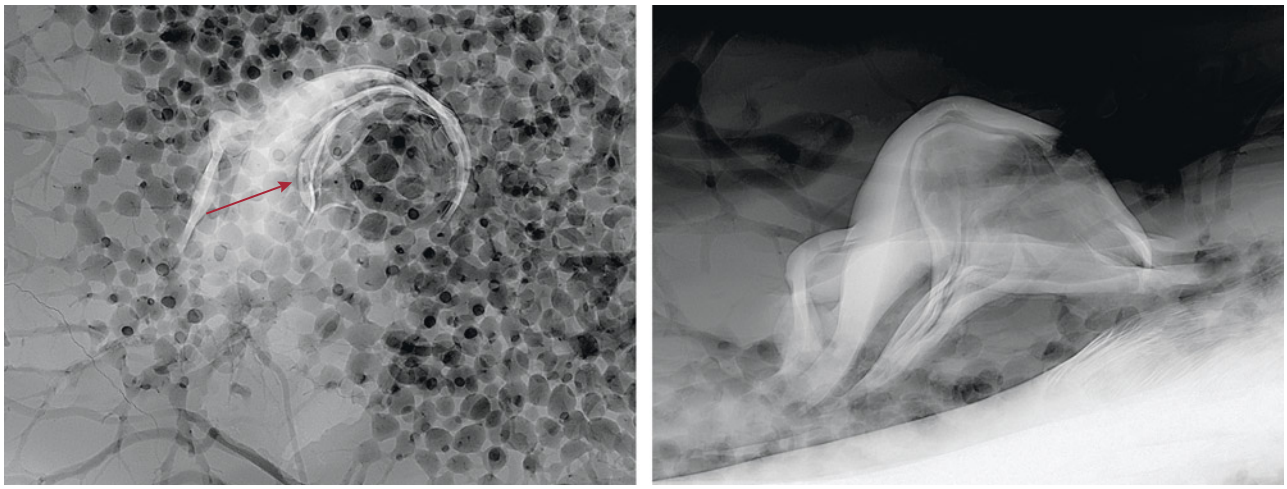

Figure 20. Left: RTX image of the top view of the 8.80 × 4.21 mm shell blister (arrow) with a network of parasitic boreholes and channels visible around it. Right: RTX image of the side of the shell blister with more radiopaque folds marking its outline.

nation. This nacreous region was bordered by a non-nacreous shell margin. The central nacre displayed a light gray coloration, transitioning to a darker purplish gray toward the margin. The center of the shell had a more translucent appearance, revealing a subsurface dendritic network of parasitic channels surrounding the blister (figure 19, right).

Real-time microradiography (RTX) revealed a network of fine channels beneath the blister and throughout the shell itself (figure 20, left). These features corresponded to the parasitic channels observed within the translucent layer on the shell's interior. RTX imaging of the blister revealed a void (figure 20, right), potentially linked to parasitic activity that may have initiated the blister formation.

X-ray fluorescence (XRF) imaging of both the shell and the blister yielded an inert reaction. Energy-dispersive X-ray fluorescence spectrometry of the blister indicated a manganese level below the instrument's detection limit and a strontium level of 1135 ppm. The inert XRF reaction, along with the chemical composition, proved the mollusk formed in a saltwater environment. Under long-wave UV radiation, the shell displayed a greenish yellow fluorescence reaction, while short-wave UV radiation yielded an inert response. Raman analysis using a 514 nm ion/argon laser excitation revealed peaks at 701/704 cm^{-1} and 1085 cm^{-1}, indicative of aragonite. Photoluminescence spectra collected from both the shell and the blister showed three broad peaks centered at 620, 650, and 680 nm, which is observed in some naturally colored pearls.

Although the *Isognomonidae* family and the *Pteridae* family belong to the Pteroidae superfamily, pearls from oysters such as the Pacific toothed oyster (*Isognomon isognomon*) are rarely seen. Therefore, it was intriguing to examine this blister. Perhaps we will someday encounter a natural pearl from this mollusk species.

Prasad Mane, Nishka Vaz, and Abeer Al-Alawi
GIA, Mumbai

Mining basalt-related gems in southeast Vietnam. A number of gemstone deposits are known in provinces all across Vietnam. These include ruby (Yen Bai and Nghe An), sapphire (Yen Bai, Nghe An, Binh Thuan, and Dak Nong), spinel (Yen Bai and the Central Highlands), aquamarine (Thanh Hoa and Khanh Hoa), tourmaline and garnet (Yen Bai), and peridot (Gia Lai). Recently, seven gemstone occurrences have been identified within the basaltic fields in southeast Vietnam, which are mainly found in Dong Nai and Ba Ria–Vung Tau provinces. These gems include sapphire, zircon, garnet, augite, brown peridot, feldspar, and hyalite opal. They are found predominantly in basalt bedrock and its regolith as xenocrysts or xenoliths deposited on hillslopes or in placer formations along streambeds. Seven gemstone species from southeast Vietnam were collected and documented (figure 21).

The sapphires usually appeared as hexagonal crystals or fragments, exhibiting mainly blue, deep to dark greenish blue, and greenish yellow colors. Most were transparent to semitranslucent and some opaque, and the luster was greasy to vitreous. The typical rough sizes ranged from 5 to 20 mm, weighing 2–10 ct.

Euhedral tetragonal crystals of zircon were very common, while the rest of them were fragmented. Colors included orange, brown-red, gray, and colorless. These zircon samples showed high luster ranging from adamantine to vitreous, with a transparent to semitransparent appearance. Zircons from southeast Vietnam were not found in fresh basalt; they were found mostly in placer and in weathered basalt instead (figure 22A).

"Red stone" is a local name for gem-quality garnet from Dong Nai. The garnets occurred in two forms of anhedral fragments: xenocrystic fragments (also called "orphan stone") weighing 1–50 ct, with a corroded surface, and xenolith-hosted garnet containing small corroded fragments that produce 1–5 ct fashioned gems. Both xenocryst (figure 22B)

Figure 21. Gem materials from southeast Vietnam. The three largest yellow and white samples on the far left are feldspar, while the brown, orange, and near-colorless samples in the center are zircon and the two greenish white samples near the top right are hyalite opal. The rest of the dark stones are sapphires, garnets, augites, and brown peridot. Photo by Le Ngoc Nang; courtesy of Tran Ngoc Vien.

and xenolith-hosted garnet were found mainly in the regolith on the hillslopes. The color ranged from deep to dark red and occasionally deep orangy yellow, with a transparent to semitransparent quality and a vitreous luster.

Euhedral crystals of Dong Nai feldspar were characterized by two directions of perfect cleavage. These feldspars were colorless, gray, and rarely light yellow, with a vitreous luster and a transparent to translucent appearance. This mineral was the most common gem material in the region and could be found in both bedrock and its regolith.

As reported recently, the augite samples appeared black under daylight-equivalent illumination but dis-

Figure 22. Basalt-hosted gem materials from southeast Vietnam: A subhedral zircon crystal in laterite (A), a garnet xenocryst in basalt (B), and a brown peridot nodule in basalt (C). Photos by Le Ngoc Nang.

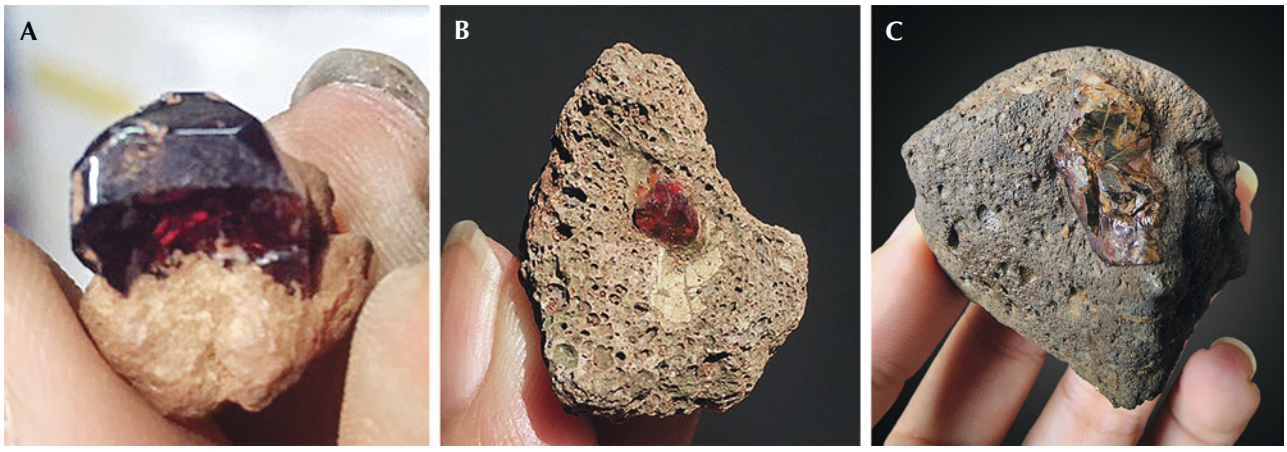

played green and brown colors under transmitted light. Most samples were transparent to translucent and had vitreous luster. The brown gems tended to be more transparent than the green ones (L.N. Nang et al., "Gem-quality augite from Dong Nai, Vietnam," Summer 2023 *G&G*, pp. 182–194).

Brown peridot was found as slightly corroded xenocrystic fragments measuring 0.5–5 cm. The samples were black under reflected light but greenish yellow-brown with transmitted light. Most samples were transparent to translucent, with a vitreous luster. The brown peridot was quite rare and frequently confused with augite due to their similar morphology and occurrence in the vesicular basalt (figure 22C).

The hyalite opal was found in Ba Ria–Vung Tau, and each sample consisted of two parts: the inner body and the outer layer. The contact between the two parts was distinct. The outer layer was opaque white, 2–5 mm thick, and porous. The inner body was usually colorless and rarely green, brown, or light pink, transparent to opaque, with a vitreous appearance. The hyalite opals with good transparency were suitable for jewelry due to their glowing green fluorescence under long-wave ultraviolet light (weak fluorescence under short-wave UV).

Several of these gem deposits in southeast Vietnam are unlicensed. Most materials were collected by locals using artisanal methods, without any commercial mining. The gem materials found along hillslopes or stream channels were extracted at shallow depths ranging from 0.3 to 0.5 m. The gems appeared more frequently after rain and were distributed by their specific gravity. For instance, light material such as hyalite opal was concentrated on the hilltop, stored in slightly weathered and broken-up rock, while heavier minerals, namely sapphire, garnet, feldspar, and peridot, usually accumulated along the hillslopes. Zircon, on the other hand, was often deposited in streambeds. Some gems stored in basalt were extracted easily by homemade tools.

Most of the rough materials are sold to gem dealers in Ho Chi Minh City, who sell fashioned products to local markets in southeast Vietnam. Gemstones in the area have long been gathered by locals during farming and well drilling, but the old-fashioned mining methods led to a significant waste of gem resources. Preliminary evaluations of gem quality have shown that gemstones from southeast Vietnam are of economic potential. The thick basaltic host rock covering a large area is a foundation for prospecting numerous gem materials and requires further research to comprehensively assess available reserves.

Le Ngoc Nang
University of Science, Vietnam National University
Ho Chi Minh City
Liu Gemological Research and Application Center

Pham Minh Tien and Ho Nguyen Tri Man
Liu Gemological Research and Application Center

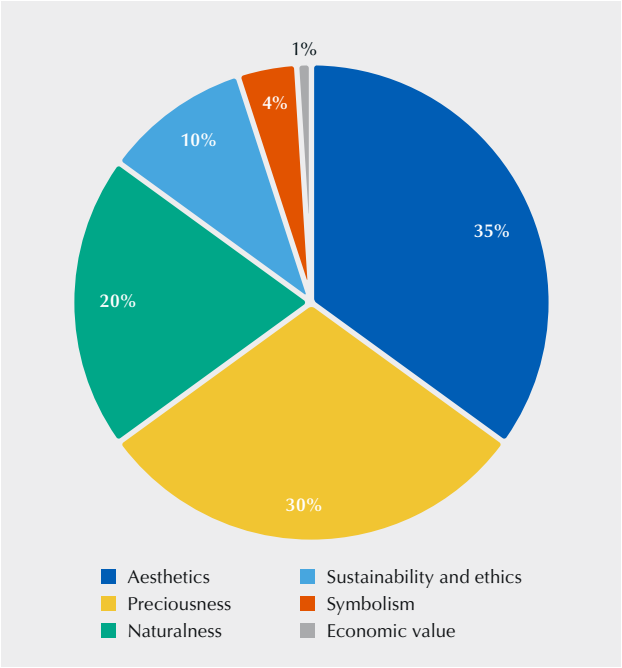

Figure 23. Survey participants identified their top consideration when purchasing colored stones or colored stone jewelry.

Survey of colored stone preferences among younger generations. The global colored stone market is dynamic and constantly evolving. To understand general perceptions and preferences regarding colored stones among designers and potential end consumers from the younger generations, the author conducted a survey in April 2023. The survey targeted 300 respondents under the age of 35, all followers of Donna Jewel (@donna.jewel), an Instagram community designed to champion jewelry from artisans and emerging talents worldwide. Although not scientific, the results of the survey are nonetheless revealing.

Demographics and background: The survey participants consisted of 50% Millennials (born between 1981 and 1996) and 50% from Generation Z (born from 1997 onward). All respondents were over the age of 18. Forty percent were from the United States and another 40% from Europe (specifically Italy, France, the United Kingdom, and Germany), with the remainder split between Latin America (mainly Brazil) and Asia (mainly India and Iran). Respondents identified themselves as gem and jewelry lovers (50%), designers (33%), or gem and jewelry experts (17%).

Colored stone preferences: Participants were asked to choose their single most important consideration when buying colored stones or colored stone jewelry: aesthetics, preciousness, naturalness, sustainability and ethics, symbolism, or economic value. As shown in figure 23, the top two responses were aesthetics (35%) and preciousness (30%). Naturalness was also an important consideration (re-

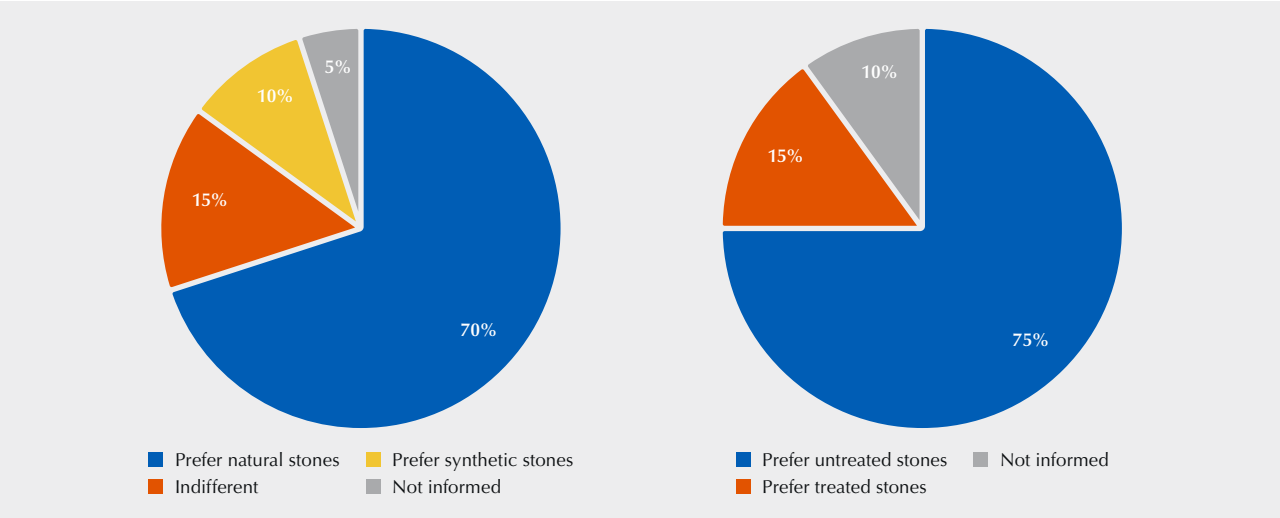

Figure 24. The preferences of survey respondents regarding natural vs. synthetic (lab-grown) gemstones and untreated vs. treated gemstones.

ceiving 20%), while sustainability and ethics was chosen by 10% of the interviewees, symbolism by 4%, and economic value by only 1%.

Given the choice between natural or synthetic gemstones (figure 24, left), 70% chose natural. Only 10% selected synthetic, while an additional 15% expressed no preference. When asked to explain their preferences, the participants who chose natural stones perceived them as unique, rare, and authentic products of nature, capable of evoking emotion, unlike their synthetic counterparts. Those who chose synthetic gemstones viewed them as more sustainable, ethical, and affordable. The topic of natural and synthetic gemstones remains extremely relevant.

Regarding treated vs. untreated natural gemstones (figure 24, right), 75% preferred untreated, which they perceive as more beautiful for their uniqueness and originality. They viewed natural imperfections as an added value lost during treatment. Only 15% preferred treated stones, while 10% acknowledged that they were not informed on the topic.

When asked whether they preferred "precious" or "semi-precious" stones, the participants proved generally indifferent (designers and potential end consumers alike). They associate preciousness with a broader definition more related to uniqueness, emotion, and originality.

Designer perspectives: Designers participating in this survey revealed that they follow both trends and personal inspiration. They noted several uncommon gemstones of particular interest: rainbow obsidian, red beryl, sphene, pargasite, chrysoberyl, scapolite, axinite, enstatite, and benitoite. Fifty percent indicated that they had purchased or used for their jewelry artificially manufactured materials such as glass or cubic zirconia.

At the end of the survey, participants were asked what topics they would be most interested in learning more about. They expressed a strong desire for more knowledge on uncommon and unique gemstones, original colors, treatments, history, lore, origin, and sustainability.

The survey highlighted the younger generations' strong interest in what is unique, original, authentic, and emotional rather than alignment with traditional notions of beauty and preciousness. Naturalness emerged as an important element for the interviewees, who appreciated imperfection as a mark of authenticity and originality. Young designers favored uncommon and original gemstones with distinct and extravagant colors (especially yellows, blues, greens, and reds). While designers sought uniqueness, rarity, and extravagance, potential end customers were also looking for a gemstone with a story to tell.

Laura Inghirami
Donna Jewel, Milan

DIAMOND

Diamondiferous mantle eclogite: Diamond surface features reveal a multistage geologic history. More than 99% of diamonds originally formed in the lithospheric mantle, the cold, rigid mantle that underlies continents, generally <300 km deep (T. Stachel and J.W. Harris, "The origin of cratonic diamonds – Constraints from mineral inclusions," *Ore Geology Reviews*, Vol. 34, No. 1-2, 2008, pp. 5–32). In the lithospheric mantle, the two major rock types—and host rocks for diamond—are peridotite (>95 vol.%), composed predominantly of olivine, and eclogite (<5 vol.%), composed of iron-magnesium-calcium garnet and sodium-rich clinopyroxene. Eclogite is a high-pressure and high-temperature metamorphic rock that can form when dense oceanic crust subducts into the mantle beneath continents at convergent margins.

We cannot directly study the deep portion of the earth where diamonds form. Instead, geologists study diamonds

Figure 25. Mantle eclogite xenolith (2.8 cm in longest dimension) consisting of clinopyroxene (green) and garnet (red-orange), with a partially exposed octahedral diamond. Photo by Annie Haynes. Gift of Mark Mauthner, GIA Museum no. 37511.

themselves, as well as pieces of mantle rock that are transported to the surface as xenoliths by volcanic magmas such as kimberlite or lamproite. The authors have studied one such mantle eclogite xenolith, part of the GIA Museum collection (figure 25). This sample was recovered from a kimberlite in Russia and contained a partially exposed octahedral diamond. The exposed portions of the diamond had visible surface features, including trigons (figure 26).

Trigons are inferred to be etch features that form after diamond crystallization, through interaction with fluids or melts either in the mantle source region or during transport to the surface (J.W. Harris et al., "Morphology of monocrystalline diamond and its inclusions," *Reviews in Mineralogy and Geochemistry*, Vol. 88, No. 1, 2022, pp. 119–166).

Figure 26. Partially exposed diamond embedded in an eclogite xenolith, with positive and negative trigons on the octahedral face. A mineral is included within the diamond, visible through the octahedral face. Photomicrograph by Matthew Hardman; field of view 5.74 mm.

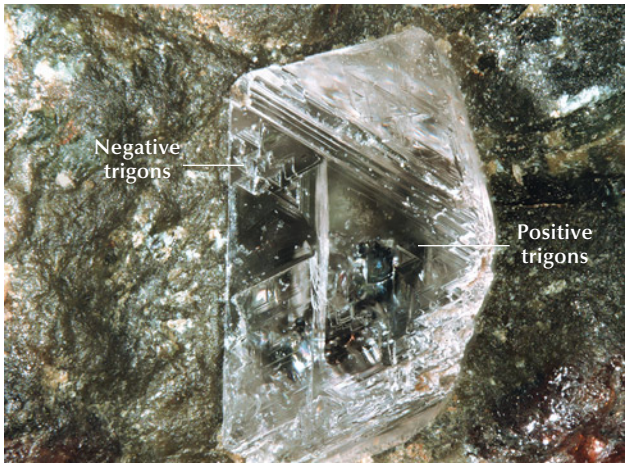

Trigons form exclusively on the octahedral faces of diamond and can have several different orientations. Positive trigons are oriented in the same direction as the octahedral face, and negative trigons have opposing orientation (figure 26). Positive trigons are very rare and may relate to interaction with carbon-oxygen-hydrogen-rich fluids at temperatures between ~800° and 1000°C at near-surface pressures (Z. Li et al., "Positively oriented trigons on diamonds from the Snap Lake kimberlite dike, Canada: Implications for fluids and kimberlite cooling rates," *American Mineralogist*, Vol. 103, No. 10, 2018, pp. 1634–1648). Trigons with negative orientation are much more common. It has been shown experimentally that increasing water content in melts could be one cause for the change of a trigon from positive to negative (e.g., A.F. Khokhryakov and Y.N. Pal'yanov, "The dissolution forms of diamond crystals in $CaCO_3$ melt at 7 GPa," *Russian Geology and Geophysics*, Vol. 41, No. 5, 2000, pp. 682–687). Diamonds with coexisting positive and negative trigons are extremely rare (e.g., Harris et al., 2022) and may indicate that the diamond experienced a complex multistage history related to thermal or fluid changes after its formation.

Using the acquired infrared absorption spectrum, the authors identified the diamond as type IaAB, containing nitrogen in the A- and B-aggregated forms. When the entire xenolith was exposed to ultraviolet light, the diamond fluoresced blue due to N3 defects (three nitrogen atoms surrounding a lattice vacancy), consistent with the presence of nitrogen impurities.

The diamond also contained an unidentified mineral inclusion with visible iridescence (figure 26). Minerals included fully within diamond (which itself is an impermeable time capsule) represent pieces of the mantle source region present at the time of diamond formation. For this sample, the mineral was too deep within the diamond to conclusively identify it nondestructively. However, if the mineral inclusion could be extracted, its chemical composition might be very useful in reconstructing the geologic

Figure 27. Pearl diver collecting shells from the wild. Photo courtesy of Pearls of Australia: Cygnet Bay Pearl Farm, Western Australia.

history of the host diamond, as well as that of the mantle rocks in which the diamond formed.

Matthew F. Hardman and Mei Yan Lai
GIA, Carlsbad

RESPONSIBLE PRACTICES

An environmental, social, and governance assessment of marine pearl farming. Farming pearl oysters is an important economic activity that, when done sustainably, can also provide valuable environmental and social benefits. To gain an evidence-based understanding of the sustainability challenges and opportunities facing marine pearl farming and their intersection with environmental, social, and corporate governance (ESG), The Nature Conservancy (TNC), a U.S.-based nonprofit, conducted an ESG assessment of an Australian pearl farm. This pilot project was intended to guide the development of a sector-wide ESG and sustainability assessment framework. The project was supported and funded by GIA as part of its global effort focused on education and the promotion of responsible practices.

Pearl oysters filter water at rates that are often higher than those reported for other oyster species. This filtration process contributes to waste treatment through the uptake of not only nutrients (nitrogen and phosphorus) but also heavy metals (S. Gifford et al., "Quantification of in situ nutrient and heavy metal remediation by a small pearl oyster (*Pinctada imbricata*) farm at Port Stephens, Australia," *Marine Pollution Bulletin*, Vol. 50, No. 4, pp. 417–422; L.T. Barrett et al., "Sustainable growth of non-fed aquaculture can generate valuable ecosystem benefits," *Ecosystem Services*, Vol. 53, 2022, article no. 101396). Pearl oysters are hung in baskets suspended from long lines, and these structures in which they are farmed provide habitat for a variety of fish and invertebrates (S.J. Theuerkauf et al., "Habitat value of bivalve shellfish and seaweed aquaculture for fish and invertebrates: Pathways, synthesis and next steps," *Reviews in Aquaculture*, Vol. 14, No. 1, 2022, pp. 54–72). If the negative impacts of pearl farming can be mitigated and effective sustainability strategies implemented through waste reduction, recovery and reuse, disease mitigation, and avoidance of overstocking, pearl farming could significantly benefit regional economies and local marine environments.

TNC's 2019 report titled *Towards a Blue Revolution* provided comprehensive guidance for evaluating critical aquaculture systems. Since the report's publication, TNC has built a science-based tool to assess industry and company operations. This tool takes into account factors related to the natural environment as well as the inherent and unique characteristics of a sector or company's operations. The tool has been designed to consider environmental data and the health of local ecosystems, enabling the identification of potential environmental benefits via restorative aquaculture, which has the potential to generate a net positive ecosystem outcome. This approach sets it apart from other sustainability assessment frameworks, risk assessments, and life cycle assessment methodologies.

Between February and May 2023, the assessment was conducted on Cygnet Bay Pearl Farm (CBPF; see figures 27–29), a company that produces pearls from *Pinctada maxima* north of Broome, Western Australia, using both wild capture and hatchery operations. CBPF is an operation of Pearls of Australia (PoA). Using the TNC framework, a number of overarching factors were assessed:

- Company capacity, ethics, and management measures
- Impacts on wild stocks from source of stock, hatchery escapes/interbreeding, and macrofauna interactions
- Reliance on added feed and chemicals
- Habitat impacts
- Water column effects (e.g., temperature, salinity, light penetration, and chemical characteristics of seawater at different depths)
- Disease
- Use of resources: fresh water, land, and energy

Figure 28. The pearl oysters are partially opened to allow seeding. Photo courtesy of Pearls of Australia: Cygnet Bay Pearl Farm, Western Australia.

The assessment showed that CBPF meets or exceeds all essential requirements within the ESG framework, including the company capacity, ethics, and management metrics. The company has no compliance issues associated with sustainability metrics, and an internal management team oversees sustainability topics and implementation. CBPF adheres to the Pearling Environmental Code of Conduct, developed by Australia's Pearl Producers Association in 2002 and updated in 2007. The farm has Marine Stewardship Council certification, meeting independent, third-party ecological sustainability standards. It operates within a country that has an effective governance, legal, and enforcement system in place to manage the industry into the future.

Regarding the social component of ESG, CBPF forms part of the Banararr Steering Committee (BSC) of the Bardi people, the traditional owners of the area. The BSC's role is to establish a positive relationship between CBPF and the Bardi traditional owners. Any amendment, use, or development of the area is discussed by the BSC together with relevant topics affecting the community at large, including school, transport, and fishing. Dedicated cultural heritage tours managed by Bardi people form part of the ecotourism offered at Cygnet Bay Pearl Farm. CBPF is active in research, housing the Kimberley Marine Research Station, and parent company PoA currently partners with the Marine Bioproducts Cooperative Research Centre. This research focuses on better understanding the implications and potential positive effects on fish and invertebrates that grow naturally on PoA farms.

CBPF could already be providing environmental benefits to the surrounding area through restorative aquaculture practices. Based on a general understanding of ecosystem services associated with oyster aquaculture, CBPF does meet the criteria for restorative outcomes, such as increased cycling of water and nutrients and providing habitat to other species. However, the extent to which these ecosystem services positively impact broader environmental outcomes remains unknown, in part because of the limited understanding of anthropogenic effects on water quality and habitat loss in the area.

Overall, the assessment provided an effective means to evaluate CBPF for its management and approach to ESG, the extent to which cultural communities are considered, the company's engagement with voluntary certification and codes of practices, and its awareness of key environmental risks and negative impacts as well as positive impacts.

Figure 29. Seeding Pinctada maxima *pearl shell. Photo courtesy of Pearls of Australia: Cygnet Bay Pearl Farm, Western Australia.*

Figure 30. Akshay Poddar, Melizza and Jennifer Tanpoco, and Julia Hackman Chafé are some of GIA's featured graduates on the Alumni Collective website.

At the same time, additional needs for TNC's ESG Assessment Framework have been identified. Brood stock sourcing and handling, biosecurity, and genetic risks are all areas that require additional research. One hundred percent utilization of the oysters farmed should be an explicit goal and assessment factor. The assessment should also consider the legacy effects of aquaculture equipment (e.g., recovery, reuse, and recycling), as well as the origin and species status of shells utilized to manufacture nuclei. Once these considerations are addressed, the TNC's ESG Assessment Framework should provide an effective sector-wide approach.

Heidi Alleway
The Nature Conservancy
Adelaide, Australia

ANNOUNCEMENTS

GIA Alumni Collective. Discover the GIA Alumni Collective, a networking and knowledge hub for GIA graduates. The online community at collective.gia.edu is a diverse group who all share a passion for the gem and jewelry industry. Users can access both live and self-paced Continuing Education seminars, join virtual chapters, connect with global alumni, and more. The site also highlights some of the GIA alums who uphold GIA's highest standards (figure 30).

Akshay Poddar earned his Graduate Gemologist diploma at GIA's Mumbai campus. A third-generation diamantaire, Poddar was driven to start his own business, dealing in both wholesale trade and retail. The diamond jewelry designer believes that while nature creates the diamond, his job is to add beauty to it.

Jennifer Tanpoco launched Jaune Pearls in 2002, later enlisting her daughter Melizza as CEO. The Tanpocos, both GIA Pearls Graduates, focus on sustainability and long-term environmental impact in their business, educating clients on how the pearls are sourced.

Julia Hackman Chafé used her marketing background and her Colored Stone Essentials Certificate from GIA to create a strong digital presence after taking over social media for her family's wholesale colored stone business. Now a successful influencer under the name JewelsWithJules, Chafé shares photos and videos of gems, jewelry, and international travel, providing her followers with a unique look at the colored stone trade.

Visit https://collective.gia.edu/meet-the-collective.html to read stories from these alumni and more.

Gübelin Gem Museum opens in Switzerland. In July 2023, the Swiss firm Gübelin, known for its luxury timepieces and jewelry and its gemological laboratory, opened the Gübelin Gem Museum in Lucerne, Switzerland (figure 31). The collection allows visitors to explore the formation, origin, and diverse colors of fascinating gemstones (figure 32), as well as the history of the family-owned business, founded in 1854.

The opening of the museum commemorates the 100th anniversary of the Gübelin Gem Lab, which became a world-renowned institution in the field under the leader-

Figure 31. A look inside the new Gübelin Gem Museum in Lucerne, Switzerland. Photo courtesy of Gübelin.

ship of Dr. Edward J. Gübelin. Recognized for his gemstone inclusion research, Dr. Gübelin's groundbreaking work is a focal point of the museum, including many of his instruments and gemstones he collected during his travels worldwide. Visitors will discover 174 gemstones selected from the company's reference collection in addition to selected Gübelin watches and jewelry pieces from various eras.

The compact space not only houses historical exhibits but also provides a window to the future. Visitors will learn about Provenance Proof, the company's blockchain technology for colored gemstones, and Gemtelligence, a colored gemstone analytical tool that uses artificial intelligence to increase consistency in data interpretation, origin determination, and identification of heat treatment. It is also the new home of the Gübelin Academy, offering courses to inspire students in the museum setting. Through digital and interactive elements, the exhibits will be continuously updated and expanded, ensuring new experiences for years to come. For more information, visit www.gubelin-gemmology.com.

Erica Zaidman
GIA, Carlsbad

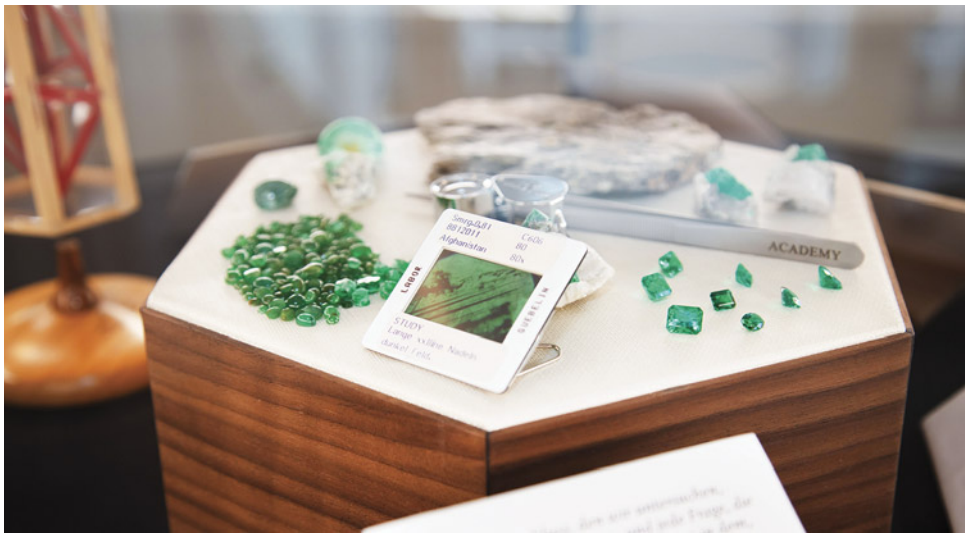

Figure 32. A display case featuring emerald at the Gübelin Gem Museum. Photo courtesy of Gübelin.

CONFERENCE REPORTS

Chicago Responsible Jewelry Conference. The seventh annual Chicago Responsible Jewelry Conference (CRJC) was held August 11–13, 2023, in Rosemont, Illinois. **Susan Wheeler**, Responsible Jewelry Transformative (RJT) founder and Virtu Gem cofounder, opened by highlighting efforts to further the United Nations Sustainable Development Goals (SDGs) and the UN Women's Generation Equality campaign. The first of the 17 SDGs is to end poverty, which disproportionately affects the roughly 40 million artisanal and small-scale miners worldwide. Wheeler said poverty poses a risk to the jewelry industry because consumers do not want to perpetuate it. Responsible supply chains can help lift miners from poverty, she noted, and the industry can make great strides toward the UN's goals.

Anna Samsonova (Samsonova Consulting) moderated a panel on opening markets for artisanal gemstone miners in East Africa. **Pauline Mundia** (Virtu Gem Zambia), **Jessica Hudson** (Virtu Gem), **Sejal Karavadia** (Brilliant Earth), and **Cristina Villegas** (PACT and Moyo Gems) discussed the importance of information exchange with miners and cutters, developing trust with the help of local associations, creating sourcing standards, and training and education. Karavadia said customers are very receptive to a gem's mine-to-market story. Sixty percent of the miners in Moyo's supply chain are women, Villegas said, and they have begun incorporating young woman cutters. "For many years, Africa was exporting raw unprocessed materials," she said. "Now it's high-end beautiful faceted gemstones, and we should celebrate that."

Deep-sea biologist **Lisa Levin** (Scripps Institution of Oceanography, University of California, San Diego) explained how deep-sea mining of minerals, including gold and silver, would disrupt ecosystems. The International Seabed Authority (ISA) has approved 31 mining exploration contracts in international waters as of January 2023 and is developing regulations. Deep-sea ecosystems host abundant life, with interdependent species that depend on specific hydrologic and geochemical properties, she said, and provide many benefits to the broader ocean. The deep sea is also home to bacteria that consume methane, a driver of global warming. Levin said mining could cause extinctions and risks destruction of deep-sea biodiversity. Additionally, scientists believe that post-mining restoration is not possible on the seafloor. Since the definition of serious harm remains unclear and much about these ecosystems is still unknown, she said, there is insufficient knowledge for evidence-based decision making by the ISA.

Holly McHugh (Mejuri, Inc.) moderated a panel on responsible silver sourcing. Panelists noted an increase in high-level guidance for responsible sourcing. Examining this market is complex because more than 70% of silver production is a byproduct of other mining, panelists said, while artisanal and small-scale mining is challenging because silver requires so much mining effort. **Torry Hoover** said Hoover & Strong's refined metals are now 100% recycled, and **Will Nevins-Alderfer's** W.R. Metalarts uses Fairmined silver for its alloys. Many of the Richline Group's larger customers now ask about sourcing, said **Mark Hanna**, and the company has begun tracking silver with blockchain. He emphasized knowing your supplier and customer to ensure ethical products.

Susan Wheeler and Virtu Gem's **Chiko Manda** (via video message) discussed Malawi's gem trade. The country exports hundreds of kilograms of high-quality aquamarine annually but is one of the poorest in the world. Manda said very few gems mined in Malawi are processed there due to lack of expertise and equipment, compounded by smuggling problems, and data indicate that less than 1% of its aquamarine is legally exported. He asked jewelry companies to allocate a small percentage of their budgets to buy cut stones from source countries to motivate cutters to improve their skills. Wheeler added that this would improve traceability. "If you support the gem processing industry in Africa, you empower a lot of people," Manda said.

In a virtual presentation, **Mkhululi Nkosilamandla Ncube** (African Minerals Development Center, AMDC) introduced the African Mining Vision (AMV), a project of the UN. The AMV aims to transform the paradox of mineral wealth and dire poverty through equitable mineral exploitation. The AMDC's methods to implement the AMV include community engagement, training, technology, and financial support. As part of the approach, the Africa Gemstones and Jewellery Exhibition and Conference (AGJEC) series promotes the trade of African gemstones within the continent. The first event was held in Zambia in July; upcoming events will take place in Nigeria and Ghana this fall.

Brecken Branstrator (GemGuide) moderated a panel on working with source country gem traders (figure 33). **Eric Braunwart** (Columbia Gem House), **Ola Erogbogbo-Oyeniyi** (Deinte Designs Limited), Pauline Mundia, **Stuart Pool** (Nineteen48), and Susan Wheeler shared key takeaways, including the importance of understanding the local market and legal system, supply chain analysis, and working with local partners. Erogbogbo-Oyeniyi said that helping a community and weaving that into a gem's story is a great benefit.

Anna Bario described founding jewelry company Bario Neal with fellow designer Page Neal in 2008 and developing a responsible supply chain. Early on, they connected with Ethical Metalsmiths, the Alliance for Responsible Mining (ARM), and artisanal miners in Tanzania and Peru. They built relationships with ethical suppliers over the next decade and in 2019 hired a consultant to help establish a process based on the UN SDGs and OECD Due Diligence Guidance for Responsible Business Conduct. This includes a code of conduct they share with suppliers, supplier interviews, and an eight-step partner and material evaluation process. In 2020, the company released its first biannual sustainability report, possibly the first by a small independent jeweler. Their next goal is Climate Neutral certification.

Figure 33. Pauline Mundia, Susan Wheeler, Eric Braunwart, and Ola Erogbogbo-Oyeniyi discuss working with gem traders in source countries. Photo courtesy of RJT.

A panel on sex trafficking in Marange, Zimbabwe, moderated by **Brandee Dallow** (Grandview Klein Diamond Group), began with a documentary clip of survivors' stories. The area has been fraught with conflict and violence since the discovery of diamonds there in 2006. The U.S. has banned imports of Marange diamonds due to reports of forced labor. According to **Abigail Sibanda** (Marange Women's Alliance, MWA) (figure 34, left), the military, police, mine guards, and informal miners collaborate to smuggle diamonds out and exploit women and girls. Vulnerability to trafficking stems from Zimbabwe's high poverty, and many victims are lured by the promise of mining work. The community questions where the diamond revenue goes because there is no development, Sibanda said. Susan Wheeler noted that RJT and MWA have facilitated support for survivors through court advocacy, but prosecution is still very limited. MWA helps survivors with peer-to-peer counseling and other support and empowers all women to speak out, holding weekly meetings on WhatsApp. The group has been planning to pur-

Figure 34. Left: Abigail Sibanda describes efforts by the Marange Women's Alliance to help women and girls in Zimbabwe. Right: Laura Galvis (ARM) speaks about Fairmined-certified projects combining gold mining and agriculture in Colombia. Photos courtesy of RJT.

chase a chicken coop to develop consistent income and pay for their cellular data, which RJT currently covers. MWA is also creating a billboard campaign for Marange to highlight the issue. "We protect the diamonds. Why don't we protect the women?" remarked Sibanda, who has relocated outside of Zimbabwe because her activism has put her at risk.

Roy Maconachie (University of Bath, England) described the relationship between mining and agriculture in Sierra Leone based on his research there since 2003, after the civil war. Most mining occurs in the dry season, with income used to farm in the rainy season. Over the last decade, artisanal miners have shifted to gold because most alluvial diamond deposits are mined out. Artisanal gold mining here is dominated by women and provides a reliable income. The interconnected nature of farming and mining can help rebuild agricultural institutions destroyed during the war, he said, but miners still need basic infrastructure, access to markets and credit, and technology.

Laura Galvis (ARM) (figure 34, right) detailed three Fairmined-certified projects—the Íquira cooperative, La Gabriela, and the Chede mine—that support almost 200 workers and show how small-scale gold mining and agriculture coexist in Colombia. The Fairmined label certifies gold, silver, and platinum from small-scale mining organizations using responsible practices, and it comes with the Fairmined Premium, an economic incentive. The Chede mine committee will use this year's premium to sponsor a coffee brand sourced by miners farming coffee; they have 5,600 Fairmined credits and need 20,000 for this project. Businesses can buy Fairmined credits to support the project of their choice.

Sarah Yood (Jewelers Vigilance Committee) and **Andrea Hill** (Hill Management Group) discussed U.S. sanctions against Russian diamonds due to the war in Ukraine. Yood explained that because diamonds are considered a product of the country in which they are cut—with 90% cut in India—Russian diamonds can still reach the U.S. She acknowledged India's difficult position and the issue of protecting jobs there. The EU and the G7 countries are working to stop the flow of Russian diamonds. (At press time, an announcement was expected shortly.) Yood said that starting in 2024, G7 countries will likely require diamonds of one carat or larger to carry proof they were not mined in Russia (the size threshold will be progressively lowered). Hill said that in theory, it will eventually be clear if a diamond originated in Russia or Zimbabwe.

Saleem Ali (University of Delaware and UN International Resource Panel, IPA) presented an IPA report analyzing resource rushes in Africa, which found that mineral resources can lead to migration within Africa and prevent migration to Europe. A key message of the report was that property rights to resources can reduce forced migration. Ali suggested jewelry companies partner with the UN High Commission on Refugees to train refugees in jewelry making.

Natasha and Eric Braunwart (Columbia Gem House), **Megan Cochran** (Megan Cochran Jewelry Design), and **Hannah Smythe** (Toast Fine Jewelry) discussed how responsibly sourced designs can engage consumers. The MJSA 2023 Design Challenge, sponsored by Columbia Gem House, asks for designs based on a set of gemstones and a fictional client story. The Jewelry for Wildlife raffle of selected pieces benefits CRRIFS, a wildlife rescue, rehabilitation, and research center in Guaymas, Mexico.

Shannon Kurzyniec and **Chelsea Rowe** of the Ethical Metalsmiths Student Committee introduced 2023's So Fresh + So Clean online responsible jewelry exhibition, which asked artists to consider the life cycle of their creations. This year's awards went to Rashele Alradaideh (Virginia Commonwealth University), Amy Beeler (Bowling Green State University), and Maria Hammond (Manchester Metropolitan University, England), with cash prizes sponsored by Hoover & Strong, Rio Grande, and Earthworks.

The conference also included a collaborative session on advancing the UN SDGs through jewelry supply chains. Sunday offered a Responsible Gem Boutique with eight suppliers, co-located with the InStore Show. After Saturday's sessions, Anna Samsonova announced that attendee donations had fully funded the Marange Women's Alliance's chicken coop project.

Erin Hogarth
GIA, Carlsbad

Turquoise United Conference 2023. The second annual Turquoise United conference was held August 10–12, 2023, at the Albuquerque Convention Center in New Mexico. The vision of the conference is to bring together members of the turquoise industry at a single event for discussion and reunion. With this goal in mind, the conference caters to every aspect of the turquoise industry, attracting miners, lapidaries, collectors, dealers, artists, treatment experts, and researchers. A year ago, GIA representatives attended the inaugural Turquoise United conference (Fall 2022 GNI, pp. 390–394).

This year, there were additional symposium sessions across a range of topics and new competitions for registered conference participants. The first session was hosted by Turquoise Museum executive director **Jacob Lowry**, with a panel consisting of **Kenneth Van Wey** (Indian Arts and Crafts Board), **Matthew Wernz** (Federal Trade Commission), and **Sean Hyrons** (U.S. Fish and Wildlife Service). The panel discussed the laws surrounding the sale and purchase of turquoise jewelry and gave examples of situations in which their respective agencies may become involved (figure 35). The panelists offered advice to consumers purchasing turquoise jewelry, noting the importance of a written receipt stating the authenticity and nature of the product in as much detail as possible.

The turquoise grading system proposed by **Joe Dan Lowry** at last year's conference has been put into practice. Attendees could attempt to grade sample stones or stones

Figure 35. From left: Jacob Lowry, Sean Hyrons, Matthew Wernz, and Kenneth Van Wey engage in a panel discussion titled "Laws: Liabilities and Protections." Photo courtesy of the Turquoise Museum.

of their own using the system based on turquoise master stone sets and grades of color, matrix, and "zat" (boldness and dynamism). Application of the grading system requires detailed knowledge of certain turquoise features present at different mines. For example, author AG did not recognize "waterweb" matrix as being a valuable pattern, and therefore gave a lower matrix score on a stone with a high value. The grading system continues to be developed with feedback from the conference, with a goal of publicly accepted use by 2027.

The conference also offered courses for attendees. A "Turquoise Basics" course taught by Jacob Lowry described the types of turquoise and turquoise imitations in the market to better inform new buyers of the stone. Joe Dan Lowry taught a class called "Collecting 101," offering guidance to consumers beginning their own turquoise collection. A follow-up course, "Collecting 102," is planned for Turquoise United 2024.

Some attendees were rewarded for their impressive specimens and extensive turquoise knowledge. A highest-grade turquoise stone contest received numerous entries from multiple mines, ranging from natural cabochons with striking color and matrix to hefty rough turquoise nuggets. Best in Show winner **Mark Baca** (American Turquoise Online) received a monetary prize and trophy (figure 36). An identification contest over both days of the conference allowed attendees to test their skills at identifying the nature and mine origin of turquoise specimens. **Michael Turano** (Michael Turano Lapidary) won the contest, with **Dye Masaki** (Native Spirit) placing second, and **Ty Gibson** (Gibson Lapidary, LLC) in third.

Author AG presented his research on the Mona Lisa mine, located in western Arkansas, in a session on August 11. He provided details about the history, geology, mineralogy, and current mining operations at the site. Discussion about the methods used and Mona Lisa turquoise's potential place in the market followed the presentation. Material from the mine was also on display at the Turquoise Museum, where the day ended with the Collectors' Circle Gala.

Figure 36. Mark Baca (American Turquoise Online) holds his winning piece (right) and trophy for Best in Show. Photo courtesy of the Turquoise Museum.

Figure 37. Left: A conference participant examines turquoise cabochons. Right: Iranian turquoise cabochon with a brown "spiderweb" matrix pattern. Photos by Aaron Palke.

The following morning, author AP presented GIA's methods for identifying turquoise in the gemological laboratory. Attendees expressed their interest in learning more about these techniques and shared their views on terminology in the turquoise industry.

Next, Joe Dan Lowry presented a session on the challenges of fingerprinting turquoise mine sources, especially in archaeological contexts. The heterogeneity of turquoise, the multitude of sources, and the stone's formation in near-surface, sedimentary environments create unique challenges when trying to determine a stone's mine origin.

Throughout the conference, a gem show focused solely on turquoise was open to the public. Roughly a dozen dealers participated, offering a wide variety of turquoise material (figure 37), including high-end jewelry pieces, natural rough material, untreated cabochons, stabilized cabochons, and beadwork. Many American turquoise localities were represented, while turquoise from Iran, China, Egypt, and Mexico was also available. A silent auction allowed conference attendees to bid on natural turquoise and turquoise jewelry pieces donated by the event sponsors.

The conference concluded with a banquet honoring the first inductees into the Turquoise Hall of Fame: Joseph Pogue, Leonard Hardy, Robert Zachary, Philip Chambless, and James Elquist. These honorees were nominated for their impact on the turquoise industry. The event sponsors reiterated their desire to grow Turquoise United, with confirmation that the annual event will be hosted in Albuquerque in 2024.

Alex Goodsuhm and Aaron Palke
GIA, Carlsbad

ERRATUM

In the Summer 2023 article on augite from Vietnam (pp. 182–194), the carving sizes in figure 1 were incorrectly presented in centimeters. These were the millimeter sizes of the two carvings.